

See discussions, stats, and author profiles for this publication at: <http://www.researchgate.net/publication/267786695>

Multiscale soil moisture retrievals from microwave remote sensing observations

ARTICLE

CITATION

1

DOWNLOADS

22

VIEWS

9

1 AUTHOR:



[Maria Piles](#)

Polytechnic University of Catalonia

53 PUBLICATIONS 205 CITATIONS

SEE PROFILE

Doctoral Thesis

Multiscale soil moisture
retrievals from microwave
remote sensing observations

Maria Piles Guillem

Remote Sensing Lab. – Dept. Teoria del Senyal i Comunicacions
Universitat Politècnica de Catalunya

Advisors: Dr. Adriano Camps and Dr. Mercè Vall-llossera

Barcelona, June 2010

©Maria Piles Guillem, 2010.

Multiscale soil moisture retrievals from microwave remote sensing observations, *Maria Piles Guillem*, Ph.D. Thesis, Universitat Politècnica de Catalunya.

This work has been funded by the Spanish Ministry of Science and Education under the FPU grant AP2005-4912 and projects ESP2007-65667-C04-02 and AYA2008-05906-C02-01/ESP.

Cover image and design: Daniel Nuñez.

A mis padres y a mi hermano

*A todas las personas con las que he compartido
estos años de tesis*

Abstract

Soil moisture is a key state variable of the terrestrial water cycle. It is the main variable that links the Earth's water, energy and carbon cycles, and soil moisture variations affect the evolution of weather and climate over continental regions. Accurate observations of the Earth's changing soil moisture are needed to achieve sustainable land and water management, to enhance weather and climate forecasting skill, and to develop improved flood and drought monitoring capability. This Ph.D. Thesis focuses on the measurement of the Earth's surface soil moisture from space at a global and regional scale.

Theoretical and experimental studies have proven that L-band passive remote sensing is optimal for soil moisture sensing due to its all-weather capabilities and the direct relationship between soil emissivity and soil water content under most vegetation covers. However, achieving a temporal and spatial resolution that could satisfy land applications has been a challenge to passive microwave remote sensing in the last decades, since a real aperture radiometer would need a large rotating antenna, which is difficult to implement on a spacecraft. Currently, There are three main approaches to solving this problem: (i) the use of an L-band synthetic aperture radiometer, which is the solution implemented in the ESA Soil Moisture and Ocean Salinity (SMOS) mission, launched on November the 2nd 2009; (ii) the use of a large lightweight radiometer and a high-resolution radar operating at L-band, which is the solution adopted by the NASA Soil Moisture Active Passive (SMAP) mission, scheduled for launch in 2014; (iii) the development of pixel disaggregation techniques using higher resolution data, which could apply to both SMOS and SMAP.

Estimation of soil moisture from passive L-band measurements is complex since there are other soil and vegetation parameters affecting the land emission that must be carefully accounted for in the retrieval process. The first part of this work focuses on the analysis of the SMOS soil moisture inversion algorithm, which is crucial to retrieve accurate soil moisture estimations from the radiometric measurements. Different retrieval configurations are examined using simulated SMOS data, considering the option of adding *a priori* information from parameters dominating the land emission at L-band –soil moisture, soil roughness, soil temperature, vegetation albedo and vegetation opacity– with different associated uncertainties. Results illustrate the effect of adding or not auxiliary information on the precision of soil moisture retrievals and an optimal retrieval configuration for SMOS is devised.

The spatial resolution of SMOS and SMAP radiometers (40-50 km) is adequate for many global applications, but is a limiting factor to its application in regional scale studies, where a resolution of 1-10 km is needed. The second part of this Thesis contains three novel approaches for the improvement of the spatial resolution of SMOS and SMAP observations:

- A deconvolution scheme for the improvement of the spatial resolution of SMOS radiometric observations has been developed. Results using simulated SMOS observations and airborne field experimental data show that with this approach it is feasible to improve the product of spatial resolution and radiometric sensitivity of SMOS observations in a 49% over land pixels and in a 30% over sea pixels.
- A downscaling algorithm for improving the spatial resolution of SMOS-derived soil moisture estimates using higher-resolution visible/infrared data from MODIS has been

developed. Results of its application to airborne field experimental data and to the first SMOS images acquired during the commissioning phase provide a first evidence of its capabilities. SMOS-derived soil moisture maps at 64, 32, 16 and 8 km have been obtained; the soil moisture variability is nicely captured at the different spatial scales, but further research is needed to validate the accuracy of the retrievals at every spatial resolution and establish a downscaling limit.

- A change detection approach for combining SMAP radar and radiometer observations into a 10 km soil moisture product has been developed and validated using airborne field experimental data and SMAP-like observations.

This work has been developed within the preparatory activities of SMOS and SMAP, the two first-ever satellites dedicated to monitoring the temporal and spatial variation on the Earth's soil moisture fields. The retrieval studies and downscaling algorithms presented will timely contribute to get the most out of these vital observations, that will further our understanding of the Earth's water cycle, will help improve weather and climate models, and will lead to a better water resource management.

Contents

1	Introduction	1
1.1	Motivation	1
1.2	Importance of soil moisture estimations	2
1.3	Earth observation for global mapping of soil moisture	5
1.3.1	The SMOS mission	6
1.3.2	The SMAP mission	11
1.4	Soil moisture downscaling algorithms	12
1.5	Thesis outline	14
2	Review of passive microwave remote sensing of soil moisture	15
2.1	Basic concepts on microwave radiometry	15
2.1.1	Brightness and power collected by an antenna	15
2.1.2	Blackbody radiation	16
2.1.3	Gray body radiation	18
2.1.4	Power-temperature correspondence	18
2.1.5	Measuring brightness temperatures from space	19
2.1.6	The Stokes parameters	21
2.2	L-band emission of land covers	22
2.2.1	Thermal radiation and surface emissivity	22
2.2.2	Water in soils	23
2.2.3	Dielectric properties of soils	23
2.2.4	Surface roughness	25
2.2.5	Vegetation effects	26
2.3	Soil moisture retrieval techniques	28
3	Auxiliary data impact on SMOS soil moisture retrievals	31
3.1	Introduction	31
3.2	Simulation and retrieval strategy	32
3.3	Simulation results	34
3.4	Discussion and conclusions	38
4	Analysis of the SMOS soil moisture retrieval algorithm	41
4.1	Introduction	41
4.2	Methodology	42
4.3	Sensitivity analysis	44
4.4	Analysis with simulated SMOS data	48
4.4.1	Simulation strategy	48
4.4.2	Simulation results	49
4.5	Discussion and conclusions	54

5	Spatial resolution enhancement of SMOS data: a deconvolution-based approach	57
5.1	Introduction	57
5.2	Deconvolution algorithms	58
5.2.1	Discrete formulation	58
5.2.2	Frequency-domain algorithms	59
5.2.3	Wavelet-domain algorithms	62
5.3	Application to SMOS simulated observations	62
5.3.1	Spatial resolution enhancement	63
5.3.2	Radiometric sensitivity evaluation	64
5.3.3	Quantitative results	68
5.4	Application to airborne observations over the Ebro river mouth	70
5.4.1	Airborne system overview	70
5.4.2	Ebro river mouth field experiment	71
5.4.3	Downscaling strategy	71
5.4.4	Experimental results	72
5.5	Conclusions	74
6	Downscaling SMOS-derived soil moisture using higher resolution visible/infrared data	75
6.1	Introduction	75
6.2	Downscaling activities at the REMEDHUS Cal/Val site	76
6.2.1	Data description	77
6.2.2	The temperature/vegetation index space	79
6.2.3	Downscaling approach	80
6.2.4	Results	81
6.3	Downscaling approach for SMOS	83
6.3.1	Data description	83
6.3.2	Method	84
6.3.3	Results	86
6.4	Discussion and conclusions	100
7	A change detection algorithm for retrieving high-resolution soil moisture from SMAP	103
7.1	Introduction	103
7.2	Change detection method	104
7.3	Test of assumptions using SMEX02 data	105
7.3.1	SMEX02 description	105
7.3.2	Validation of the assumptions	105
7.4	Application to OSSE data	108
7.4.1	OSSE data set	108
7.4.2	Results	109
7.5	Error budget	110
7.6	Conclusions	112
8	Conclusions and future lines	113
8.1	Main conclusions	113
8.2	Original contributions	116
8.3	Future lines	116

A Acronyms	119
B Symbols	121
List of Figures	126
List of Tables	129
References	143
List of publications	143

*Every so often, I like to go to the
window, look up, and smile for a
satellite picture*

Stephen Wright (1955-)

1

Introduction

Two space missions have been proposed to provide the first dedicated global measurements of the Earth's surface soil moisture: the European Space Agency (ESA) launched the SMOS mission in November 2009 and the US National Aeronautics and Space Administration (NASA) plans to launch the SMAP mission in 2014. This thesis has been performed within the preparatory activities of these missions, involving the analysis of the retrieval techniques, which have an impact on the accuracy of the estimations, and the development of downscaling algorithms to enhance the spatial resolution of the observations. As it will be presented along this document, the spatial resolution of SMOS and SMAP measurements can be improved from ~ 50 - 60 km down to ~ 10 km, without a significant degradation of the Root Mean Square Error (RMSE).

This Chapter describes the motivation of this work and the context in which it has been developed. It contains background information related to SMOS and SMAP space-borne projects, reviews the the state-of-the-art of the soil moisture downscaling algorithms, and presents the Thesis outline.

1.1 Motivation

Although soil only holds a small percentage of the total global water budget, soil moisture plays an important role in the Earth's water cycle; it is a key variable in the water and energy exchanges that occur at the land-surface/atmosphere interface and conditions the evolution of weather and climate over continental regions. Global observations of the Earth's changing soil moisture are needed to enhance climate prediction skills and weather forecasting, which will benefit climate-sensitive socio-economic activities, including water management, agricultural productivity estimation, flood prediction and drought monitoring [*Entekhabi et al.*, 1999; *Krajewski et al.*, 2006; *Wagner et al.*, 2007].

Experimental and theoretical studies have shown that passive L-band microwave remote sensing is the most promising technique for global monitoring of soil moisture due to its all weather capability and the direct relationship of soil emissivity with soil water content [*Shutko and Reutov*, 1982; *Schmugge et al.*, 1986; *Njoku et al.*, 2002]. Microwave remote sensing encompasses both active and passive forms, depending on the sensor and its mode of operation [*Ulaby et al.*, 1981]. Active sensors (radars) are capable of remotely sensing soil moisture at high spatial resolution (~ 1 km or even higher with SAR), but radar backscatter

is highly influenced by surface roughness, topography, vegetation canopy structure and water content [Dubois *et al.*, 1995; Shi *et al.*, 1997]. In contrast, passive sensors (radiometers) have a reduced sensitivity to land surface roughness and vegetation cover, but their spatial resolution is typically low ($\sim 40\text{-}50$ km) [Jackson *et al.*, 1996; Njoku and Entekhabi, 1996]. The limited-duration SkyLab mission in the 1970s was the earliest demonstration of soil moisture retrieval from passive L-band observations on orbit [Jackson *et al.*, 2004]. In the near future, two space missions will measure soil moisture at global scale using L-band microwave radiometers: the ESA launched the Soil Moisture and Ocean Salinity (SMOS) mission in November 2009 [Kerr *et al.*, 2001], and the NASA will launch the Soil Moisture Active Passive (SMAP) mission in 2014 [National Research Council, 2007]. These two missions will provide unprecedented decade-long global mapping of the Earth's surface soil moisture fields with high accuracy and a ground resolution between 40-50 km. SMAP has a high-resolution radar to enhance the spatial resolution of the retrievals up to 10 km.

Estimation of soil moisture from radiometric measurements is not simple since there are many soil and vegetation parameters affecting the land emission. An analysis of the algorithms to retrieve bio/geophysical variables from brightness temperature measurements and the assessment of the impact of each of the parameters involved is crucial for obtaining accurate soil moisture estimations. Due to technological limitations, the spatial resolution of SMOS and SMAP radiometers is limited to 40-50 km. This resolution, while adequate for many global applications, is a limiting factor to its application in regional scale studies, where a resolution of 1-10 km is needed [Entekhabi *et al.*, 1999; Crow *et al.*, 2005a]. This Ph.D. Thesis focuses on the measurement of the Earth's surface soil moisture from space – both on a global level, through the analysis of retrieval algorithms that impact the accuracy of the observations, and on a local level, through the development of downscaling techniques that could enhance the spatial resolution of the observations.

The research described on this Thesis has been carried out at the UPC Remote Sensing Laboratory, which has been involved in the SMOS instrument concept and science applications since 1993, and where more than 15 Ph.D. Thesis have been pursued covering different aspects of the mission and potential improvements. This working context has provided a unique opportunity for participating in both the engineering and the scientific sides of the SMOS mission. Also, a 4-month stay at MIT with professor D. Entekhabi made possible the work conducted in the frame of the SMAP mission.

1.2 Importance of soil moisture estimations

Soil moisture, as the state variable of the water cycle over land, controls water fluxes between the atmosphere, the surface, and the subsurface (See Fig. 1.1). Because a large amount of heat is exchanged when water changes phase, the water cycle is fundamental to the dynamics of the Earth's energy cycle. Also, since water is the ultimate solvent in the Earth system, biogeochemical cycles such as carbon, nitrogen and methane are embedded in the water cycle. Through these dynamics, soil moisture conditions the evolution of weather and climate over continental regions. Hence, global measurements of soil moisture are needed to improve our understanding of water cycle processes, ecosystem productivity, and the linkages between the Earth's water, energy, and carbon cycles.

Global soil moisture information will be transformational for the Earth's system science; it will help characterize the relationship between soil moisture, its freeze/thaw state, and the associated environmental constraints to ecosystem processes including land-atmosphere

carbon, water and energy exchange, and vegetation productivity. At the same time, global soil moisture information will enable societal benefit applications such as better water resource assessment, improved weather forecasts, natural hazards mitigation, predictions of agricultural productivity, and enhanced climate prediction, human health and defense services. The prospective use of remotely-sensed soil moisture data on these applications is briefly described in the following sections. More information can be found in SMOS and SMAP home pages, which are www.esa.int and smap.jpl.nasa.gov, respectively.

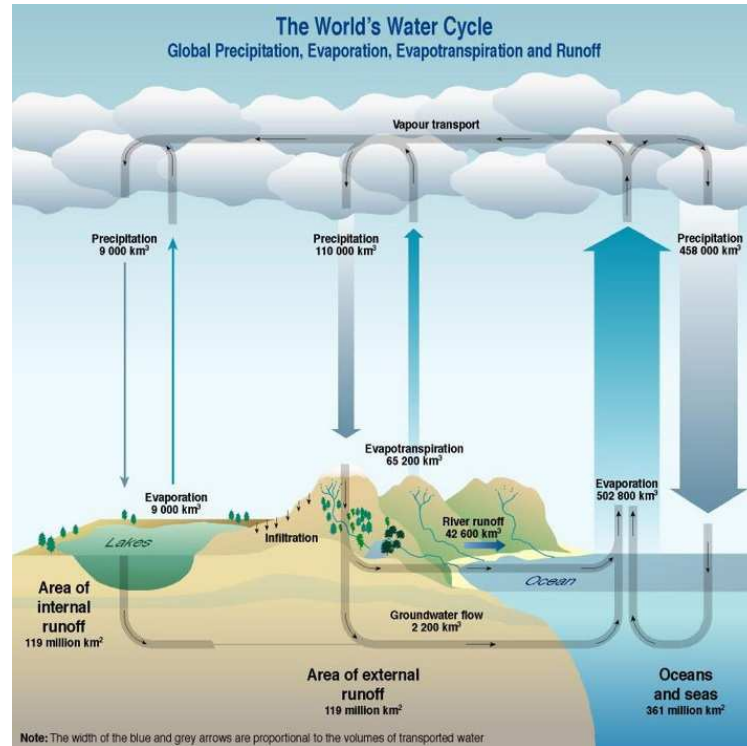


Figure 1.1 Precipitation, evaporation, evapotranspiration and runoff are the processes that move water through the water cycle. Values in the diagram show the volume of water that moves along each path in a year (www.unep.org)

Weather forecast applications

The quality of weather forecasts is significantly dependent on the availability of accurate initial states for key atmospheric variables, due to the chaotic nature of the atmosphere. To date, significant effort has been concentrated on measuring the initial states of temperature, air density, winds, and water vapor to improve weather forecasts; however, it is now recognized that the next significant advances in the quality of weather forecasts will come from constraining the systems coupled to the atmosphere such as soil moisture over land. Numerous studies show that the initialization of global weather forecast models with accurate soil moisture information will enhance their prediction skills and extend their forecast lead-times. While the spatial resolution of SMOS and SMAP radiometers ($\sim 40\text{-}50$ km) is adequate for global applications, downscaling techniques must be developed to extend the use of the data to regional scale studies, where a resolution of 1-10 km is needed [*Entekhabi et al.*, 1999].

Temporal sampling requirements for surface soil moisture follow from the time scales of surface wetting and drying. Capturing the impacts of storm/interstorm sequences, combined

with the inertia of surface storage, requires a revisit of ~ 3 days [Calvet et al., 1998; Walker and Houser, 2004]. The baseline SMOS and SMAP implementation meets this measurement requirement, though improved latency might increase operational use.

Hydrological hazards mitigation: drought, flood, and landslides

Prediction of droughts, floods and flash-floods requires not only precipitation information, but also soil moisture and freeze/thaw state information. Also, soil moisture in mountainous areas is one of the most important factors of landslides. To date, there is no global *in situ* or current satellite capability to monitor and map soil moisture, and estimations are produced from models, with a high degree of uncertainty [Crow et al., 2005a]. The assimilation of accurate soil moisture observations at the scale of severe weather phenomena over land (1-10 km) on model predictions will therefore help to improve both drought and flood forecasts, enabling more effective hazards monitoring and mitigation efforts (see Fig. 1.2).

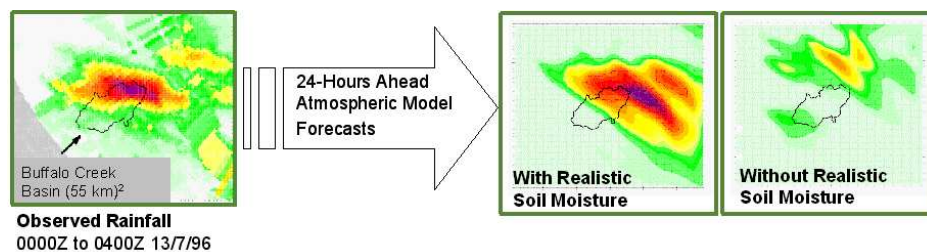


Figure 1.2 Soil moisture initialization of Numerical Weather Prediction models leading to an improved precipitation forecasts (adapted from Chen et al. [2001])

Agricultural productivity

Ecosystem services require direct monitoring of soil moisture availability to plants (natural and cropped) to assess productivity. Hence, the use of realistic soil moisture data on the models will allow significant improvements in agricultural productivity forecasting and operational crop productivity and water stress information systems.

Climate prediction applications

Soil moisture data will help improve seasonal climate predictions, which will benefit climate-sensitive socio-economic activities, including water management, agriculture, and fire, flood, and drought hazards monitoring [Douville and Chauvin, 2004]. Also, projections of the terrestrial water cycle and fresh-water supplies under global change are critically dependent on how models link the water cycle to the energy cycle. How the water cycle responds to an increased radiative forcing due to accumulation of greenhouse gases in the atmosphere depends on how the models parameterize surface energy flux rate dependencies on soil moisture. Thus, global observations of soil moisture provide a clear opportunity to improve our understanding of global change impacts.

Human health services

Soil moisture mapping will allow monitoring and prediction of factors that impact human health. For instance, soil moisture information at high resolution might contribute to a

better water resource assessment, and will allow monitoring of soil moisture anomalies, which could be linked to human diseases [*Shaman and Day, 2005*]. Also, soil moisture information will indirectly benefit human health applications, e.g. better weather forecasts, leading to predictions of virus spreading rates and heat stress; better flood forecasting, leading to improved disaster preparation and response, and improved seasonal soil moisture forecasts, leading to improved famine early warning systems.

Defense applications

High resolution soil moisture data would be very helpful for terrain trafficability assessment, which is a major element on land autonomous deployments and has a significant tactical value [*Flores et al., 2009*]. Also, soil moisture estimates are required to initialize aviation weather forecast models, and will enable improved forecasts of density altitude, fog formation, and dust generation.

1.3 Earth observation for global mapping of soil moisture

Currently, there are two space missions dedicated to monitoring the temporal and spatial variation of the Earth's soil moisture: the ESA Soil Moisture and Ocean Salinity (SMOS) mission, launched in November 2009, and the NASA Soil Moisture Active Passive (SMAP) mission, that will be launched in 2014. These two missions will provide unprecedented global mapping of the Earth's surface soil moisture fields, and are expected to satisfy the science and applications needs on Section 1.2.

Both SMOS and SMAP use microwave radiometry at L-band (1.400-1.427 GHz) to make soil moisture measurements. Theoretical and experimental studies have shown that L-band radiometry is optimal for soil moisture sensing due to the direct relationship of soil emissivity with soil water content [*Wang and Choudhury, 1981; Schmugge et al., 1986; Jackson et al., 2004*]. Also, the atmosphere at microwave frequencies may be considered transparent, and vegetation is semi transparent (up to $\sim 5 \text{ kg/m}^2$), which allows observations of the underlying layers [*Jackson et al., 1982; Jackson and Schmugge, 1991; Njoku and Entekhabi, 1996*]. SMOS and SMAP radiometers are expected to provide highly accurate soil moisture estimations with a ground resolution of about 40-50 km. SMAP also has a high-resolution radar to enhance the spatial resolution of the retrievals up to 10 km.

Alternatives to L-band radiometry for soil moisture sensing include the use of higher frequency radiometers, the use of radars operating at L-band, or the use of visible/infrared sensors. However, they suffer from major drawbacks that limit their applicability, as will be discussed hereafter.

Higher frequency microwave radiometers such as those at C-band or X-band (i.e. AMSR-E, WindSat, TMI) are sensitive to soil moisture, but present the disadvantage of being highly attenuated by vegetation. Therefore, its applicability is limited to areas with moderate vegetation ($< 3 \text{ kg/m}^2$). In contrast, L-band radiometric observations are sensitive to soil moisture through vegetation of up to $\sim 5 \text{ kg/m}^2$, which corresponds to about 70% of the non-frozen land regions on Earth, excluding dense forests. Also, at higher frequencies the atmosphere is less opaque –its effects need to be corrected– and the soil penetration depth is lower ($\sim 1 \text{ cm}$ *vs.* the $\sim 5 \text{ cm}$ at L-band). Note that greater penetration depths are desirable to characterize the soil moisture below the skin layer of the emitting surface.

Radars operating at L-band (i.e. JERS, PALSAR), in turn, are capable of sensing soil moisture and provide higher spatial resolution than radiometers (< 1 km). However, they typically operate with narrow swaths, meaning that they do not meet the temporal requirements of global land hydrology applications (~ 3 days). Also, radar measurements are highly affected by soil surface roughness and vegetation scattering, which leads to a high uncertainty in the soil moisture retrieval algorithms [Dubois *et al.*, 1995; Shi *et al.*, 1997].

Visible/infrared sensors are also capable of providing high spatial resolution (< 1 km), and controlled experiments have shown their potential to sense soil moisture [Idso *et al.*, 1975; Price, 1977; Adegoke and Carleton, 2002; Wang *et al.*, 2007]. However, they are equally sensitive to soil types, and it is difficult to decouple the two signatures. Hence, visible/infrared sensors are commonly used to provide an indirect measurement of soil moisture, but not to retrieve it. Also note that observations in the optical domain are totally masked in the presence of cloud cover.

All things considered, it is generally recognised that passive microwave is the most promising remote sensing method for soil moisture measurement [Njoku *et al.*, 2002]. However, achieving a spatial resolution that could satisfy land applications has been a challenge to passive microwave remote sensing in the last decades, and the reason why soil moisture estimation by satellite has not been planned until recently. The problem is that to achieve adequate coverage and spatial resolution at L-band, a real-aperture radiometer would require a large rotating antenna, which is difficult to implement on a spacecraft. There are three main approaches to solving this problem that are currently under investigation and that will be widely covered in this Thesis:

- The use of synthetic aperture radiometry, which is the solution adopted by SMOS.
- The use of large lightweight antennas, which is the solution adopted by SMAP.
- The development of pixel disaggregation techniques using higher resolution data, which could apply to both SMOS and SMAP.

1.3.1 The SMOS mission

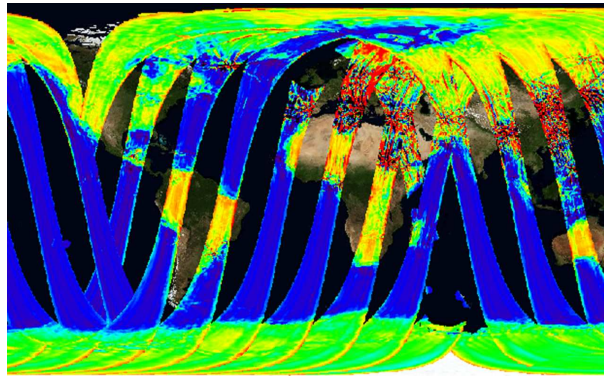
The Soil Moisture and Ocean Salinity (SMOS) mission, launched on November the 2nd 2009, is the first satellite ever attempted to globally measure the Earth's soil moisture and ocean salinity by means of L-band microwave radiometry. Soil moisture is a critical state variable of the terrestrial water cycle and the factor that links the global water, energy and carbon cycles. Moreover, sea surface salinity, jointly with sea surface temperature, determines the water density and regulates the global ocean circulation currents that moderate the Earth's climate system. The data acquired from this mission will contribute to furthering our knowledge of the Earth's water cycle [Kerr *et al.*, 2001; Barré *et al.*, 2008].

SMOS is the second Earth Explorer Opportunity mission as part of the ESA's Living Planet Programme. ESA's Opportunity missions are intended to be small research missions that focus on specific aspects of the Earth's environment and/or demonstrate new remote sensing technologies. The SMOS mission is a direct response to the current lack of global observations of soil moisture and ocean salinity, and was thought of as a cost-effective, demonstrator mission with a nominal (extended) lifetime of 3 (5) years. It has a Sun-synchronous, quasi-circular, dusk-dawn orbit, with a mean altitude of 758 km, and with 6 am/6 pm overpass times. The SMOS single payload is a completely new type of instrument: an L-band two dimensional synthetic aperture radiometer with multiangular and

Table 1.1 Main scientific requirements of the SMOS mission. See also *Mission Objectives and Scientific Requirements of the SMOS mission* [2003]

Land: global Soil moisture and vegetation water content maps	0.04 m ³ /m ³ (4%) every 3 days 0.2 kg/m ² every 6 days < 50 km spatial resolution
Ocean: global Sea Surface Salinity maps	0.1 psu every 30 days 200 km spatial resolution
Cryosphere (experimental):	Improved snow mantle monitoring and multilayer ice structure

dual-polarization/full-polarimetric capabilities, the Microwave Imaging Radiometer using Aperture Synthesis (MIRAS)(Fig. 1.4).

**Figure 1.3** First uncalibrated data sent to Earth by the MIRAS instrument on ESA's SMOS satellite (from www.esa.int, 20 November 2009)

SMOS is expected to provide global maps of soil moisture every 3 days –compatible with the temporal variability of the near surface soil moisture over continental surfaces–, with a ground resolution better than 50 km, and an accuracy of 0.04 m³/m³ volumetric humidity. This is comparable to being able to detect one teaspoonful of water mixed into a handful of dry soil. For ocean salinity, maps with an accuracy better than 0.1 practical salinity units (psu) and 200 km ground resolution will be acquired every 30 days, which is comparable to detecting 0.1 g of salt in a liter of water. As secondary objectives, SMOS is expected to provide vegetation water content maps with an accuracy of 0.2 kg/m² every 6 days, and will contribute to studies of the cryosphere [*Mission Objectives and Scientific Requirements of the SMOS mission*, 2003]. The SMOS mission requirements are summarized in Table 1.1.

L-band is a protected frequency band for radio-astronomy and remote sensing satellite services. However, it is bordered by radio location and communications services, and field experimental campaigns have provided an evidence that there is a potential risk for corruption due to out-of-band emission or Radio Frequency Interferences (RFIs). Indeed, first SMOS data (on Fig. 1.3) presented a clear RFI contamination (in red); as a consequence, the development of a RFI detection and mitigation approach has become a high priority activity during the SMOS commissioning phase.

The Microwave Imaging Radiometer by Aperture Synthesis

The SMOS single payload is MIRAS, a novel two-dimensional synthetic aperture radiometer with dual-polarization/full-polarimetric imaging capabilities that provides brightness temperature measurements of the Earth’s surface at different incidence angles.

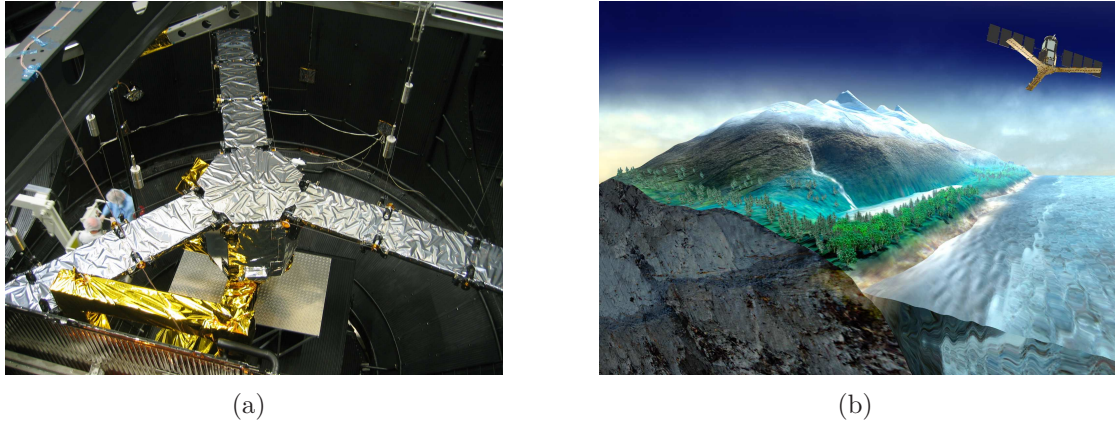


Figure 1.4 SMOS-MIRAS undergoing testing in the Large Space Simulator at ESA-ESTEC (a), and SMOS-MIRAS artist’s view (b), from www.esa.int

As said, in order to achieve adequate coverage and spatial resolution for observing soil moisture at L-band, a large rotating antenna is needed, which is a difficult and costly solution for a spacecraft. An elegant alternative was proposed by the SMOS mission by means of an innovative interferometric radiometer concept: the required antenna aperture is synthesized from 69 separate receivers, which are equally distributed over a Y-shaped antenna array –formed by three deployable arms of about 3.5 m length, and a central structure. The interferometric approach, inspired by the techniques used in radio astronomy over several decades, is based on measuring the cross-correlation of the observations from all possible combinations of receiver pairs in order to sample the signal that would have been received by a real aperture antenna.

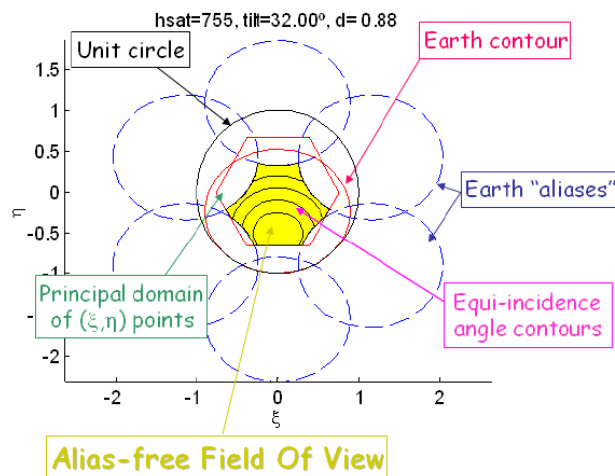


Figure 1.5 SMOS observation geometry, from *Camps et al. [2005]*

A synthetic aperture interferometric radiometer forms a brightness temperature image in the director cosines domain $(\xi, \eta) = (\sin \theta \cos \phi, \sin \theta \sin \phi)$ by a Fourier synthesis technique

of the cross-correlation of the signals collected by each pair of receiving elements [Camps *et al.*, 2008]. In MIRAS, the receiving elements are distributed along three arms 120° apart, and they are spaced $d = 0.875$ wavelengths. This antenna spacing was selected to optimize the instrument’s angular resolution, while keeping a swath wide enough so as to meet the revisit time requirement [Waldteufel *et al.*, 2003]. However, since the Nyquist criterion for hexagonal sampling ($d=1/\sqrt{3}=0.577$ wavelengths Camps *et al.* [1997]) is not satisfied, the reconstructed 2-D brightness temperature images present aliasing. Figure 1.5 illustrates the SMOS observation geometry: the half space in front of the antenna array is mapped into the unit circle in (ξ, η) coordinates, and the Earth aliases overlap with the Earth image, determining the alias-free Field Of View (FOV), marked in yellow. Sophisticated image reconstruction algorithms are required to account for instrument imperfections and obtain brightness temperature maps in the antenna reference frame (Level 1b data) from the calibrated visibilities (Level 1a data). Note that the image reconstruction process induces radiometric accuracy and bias errors, in addition to the random noise errors induced by a conventional radiometer.

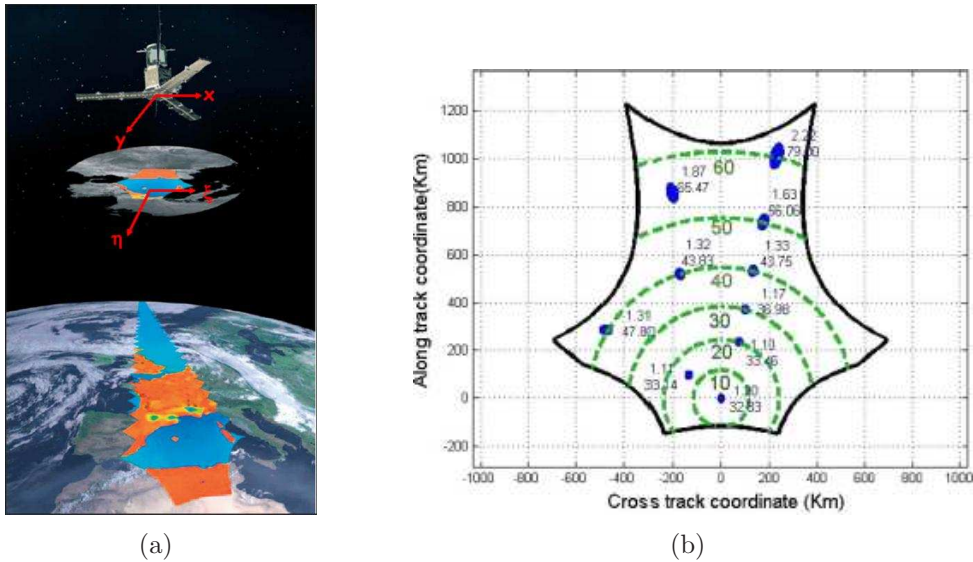


Figure 1.6 MIRAS brightness temperature imaging process, from www.esa.int (a), and SMOS simulated field-of-view in the Earth reference frame, from Piles *et al.* [2009] (b)

MIRAS takes a two-dimensional brightness temperature image every 1.2 seconds with a characteristic irregular curved hexagon-shaped field-of-view (FOV) of about 1000 km swath width (Fig. 1.6 (a)). The SMOS FOV in cross-track/along-track coordinates (Earth reference frame) is shown in Fig. 1.6 (b). As the satellite moves along its orbital path, each pixel is observed under different viewing angles (from 0° to 65°; dashed contours centered at nadir). SMOS observations are characterized for having a different pixel size, orientation, and noise level, depending on the pixel’s location within the instrument FOV. The spatial resolution varies from 30 km at nadir to 90 km at the upper borders; The radiometric sensitivity varies from 3.5 K at boresight to 5.8 K off-boresight. By registering a lot of independent information of each pixel, it is expected that soil and vegetation contributions could nicely be separated [Kerr *et al.*, 2001].

The grid chosen for the delivery of SMOS data is the Icosahedral Snyder Equal Area (ISEA) 4H9, which provides a uniform inter-cell distance of ~ 15 km [Sahr *et al.*, 2003]. This fine grid has been adopted in order to provide the correct sampling for the measurements at

the highest spatial resolution (30 km at nadir direction, Fig. 1.6(b)) since, according to the Nyquist sampling theorem, the sampling frequency must be greater than twice the highest frequency of the input signal in order to be able to reconstruct the original perfectly from the sampled version.

MIRAS can work in two operation modes: the dual-polarization and the full-polarimetric mode [Martín-Neira *et al.*, 2002]. In the dual-polarization mode, MIRAS measures the brightness temperatures in horizontal and vertical polarization. In full-polarimetric mode, MIRAS measures the four Stokes parameters (see Section 2.1.6). Receivers need to be calibrated to ensure that the accuracy requirements of the mission can be met. On board calibration is performed by injecting stable noise signals into all the receivers several times per orbit. In addition, an external absolute calibration is performed every two weeks with celestial targets [McMullan *et al.*, 2008]. Data is stored on-board and transmitted using an X-band down-link whenever a ground station is seen by the satellite.

SMOS mission products

The SMOS mission products are divided into four categories:

- *Level 0 products* consist of unprocessed SMOS data with added Earth Explorer headers. Level 0 products include, for instance, satellite data and calibration data from correlators.
- *Level 1 products* are divided into three subcategories:
 1. *Level 1a products* are calibrated visibilities (cross-correlations) grouped as snapshots.
 2. *Level 1b products* are snapshot maps of radiometrically corrected and calibrated brightness temperatures, referred to the antenna polarisation reference frame (T_{xx} , T_{yy} , and T_{xy} , as well in the full-polarimetric mode).
 3. *Level 1c products* are swath-based maps of brightness temperatures referred to a fixed grid on an Earth ellipsoid (T_{hh} , T_{vv} , and $T_I = T_{hh} + T_{vv} = T_{xx} + T_{yy}$). Level 1c products are generated separately for land and sea applications.
- *Level 2 products* are soil moisture or surface salinity swath-based maps which have been computed from Level 1c products. The conversion from Level 1c brightness temperatures to Level 2 maps includes a first step to mitigate the impact of Faraday rotation, Sun/Moon/galactic glint, atmospheric attenuation, etc. and it is done separately for soil moisture and ocean salinity.
- *Level 3 products* are based upon the spatio-temporal aggregation of Level 2 data.
- *Level 4 products* are improved Level 2/3 products through the use of auxiliary data from other sources.

Level 0 to Level 2 data products will be archived for 10 years after the end of the SMOS extended operational lifetime in orbit. Further information on these levels is given in Zundo *et al.* [2005].

Simulation and processing tools

In this Ph.D. Thesis, the SMOS End-to-end Performance Simulator (SEPS) has been used to generate SMOS-like brightness temperatures, waiting for the true satellite measurements. In turn, a dedicated L2 Processor Simulator has been implemented to retrieve soil moisture from SEPS simulated data.

SEPS is a simulation tool that covers the complete simulation of the environmental conditions seen by the radiometer, the full MIRAS instrument modelling, the determination of the retrieved relevant data measured by the instrument, image reconstruction algorithms, and graphic outputs such as fully-polarimetric brightness temperature maps reconstructed on the Earth [Camps *et al.*, 2003; *SEPS Architectural Detailed Design Document*, 2006]. Due to the unique characteristics of SMOS observations, the use of SEPS in this Ph.D. Thesis was essential and permits a better understanding of the problems that may arise at a later stage using real SMOS data. The L2 Processor Simulator is a dedicated software, originally developed for SMOS salinity retrieval studies by Talone *et al.* [2009]; Sabia *et al.* [2010], which was modified in the frame of this Ph.D. Thesis for soil moisture retrieval studies; it is a simplified version of the SMOS Level 2 Processor, which integrates the forward model and optimization algorithm described in Sections 2.2 and 2.3, incorporates the experience gained from experimental land emissivity studies [Monerris, 2009], and is designed to be used directly with SEPS output data. The L2 Processor Simulator has been entirely implemented during this research work and is key to devise an optimal soil moisture retrieval configuration for SMOS.

1.3.2 The SMAP mission

The Soil Moisture Active Passive (SMAP) space mission, scheduled for launch in 2014, has been recommended by the NRC Earth Science Decadal Survey Panel to provide global measurements of the Earth's near-surface soil moisture, and to distinguish frozen from thawed land surfaces [National Research Council, 2007].

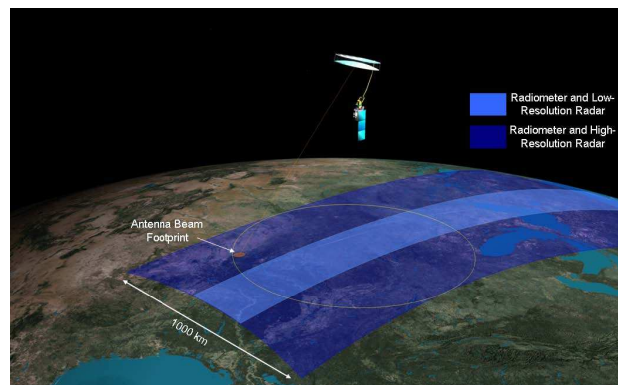


Figure 1.7 SMAP measurement geometry (from smap.jpl.nasa.gov)

In order to solve the size-mass issues of real aperture antennas working at L-band, SMAP incorporates a deployable light-weight mesh antenna with a 6 m diameter. SMAP is based on the NASA Hydros (Hydrosphere State) mission [Entekhabi *et al.*, 2004] that progressed through Phase A development until it was put on hold in 2005 due to NASA budgetary constraints. The mission payload consists of an approximately 40 km footprint L-band microwave radiometer measuring the first three Stokes parameters T_{vv} , T_{hh} and T_U , and a 3 km

footprint L-band synthetic aperture radar sensing backscattering coefficients at hh , vv and hv polarizations. The SMAP radar and radiometer share a single feedhorn and parabolic mesh reflector to make coincident measurements of surface backscatter and emission. The reflector rotates about its nadir axis at 14.6 rpm, providing a conically scanning antenna beam with a surface incidence angle of approximately 40° ; this angle maximizes the independent information obtainable from the vertical and horizontal polarized brightness temperatures. The SMAP measurement geometry is illustrated in Fig. 1.7.

Soil moisture retrieval over smooth bare soils is well established using microwave radar and radiometer sensors. However, roughness and vegetation effects are more difficult to decouple using radar, which leads to a higher uncertainty in radar only soil moisture retrieval algorithms. It is expected that the high resolution radar could serve to improve the spatial resolution of the accurate radiometer observations. Also, SMAP provides the option of exploring data fusion of passive and active microwave observations in soil moisture retrieval algorithms.

SMAP aims at providing global scale land surface soil moisture observations with a 3 day revisit time and its key derived products are:

- Soil moisture at 40 km for hydroclimatology, obtained from the radiometer measurements.
- Soil moisture at 10 km resolution for hydrometeorology, obtained by combining the high radar spatial resolution and the high radiometer accuracy in a joint retrieval algorithm.
- Freeze/thaw state at 3 km resolution from the radar measurements.

1.4 Soil moisture downscaling algorithms

The retrieval of surface soil moisture is optimal in the microwave domain, and has been demonstrated through a number of field experiments using ground-based or aircraft mounted radiometers (e.g. [[Jackson et al., 1999](#); [Narayan et al., 2004](#); [Saleh et al., 2009](#); [Monerris, 2009](#)]). Therefore, global estimation of soil moisture from remote sensing observations holds great promise for many applications. However, the spatial resolution of the upcoming satellite-based microwave radiometers (~ 40 - 50 km) is too coarse to serve regional scale applications, where a resolution of 1 to 10 km is needed [[Entekhabi et al., 1999](#); [Crow et al., 2000](#)].

The combination of radiometric data at low spatial resolution with higher resolution data coming from other sensors offers a potential solution to decompose or disaggregate large pixels into smaller ones. Also, additional information on factors controlling soil moisture variability such as soil properties, vegetation characteristics, or meteorologic observations could be used, given that reasonable physical models or empirical relationships apply.

In this context, different approaches have been explored to disaggregate low-resolution passive microwave remote sensing data to the higher resolution required. Some of these methods are based on the use of topographic and surface properties. For example, [Pellenq et al. \[2003\]](#) coupled a radiative transfer model with a hydrological model to spatially redistribute the soil water content as a function of topography and soil properties. Also, [Kim and Barros \[2002\]](#) developed an algorithm to downscale a coarse resolution soil moisture pixel using empirical connections between the spatial and temporal variability of soil moisture and

the behavior of auxiliary data such as topography, soil texture, vegetation water content, and rainfall.

The use of visible-near infrared, and thermal infrared remote sensing data for downscaling passive microwave observations has also been proposed. Most of these approaches are based on the so-called “triangle method” that relates land surface parameters to soil moisture [Carlson, 2007]; high resolution surface temperature and a vegetation index are aggregated to the scale of the microwave observation for the purpose of building a linking model that is then applied at fine scale to disaggregate the passive soil moisture observations into high-resolution soil moisture. Chauhan *et al.* [2003] demonstrated this strategy using 1-km Advanced Very High Resolution Radiometer (AVHRR) and 25 km Special Sensor Microwave/Imager (SSM/I) data; Merlin *et al.* [2008a] propose a variant of this method for SMOS using 1-km MODerate resolution Imaging Spectroradiometer (MODIS) data, soil dependant parameters, and wind speed data. As an alternative to these empirically-based approaches, a physically-based algorithm that includes a complex surface process model and high resolution multispectral data and surface variables involved in a land-surface-atmosphere model is presented in Merlin *et al.* [2005]. This method is simplified using an energy balance model in Merlin *et al.* [2008b]. However, the applicability of these algorithms to the upcoming space-borne observations is limited to the availability of the high resolution soil and vegetation parameters they need at global scale. Also, note that the use of optical data limits the use of these approaches to clear-sky conditions.

There is another approach to disaggregation that is central to the SMAP mission design. It is expected that a 10 km soil moisture product could result from the integration of passive and active technologies, based on different studies devoted to the combination of complementary radiometer and radar microwave observations. Njoku *et al.* [2002] found that radar and radiometer data from the Passive and Active L- and S-band airborne sensor (PALS) showed similar sensitivities to soil moisture spatial distributions when observed as temporal changes, and demonstrated the feasibility of a change detection approach to monitor the temporal evolution of soil moisture. A similar approach is used in Narayan *et al.* [2006] to downscale PALS data using AIRborne Synthetic Aperture Radar (AIRSAR) data, and vegetation water content measurements. A totally different strategy is followed in Zhan *et al.* [2006], where a Bayesian method is used to downscale radiometer observations using radar measurements in an Hydros-like simulated environment.

Other schemes for disaggregating passive microwave pixels include the work of Cardot *et al.* [2005], where a temporal interpolation method is proposed to couple high and low spatial resolution images of mixed pixels, and in the work of Tsegaye *et al.* [2003], where a neural network is proposed to downscale low-resolution satellite microwave remote sensing using a coupled hydrologic/radiative transfer model as input for its training.

It is likely that the minimum pixel size will be limited, with the main restrictions being: i) the spatial/temporal resolution that is technically achievable by the spaceborne remote sensing systems, ii) the noise amplification that the smaller pixels will exhibit, and iii) the strength of the physical link between soil water content and the dominant processes that control its variability at the two spatial scales used when disaggregating. With current technologies, it is expected that the downscaling limit will be on the range of tens of km. However, new passive technologies could lead the way to future missions with higher spatial resolutions, and innovative downscaling approaches could also be developed to eventually result in products < 1 km.

Spatial resolution is still a challenge for passive microwave remote sensing of land. The study and development of downscaling techniques for upcoming microwave remote sensors

is of great importance and will considerably increase its range of applications. The original contributions of this work in the field of soil moisture downscaling algorithms are fully contained in Chapters 5, 6, and 7.

1.5 Thesis outline

This Ph.D. Thesis is devoted to the retrieval of accurate and high-resolution soil moisture retrievals from microwave remote sensing observations, and is organized as follows:

Chapter 1 describes the motivation of this work and justifies its scientific and technological interest within the SMOS and the upcoming SMAP missions. The state-of-the-art of soil moisture downscaling algorithms is presented.

Chapter 2 reviews the basics of microwave radiometry, and presents the theoretical and experimental background to remote sensing of soil moisture using microwave radiometry. The state-of-the-art of soil moisture retrieval techniques is outlined.

Chapter 3 examines different SMOS retrieval configurations, depending on the ancillary information that is used in the retrievals and its associated uncertainty. The auxiliary data impact on soil moisture retrievals is thoroughly evaluated using SMOS simulated data and an optimal retrieval configuration is devised.

Chapter 4 analyzes the soil moisture inversion algorithm, both theoretically and in terms of performance. A sensitivity analysis of the SMOS soil moisture inversion algorithm illustrates the effect of adding or not *a priori* information on the precision of the retrievals. An analysis with simulated SMOS data gives a first feeling of the quantitative errors that should be expected from real upcoming measurements.

Chapter 5 introduces a deconvolution scheme to improve the spatial resolution of SMOS data. Different deconvolution techniques are presented that optimally perform noise regularization and include different levels of auxiliary information in the image reconstruction process. Results with simulated SMOS data and passive L-band airborne observations are shown in terms of both spatial resolution and radiometric sensitivity enhancement.

Chapter 6 explores the possibility of improving the spatial resolution of SMOS-derived soil moisture estimates using higher resolution visible/infrared satellite data. Preliminary results using passive L-band airborne data and the first SMOS brightness temperature images acquired during the commissioning phase are shown.

Chapter 7 presents a change detection algorithm to obtain high resolution soil moisture estimates from SMAP radar and radiometer observations. The downscaling approach is tested using simulated SMAP data and active/passive airborne observations.

Chapter 8 summarizes the main conclusions of this work, remarks its original contributions, and presents suggestions for follow-on research.

It remains completely unknown to us what the objects may be by themselves apart from the receptivity of our senses. We know nothing but our manner of perceiving them...

Immanuel Kant (1724-1804)

2

Review of passive microwave remote sensing of soil moisture

The emission of thermal microwave radiation from soils is strongly dependent on its soil moisture content. The theoretical basis for measuring soil moisture at microwave frequencies lies in the large contrast between the dielectric properties of liquid water and soil material. This chapter reviews the theoretical and experimental background to remote sensing of soil moisture using microwave radiometry. The state-of-the-art of the soil moisture retrieval techniques is also included.

2.1 Basic concepts on microwave radiometry

The Earth continuously receives electromagnetic radiation coming mainly from the Sun. Part of it is scattered and/or absorbed by the atmosphere, and the other part is transmitted to the Earth's surface. At the Earth's surface, part of this energy is absorbed, and part is scattered outwards. The energy absorbed is then transformed into thermal energy, which leads to a temperature increase until the thermodynamic equilibrium is reached. At this state, according to Thermodynamics, all media (gases, liquids, solids and plasma) radiate energy to keep the energy balance. Radiometry is the field of science that studies the thermal electromagnetic energy radiated by the bodies. Radiometers are instruments capable of measuring the power emitted by a body with high accuracy. The basic concepts of microwave radiometry are reviewed in this section.

2.1.1 Brightness and power collected by an antenna

The power emitted by a source in a solid angle Ω by unit surface is called radiance or brightness $B(\theta, \phi)$ [$\text{Wsr}^{-1}\text{m}^{-2}$],

$$B(\theta, \phi) = \frac{F_t(\theta, \phi)}{A_t}, \quad (2.1)$$

and depends on the source's normalized radiation pattern $F_t(\theta, \phi)$ and the total radiating area A_t .

Considering the case represented in Fig. 2.1, where an antenna with effective area A_r and normalized radiation pattern $F_n(\theta, \phi)$ is receiving an incident brightness coming from

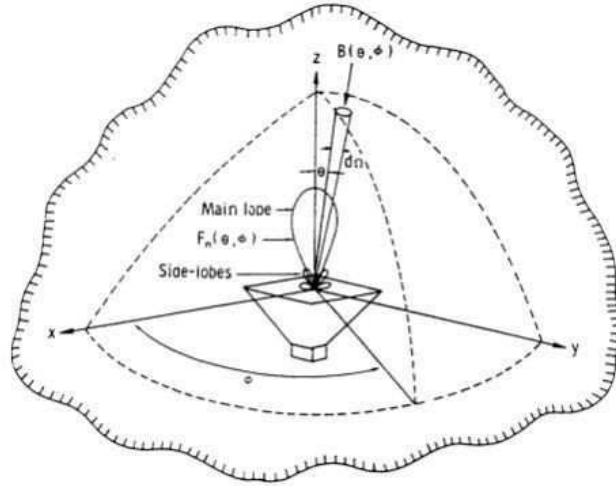


Figure 2.1 Geometry of the incident radiation from an extended source on an antenna, from *Ulaby et al. [1981]*

an extended source (such as the sky or the terrain), the total power received by the antenna is given by

$$P = \frac{Ar}{2} \int_f^{f+\Delta f} \iint_{4\pi} B_f(\theta, \phi) F_n(\theta, \phi) d\Omega df, \quad (2.2)$$

where $B_f(\theta, \phi)$ is the spectral brightness, defined as the brightness per unit bandwidth df , $d\Omega$ is the differential of soil angle, and Δf is the bandwidth of the receiving antenna. The factor $1/2$ accounts for the fact that thermal radiation is randomly unpolarized, while antennas can only collect one polarization.

2.1.2 Blackbody radiation

All bodies at a non-zero absolute physical temperature radiate electromagnetic energy. The increase of radiated energy is proportional to the temperature increase. In 1901, Planck introduced the concept of a blackbody radiator in his quantum theory, which represents a reference, relative to which the radiant emittance of a material can be expressed.

A blackbody is defined as an idealized, perfectly opaque material that absorbs all the incident radiation at all frequencies, reflecting none. Also, a blackbody is a perfect emitter, since otherwise its temperature would indefinitely increase. Therefore, when a black-body reaches the thermodynamic equilibrium, it radiates all the absorbed energy omnidirectionally. The blackbody spectral brightness B_f is given by the Planck's radiation law:

$$B_f \cong \frac{2hf^3}{c^2} \left(\frac{1}{e^{hf/k_B T} - 1} \right), \quad (2.3)$$

where f is the frequency in Hz, $h = 6.63 \cdot 10^{-34}$ J·s is the Planck's constant, $k_B = 1.38 \cdot 10^{23}$ J/K is the Boltzmann's constant, T is the physical temperature in K, and $c = 3 \cdot 10^8$ m/s is the speed of light.

At microwave frequencies, $hf/k_B T \ll 1$, and the Taylor's approximation

$$e^x - 1 = \left(1 + x + \frac{x^2}{2} + \dots \right) - 1 \simeq x, \text{ for } x \ll 1 \quad (2.4)$$

can be used to simplify (2.3) to

$$B_f = \frac{2f^2 k_B T}{c^2} = \frac{2k_B T}{\lambda^2}, \quad (2.5)$$

where $\lambda = c/f$ is the wavelength. This is the Rayleigh-Jeans law, a low-frequency approximation of the Planck's radiation law. The Rayleigh-Jeans law is widely used in microwave radiometry since it is mathematically simpler than the Planck law and has a deviation error smaller than 1% for $f < 117$ GHz and $T=300$ K. A graphical comparison of the Planck law and the Rayleigh-Jeans law is provided in Fig. 2.2 for $T=300$ K (\sim the Earth's temperature) and $T=6000$ K (\sim the Sun's temperature).

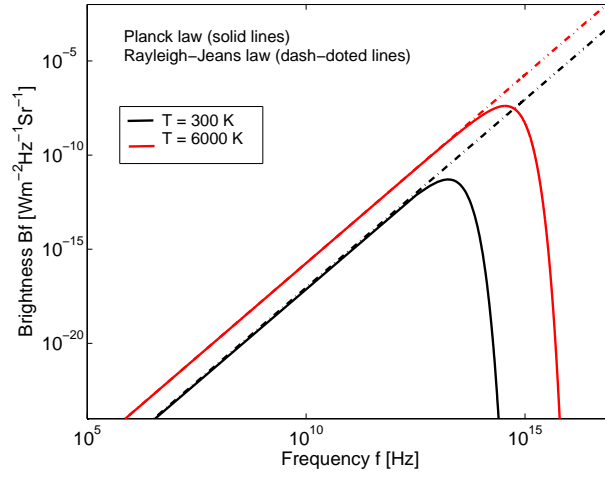


Figure 2.2 Comparison of Planck radiation law with its low-frequency approximation (Rayleigh-Jeans law) for $T=300$ K and $T=6000$ K.

Hence, the brightness of a blackbody B_{bb} at a physical temperature T and a bandwidth Δf in the microwave region can be expressed as

$$B_{bb} = B_f \cdot \Delta f = \frac{2k_B T}{\lambda^2} \Delta f. \quad (2.6)$$

The power collected by an antenna with normalized radiation pattern $F_n(\theta, \phi)$ surrounded by a blackbody at a constant physical temperature T is given by (2.2) and (2.5), and can be expressed as

$$P_{bb} = \frac{A_r}{2} \int_f^{f+\Delta f} \iint_{4\pi} \frac{2k_B T}{\lambda^2} F_n(\theta, \phi) d\Omega df. \quad (2.7)$$

The antenna solid angle can be expressed as a function of its effective area

$$\Omega_p = \iint_{4\pi} F_n(\theta, \phi) d\Omega = \frac{\lambda^2}{A_r}. \quad (2.8)$$

Hence, assuming the system bandwidth Δf small enough so that B_f can be considered constant over the frequency range, (2.7) becomes

$$P_{bb} = k_B T \Delta f. \quad (2.9)$$

This direct linear relationship between power and temperature is of fundamental importance in microwave remote sensing, where the power received by an antenna is commonly given in units of temperature (see Section 2.1.4).

2.1.3 Gray body radiation

A blackbody is a useful theoretical concept for describing radiation principles, but real materials or gray bodies do not behave like blackbodies: they do not absorb all the energy incident upon them and its emission is lower than that of perfect blackbodies. It is therefore convenient to define a microwave brightness temperature $T_B(\theta, \phi)$, so that the brightness of a gray body can be expressed, similarly to (2.6), as

$$B(\theta, \phi) = \frac{2k_B}{\lambda^2} T_B(\theta, \phi) \Delta f. \quad (2.10)$$

$T_B(\theta, \phi)$ is the temperature that a blackbody would have to produce the observed brightness $B(\theta, \phi)$; it is not the real temperature of the object, but an effective temperature. The brightness of gray bodies relative to that of blackbodies at the same physical temperature is called the emissivity $e(\theta, \phi)$,

$$e(\theta, \phi) = \frac{B(\theta, \phi)}{B_{bb}} = \frac{T_B(\theta, \phi)}{T}. \quad (2.11)$$

Note that, since real materials emit less than a blackbody, $B(\theta, \phi) \leq B_{bb}$, and therefore $0 \leq e(\theta, \phi) \leq 1$. The emissivity equals 0 in the case of a perfect reflector (e.g. a lossless metal), and 1 in the case of a perfect absorber, a blackbody. Thus, the brightness temperature $T_B(\theta, \phi)$ of a material is always smaller than, or equal to, its physical temperature T .

2.1.4 Power-temperature correspondence

In the microwave region, since the radiance emitted by an object is proportional to its physical temperature (from (2.5)), it is convenient to express the radiance in units of temperature. Hence, the brightness temperature $T_B(\theta, \phi)$ is used to characterize the radiation of an object (from (2.10)). Similarly, an apparent temperature T_{AP} is defined to characterize the total brightness incident over a radiometer antenna $B_i(\theta, \phi)$, as

$$B_i(\theta, \phi) = \frac{2k_B}{\lambda^2} T_{AP}(\theta, \phi) \Delta f. \quad (2.12)$$

Therefore, the power collected by an antenna with normalized radiation pattern $F_n(\theta, \phi)$ receiving a non-blackbody incidence brightness is given by (2.2) and (2.12),

$$P = \frac{A_r}{2} \int_f^{f+\Delta f} \iint_{4\pi} \frac{2k_B}{\lambda^2} T_{AP}(\theta, \phi) F_n(\theta, \phi) d\Omega df. \quad (2.13)$$

It is convenient to define an antenna temperature T_A as the temperature equivalent of the power received with an antenna, so that (2.9) holds as $P = k_B T_A \Delta f$ for gray bodies. Hence, T_A can be expressed as

$$T_A = \frac{A_r}{\lambda^2} \iint_{4\pi} T_{AP}(\theta, \phi) F_n(\theta, \phi) d\Omega. \quad (2.14)$$

Note that T_A includes contributions from the target being observed as well as from radiation emitted and scattered from other sources, but not from internal elements.

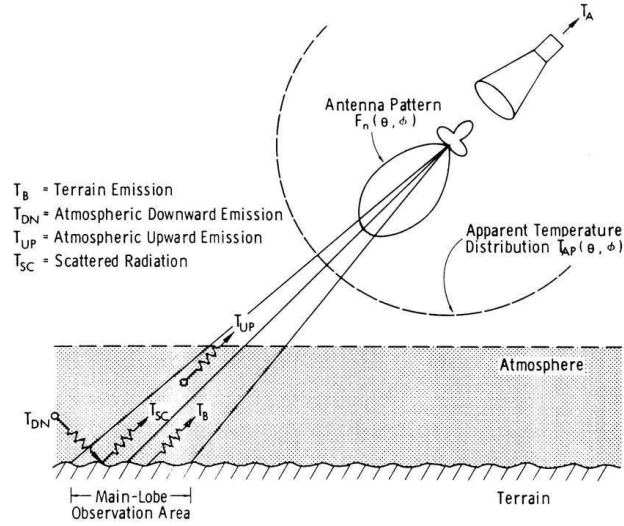


Figure 2.3 Radiation incident upon an Earth-looking radiometer. Relationships between the antenna temperature T_A , apparent temperature T_{AP} , and brightness temperature T_B , from [Ulaby et al. \[1981\]](#)

The case of prime interest in passive remote sensing is that of an Earth-looking radiometer, as illustrated in Fig. 2.3. In this case, the radiation incident upon the antenna is a function of both the land surface and the atmosphere, and may be expressed as

$$T_{AP}(\theta, \phi) = T_{UP} + (T_B + T_{SC}) \frac{1}{L_a}, \quad (2.15)$$

where T_B is the brightness temperature of the observed scene, T_{UP} is the atmospheric upward radiation, T_{SC} is the downward atmospheric radiation scattered by the Earth's surface in the direction of the antenna, and L_a represents the attenuation of the atmosphere. At the lower microwave frequencies used in soil moisture sensing, the atmospheric effects are small and may be safely neglected in most cases.

2.1.5 Measuring brightness temperatures from space

Space-borne radiometers are very sensitive receivers capable of measuring the radiance emitted by the Earth's surface with high accuracy. They are designed to transform the radiation collected by an antenna into mappable electric signals, and its performance is usually characterized by its radiometric resolution, accuracy, and spatial resolution [[Randa et al., 2008](#)]:

- The *radiometric resolution* (sometimes called sensitivity) is computed as the smallest change in input brightness temperature or radiance that can be detected in the system output.
- The *radiometric accuracy* represents the closeness of the agreement between the measured antenna temperature and its true value (systematic error). Because the true value cannot be determined exactly, the measured or calculated value of highest available accuracy is typically taken to be the true value.
- The *spatial resolution* is the ability of the sensor to separate two closely spaced identical point sources.

In a remote sensing mission, in addition to instrumental errors, other phenomena can degrade the radiometric resolution and must be corrected (compensated for). At L-band, the atmosphere is almost transparent, and the main error sources are the Faraday rotation and the space radiation, which are described hereafter.

Faraday Rotation

When propagating through the ionosphere, a linearly polarized wave undergoes a progressive rotation of its plane of polarization due to the presence of the geomagnetic field and the anisotropy of the plasma medium [ITU-R P.531-6, 2001]. This phenomena is known as Faraday rotation, which may be expressed as:

$$\varphi = 2.36 \cdot 10^{-14} B_{av} N_T f^{-2}, \quad (2.16)$$

where φ [rad] is the rotation angle, f [GHz] is the frequency, N_T [electrons/m²] is the ionospheric total electron content (TEC), and B_{av} [Wb/m²] is the average Earth's magnetic field along the propagation path.

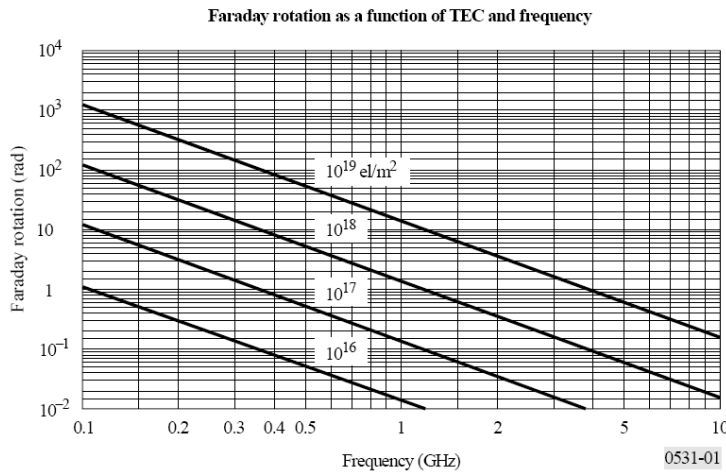


Figure 2.4 Typical values of Faraday rotation angle as a function of TEC and frequency, from ITU-R P.531-6 [2001].

Figure 2.4 shows typical values of the Faraday rotation angle as a function of TEC and frequency. TEC is significantly affected by the solar radiation, and shows significant temporal and latitudinal variations; assuming low latitudes, the Faraday rotation angle at L-band can be as low as 4° at night (TEC of 10¹⁶ electrons/m²) and as high as 30° at noon (TEC of 10¹⁸ electrons/m²). This rotation may result in errors on the brightness temperatures of 1-10 K, which is sufficient to cause errors in the retrieval of the surface parameters [Yueh, 2000]. As it will be seen, an effective way to avoid this problem is to use the first Stokes parameter $T_I = T_{xx} + T_{yy} = T_{hh} + T_{vv}$, which is invariant to rotations (see Section 2.1.6). Fully polarimetric measurements are also useful here since the Faraday effect only rotates the polarization, rather than changing the nature of the polarization. Note that, although the Faraday rotation could be compensated for, the accuracy of the Faraday estimations may not be enough for the required parameter's accuracy.

Space radiation

Microwave radiation from space reflects over the Earth's surface and is also measured by the antenna. Three main space phenomena should be considered, and their contribution to the antenna temperature needs to be taken into account:

- *The cosmic radiation level*: It is fairly constant (~ 2.7 K) and, therefore, it does not affect the quality of measurements.
- *The galactic noise*: It comes from the reflection over the Earth's surface of the pole or the center of the galaxy, and varies from 0.8 K to 40 K at L-band [*LeVine and Abraham, 2002*]. It should be either avoided, by selecting a convenient orbit, or corrected through the use of existing galactic noise maps. However, the absolute accuracy of these maps is still questionable and the scattering models present errors.
- *Sun glint*: It is the most important noise source, the Sun brightness temperature value is higher than 100,000 K, and any reflection of Sun radiation collected by the antenna would seriously affect measurements. Hence, direct reflections should be avoided by pointing the instrument to the shadow zone of a polar sun-synchronous orbit.

2.1.6 The Stokes parameters

The polarization of an electromagnetic wave can be completely described by the four Stokes parameters I , Q , U , V . The first Stokes parameter (I) describes the total intensity of electromagnetic emission and the second Stokes parameter (Q) is the difference between the intensity in two orthogonal directions in a given polarization frame, i.e. vertical and horizontal polarizations. The third (U) and fourth (V) Stokes parameters, respectively, represent the real and imaginary parts of the cross-correlation between these orthogonal polarizations [*Randa et al., 2008*]:

$$\begin{aligned}
 I &= \frac{\langle |E_v|^2 \rangle + \langle |E_h|^2 \rangle}{\eta_o}, \\
 Q &= \frac{\langle |E_v|^2 \rangle - \langle |E_h|^2 \rangle}{\eta_o}, \\
 U &= \frac{2 \cdot \text{Re}\langle E_v E_h^* \rangle}{\eta_o}, \\
 V &= \frac{2 \cdot \text{Im}\langle E_v E_h^* \rangle}{\eta_o},
 \end{aligned} \tag{2.17}$$

where E_v and E_h are the electric field components at vertical and horizontal polarizations, respectively, and η_o is the electromagnetic wave impedance of the medium ($120\pi \Omega$ in vacuum).

In polarimetric remote sensing radiometry the Stokes parameters are conventionally expressed in terms of brightness temperature:

$$\begin{aligned}
 T_I &= T_{vv} + T_{hh} = \frac{\lambda^2}{k_B \cdot B_w} \cdot I, \\
 T_Q &= T_{vv} - T_{hh} = \frac{\lambda^2}{k_B \cdot B_w} \cdot Q, \\
 T_U &= T_{45} + T_{-45} = \frac{\lambda^2}{k_B \cdot B_w} \cdot U, \\
 T_V &= T_{lc} + T_{rc} = \frac{\lambda^2}{k_B \cdot B_w} \cdot V,
 \end{aligned} \tag{2.18}$$

where λ is the wavelength, and B_w is the noise-equivalent bandwidth. T_{vv} and T_{hh} are the vertical and horizontal brightness temperatures, T_{45} and T_{-45} represent orthogonal measurements skewed $\pm 45^\circ$ with respect to normal, and T_{lc} and T_{rc} refer to left-hand and right-hand circular polarized quantities. Note that in previously published literature, I , Q , U , and V have also been used for the Stokes parameters in brightness temperature – instead of T_I , T_Q , T_U , T_V –, which was a source of confusion. This practice was agreed to be discouraged in [Randa et al. \[2008\]](#).

Generally, the energy emitted from the Earth’s surface is partly polarized, meaning that the vertical brightness temperature is different from the horizontal. Whereas conventional dual-polarization radiometers only measure vertical and horizontal polarized brightness temperatures, a polarimetric radiometer is capable of directly or indirectly measuring all four Stokes parameters, which provides a full characterization of the polarization properties of the emitted energy.

Note that the Faraday rotation φ mixes the polarization as follows

$$\begin{aligned} E_v^{Faraday} &= E_v \cos\varphi + E_h \sin\varphi, \\ E_h^{Faraday} &= -E_v \sin\varphi + E_h \cos\varphi. \end{aligned} \quad (2.19)$$

Hence, the first and fourth Stokes parameter are invariant to rotations, whereas the second and third Stokes parameter are not. In remote sensing, third and fourth Stokes parameters are primarily used for correcting polarization rotation [[Yueh et al., 1995](#); [Martín-Neira et al., 2002](#)] or, in the case of the ocean for instance, to infer wind direction information [[Brown et al., 2006](#)].

2.2 L-band emission of land covers

The theory behind L-band microwave remote sensing is based on the large contrast between the dielectric constant of dry soil (~ 4) and water (~ 80). This contrast results in a broad range in the dielectric properties of soil-water mixtures (4-40), and is the primary influence on the natural microwave emission from the soil [[Schmugge et al., 1986](#)]. The large dielectric constant of water is the result of the water molecule’s alignment of its permanent dipole in response to an applied electromagnetic field. Therefore, when water is added to the soil, its dielectric constant is strongly increased [[Behari, 2005](#)]. The emissivity of land covers depends on the dielectric constant of the soil surface –which is governed by the moisture content and soil type–, but also on other surface characteristics such as soil temperature, soil roughness, and vegetation canopy. The effects of these parameters on the emitted radiation are presented hereafter.

2.2.1 Thermal radiation and surface emissivity

The thermal radiation or brightness temperature emitted by the Earth’s surface (T_{Bp}) is determined by its physical temperature T and its emissivity e_p (see Section 2.1.3), according to:

$$T_{Bp} = e_p \cdot T, \quad (2.20)$$

where the subscript p denotes either vertical (v) or horizontal (h) polarization. The emissivity may be further related to the reflectivity $\Gamma_{s,p}$ of the surface:

$$e_p = 1 - \Gamma_{s,p}. \quad (2.21)$$

For a flat surface, and a medium of uniform dielectric constant, the expressions for reflectivity at vertical and horizontal polarizations are given by the power Fresnel reflection coefficients ($\Gamma_{s,p} \cong \Gamma_{o,p}$), as:

$$\begin{aligned}\Gamma_{ov} &= \left| \frac{\epsilon_s \cos \theta - \sqrt{\epsilon_s - \sin^2 \theta}}{\epsilon_s \cos \theta + \sqrt{\epsilon_s - \sin^2 \theta}} \right|^2, \\ \Gamma_{oh} &= \left| \frac{\cos \theta - \sqrt{\epsilon_s - \sin^2 \theta}}{\cos \theta + \sqrt{\epsilon_s - \sin^2 \theta}} \right|^2,\end{aligned}\quad (2.22)$$

where θ is the incidence angle and ϵ_s is the complex dielectric constant of soils, which is in turn governed by the moisture content and the soil type.

2.2.2 Water in soils

Water in soils is commonly classified as bound and free water; bound water is the water absorbed by the surface of soil particles, while free water is the liquid water located in the pore spaces. The porosity of a soil determines the total volume occupied by pores per unit volume of soil. Soils with small pores (clayey soils) will hold more water per unit volume than soils with large pores (sandy soils). While pore spaces of dry soils are mostly filled with air, pore spaces of wet soils are filled with water. Processes such as infiltration, ground-water movement, and storage occur in these void spaces.

The soil moisture, or water in a soil, is expressed as a ratio, which can range from 0 (completely dry) to the value of the materials' porosity at saturation (~ 0.5). It is usually expressed in per cent, and can be determined in two ways:

1. Gravimetric soil moisture m_g , which is defined as the mass of water per unit mass of dry soil, and can be calculated from the wet w_w and dry w_d weights of a soil sample, as:

$$m_g = \frac{w_w - w_d}{w_d}. \quad (2.23)$$

2. Volumetric soil moisture m_v , defined as the volume of water per unit volume of soil, determined from the volume of water V_w and the total volume V_T (soil volume + water volume + void space), and related to m_g through the soil bulk density ρ_b :

$$m_v = \frac{V_w}{V_T} = m_g \rho_b = m_g \frac{w_d}{V_T}. \quad (2.24)$$

Since precipitation, evapotranspiration and other water-related variables are commonly expressed in terms of flux, volumetric expressions for water content are often preferred in environmental studies. Furthermore, the *in situ* soil moisture measurements used to validate remote sensing observations are commonly acquired using dielectric probes, which directly provide volumetric measurements. Hence, soil moisture measurements are expressed in volumetric units throughout this work.

2.2.3 Dielectric properties of soils

Soil emission at microwave frequencies is related to the soil water content by the dielectric constant. The dielectric constant is a measure of the soil response to an electromagnetic

wave; it is defined as a complex number ($\epsilon_s = \epsilon'_s + j\epsilon''_s$), where the real part determines the propagation characteristics of the energy as it passes through the soil, and the imaginary part determines the energy losses. In a heterogeneous medium such as the soil, the complex dielectric constant is a combination of the individual constituent parts, including air, water, rock, etc. Other factors which influence the dielectric constant are soil texture, temperature, salinity, and wavelength. The dielectric constant is a difficult quantity to measure on a routine basis outside the laboratory, and values are generally derived from semi-empirical models that use an estimation of the ratio rock/water/air based on the given soil properties [Wang and Schmugge, 1980; Hallikainen et al., 1985; Dobson et al., 1985; Mironov et al., 2004]. Comprehensive information on the different dielectric constant models is reported, among others, in [Behari, 2005] and [Chukhlantsev, 2006].

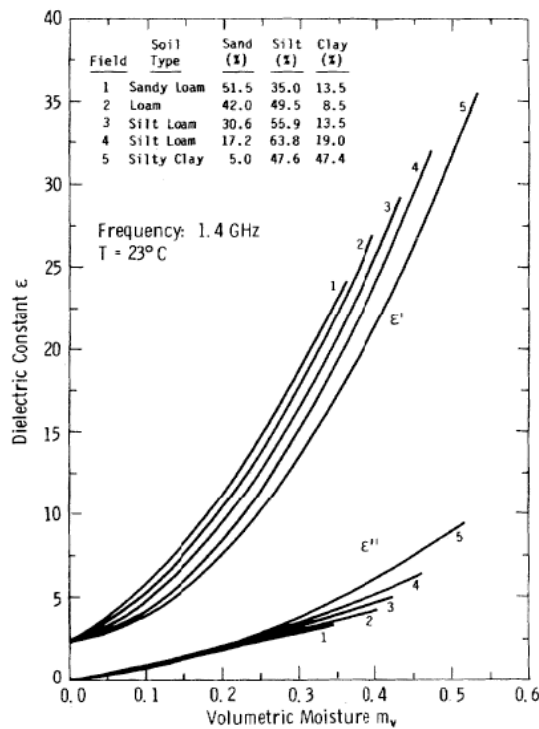


Figure 2.5 Measured dielectric constant at 1.4 GHz for five soils with different textural composition, from Hallikainen et al. [1985]

The relationship between the measured dielectric constant and the volumetric soil moisture content for a variety of soil types at a frequency of 1.4 GHz is shown in Fig. 2.5. The dependence on soil type is due to the different percentages of water bound to the particle surfaces in the different soils, which takes minimum values in sands (2-3%) and maximum values in clays (20-40%). Bound water exhibits molecular rotation less freely than free water, and contributes little to the dielectric constant of the soil water mixture. This is evident in clay soils, which hold greater percentages of bound water, and therefore have a lower dielectric constant than sandy or silty soils at the same moisture content. Also, Fig. 2.5 shows that the relationship between dielectric constant and volumetric soil moisture is almost linear, except at low moisture contents. This non-linearity at low moisture contents is due to the strong bonds developed between the surfaces of soil particles and the thin films of water that surround them, which impede the free rotation of the water molecules. As more water is added, the molecules are further from the particle surface and are able to rotate

more freely, hence increasing the soil dielectric constant [*de Jeu et al.*, 2008].

Soil moisture, through its relationship to the real and imaginary parts of the dielectric constant, has an impact on the soil penetration depth. The penetration depth γ_D is defined as the soil depth from above which 63% ($1 - 1/e$) of the radiation emitted by the surface originates [*Ulaby et al.*, 1981], and can be expressed as:

$$\gamma_D = \frac{\lambda \sqrt{\epsilon_s'}}{2\pi \epsilon_s''}. \quad (2.25)$$

The penetration depth of microwaves rapidly decreases with increasing soil wetness; for a wavelength λ of 21 cm (L-band), γ_D varies from approximately 75 cm for a normally dry soil ($\epsilon_s' = 5$ and $\epsilon_s'' = 0.1$) to about 3.7 cm for a wet soil ($\epsilon_s' = 30$ and $\epsilon_s'' = 5$). Knowledge of the penetration depth is important because it is an indicator of the thickness of the surface layer within which variations in moisture and temperature can significantly affect the emitted radiation.

The dielectric constant of dry soils is almost independent of temperature; for wet soils, the dielectric constant is only weakly dependent on temperature, and for the range of temperatures encountered in nature this dependence may be ignored. However, frozen soils have much lower dielectric constants than unfrozen soils, as the contained water is no longer in liquid phase. This feature has led to studies of microwave radiometry for detecting areas of permafrost and freeze-thaw boundaries in soils [*England*, 1990].

2.2.4 Surface roughness

The effect of surface roughness on the microwave emission from bare soils is illustrated in Fig. 2.6, which shows experimental data measured at 1.4 GHz for three fields with different surface roughness conditions [*Newton and Rouse*, 1980]. It shows that surface roughness increases the emissivity of natural surfaces –due to the increase in the soil area interacting with the atmosphere– and reduces the difference between the vertical and horizontal polarizations. Also, the sensitivity of emissivity to soil moisture variations decreases significantly as the surface roughness increases, since it reduces the range in measurable emissivity from dry to wet soil conditions [*Wang*, 1983].

The effect of soil surface roughness on the emissivity has been an issue widely addressed in the literature, and different approaches have been proposed to modify the reflectivity in (2.21) for rough surfaces. *Peake* [1959] developed an integral equation model to fully characterize the scattered radiation. A simpler, semi-empirical expression for rough surface reflectivity was reported in *Choudhury et al.* [1979]:

$$\Gamma_{sp} = \Gamma_{op} \exp(-h_s \cos^2(\theta)), \quad (2.26)$$

where Γ_{op} is the reflectivity at p -polarization ($p=v$ or h) of a flat surface given by (2.22), $h_s = 4k^2\sigma_s^2$ is the soil roughness parameter, related to the electromagnetic wavenumber k and the standard deviation of the surface height σ_s , and θ is the incidence angle. A more elaborated formulation was proposed in *Wang and Choudhury* [1981]:

$$\Gamma_{sp}(\theta) = [(1 - Q_s)\Gamma_{op}(\theta) + Q_s\Gamma_{op}(\theta)] \exp(-h_s \cos^n(\theta)), \quad (2.27)$$

where Q_s models the effects of the polarization mixing and n expresses the angular dependence of roughness.

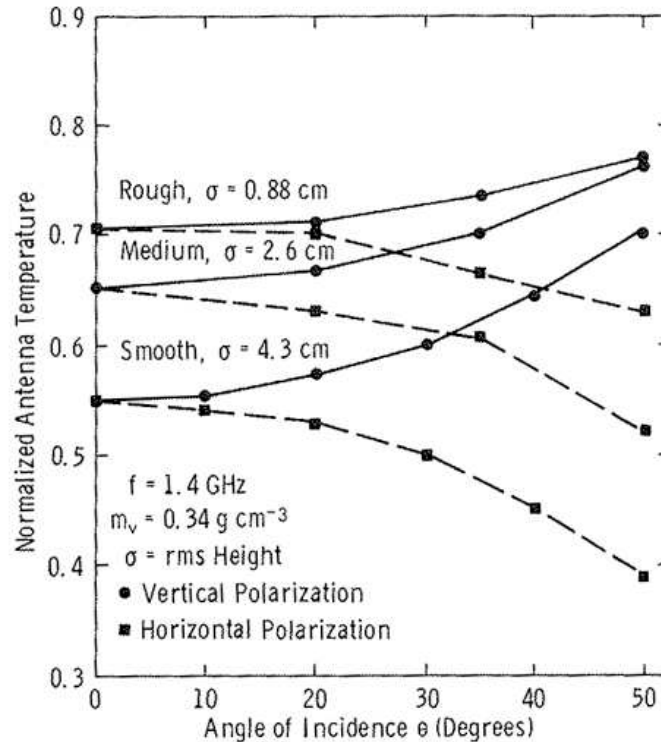


Figure 2.6 Measured normalized antenna temperature (emissivity) vs. incidence angle at 1.4 GHz for three bare soil field with different surface roughnesses, from *Newton and Rouse [1980]*

A detailed analysis of the soil roughness effects performed by *Wigneron et al. [2001]* showed that both Q_s and n could be set equal to zero at L-band and that the roughness parameter h_s could be semi-empirically estimated comprising most surface roughness conditions. Typical values for h_s have been suggested, ranging from 0.2 for a smooth surface, to 1 for a rough ploughed field. This is consistent with L-band airborne and ground-based experiments, where soil roughness has generally found to be rather smooth over agricultural or natural areas [*Jackson et al., 1999; Panciera et al., 2009; Saleh et al., 2009*].

Also, recent studies have introduced an h_s parametrization dependent on soil moisture [*Wigneron et al., 2001; Schneeberger et al., 2004; Escorihuela et al., 2007*]. However, these studies have been performed under very local conditions, and there is no evidence of the potential benefits that they may introduce at global scale. To date, the accuracy of the approaches linking h_s and soil moisture is not well established for a variety of roughness conditions and the relationship between h_s , surface roughness characteristics such as σ_s or correlation length, and soil moisture has not been fully understood.

2.2.5 Vegetation effects

When the soil is covered by vegetation, its emission is affected by the canopy layer: it absorbs and scatters the radiation emanating from the soil and also adds its own contribution. In areas of sufficiently dense canopy, the emitted soil radiation will become masked, and the observed emissivity will be due largely to the vegetation. The magnitude of the absorption by the canopy depends upon the wavelength and the vegetation water content.

A variety of models have been developed to account for the effects of vegetation on the observed microwave signal [*Kirdiashev et al., 1979; Mo et al., 1982; Jackson et al., 1982;*

[*Ulaby and Wilson, 1985; Wigneron et al., 1995; Meesters et al., 2005*]. Altogether, the radiation from the land surface as observed from above the canopy is usually expressed as a simple radiative transfer equation known as the $\tau - \omega$ model [*Mo et al., 1982*]:

$$T_{Bp} = e_p T_s \gamma + (1 - \omega) T_v (1 - \gamma) + (1 - e_p) (1 - \omega) T_v (1 - \gamma) \gamma, \quad (2.28)$$

where T_s and T_v are the effective temperatures of the soil and the vegetation respectively, γ is the transmissivity of the vegetation layer, and ω is the single scattering albedo. The first term of the above equation defines the radiation from the soil as attenuated by the overlying vegetation. The second term accounts for the upward radiation directly from the vegetation, while the third term defines the downward radiation from the vegetation, reflected upward by the soil and again attenuated by the canopy.

The single scattering albedo ω describes the scattering of the soil emissivity within the vegetation, and is a function of soil geometry. The transmissivity of the vegetation can be further defined in terms of the vegetation optical depth τ and the incidence angle θ :

$$\gamma = \exp(-\tau / \cos(\theta)). \quad (2.29)$$

The optical depth is related to the vegetation density and frequency, and can be linearly related to the vegetation water content VWC [kg/m²] at L-band through an empirical parameter, b [*van de Griend and Wigneron, 2004*]:

$$\tau = b \cdot \text{VWC}. \quad (2.30)$$

Alternatively, the vegetation optical depth could also be linearly related to the log of the the Normal Difference Vegetation Index (NDVI) [*Burke et al., 2001*]:

$$\tau = \alpha + \beta(1 - \log(\text{NDVI})). \quad (2.31)$$

There is some experimental evidence indicating possible polarization and angle dependence of both τ and ω . However, this dependence has been observed mainly during field experiments over vegetation that exhibits a predominant orientation, such as vertical stalks in tall grasses, grains and maize [*Kirdiashev et al., 1979; Wigneron et al., 1995; Hornbuckle et al., 2003*], whereas canopy and stem structure of most vegetation covers are randomly oriented. However, the effects of any systematic orientation of vegetation elements would most likely be minimized at satellite scales [*Owe et al., 2001; Martínez-Vázquez et al., 2009*].

Both SMOS and SMAP orbits were chosen with overpass times of 6 am/6 pm, so that temperature gradients within the soil and vegetation are minimized. Hence, (2.28) can be simplified assuming that the temperature of the vegetation canopy is in equilibrium with the soil temperature ($T_s = T_v$) [*Hornbuckle and England, 2005*]. Therefore, (2.28) may be rewritten as:

$$T_{Bp} = [e_p \gamma + (1 - \omega)(1 - \gamma)(1 + (1 - e_p)\gamma)] T_s. \quad (2.32)$$

Figure 2.7 shows the dependence of brightness temperature with incidence angle and polarization for six main surface conditions combining dry, moist and wet soils with bare and vegetation-covered surfaces, from (2.32). In the bare soil scenarios on Fig. 2.7 (a), it can be seen that V-pol increases with the incidence angle, whereas H-pol decreases with increasing incidence angle. Fig. 2.7 (b) shows that vegetation increases the soil emissivity, and decreases the difference between the vertically and horizontally polarized brightness temperatures, and between the dry and wet soil conditions. This indicates that correction for the vegetation effects is necessary to obtain accurate soil moisture estimates. Furthermore,

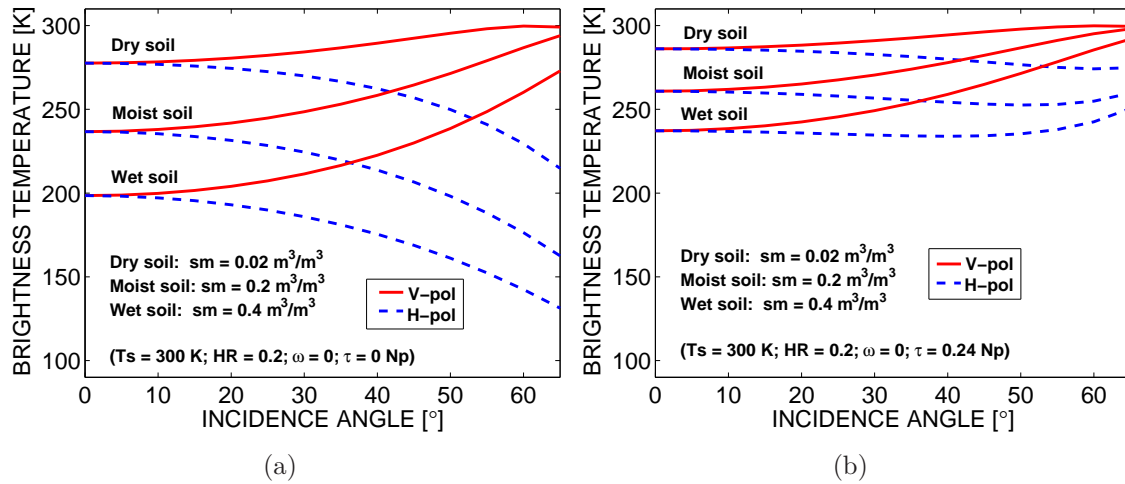


Figure 2.7 Graphical plots illustrating the brightness temperature dependence with incidence angle of (a) bare, and (b) vegetation-covered dry, moist and wet soils, from (2.32) (from *Piles et al.* [2010]).

retrievals become increasingly unreliable as the opacity of the vegetation layer increases [*Jackson and Schmugge*, 1991]. Figure 2.7 also illustrates that the emissivity of dry soils is greater than the emissivity of wet soils, with a soil brightness temperature variation at nadir of ~ 80 K in the bare soil scenarios and of ~ 40 K in the vegetation-covered scenarios. In the two cases, this variation is much larger than the noise sensitivity threshold of a microwave radiometer (typically < 1 K), so that a large signal-to-noise ratio is obtained. This is a major advantage of the passive microwave technique for soil moisture remote sensing.

2.3 Soil moisture retrieval techniques

The brightness temperature of land covers is influenced by many variables, the most important being soil moisture s_m , soil roughness (parameterized by the soil roughness parameter h_s), soil temperature T_s , and vegetation characteristics such as albedo ω and opacity τ . The challenge of retrieval or inversion techniques is to reconstruct the environmental parameters from the measured signal by using a minimum of auxiliary data. Within the SMOS and SMAP preparatory activities, different soil moisture retrieval algorithms have been developed and validated from microwave modeling and field experiments using ground-based, airborne, and space shuttle instruments.

The first retrieval techniques were based on deriving an empirical relationship between the geophysical variables and the radiative transfer equation through a regression technique (see the review by *Wigneron et al.* [2003]). However, these approaches have limited applicability, since the regression is often valid only for the test sites where they were obtained.

Another approach to soil moisture retrieval is based on the use of neural networks. These algorithms have been used with satisfactory results in the retrieval of agricultural parameters from radiometric data [*Frate et al.*, 2003], but need a training phase that is not always feasible.

A third type of algorithms are based on the inversion of geophysical model functions. This is the most widely-used retrieval technique; it is the one adopted by SMOS, and by

SMAP for the passive-only soil moisture product. The SMOS retrieval algorithm is designed so as to make full use of its multi-angular dual-polarization/full-polarimetric observations, whereas the SMAP algorithm is based in observations at a constant incidence angle $\theta = 40^\circ$.

In the case of SMAP, the high resolution radar will be additionally used to identify inland water bodies, topography, and vegetation characteristics within the 40 km radiometer resolution. The use of radar-derived information in the retrievals for the estimation of vegetation characteristics is also under consideration [Meesters *et al.*, 2005; Kurum *et al.*, 2009].

SMOS multi-angular retrieval algorithm approach

The SMOS soil moisture retrieval algorithm consists of inverting a geophysical model function by finding the set of input variables (mainly five: s_m , T_s , h_s , ω and τ) which generate the brightness temperatures that best match the observed brightness temperatures. This inversion is performed by minimizing a cost function that accounts for the weighted squared differences between model and measured data, using the iterative Levenberg-Marquardt method [Marquardt, 1963]. The $\tau - \omega$ geophysical model function in (2.28) is the core of the forward model used to mimic the Earth's emission at L-band (the L-MEB model [Wigneron *et al.*, 2007]).

Assuming that the measurement errors are Gaussian, the fundamental least-squares cost function (CF) for observation-model misfits is:

$$CF = (\bar{F}^{meas} - \bar{F}^{model})^T C_F^{-1} (\bar{F}^{meas} - \bar{F}^{model}) + (p_i - p_{i0})^T C_p^{-1} (p_i - p_{i0}), \quad (2.33)$$

where \bar{F}^{meas} and \bar{F}^{model} are vectors of length N containing the microwave radiometer observations at different incidence angles, measured by MIRAS and obtained using the forward model, respectively. N is the number of observations of the same point at different incidence angles acquired in a satellite overpass; C_F is the covariance matrix of the observations, which depends on the SMOS operation mode and the reference frame [Camps *et al.*, 2005]; p_i are the retrieved physical parameters that may influence the modeled T_B , including s_m , T_s , h_s , τ and ω ; p_{i0} are prior estimates of parameters p_i (obtained from other sources such as satellite measurements or model outputs, the auxiliary information); and C_p is a diagonal matrix containing the variances of the prior estimates of parameters $\sigma_{p_{i0}}^2$ [SMOS Algorithm Theoretical Bases Document, 2007].

If the model error is uncorrelated between different measurements, then C_F is diagonal, and (2.33) can be expressed as:

$$CF = \sum_{n=1}^N \frac{\|\bar{F}_n^{meas} - \bar{F}_n^{model}\|^2}{\sigma_{F_n}^2} + \sum_{i=1}^M \frac{(p_i - p_{i0})^2}{\sigma_{p_{i0}}^2}, \quad (2.34)$$

where σ_{F_n} is the radiometric accuracy for the n^{th} observation, and M is the number of parameters p_i to be retrieved. $\sigma_{p_{i0}}$ represents the uncertainty on the *a priori* parameter p_{i0} , and its value is used to parameterize the constraint on the parameter p_i in the retrievals: p_i can be set to be free ($\sigma_{p_{i0}} = 100$, no *a priori* information is used), it can be constrained to be more or less close to the reference value p_{i0} , or it can be constant ($\sigma_{p_{i0}} < 10^{-3}$, assuming high accuracy on the *a priori* information). Note that p_{i0} are specified *a priori*, whereas p_i values are adjusted during the minimization process.

The retrieval of the geophysical parameters can be formulated using the vertical (T_{vv}) and horizontal (T_{hh}) polarizations separately ($\bar{F}_n = [T_{vv}, T_{hh}]^T$ in the Earth reference frame and

$\overline{F}_n = [T_{xx}, T_{yy}]^T$ in the antenna frame), or using the first Stokes parameter ($\overline{F}_n = [T_I]^T = [T_{xx} + T_{yy}]^T = [T_{hh} + T_{vv}]^T$) [Camps *et al.*, 2005]. These two approaches will be considered in this work. Note that, up to date, the formulation of the soil moisture retrieval problem on the Earth reference frame is the preferred option for SMOS [Pardé *et al.*, 2004; Saleh *et al.*, 2009]. Hence, the formulation of the problem in terms of the first Stokes parameter is presented as an alternative approach, since retrievals using T_I could benefit of having less angular dependency than (T_{vv}, T_{hh}) , therefore reducing the degrees of freedom during the inversion process, which could lead to better soil moisture retrievals. Also, retrievals using T_I are unaffected by Faraday rotations, which is critical from an operational point of view.

The SMOS soil moisture retrieval algorithm is robust and has been demonstrated using both field campaign and synthetic model-generated data. However, radiometer observations must be combined with auxiliary data in the inversion process to achieve the required accuracy ($0.04 \text{ m}^3/\text{m}^3$) and the retrieval setup needs yet to be optimized. In this Thesis, key aspects for the retrieval of accurate soil moisture estimations from SMOS have been addressed: in Chapter 3, the auxiliary data impact on soil moisture retrievals is thoroughly evaluated and an optimal retrieval configuration is devised; in Chapter 4, the soil moisture inversion algorithm is analyzed both theoretically and in terms of performance with simulated SMOS data. After the successful launch of SMOS in November 2009, these studies will timely contribute to consolidate the operational soil moisture retrieval algorithm, which is essential to demonstrate the SMOS capabilities over land.

*It is better to be “roughly” right
than to be “precisely” wrong*

Albert Einstein (1879-1955)

3

Auxiliary data impact on SMOS soil moisture retrievals

Previous studies have remarked the necessity of combining SMOS brightness temperatures with auxiliary data to retrieve soil moisture with an accuracy better than the $0.04 \text{ m}^3/\text{m}^3$ benchmark. However, the required auxiliary data and optimal soil moisture retrieval setup need yet to be optimized. This chapter examines the performance of the SMOS soil moisture retrieval algorithm for different retrieval configurations, depending on the ancillary information that is used in the retrievals and its associated uncertainty. Also, the impact of using vertical and horizontal brightness temperatures, or using the first Stokes parameter in the minimization process is analyzed. Results with simulated SMOS data show the accuracy obtained with the different retrieval setups for four main surface conditions combining wet and dry soils with bare and vegetation-covered surfaces, and an optimum soil moisture retrieval configuration is devised.

3.1 Introduction

The SMOS mission aims at providing the first global soil moisture measurements with an accuracy of $0.04 \text{ m}^3/\text{m}^3$ over $50 \times 50 \text{ km}^2$ and a temporal resolution of 3 days. There is also a high interest in obtaining vegetation water content (VWC) maps with an accuracy of $0.2 \text{ kg}/\text{m}^2$ from SMOS observations [*Mission Objectives and Scientific Requirements of the SMOS mission, 2003*]. The retrieval of soil moisture from passive microwave remote sensing observations has been described in considerable detail in Chapter 2.

The bare soil emissivity depends mainly on its surface roughness (determined using the soil roughness parameter h_s), surface temperature T_s , and soil dielectric constant, which is in turn related to the soil moisture content s_m and soil type. When the soil is covered by vegetation, its emission is affected by the canopy layer: it attenuates the soil emission and adds its own contribution. The vegetation optical depth τ (from which vegetation water content maps can be derived [*van de Griend and Wigneron, 2004*]) is used to account for the vegetation attenuation, and the vegetation albedo ω is used to describe the dispersion of the radiation within the vegetation (see Section 2.2). Several configurations have been proposed for de-coupling the contribution of each of these surface parameters in the L-band emission and hence retrieving soil moisture from SMOS observations. For instance, *Wigneron et al.*

[1995] presented the possibility of simultaneously retrieving s_m and τ (the two parameter 2-P retrieval method) using experimental L-band observations over crop fields. The so-called 3-P retrieval method, in which T_s is retrieved in addition to s_m and τ , is applied to a synthetic simulated dataset in [Pellarin et al. \[2003\]](#). By extension, the N-P retrieval method, where N corresponds to the number of parameters that are retrieved, is analyzed in [Pardé et al. \[2004\]](#) and [Camps et al. \[2005\]](#). In all these studies, the parameters are retrieved by minimizing a Cost Function (CF) which accounts for the weighted squared differences between measured and simulated brightness temperatures –using for the later the $\tau - \omega$ radiative model [[Ulaby and Wilson, 1985](#); [Mo et al., 1982](#)]– and between the retrieved quantities and their estimated values, with weights reflecting *a priori* uncertainties on these variables (see Section 2.3).

Since different retrieval setups lead to different accuracy results, an in-depth study of the different cost function configurations for retrieving soil moisture estimates from SMOS observations is paramount. Although some retrieval issues regarding the parameters to be retrieved have been analyzed in the above-cited studies, the *a priori* information used in the retrievals and its required uncertainty are key aspects yet to be determined. Also, the optimum MIRAS operation mode (dual-polarization or full-polarimetric) is an open issue to be addressed during the commissioning phase activities. In this study, the ancillary data impact on soil moisture and vegetation optical depth retrievals is thoroughly evaluated using SMOS simulated data, the use of the vertical (T_{vv}) and horizontal (T_{hh}) brightness temperatures separately, and of the first Stokes parameter (T_I) on the minimization process is explored, and an optimal retrieval configuration is devised. The simulation strategy is described in Section 3.2, and simulation results are analyzed in Section 3.3. The main findings and contributions of this work are discussed in Section 3.4.

3.2 Simulation and retrieval strategy

The performance of different retrieval configurations, depending on the *a priori* information that is used in the retrievals and its associated uncertainty, is analyzed using SMOS-like brightness temperatures (T_B) generated by SEPS. The L2 Processor Simulator, in turn, is used to retrieve soil moisture from SEPS realistic T_B (see Section 1.3.1). The L2 Processor integrates the forward model in Section 2.2 and the optimization algorithm in Section 2.3.

In the forward modeling, the effect of surface roughness on the microwave emission has been corrected using (2.27), where Q_s and n have been set equal to zero, according to [Wigneron et al. \[2001\]](#), and the roughness parameter h_s has been retrieved as a free parameter, without using any interdependency on soil moisture or surface roughness characteristics (see Section 2.2.4). The vegetation contribution has been modeled using (2.32), where it is assumed that: (i) vegetation canopy is in equilibrium with soil temperature, (ii) τ and ω are polarization and angle independent (see Section 2.2.5). The dielectric mixing model in [Wang and Schmugge \[1980\]](#) has been used to relate soil moisture to soil emissivity, where soil texture has been assumed to be equal to the ECOCLIMAP’s mean global clay and sand fractions [[Masson et al., 2003](#)], which are 20.4% and 48.3%, respectively, and soil porosity has been set to 38%.

In the present study, the impact that the uncertainty of the ancillary data used in the minimization process has on the retrieval of soil moisture and vegetation optical depth from SMOS observations has been thoroughly evaluated. To do so, the five parameters dominating the microwave emission at L-band (s_m , h_s , T_s , ω and τ) have been considered as possible *a priori* information to be used in the retrievals; the uncertainties of s_m and h_s

over the bare soils scenarios, and of τ and ω over the vegetation-covered scenarios have been progressively tuned in different L2 Processor simulations, starting from very large values (no prior information is added) to very restrictive conditions (high confidence on the *a priori* information). T_s is set to its first-guess value during the retrieval process with an accuracy of 2 K, in agreement with results of previous studies [Pellarin *et al.*, 2003; Pardé *et al.*, 2004; Davenport *et al.*, 2005]. Then, when all uncertainties are set to large values, all parameters are free and retrieved (i.e. an N-P approach). In contrast, when a high constraint is imposed on a parameter, it is set to a constant value and, therefore, it is not retrieved (i.e. 2-P is explored when a high constraint is imposed on h_s and ω , and s_m and τ are free and retrieved).

Also, each simulation has been formulated using vertical (T_{vv}) and horizontal (T_{hh}) polarizations separately and using the first Stokes parameter (T_I) so as to compare these two approaches. Note that, up to date, the formulation of the SMOS-derived soil moisture retrieval problem on the Earth reference frame (and therefore the use of the full-polarimetric mode) is the preferred one [Pardé *et al.*, 2004; Saleh *et al.*, 2009]. Hence, in this study the retrieval is formulated in terms of T_I as an alternative approach, since retrievals using the first Stokes parameter could benefit of having less angular dependency than $T_{vv} - T_{hh}$, therefore reducing the degrees of freedom during the inversion process, which could lead to better soil moisture retrievals. Also, retrievals using T_I are more robust to geometric and Faraday rotations, which is critical from an operational point of view.

Note that the use of $T_{vv} - T_{hh}$ or T_I may be linked to the choice of the MIRAS full-polarimetric mode or the dual-polarization mode, respectively. If retrievals are formulated using the two polarizations separately, the Faraday rotation in the ionosphere should be corrected since at L-band it can be sufficient so as to cause errors in the retrieval of the surface parameters (see Section 2.1.5). Therefore, as third and/or fourth Stokes parameters could be highly useful for a precise Faraday correction, the CF formulation in the Earth or antenna frame is usually linked to the use of the full-polarimetric mode. Also, large singularities are induced by the inversion of the geometric and Faraday rotations while passing the measured brightness temperatures from antenna to Earth frame in dual-polarization mode [Waldteufel and Caudal, 2002]. In contrast, T_I is unaffected by Faraday rotation; retrievals using the first Stokes parameter can be calculated in the two operation modes, with the difference that when the dual-polarization mode is used the integration time is maximized and better radiometric sensitivity could be obtained [Camps *et al.*, 2005].

It is important to outline that retrievals are performed under the following guidelines and assumptions:

- The geophysical models used in the L2 Processor Simulator are the same as in SEPS. Then, the effect of the model used is not affecting the results.
- The performance of the cost function configuration is not dependent on σ_{F_n} , since the absolute accuracy of the radiometric measurements is available on the SEPS output and is used in the retrievals.
- The search limits of the retrieved variables in the CF have been reduced within reasonable bounds, namely $0 \leq s_m \leq 0.5 \text{ m}^3/\text{m}^3$, $250 \leq T_s \leq 350 \text{ K}$, $0 \leq h_s \leq 5$, $0 \leq \tau \leq 3 \text{ Np}$, and $0 \leq \omega \leq 0.3$, to reduce the computational time.
- The reference values of the parameters used in the CF are determined from a normal distribution with a standard deviation of 2 K for T_s , 0.05 for h_s , 0.1 for ω , 0.1 Np for τ , and $0.04 \text{ m}^3/\text{m}^3$ for s_m , added to the original values. Thus, since realistic initial values

are used on the minimization process, the study focuses on selecting the optimum level of *a priori* information to be used in the retrievals and its associated uncertainty.

These simplifications are needed to make an homogeneous and approachable intercomparison study of the different retrieval configurations. However, note that further studies will be required to assess the limitations imposed by heterogeneity of vegetation cover and soil characteristics within a satellite footprint.

Four master scenarios (bare dry soil, bare wet soil, vegetation-covered dry soil and vegetation-covered wet soil) have been created using SEPS with the aim of comparing the different retrieval configurations and addressing separately the contribution of the bare soil parameters (s_m , T_s and h_s), and of the vegetation descriptors (τ and ω), on a dry and on a wet soil. Constant input parameters have been used in the simulations to evidence the contribution of each parameter in the final result and facilitate the analysis. Soil moisture values of $0.02 \text{ m}^3/\text{m}^3$ and $0.2 \text{ m}^3/\text{m}^3$ have been defined to represent dry and wet soils, respectively, the h_s is set to 0.2 –representing rather smooth roughness conditions–, and nominal values are given to the vegetation parameters $\tau = 0.24 \text{ Np}$ and $\omega = 0$ [*SMOS Algorithm Theoretical Bases Document*, 2007]. These parameters have been summarized in Table 3.1.

Table 3.1 Selected values of soil moisture (s_m), soil roughness parameter (h_s), soil temperature (T_s), vegetation optical depth (τ) and vegetation albedo (ω) for the four master scenarios

	s_m [m^3/m^3]	h_s	T_s [K]	τ [Np]	ω
Bare dry soil	0.02	0.2	300	0	0
Bare wet soil	0.2	0.2	300	0	0
Dry soil + canopy	0.02	0.2	300	0.24	0
Wet soil + canopy	0.2	0.2	300	0.24	0

3.3 Simulation results

On a first stage, a bare soil scenario is simulated to retrieve s_m , T_s and h_s . It is assumed that T_s is known by means of thermal infrared observations and/or meteorological models with an accuracy of 2 K, so σ_{T_s} is set to 2 K [*Wan, 2008*]. The entire range of variability of s_m and h_s on the *CF* is analyzed and results are shown for bare dry and wet soil on Fig. 3.1 (a) and (b), respectively, using $T_{vv} - T_{hh}$ and on Fig. 3.2 (a) and (b), respectively, using T_I . From these results, it can be inferred that it is important –although not critical– to add a restriction on the soil roughness parameter h_s . An expected error of 0.05 on h_s is therefore suggested for the soil moisture retrieval scheme. With this constraint, SMOS scientific requirements are met in the case of using T_I (a s_m RMSE of $0.02 \text{ m}^3/\text{m}^3$ is obtained over dry soils and of $0.04 \text{ m}^3/\text{m}^3$ over wet soils). In the case of using $T_{vv} - T_{hh}$, however, a s_m RMSE of $\approx 0.08 - 0.09 \text{ m}^3/\text{m}^3$ is obtained over both dry and wet soils.

After this initial study, a vegetation-covered scenario is simulated to retrieve s_m , T_s , τ and ω . On these experiments h_s is set to 0.2 and will not be retrieved so as to de-couple the effect of soil roughness, and no restrictions are added on soil moisture ($\sigma_{s_m} = 100 \text{ m}^3/\text{m}^3$). Therefore, the simulations over vegetation-covered scenes embrace the entire range of variability of the vegetation descriptors τ and ω , keeping $\sigma_{s_m} = 100 \text{ m}^3/\text{m}^3$ and $\sigma_{T_s} = 2$

K. Retrieved s_m RMSE versus the uncertainty on τ is shown for dry and wet soils on Fig. 3.1 (c) and (d), respectively, using $T_{vv} - T_{hh}$ and on Fig. 3.2 (c) and (d) using T_I . From these figures, it can be noted that there is a strong decrease of the brightness temperatures sensitivity to s_m in the presence of vegetation and that s_m RMSE increases with σ_τ . When $\sigma_\tau \rightarrow \infty$, s_m RMSE converges nearly to the same values in the two formulations (s_m RMSE $\approx 0.11 - 0.14 \text{ m}^3/\text{m}^3$ for vegetation-covered dry soils and s_m RMSE $\approx 0.10 - 0.11 \text{ m}^3/\text{m}^3$ for vegetation-covered wet soils). Since there is also a high interest in deriving VWC maps from future SMOS observations, the optical depth RMSE obtained with the different simulations has also been analyzed and is plotted versus the uncertainty on τ on Fig. 3.1 (e) and (f) for vegetation-covered dry and wet soils, respectively, using $T_{vv} - T_{hh}$ and on Fig. 3.2 (e) and (f), respectively, using T_I . From these figures, it can be remarked that optical depth RMSE increases monotonically with σ_τ when using the two formulations. In the case of high uncertainty on the vegetation parameters ($\sigma_\tau = 3, \sigma_\omega \rightarrow \infty$), τ RMSE converges to the same values for dry and wet soils: τ RMSE $\approx 0.8 - 0.9 \text{ Np}$ using $T_{vv} - T_{hh}$ and τ RMSE $\approx 0.5 \text{ Np}$ using T_I .

The most beneficial retrieval configuration will be the one providing the minimum s_m and τ RMSE. The choice of σ_τ is clear: since s_m and τ RMSE increase monotonically with σ_τ , the ideal case would be to fix it ($\sigma_\tau = 0.001 \text{ Np}$). Yet, although the study is theoretical and covers all the range of variability of the parameters, only realistic uncertainties in the ancillary data must be considered in selecting the optimum. Thus, considering the auxiliary sources available, an expected error of 0.1 Np in vegetation optical depth is suggested in the *CF* formulation.

Regarding the choice of σ_ω , a clear improvement can be observed on τ RMSE when a high constraint is imposed on ω ($\sigma_\omega = 0.001$) and $\sigma_\tau > 0.3 \text{ Np}$, whereas a lower constraint of 0.1 seems to have little or no effect (compared to the case of no restrictions on ω , $\sigma_\omega \rightarrow \infty$); adding or not restrictions on ω , though, does not cause s_m RMSE to vary significantly. From these results, it can be inferred that no constraints on ω are needed under nominal vegetation conditions. Nonetheless, note that auxiliary information of ω could be needed in the case of heterogeneous areas and dense vegetation covers [*Pardé et al., 2004; Davenport et al., 2005*]. With these constraints ($\sigma_\tau = 0.1 \text{ Np}$, $\sigma_\omega \rightarrow \infty$), a s_m RMSE of $0.11 \text{ m}^3/\text{m}^3$ is obtained on vegetation-covered scenarios using $T_{vv} - T_{hh}$, and a s_m RMSE of $\approx 0.06 - 0.07 \text{ m}^3/\text{m}^3$ using T_I . These results indicate that the s_m RMSE mission requirement of $0.04 \text{ m}^3/\text{m}^3$, which is also the accuracy of most soil moisture sensors [*Delta-T Devices Ltd., 2007*], could not be fully satisfied in the presence of vegetation.

Regarding τ retrievals, adding the suggested restrictions on the *CF* of $\sigma_\tau = 0.1 \text{ Np}$ and $\sigma_\omega = 0.1$ is notably improving the accuracy of the results (a τ RMSE of 0.2 Np is obtained using $T_{vv} - T_{hh}$ and of 0.1 Np using T_I).

From (2.30), the optical depth can be linearly related to the VWC using the so-called b parameter, which depends mainly of crop type and frequency. At L-band, a value of $b = 0.15 \text{ m}^2/\text{kg}$ was found to be representative of most agricultural crops at L-band, with the exception of grasses [*van de Griend and Wigneron, 2004*]. Using this value, VWC maps with an accuracy of $\approx 3.3 - 6 \text{ kg}/\text{m}^2$ could be obtained in the case of complete uncertainty on the vegetation parameters ($\sigma_\tau = 3 \text{ Np}$, $\sigma_\omega \rightarrow \infty$), and VWC maps with an accuracy of $\approx 0.6 - 1.3 \text{ kg}/\text{m}^2$ could be obtained in the case of adding the suggested τ and ω restrictions. These calculations, although not precise, indicate that the use of vegetation optical depth data as auxiliary information in the minimization process is critical to derive VWC maps from SMOS at the required accuracy of $0.2 \text{ kg}/\text{m}^2$.

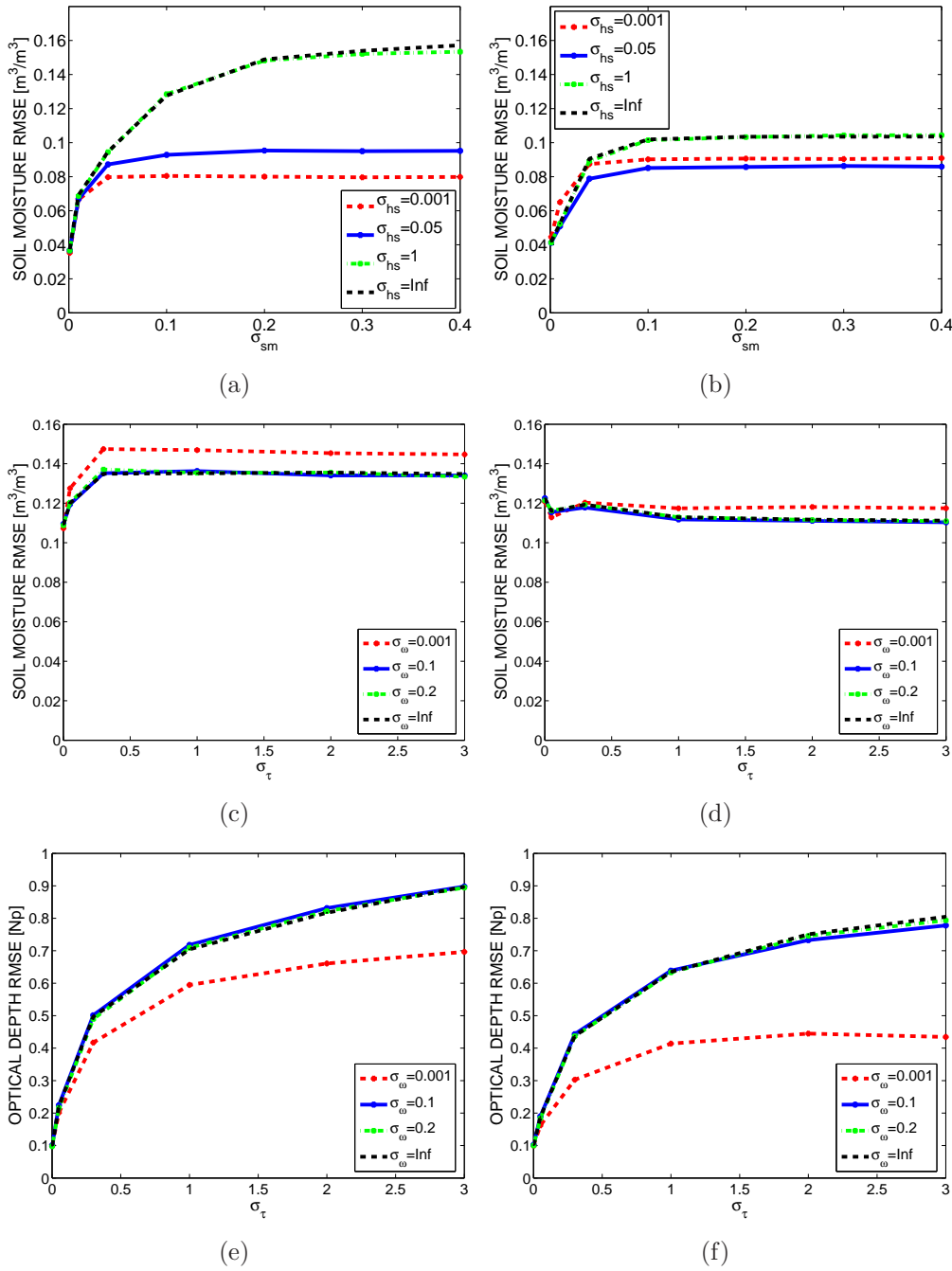


Figure 3.1 Graphical plots of retrievals formulated using vertical (T_{vv}) and horizontal (T_{hh}) polarizations. Retrieved soil moisture RMSE over a (a) bare dry soil, and (b) bare wet soil scenario, for different uncertainties on auxiliary soil moisture (σ_{sm}) and roughness parameter (σ_{hs}). Retrieved optical depth RMSE over a (c) vegetation-covered dry soil, (d) vegetation-covered wet soil, (e) vegetation-covered dry soil, and (f) vegetation-covered wet soil scenario, for different uncertainties on auxiliary optical depth (σ_τ) and albedo (σ_ω).

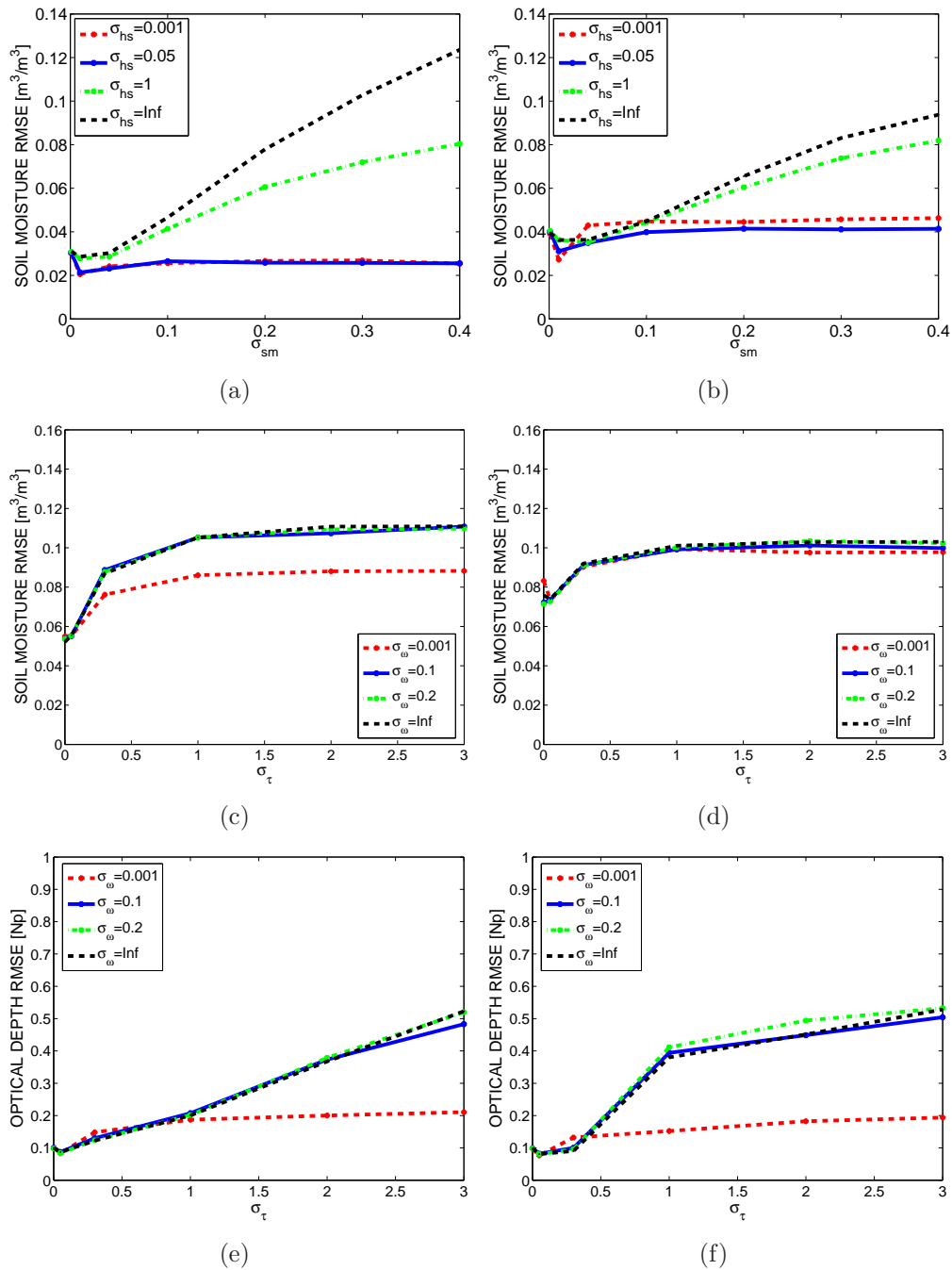


Figure 3.2 Graphical plots of retrievals formulated using the first Stokes parameter (T_1). Retrieved soil moisture RMSE over a (a) bare dry soil, and (b) bare wet soil scenario, for different uncertainties on auxiliary soil moisture (σ_{sm}) and roughness parameter (σ_{hs}). Retrieved optical depth RMSE over a (c) vegetation-covered dry soil, (d) vegetation-covered wet soil, (e) vegetation-covered dry soil, and (f) vegetation-covered wet soil scenario, for different uncertainties on auxiliary optical depth (σ_{τ}) and albedo (σ_{ω}).

3.4 Discussion and conclusions

This study has analyzed the impact in the soil moisture retrieval performance of adding ancillary data with different associated uncertainty, and of using vertical (T_{vv}) and horizontal (T_{hh}) polarizations separately or the first Stokes parameter (T_I), which may be linked to the choice of the full-polarimetric or dual-polarization SMOS operation mode. The performance of the different methods has been analyzed using SMOS simulated observations, and results are presented in terms of retrieved soil moisture RMSE and retrieved optical depth RMSE over four master homogeneous scenarios: 1) bare dry soil, 2) bare wet soil, 3) vegetated dry soil, and 4) vegetated wet soil. The main conclusions can be summarized as follows:

- Over bare soils, this study shows that adding ancillary information of soil roughness (h_s) on the cost function considerably improves the accuracy of s_m retrievals. It is in good agreement with other L-band retrieval studies [*Pardé et al., 2004; Davenport et al., 2005*]. With the suggested uncertainty of 0.05 on ancillary h_s data, and of 2 K on T_s data ($\sigma_{T_s} = 2$ K, from thermal infrared observations or meteorological models), SMOS science requirements could be met in the case of using T_I (s_m RMSE of 0.02 m^3/m^3 and 0.04 m^3/m^3 are obtained over dry and wet soils, respectively). Using $T_{vv} - T_{hh}$, however, a s_m RMSE of $\approx 0.08 - 0.09 \text{ m}^3/\text{m}^3$ is obtained over both dry and wet soils.
- As expected, there is a strong decrease of the brightness temperatures sensitivity to s_m in the presence of vegetation. Results indicate that adding vegetation albedo does not cause s_m and τ retrievals to vary significantly and $\sigma_\omega \rightarrow \infty$ is proposed. Note that ω information is not needed in the particular nominal vegetation case studied ($\tau = 0.24$ Np and $\omega = 0$), but could be needed in the general case of heterogeneous areas and dense vegetation covers [*Pardé et al., 2004; Davenport et al., 2005*]. In contrast, the uncertainty on the auxiliary optical depth data used on the CF is highly affecting s_m retrievals; s_m RMSE increases with σ_τ , converging to $\approx 0.11 - 0.14 \text{ m}^3/\text{m}^3$ for vegetation-covered dry soil and of $\approx 0.10 - 0.11 \text{ m}^3/\text{m}^3$ for wet soil, when $\sigma_\tau \rightarrow \infty$. From these results, and considering the auxiliary sources available, a constraint of $\sigma_\tau = 0.1$ Np in the CF is recommended. With this constraint, a s_m RMSE of 0.11 m^3/m^3 is obtained over vegetation-covered scenarios using $T_{vv} - T_{hh}$, and of $\approx 0.06 - 0.07 \text{ m}^3/\text{m}^3$ using T_I .
- The use of τ ancillary information on the CF is critical to obtain VWC maps from τ retrievals with the required accuracy (0.2 kg/m^2). Retrieved τ RMSE increases monotonically with the uncertainty of the τ ancillary information used (σ_τ) on the CF , converging to $\approx 0.8 - 0.9$ Np using $T_{vv} - T_{hh}$ and to ≈ 0.5 Np using T_I , in the case of high uncertainty on the vegetation parameters ($\sigma_\tau = 3$ Np, $\sigma_\omega \rightarrow \infty$). With the suggested τ and ω constraints ($\sigma_\tau = 0.1$, $\sigma_\omega \rightarrow \infty$), a τ RMSE of 0.2 Np is obtained using $T_{vv} - T_{hh}$ and of 0.1 Np using T_I . τ retrievals in a previous overpass could be used as auxiliary information in retrievals at time t , as in *Wigneron et al. [2000]*, *Pardé et al. [2004]*. If no τ auxiliary information is available, an alternative approach is presented in *Meesters et al. [2005]*, where τ is retrieved from passive observations at 6.6 GHz using only land surface temperature as ancillary information.
- Soil moisture and vegetation optical depth retrievals show a better performance if the minimization is formulated using the Stokes parameter T_I than using the Earth

reference frame $T_{vv} - T_{hh}$. This result suggests that the dual-polarization mode should not *a priori* be discarded, since T_I in the dual-polarization mode should have better radiometric sensitivity than in full-polarimetric mode. In addition, retrievals using T_I are more robust to geometric and Faraday rotations than $T_{vv} - T_{hh}$. Note that this effect has been perfectly corrected in the simulations, but can be critical from an operational point of view.

- It must be remarked that, if *a priori* information on the land surface conditions can be available, restrictions on h_s , T_s , and τ are highly recommended. The better the accuracy of these auxiliary sources, the better are the s_m and τ retrievals that could be obtained. All things considered, the required uncertainty levels for auxiliary input data are $\sigma_{h_s} = 0.05$, $\sigma_{T_s} = 2$ K, and $\sigma_\tau = 0.1$ Np.

This study has presented a concise error analysis of the SMOS soil moisture retrieval algorithm, and an optimal retrieval configuration for SMOS has been devised. Results preference the use of the first Stokes parameter, and the use of constraints on h_s , T_s , and τ with associated uncertainties $\sigma_{h_s} = 0.05$, $\sigma_{T_s} = 2$ K, and $\sigma_\tau = 0.1$ Np. But then, what are current uncertainties of available global datasets that could be used as sources for ancillary data? are auxiliary data available with the required uncertainty bounds? the answer to these questions is complex at this point; there are global datasets that could provide the auxiliary information needed, namely, ECOCLIMAP for h_s or vegetation characteristics, Global Land Cover Characterization (GLCC) or MODIS-derived Leaf Area Index (LAI) for vegetation optical depth, AVHRR or METEOSAT-derived global albedo and ERA40 or ERAINTERIM reanalysis of the different parameters from the European Center for Medium-range Weather Forecasts (ECMWF). However, very little information about its associated uncertainty is available or has been evaluated at the time of writing. In the last version of the SMOS Algorithm Theoretical Bases Document (ATBD) the use of auxiliary information from ECOCLIMAP and ECMWF forecasts is recommended, but no precise information of its uncertainty can be found. Due to this lack of information, a discussion regarding the uncertainty of the existing global datasets and its possible use as auxiliary input data has not been included. Still, the results presented in this work can timely help to define the SMOS operation mode, which will be decided at the end of the commissioning phase, and to define the soil moisture retrieval scheme and the auxiliary data needed in the operational SMOS Level 2 Processor. These are crucial issues that have to be addressed to retrieve accurate global soil moisture estimates from SMOS.

*Those who wish to succeed must
ask the right preliminary questions*
Aristotle (384BC-322BC)

4

Analysis of the SMOS soil moisture retrieval algorithm

This chapter analyzes the SMOS soil moisture inversion algorithm, both theoretically and in terms of performance. Different soil moisture retrieval configurations are examined, depending on whether prior information is used in the inversion process or not. Retrievals are formulated in terms of vertical (T_{vv}) and horizontal (T_{hh}) polarizations separately and using the first Stokes parameter (T_I), over six main surface conditions combining dry, moist and wet soils with bare and vegetation-covered surfaces. A sensitivity analysis illustrates the influence that the geophysical variables dominating the Earth's emission at L-band have on the precision of the retrievals, for each configuration. It shows that, if adequate constraints on the auxiliary data are added, the algorithm should converge to more accurate estimations. SMOS-like brightness temperatures are also generated by the SMOS End-to-end Performance Simulator (SEPS) to assess the retrieval errors produced by the different cost function configurations. Better soil moisture retrievals are obtained when the inversion is constrained with prior information, in line with the sensitivity study, and more robust estimates are obtained using T_I than using T_{vv} and T_{hh} .

4.1 Introduction

The SMOS mission is the first-ever satellite dedicated to provide global measurements of soil moisture. Its payload is MIRAS, a novel 2-D interferometric radiometer that provides brightness temperature measurements of the Earth at different polarizations and incidence angles (see Section 1.3.1). SMOS-derived soil moisture products are expected to have an accuracy of $0.04 \text{ m}^3/\text{m}^3$ over $50 \times 50 \text{ km}^2$ and a revisit time of 3 days. Also, there is a high interest in obtaining VWC maps with an expected accuracy of $0.2 \text{ kg}/\text{m}^2$ every 6 days from SMOS observations [*Mission Objectives and Scientific Requirements of the SMOS mission*, 2003]. Previous studies have pointed out the need to combine SMOS brightness temperatures (T_B) with auxiliary data to achieve the required accuracy and several retrieval configurations have been proposed [*Pellarin et al.*, 2003; *Pardé et al.*, 2004; *Camps et al.*, 2005]. However, the optimal soil moisture retrieval setup needs yet to be optimized.

The dielectric constant of soils is highly related to the soil moisture content s_m , and also depends on the soil type [*Wang and Schmugge*, 1980; *Dobson et al.*, 1985]. In addition to the

soil dielectric constant, other soil and vegetation parameters are known to play a significant role in the L-band microwave emission and therefore must be accounted for in the retrieval process, namely vegetation optical depth τ , from where vegetation water content maps can be derived [van de Griend and Wigneron, 2004], vegetation albedo ω , soil surface temperature T_s , and soil surface roughness (parameterized using the soil roughness parameter h_s). In this study, different Bayesian-based retrieval configurations have been examined depending on whether *a priori* information of these geophysical variables is used in the inversion process or not. Retrievals have been formulated in terms of vertical (T_{vv}) and horizontal (T_{hh}) polarizations separately, and using the first Stokes parameter (T_I), over six main surface conditions combining dry, moist and wet soils with bare and vegetation-covered surfaces. Hence, this study analyzes four critical aspects which will provide valuable information for the inversion of soil moisture from L-band passive microwave observations:

1. The use of no *a priori* information in the *CF* vs. the use of *a priori* information about all the auxiliary parameters excluding s_m on the cost function.
2. The effect of the presence of a vegetation canopy.
3. The effect of the soil moisture content (dry/moist/wet).
4. The retrieval formulation using the vertical and horizontal polarizations separately or using the first Stokes parameter.

In Section 4.2, a description of the scenarios, the forward model and the optimization scheme used in this study to analyze the retrieval of soil moisture from L-band passive observations is provided. A sensitivity analysis of the inversion algorithm is afterwards presented in Section 4.3. It illustrates the influence that the geophysical variables dominating the Earth's emission at L-band have on the precision of the retrievals, for the different retrieval configurations. In Section 4.4, the performance of the different retrieval configurations is analyzed using SMOS-like T_B generated with the SEPS. The L2 Processor Simulator (see Section 1.3.1), in turn, is used to retrieve soil moisture from SEPS synthetic T_B . The sensitivity analysis and the analysis with simulated SMOS data are necessary to characterize the different cost function configurations both theoretically and in terms of performance. In Section 4.5 the main results of this work are summarized, and their applicability to upcoming SMOS data on an operational basis is discussed.

4.2 Methodology

Soil moisture inversion from passive microwave observations is complex, since the microwave emission from soils depends strongly on its moisture content, but also on other surface characteristics such as soil type, soil roughness, surface temperature and vegetation cover, and their contributions must be carefully de-coupled in the retrieval process. The geophysical model function used on this study to mimic the Earth's emission at L-band – the so-called forward model – is thoroughly described in Section 2.2. Particularly, (i) the effect of surface roughness on the microwave emission has been corrected using (2.27), with $Q_s = n = 0$, according to Wigneron *et al.* [2001]; (ii) the vegetation contribution has been modeled using (2.32), where it is assumed that vegetation canopy is in equilibrium with soil temperature, and τ and ω are polarization and angle independent; and (iii) the dielectric

mixing model in [Wang and Schmugge \[1980\]](#) has been used to relate soil moisture to soil emissivity.

Six master scenarios (bare dry/moist/wet soil and vegetation-covered dry/moist/wet soil) have been defined to evaluate how the soil moisture retrievals can be affected by both the presence of a canopy layer and the soil moisture content itself. These scenarios are homogeneous, described by parameters s_m , T_s , h_s , τ and ω , which are constant in all the area; soil moisture values of $0.02 \text{ m}^3/\text{m}^3$, $0.2 \text{ m}^3/\text{m}^3$, and $0.4 \text{ m}^3/\text{m}^3$ have been used for dry, moist and wet soil, respectively, the roughness parameter h_s has been set to 0.2 – which represents a rather smooth surface –, and nominal values are given to the vegetation parameters $\tau = 0.24 \text{ Np}$ and $\omega = 0$ [[SMOS Algorithm Theoretical Bases Document, 2007](#)]. A summary of the parameters' value for each scenario is given in Table 4.1. Soil texture was assumed to be equal to the mean global clay and sand fractions derived from ECOCLIMAP [[Masson et al., 2003](#)], which are 20.4% and 48.3%, respectively, while soil porosity was assumed to be equal to 38%.

Table 4.1 Selected original values of soil moisture (s_m), soil roughness (h_s), soil temperature (T_s), vegetation albedo (ω) and vegetation optical depth (τ) for the six master scenarios. $\sigma_{p_i}^0$ is the nominal uncertainty of parameter p_i .

		s_m [m^3/m^3] ($\sigma_{s_m}^0 = 0.04$)	h_s ($\sigma_{h_s}^0 = 0.05$)	T_s [K] ($\sigma_{T_s}^0 = 2$)	ω ($\sigma_{\omega}^0 = 0.1$)	τ [Np] ($\sigma_{\tau}^0 = 0.1$)
Bare	dry soil	0.02	0.2	300	0	0
	moist soil	0.2	0.2	300	0	0
	wet soil	0.4	0.2	300	0	0
Vegetation-covered	dry soil	0.02	0.2	300	0	0.24
	moist soil	0.2	0.2	300	0	0.24
	wet soil	0.4	0.2	300	0	0.24

The SMOS multi-angular retrieval algorithm approach is described in Section 2.3. In this study, retrievals have been formulated using the vertical and horizontal polarizations separately, and using the first Stokes parameter. Up to date, the formulation of the SMOS-derived soil moisture retrieval problem in the Earth's reference frame (using $T_{vv} - T_{hh}$) is the preferred one [[Pardé et al., 2004](#); [Saleh et al., 2009](#)]. Thus, the formulation in terms of T_I is presented as an alternative approach, since retrievals using T_I are unaffected by geometric and Faraday rotations, which is critical from an operational point of view. Also, retrievals using T_I could benefit of having less angular dependency than $T_{vv} - T_{hh}$, therefore reducing the degrees of freedom during the inversion process, which could lead to better soil moisture retrievals.

To explore the effect of adding *a priori* (background) information of other geophysical variables on the minimization process, the two Bayesian-based *CF*s in Table 4.2 have been formulated: CF_1 represents the case in which no *a priori* information is added, i.e. the cost function consists of an observational term and all parameters are free in the minimization; and CF_2 stands for the case in which *a priori* information of all auxiliary parameters is added, excluding s_m . Note that, in addition to using or not auxiliary information in the retrievals, it is important to have a good knowledge of the quality of the prior information. Thus, in the present study, T_s is assumed to be known by means of thermal infrared observations and/or meteorological models with an accuracy of 2 K, and the accuracies of h_s , ω and τ estimations are comprehensively set according to 1) the simulated study in Chapter 3, where a large number of retrieval configurations, depending on the *a priori* information used in

the retrievals and its associated uncertainty were tested, and 2) the field experiments in [Monerriis \[2009\]](#).

Table 4.2 Selected standard deviations of soil moisture (s_m), soil roughness (h_s), soil temperature (T_s), vegetation albedo (ω) and vegetation optical depth (τ) for the two selected cost function configurations CF_1 and CF_2

	σ_{s_m} [m ³ /m ³]	σ_{h_s}	σ_{T_s} [K]	σ_{ω}	σ_{τ} [Np]
CF_1	100	100	100	100	100
CF_2	100	0.05	2	0.1	0.1

4.3 Sensitivity analysis

To get a visual understanding of the CF shape under different configurations, a set of retrieval setups has been formulated from (2.34), and the most interesting sections (2-D contours) are visualized showing the behavior of the minima in 2-D cuts through a 5-D CF , where the 5-D are the parameters of the forward model, namely s_m , T_s , h_s , ω and τ . These contour plots indicate in the first place that the CF has only one minimum and converges to the original values, as expected. Note that it is important to ensure that the minimization algorithm will be approaching the “true” solution, and not a local minimum. Also, the CF can be interpreted as the misfit of the measurements with the solution lying on the geophysical model function surface. Therefore, the shape of its minimum determines the precision of the retrieval. The broader the minimum, the larger is the effect of noise and the less accurate are the retrieved parameters, since we are ignoring all the neighboring solutions, which have a comparable probability of being the true state (as represented by the original s_m , h_s , T_s , ω and τ in Table 4.1) [[Portabella and Stoffelen, 2004](#); [Gabarró et al., 2009](#)].

The weights of (2.34) were set according to Table 4.2, with $\sigma_{T_B} = 2$ K. The original parameters (“measured”) were set according to the simulated scenario (see the parameters’ original values for each scenario in Table 4.1) and the forward model on Section 2.2 was used to simulate T_B^{meas} for incidence angles between 0° and 65°. Likewise, this was done to obtain T_B^{model} over the ranges $0 \leq s_m \leq 0.5$ m³/m³, $250 \leq T_s \leq 350$ K, $0 \leq h_s \leq 5$, $0 \leq \tau \leq 3$ Np, and $0 \leq \omega \leq 0.3$ [[SMOS Algorithm Theoretical Bases Document, 2007](#)]. Hence, when the scenario’s original values are used T_B^{model} equals T_B^{meas} , which corresponds to the CF ’s absolute minimum. Note that the axes on the figures have been normalized to the parameters’ original values $\pm 3 \cdot \sigma_{p_i}^0$ to cover the 99.7% of the values the retrieved parameters could have and properly compare the different contours. Since the purpose of this experiment is to evaluate the sensitivities (gradients) of the different cost-function configurations, no bias errors are assumed in measurements or references; the effect of having an *a priori* value which is far from the true state is analyzed in Section 4.4.

Figure 4.1 shows CF ’s formulated using the first Stokes parameter over a bare dry soil scenario for the case where no constraints are added (Fig. 4.1 (a) and (b)) and for the case where *a priori* information about all the auxiliary parameters, except for s_m , is added (Fig. 4.1 (c) and (d)). It can be seen that the minimum in the case of no constraints is elliptical with its major axis covering almost the entire range of roughness parameter and soil temperature values for the contour line $CF = 1$. This indicates a low sensitivity to

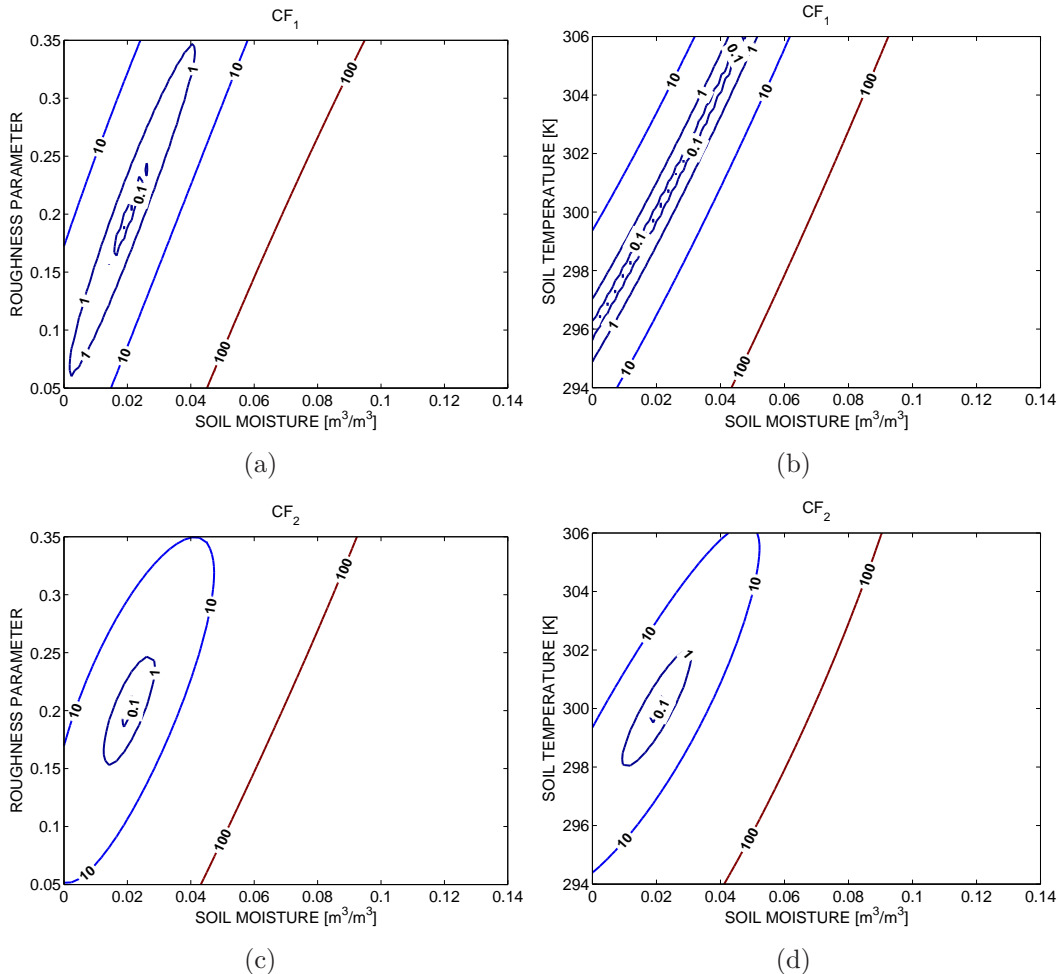


Figure 4.1 Cost functions formulated using T_I over a bare dry soil scenario. Contours of h_s vs. s_m (a) and T_s vs. s_m (b), with no constraints on the cost function (CF_1). Contours of h_s vs. s_m (c) and T_s vs. s_m (d), adding constraints on all parameters, except for s_m (CF_2).

h_s and T_s and a high sensitivity to s_m . When the constraints are used the minimum is better defined, i.e. there is a higher probability of finding the true state. This effect is also manifested on vegetation-covered simulations (see Fig. 4.2). Therefore, assuming that both the real errors in T_B and the reference values are Gaussian, a constrained CF should lead to a more accurate s_m retrieval than a non-constrained CF . Also, it is important to note that the position of the minimum does not change when adding constraints on the CF .

The presence of a sparse vegetation layer is examined in Fig. 4.2. It can be noticed that the contours plotted are clearly widened if compared to those on Fig. 4.1, which indicates a higher uncertainty in the soil moisture retrievals over vegetation-covered surfaces, as expected. The vegetation canopy attenuates the soil emission and diminishes the forward model sensitivity to s_m ; as the observed soil emissivity decreases with an increase in vegetation biomass, the soil moisture information contained in the microwave signal decreases [Ulaby *et al.*, 1981].

The difference between CF s simulated over a bare dry, moist, and wet soil scenario can be seen in Fig. 4.3. The cost function sensitivity to h_s is the highest on wet soils (Fig. 4.3 (e)) and the lowest on dry soils (Fig. 4.3 (a)). In contrast, the cost function sensitivity to T_s

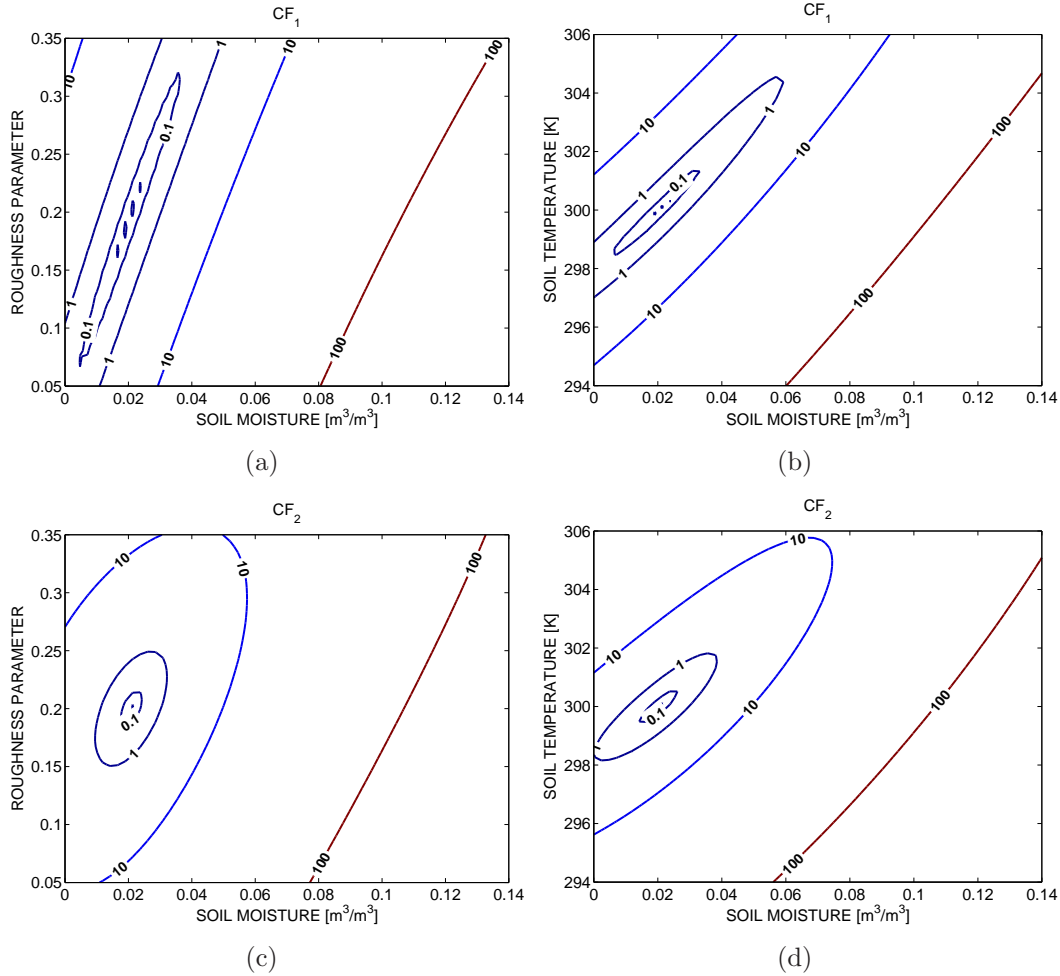


Figure 4.2 Cost functions formulated using T_I over a vegetation-covered dry soil scenario. Contours of h_s vs. s_m (a) and T_s vs. s_m (b), with no constraints on the cost function (CF_1). Contours of h_s vs. s_m (c) and T_s vs. s_m (d), adding constraints on all parameters, except for s_m (CF_2).

is the highest on dry soils (Fig. 4.3 (b)) and the lowest on wet soils (Fig. 4.3 (f)). Therefore, constraints on both h_s and T_s should be needed to improve the accuracy of soil moisture retrievals over bare soils under diverse moist conditions. This result can also be extended to vegetation-covered scenarios, where the same behavior has been observed in the CF s. Note that the plots on Fig. 4.1 and Fig. 4.3 are in good agreement with other L-band retrieval studies, where adding constraints on h_s and T_s was also shown to be preferable [Pardé et al., 2004; Davenport et al., 2005].

Regarding the vegetation parameters, Fig. 4.4 shows that the CF sensitivity to τ is the highest over vegetation-covered wet soils and decreases as the soil under the vegetation canopy dries out, as can be easily appreciated in the contour line $CF = 10$. This indicates that better τ retrievals should be expected over wet than over dry soils. The soil contribution to the overall above-canopy emission is lower under wet than over dry soil conditions (because of the lower soil emission), and the canopy contribution thus becomes relatively larger. This could probably lead to the higher sensitivity for canopy parameters that are observed under wet conditions.

The effect of adding restrictions on τ and ω in the CF is not clearly visible in the contours

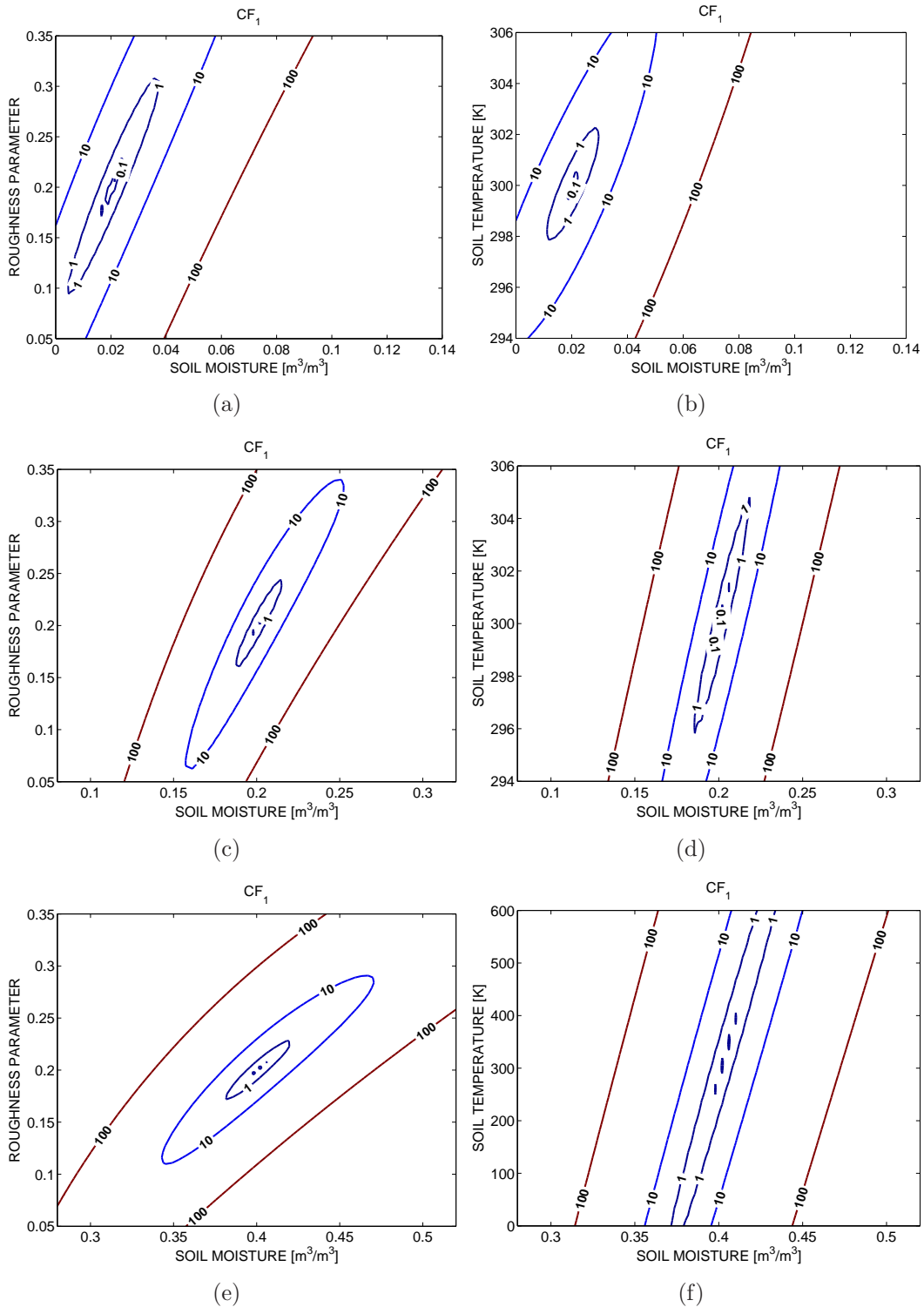


Figure 4.3 Cost functions formulated using $T_{vv} - T_{hh}$ with no constraints. Contours of h_s vs. s_m (a) and T_s vs. s_m (b) over a bare dry soil scenario. Contours of h_s vs. s_m (c) and T_s vs. s_m (d) over a bare moist soil scenario. Contours of h_s vs. s_m (e) and T_s vs. s_m (f) over a bare wet soil scenario.

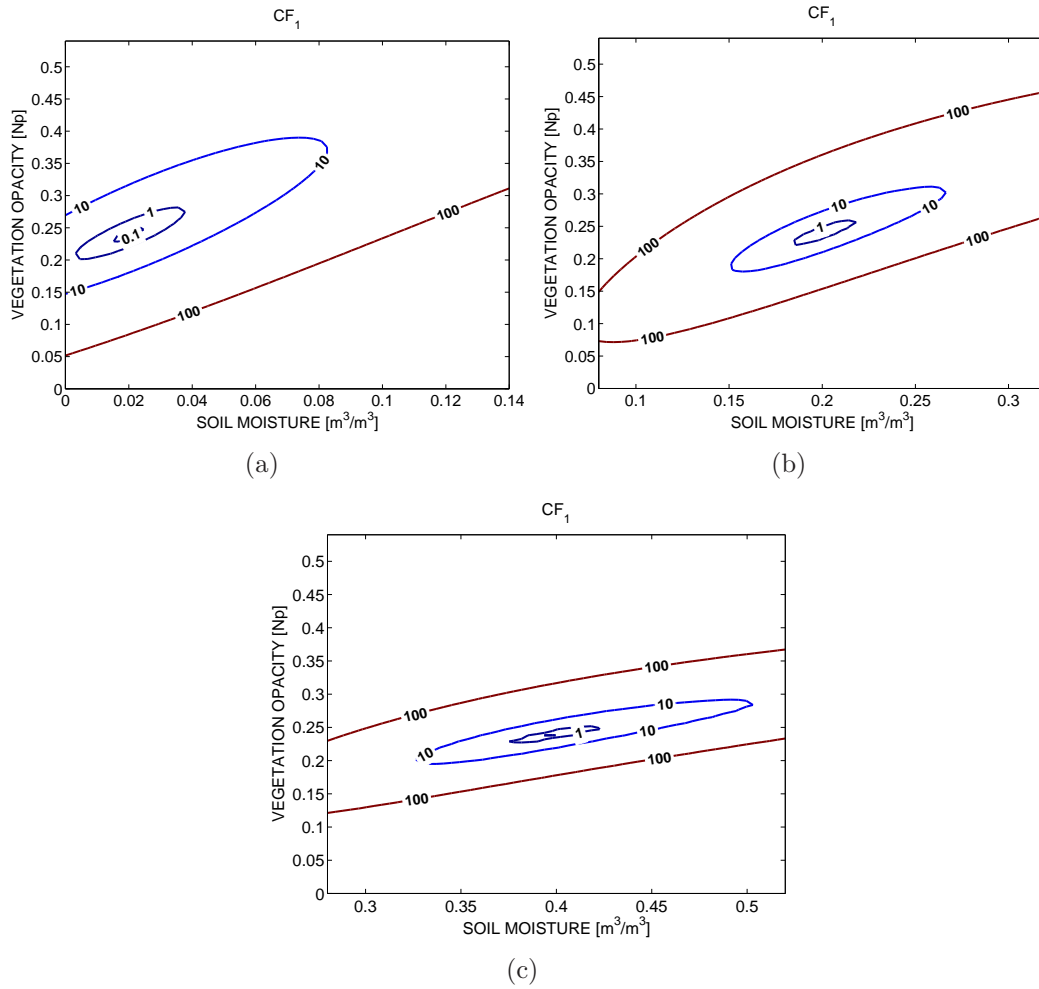


Figure 4.4 Cost functions formulated using $T_{vv} - T_{hh}$ with no constraints. Contours of τ vs. s_m (a) over a vegetation-covered dry scenario. Contours of τ vs. s_m (b) over a vegetation-covered moist scenario. Contours of τ vs. s_m (c) over a vegetation-covered wet scenario.

on Fig. 4.4, probably because the restrictions imposed on these variables are not very severe ($\sigma_\tau = \sigma_\omega = 0.1$). However, it is shown to actually improve s_m and τ retrievals when applied to SMOS-like simulated data on Section 4.4.2

Comparing Figs. 4.1(a) and (b) with Figs. 4.3(a) and (b), it can be observed that the CF sensitivity to T_s is higher when using the $T_{vv} - T_{hh}$ than when using T_I (narrower, better defined minimum, less solutions with a comparable probability of being the true state), whereas the sensitivity to h_s remains the same. No remarkable differences have been found between the two formulations over vegetation-covered scenarios.

4.4 Analysis with simulated SMOS data

4.4.1 Simulation strategy

L-band 2-D multi-angular brightness temperatures over land have been simulated over the six main surface conditions of Table 4.1 using SEPS. Next, these data have been used as

input to the L2 Processor Simulator, where retrievals have been performed using the two CF configurations of Table 4.2, formulated in terms of vertical (T_{vv}) and horizontal (T_{hh}) polarizations separately and using the first Stokes parameter (T_I). Note that over the bare soil scenarios $\tau = \omega = 0$ will not be retrieved. It is important to outline that SEPS simulated error on T_B includes all the instrument specific features (measured antenna pattern, measured receivers' frequency response, thermal drifts, etc.) and all the realistic features induced by the image reconstruction algorithms, such as biases and the pixel-dependent radiometric accuracy [*SEPS Architectural Detailed Design Document, 2006*].

Retrievals on the L2 Processor Simulator have been performed under the following guidelines and assumptions:

- The geophysical models and the ancillary used in the L2 processor Simulator are the same as in SEPS, so that the effect of the model used is not affecting the results.
- The performance of the CF configuration is not dependent on σ_{F_n} , since the absolute accuracy of the radiometric measurements is available on the SEPS output and is used in L2 Processor Simulator.
- To reduce the computational time, the search limits of the retrieved variables in the CF have been reduced within reasonable bounds, namely $0 \leq s_m \leq 0.5 \text{ m}^3/\text{m}^3$, $250 \leq T_s \leq 350 \text{ K}$, $0 \leq h_s \leq 5$, $0 \leq \tau \leq 3 \text{ Np}$, and $0 \leq \omega \leq 0.3$ [*SMOS Algorithm Theoretical Bases Document, 2007*].
- The reference values of the parameters on the CF (p_{i0}) are randomly determined from a normal distribution with the nominal standard deviations in Table 4.1, added to the original values.
- Homogeneous pixels have been assumed in the simulations to evidence the contribution of each parameter in the results and facilitate the analysis. However, further studies will be required to assess the limitations imposed by heterogeneity of vegetation cover and soil characteristics within a satellite footprint.

4.4.2 Simulation results

The mean, standard deviation, and RMSE of the retrieved soil moisture ($s_m^{ret} - s_m^{orig}$) are shown in Table 4.3 for the bare soil scenarios and in Table 4.4 for the vegetation-covered scenarios defined in Table 4.1. The soil moisture retrieval configurations that meet the SMOS science requirement of $s_m \text{ RMSE} \leq 0.04 \text{ m}^3/\text{m}^3$ are marked in bold. It can be seen that in the case of no constraints (CF_1), the s_m RMSE is far from the $0.04 \text{ m}^3/\text{m}^3$ benchmark: a retrieval error of ≈ 0.10 to $0.21 \text{ m}^3/\text{m}^3$ is obtained over bare soils and of ≈ 0.11 to $0.24 \text{ m}^3/\text{m}^3$ over vegetation-covered soils.

Table 4.3 shows that the s_m retrieval error over bare soil scenarios is considerably improved when constraints on h_s and T_s are added (CF_2): s_m RMSE retrievals of ≈ 0.07 to $0.09 \text{ m}^3/\text{m}^3$ are obtained using $T_{vv} - T_{hh}$ and of ≈ 0.03 to $0.05 \text{ m}^3/\text{m}^3$ using T_I . This result is in line with Fig. 4.1 and with other L-band retrieval studies [*Pardé et al., 2004; Davenport et al., 2005*]. The special case of having $h_s=1$ on the bare soil scenarios has also been simulated. Results show that a higher roughness leads to an increased s_m RMSE in all the scenarios and configurations studied, and only in the case of using T_I and CF_2 the s_m retrieval error is below $0.05 \text{ m}^3/\text{m}^3$. Table 4.4 shows that the s_m retrieval error over vegetation-covered scenarios ($\tau = 0.24 \text{ Np}$ and $\omega = 0$) is also improved when constraints on

Table 4.3 Retrieved mean, standard deviation and root mean square soil moisture error of simulated SMOS observations over the bare soil scenarios in Table 4.1, using the cost-function configurations of Table 4.2, formulated on the Earth’s reference frame or using the first Stokes parameter. Soil moisture retrieval configurations with s_m RMSE $\leq 0.04 \text{ m}^3/\text{m}^3$ are marked in bold.

Scenario	Retrieved s_m error	CF_1 ($h_s=0.2/h_s=1$)		CF_2 ($h_s=0.2/h_s=1$)	
		Earth	Stokes	Earth	Stokes
Bare Dry Soil	Mean	0.149/0.185	0.106/0.140	0.026/0.038	0.010/0.021
	Std. dev.	0.157/0.179	0.164/0.160	0.092/0.102	0.024/0.039
	RMS	0.216/0.257	0.196/0.211	0.096/0.108	0.027/0.044
Bare Moist Soil	Mean	0.069/0.059	0.018/0.056	0.014/0.050	0.006/0.006
	Std. dev.	0.122/0.160	0.134/0.143	0.085/0.105	0.039/0.054
	RMS	0.140/0.171	0.135/0.154	0.085/0.116	0.039/0.054
Bare Wet Soil	Mean	-0.056/-0.100	-0.081/-0.090	-0.052/-0.113	-0.038/-0.031
	Std. dev.	0.084/0.142	0.096/0.130	0.050/0.088	0.032/0.037
	RMS	0.101/0.173	0.125/0.158	0.072/0.143	0.050/0.048

Table 4.4 Retrieved mean, standard deviation and root mean square soil moisture error of simulated SMOS observations over the vegetation-covered scenarios in Table 4.1, using the cost function configurations of Table 4.2, formulated on the Earth’s reference frame or using the first Stokes parameter.

Scenario	Retrieved s_m error	CF_1		CF_2	
		Earth	Stokes	Earth	Stokes
Dry Soil + Canopy	Mean	0.169	0.170	0.060	0.049
	Std. dev.	0.162	0.169	0.116	0.053
	RMS	0.235	0.240	0.131	0.072
Moist Soil + Canopy	Mean	0.076	0.095	0.003	0.048
	Std. dev.	0.143	0.121	0.120	0.076
	RMS	0.162	0.153	0.120	0.090
Wet Soil + Canopy	Mean	-0.062	-0.040	-0.061	-0.021
	Std. dev.	0.119	0.102	0.093	0.050
	RMS	0.134	0.109	0.111	0.054

Table 4.5 Retrieved mean, standard deviation and root mean square vegetation optical depth error of simulated SMOS observations over the vegetation-covered scenarios in Table 4.1, using the cost function configurations of Table 4.2, formulated on the Earth reference frame or using the first Stokes parameter.

Scenario	Retrieved τ error	CF_1		CF_2	
		Earth	Stokes	Earth	Stokes
Dry Soil + Canopy	Mean	0.439	0.369	0.110	0.036
	Std. dev.	0.888	0.606	0.307	0.085
	RMS	0.991	0.709	0.326	0.092
Moist Soil + Canopy	Mean	0.224	0.100	0.049	0.025
	Std. dev.	0.732	0.342	0.267	0.078
	RMS	0.765	0.356	0.272	0.082
Wet Soil + Canopy	Mean	0.187	0.019	0.053	-0.029
	Std. dev.	0.714	0.208	0.274	0.056
	RMS	0.738	0.209	0.279	0.063

h_s , T_s , ω , and τ are used (CF_2): s_m RMSE retrievals of ≈ 0.11 to $0.13 \text{ m}^3/\text{m}^3$ are obtained using $T_{vv} - T_{hh}$ and of ≈ 0.05 to $0.09 \text{ m}^3/\text{m}^3$ using T_I . This result is in agreement with Fig. 4.2. Hence, simulation results show that the use of adequate constraints on the CF improve the accuracy of s_m retrievals in all the cases studied, and that the formulation in terms of T_I is advantageous. Note that the improvement in s_m retrievals when using CF_2 is specially noticeable in all the scenarios under dry soil conditions, where a remarkably high s_m RMSE is obtained using CF_1 . In fact, lower s_m RMSE is obtained over wet soils than over dry soils (bare and vegetation-covered), except for the case of bare soil retrievals using T_I and CF_2 . This could be due to the reduced sensitivity of the dielectric constant at low moisture levels [*de Jeu et al., 2008*].

Vegetation optical depth retrievals are analyzed in Table 4.5. It shows that a notable improvement on τ RMSE is obtained when adequate constraints on the CF are used (CF_2) than when all parameters are free (CF_1). Also, results indicate that better τ retrievals should be obtained over wet soils than over dry soils, in agreement with Fig. 4.4. It can also be seen that better τ retrievals are obtained using T_I than using $T_{vv} - T_{hh}$ in all scenarios and configurations, specially under moist and wet soil conditions. From 2.30, the optical depth can be linearly related to the VWC using the so-called b parameter, which depends mainly of crop type and frequency. At L-band, $b = 0.15 \text{ m}^2/\text{kg}$ was found to be representative of most agricultural crops, with the exception of grasses [*van de Griend and Wigneron, 2004*]. This value has been used in this study to evaluate if VWC maps with an accuracy of $0.2 \text{ kg}/\text{m}^2$ could be obtained from the τ retrievals in Table 4.5. Thus, using this approach and considering that no constraints are added, VWC with an accuracy of ≈ 4.9 to $6.6 \text{ kg}/\text{m}^2$ could be obtained using $T_{vv} - T_{hh}$ and of ≈ 1.4 to $4.7 \text{ kg}/\text{m}^2$ using T_I . If constraints are added, the accuracy of VWC improves to ≈ 1.9 to $2.2 \text{ kg}/\text{m}^2$ using $T_{vv} - T_{hh}$ and to ≈ 0.4 to $0.6 \text{ kg}/\text{m}^2$ using T_I . These results show that the formulation in terms of T_I and the use of constraints on the CF substantially improve τ retrievals, although the VWC requirement of $0.2 \text{ kg}/\text{m}^2$ is not fully satisfied.

It must be remarked that, in the results presented on Tables 4.3, 4.4, and 4.5, all pixels

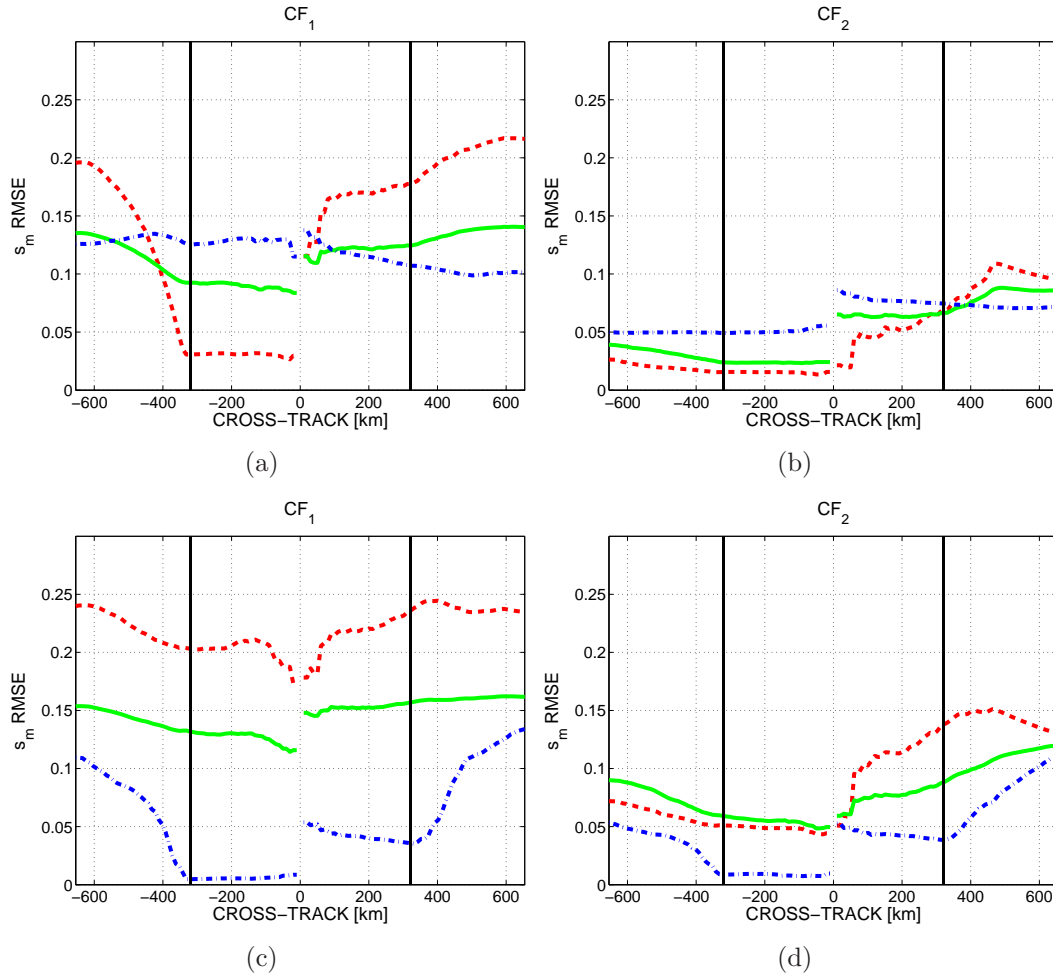


Figure 4.5 Retrieved soil moisture RMSE of simulated SMOS observations versus pixel position in the swath. Simulations over the dry (red, dashed lines), moist (green, solid lines), and wet (blue, dashed-dotted lines) scenarios of Table 4.1. First row: bare soil scenarios, second row: vegetation-covered scenarios. Left column: with no constraints on the cost-function (CF_1), right column: adding constraints on all parameters, except s_m (CF_2). In each plot: first Stokes parameter (left side) and Earth's reference frame (right side). Vertical lines denote the Narrow Swath.

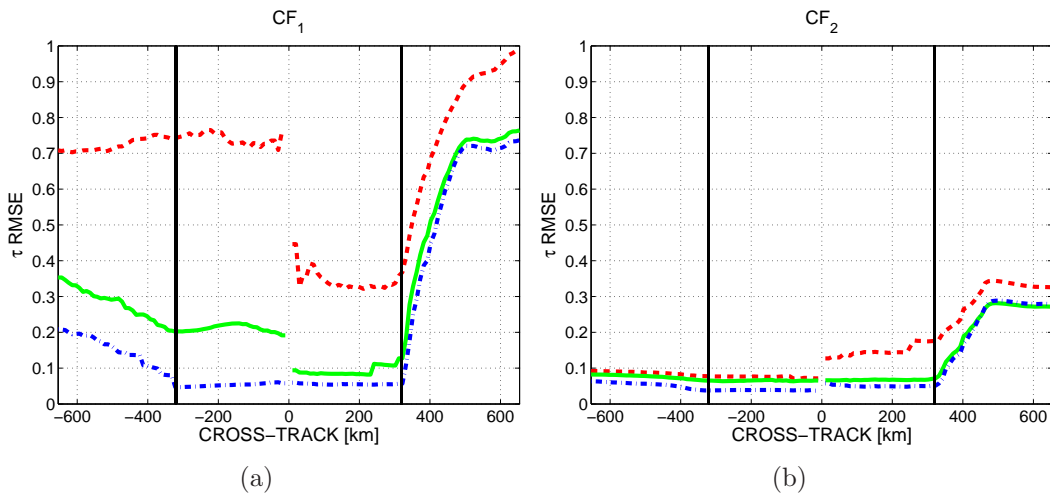


Figure 4.6 Retrieved vegetation optical depth RMSE of simulated SMOS observations versus pixel position in the swath; Simulations over the vegetation-covered dry (red, dashed lines), moist (green, solid lines), and wet (blue, dashed-dotted lines) scenarios of Table 4.1, (a) with no constraints on the cost-function (CF_1), and (b) adding constraints on all parameters, except s_m (CF_2). In each plot: first Stokes parameter (left side) and Earth’s reference frame (right side). Vertical lines denote the Narrow Swath.

in the SMOS FOV are considered, regardless of the number of measurements on each pixel. However, due to the SMOS observation geometry, all pixels in the FOV do not have the same properties: as the pixel’s distance to the ground-track increases, the pixel is imaged fewer times, its angular variation is reduced, and the instrument’s noise increases [Camps *et al.*, 2005]. This fact indicates that better accuracies should be expected if only the central part of the FOV – the so-called Narrow Swath (640-km) [Barré *et al.*, 2008] – is considered. However, note that the use of Narrow Swath implies a temporal resolution of 7-days, which will limit the applicability of the data. Still, the possibility of increasing the accuracy of the retrievals by considering a narrower swath should not be neglected. Hence, the retrieval performance has been explored further in Figs. 4.5 and 4.6, as a function of the ground-track distance.

Figure 4.5 illustrates the soil moisture retrieval performance *vs.* the pixel position, for all the retrieval configurations and scenarios studied. On the left-hand side of each plot simulation results correspond to the use of the first Stokes parameter, and on the right-hand side to the use of the Earth reference frame. Figures 4.5 (a) and (b) show results over bare soil scenarios using CF_1 and CF_2 , respectively. Figures 4.5 (c) and (d) show results over vegetation-covered scenarios using CF_1 and CF_2 , respectively. Vertical lines denote the Narrow Swath. These plots effectively show how the s_m RMSE increases with the distance to the ground-track. Also, it can be seen that the use of adequate constraints (CF_2) dramatically improves soil moisture retrievals. Note that either in the case of considering the nominal or the Narrow Swath, the use of CF_2 and formulation in terms of T_I should provide more accurate soil moisture retrievals.

Likewise, Fig. 4.6 illustrates the vegetation optical depth retrieval performance *vs.* the pixel position, for all the retrieval configurations and scenarios studied. When no constraints are added (Fig. 4.6 (a)), the retrieval error rapidly increases beyond the Narrow Swath width. If adequate constraints are added (Fig. 4.6 (b)), the error dependence on the ground-track distance is reduced, specially in the case of using T_I . As in the case of soil moisture retrievals,

the use of adequate constraints (CF_2) and the formulation in terms of T_I should lead to more accurate τ retrievals in the case of considering either the nominal or the Narrow Swath.

4.5 Discussion and conclusions

The SMOS mission has the unique capability to map the Earth's surface soil moisture globally using L-band multi-angular and dual-polarization/full-polarimetric observations. In this paper, the soil moisture inversion algorithm from SMOS observations has been analyzed through the use of different cost function configurations covering four critical aspects: 1) the use of auxiliary information on the cost function, 2) the effect of the presence of a vegetation canopy, 3) the effect of the soil moisture content (dry/moist/wet), and 4) the retrieval formulation in terms of $T_{vv} - T_{hh}$ (Earth reference frame) or T_I (the first Stokes parameter).

First, the sensitivity of the different cost function configurations to the geophysical variables dominating the L-band emission (s_m , h_s , T_s , τ and ω) has been examined by looking at the shape of the most interesting cuts (2-D contours). Then, a simplified version of the operational SMOS Level 2 Processor has been used to test the accuracy of the different retrieval setups with realistic SMOS-like brightness temperatures generated by SEPS. Simulated results are consistent with the theoretical study, therefore reinforcing the conclusions of this work, which can be summarized as follows:

- The use of adequate ancillary information on the cost function significantly improves the accuracy of s_m retrievals, and is needed to satisfy the SMOS science requirement of $0.04 \text{ m}^3/\text{m}^3$. Using CF_2 constraints (Table 4.2), s_m RMSE retrievals of ≈ 0.07 to $0.09 \text{ m}^3/\text{m}^3$ are obtained using $T_{vv} - T_{hh}$, and of ≈ 0.03 to $0.05 \text{ m}^3/\text{m}^3$ using T_I over bare soil scenarios. As expected, there is a strong decrease of the brightness temperatures sensitivity to s_m in the presence of vegetation, and s_m RMSE retrievals of ≈ 0.11 to $0.13 \text{ m}^3/\text{m}^3$ are obtained using $T_{vv} - T_{hh}$, and of ≈ 0.05 to $0.09 \text{ m}^3/\text{m}^3$ using T_I (with $\tau = 0.24, \omega = 0$).
- The use of adequate constraints on the cost function (CF_2) highly improves the accuracy of τ estimations and it is therefore critical to derive VWC maps from SMOS at the required accuracy of $0.2 \text{ kg}/\text{m}^2$. Preliminary calculations indicate that VWC maps with an accuracy of ≈ 1.9 to $2.2 \text{ kg}/\text{m}^2$ could be estimated from τ retrievals using $T_{vv} - T_{hh}$, and of ≈ 0.4 to $0.6 \text{ kg}/\text{m}^2$ using T_I .
- More accurate soil moisture estimates have been obtained over wet soils than over dry soils (bare and with low vegetation), except for the case of retrievals using T_I and CF_2 . Regarding τ retrievals, better estimates have been obtained over wet soils in all the configurations.
- Better s_m retrievals have been obtained when using T_I than when using $T_{vv} - T_{hh}$. Also, the formulation in terms of T_I leads to better τ retrievals in all the configurations. These results suggest that, although $T_{vv} - T_{hh}$ is the formulation generally adopted in most studies, the use of T_I should not be disregarded. In addition, T_I is more robust in the presence of geometric and Faraday rotations (at any spatial scale) than $T_{vv} - T_{hh}$. These effects have been perfectly corrected on the simulations, but are critical from an operational point of view.

- Due to SMOS observation geometry, better accuracies could be obtained if only the Narrow Swath (640-km, the central part of the FOV) is used. The use of adequate constraints (CF_2) and the retrieval formulation in terms of T_I provide the most accurate s_m and τ retrievals over all scenarios in the case of considering either the nominal or the Narrow Swath.

From an operational perspective, it should be pointed out that the forward model used in SEPS and in the L2 Processor Simulator is not as complex as the one used in the ESA's SMOS Level 2 Processor (the L-MEB model). The L2 processor Simulator uses the $\tau - \omega$ model –which is the core of the L-MEB model–, and does not take into account any specific land cover parametrization for heterogeneous pixels. The main difference in the forward model is in the optical depth formulation, that in L-MEB is dependent on the incidence angle and the vegetation structure. In this study, it is considered that most vegetation covers are randomly oriented, and the optical depth parametrization has been simplified (see Section 4.2). However, note that the optimization algorithm used in the L2 Processor Simulator is exactly as described in the SMOS Algorithm Theoretical Bases Document [*SMOS Algorithm Theoretical Bases Document*, 2007]. Thus, the results presented in this work are potentially applicable to SMOS data.

Following the successful deployment of SMOS in orbit, continuous efforts will be needed to consolidate an optimal soil moisture retrieval configuration. The present study has analyzed the soil moisture inversion algorithm, both theoretically and in terms of performance with simulated data; it addresses key aspects for the retrieval of accurate soil moisture estimations from SMOS, and the results presented can be readily transferred to the operational Level 2 Processor to produce the much needed global maps of the Earth's surface soil moisture.

*From error to error, one discovers
the entire truth*

Sigmund Freud (1856-1939)

5

Spatial resolution enhancement of SMOS data: a deconvolution-based approach

A deconvolution scheme to improve the spatial resolution of future SMOS data is presented. Different deconvolution techniques using improved Wiener, Constrained Least Squares and wavelet filters that may include different levels of auxiliary information in the reconstruction process have been developed and results of its application to simulated SMOS brightness temperatures and to passive L-band airborne observations are presented. With these techniques, the product of spatial resolution and radiometric sensitivity of SMOS-like images was improved in a 49% over land pixels and in a 30% over sea pixels. Results with airborne field experimental data confirm that with these methods it is possible to improve the radiometric sensitivity of the observations as well as to improve the coast line definition.

5.1 Introduction

The SMOS mission is an unprecedented initiative to provide global land moisture and surface salinity mapping; its unique payload is MIRAS, a novel L-band 2-D synthetic aperture radiometer with dual-polarization/fullpolarimetric capabilities (see Section 1.3.1). SMOS provides a totally new type of multiangular Earth observations, characterized by having a different pixel size and orientation, and a different noise level and spatial resolution for each pixel (Fig. 5.1(a)).

SMOS observations have a temporal resolution of 3 days, compatible with the temporal variability of the near surface land moisture over continental surfaces, and a ground spatial resolution of 30–60 km at best. This resolution, while adequate for many global applications, is a limiting factor to its application in regional scale studies. As mentioned in *Entekhabi et al.* [1999], the use of space-based passive microwave data in hydrological modeling is not straightforward because of the scale discrepancy between the typical spatial resolution of microwave radiometers (several tens of kilometers) and the scale at which most hydrological processes occur (approximately 1–10 km). Therefore, the possibility of assimilating future SMOS data in land surface hydrologic applications relies on the prospect of improving its spatial resolution.

Within this context, different downscaling approaches have been adopted in order to distribute fine-scale land moisture within coarse SMOS observations (see Section 1.4). This

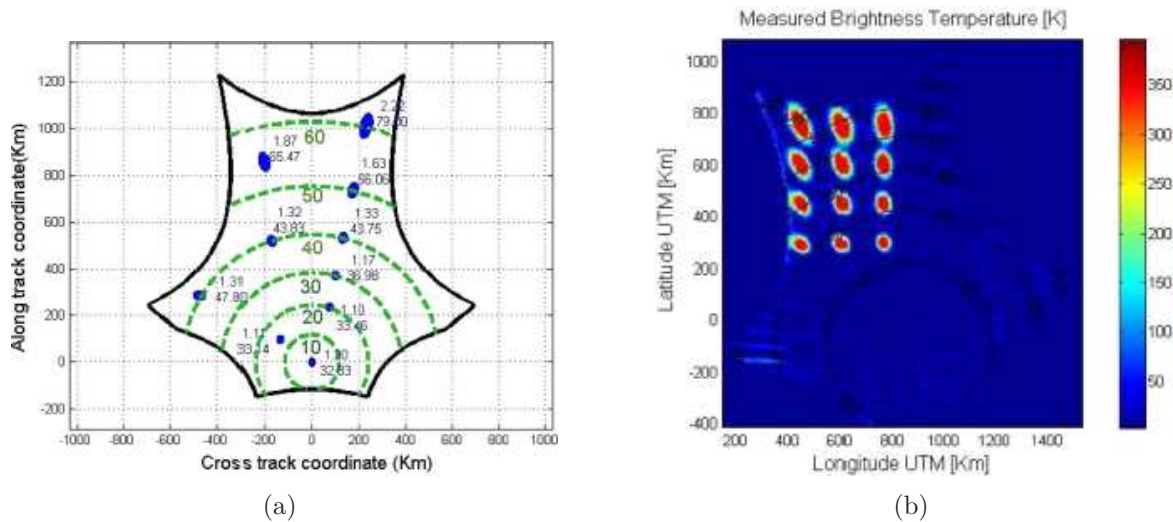


Figure 5.1 SMOS observations with varying incidence angles, pixel spatial resolutions, and axial ratios (a). Reconstructed synthetic image with point sources over the area under study processed by SEPS (b)

work explores the possibility of improving the spatial resolution of SMOS products by the use of deconvolution algorithms that optimally perform noise regularization and include auxiliary information in the reconstruction process.

The prospective deconvolution algorithms expected to be applied to SMOS' radiometric measurements should be newly created due to the unique characteristics of the mission instrument and to its specific way of observing the Earth's surface. In Section 5.2, a linear algebra framework is given to the deconvolution process, and the different algorithms developed are presented. Frequency-domain-based methods and combined frequency-wavelet-domain-based methods have been found to be the most suitable for this task. In Section 5.3, an exhaustive test of these methods using SEPS is shown, and comparisons are made in terms of both spatial resolution and radiometric sensitivity enhancement. Section 5.4 evaluates the performance of the deconvolution approach using airborne field experimental data. In the final section, the most significant results of this study are summarized, and the applicability and usefulness of the presented algorithms to future SMOS data on an operational basis is discussed.

5.2 Deconvolution algorithms

5.2.1 Discrete formulation

Satellite microwave radiometric observations may be expressed as the convolution of the sensor antenna beam projected onto the Earth's surface with the Earth's brightness temperatures (T_B) integrated over the sensor footprint. Adjacent observations mostly cover the same target features on the ground, but with different contributions to the overall signal, and that overlap can be effectively used to estimate more accurately the T_B of those grid cells. Typically, in a regional scale study, the number of observations outnumbers by far the grid cells for which the unknown T_B has to be estimated. Mathematically, it derives from an ill-conditioned or ill-posed linear problem that must be carefully inverted, and proper

regularization techniques must be considered to have noise amplification under control when inversion is accomplished [Hansen, 1998]. Consequently, the existence, uniqueness, and stability of the solution are not guaranteed for the general problem even when noise is not present. In addition, the presence of noise makes an exact solution unfeasible. In this context and following the lexicographic notation [Andrews and Hunt, 1977], the formation of a T_B image can be described as:

$$g = h \otimes f + n, \quad (5.1)$$

where g is a column vector containing the real observations, f is a column vector containing the unknown T_B at the desired spatial resolution, n is a column vector that includes the noise, h is the column vector representation of the synthetic antenna response function [Bará et al., 1998], and \otimes indicates the convolution operator. A discrete convolution formulation can be derived from (5.1). Assuming that f and h are 2-D periodic functions of periods M and N adequately padded with zeros to avoid overlap between different periods and using the lexicographic notation as aforementioned:

$$g = H \cdot f + n, \quad (5.2)$$

where f , g , and n are of dimension $(M \cdot N) \times 1$ and H is of dimension $M \cdot N \times M \cdot N$. This matrix consists of M^2 partitions, each partition being of size $N \times N$ and ordered according to:

$$H = \begin{bmatrix} H_0 & H_{M-1} & H_{M-2} & \cdots & H_1 \\ H_1 & H_0 & H_{M-1} & \cdots & H_2 \\ H_2 & H_1 & H_0 & \cdots & H_3 \\ \vdots & & & & \\ H_{M-1} & H_{M-2} & H_{M-3} & \cdots & H_0 \end{bmatrix}. \quad (5.3)$$

Each partition H_j is constructed from the j^{th} row of the extended function h by a circular shifting it to the right (see Andrews and Hunt [1977] for more details).

A direct solution of (5.3) is computationally unfeasible; for practical size images, it will require the inversion of a very high number of simultaneous linear equations. Fortunately, since the matrix H is block circulant, it can be diagonalized, and the problem can be considerably reduced by working in the frequency domain, where convolution simplifies to scalar operations [Gonzalez and Woods, 1993]. Using frequency-domain-based deconvolution methods, the computation time is no longer a limitation, since nowadays, there are very powerful tools to perform fast Fourier transforms.

5.2.2 Frequency-domain algorithms

The Fourier space equivalent of (5.1) can be written as

$$G = H \cdot F + N, \quad (5.4)$$

where G , H , F , and N are the Fourier transforms of g , h , f , and n , respectively.

Linear deconvolution can be stated as the task of finding a linear operator K such that

$$F = K \cdot G. \quad (5.5)$$

The most elementary deconvolution will be performed by the simple inverse filter, given by $K = H^{-1}$. However, such filtering tends to be very error sensitive and unstable.

To perform the deconvolution, a constrained least squares (CLS) filter can be developed in which the constraint gives the designer additional control over the process. This approach consists of minimizing functions of the form $\|Q \cdot f\|^2$, where Q is a linear operator on f subject to the constraint $\|g - H \cdot f\|^2 = \|n\|^2$ (from (5.2)). Then, using the method of Lagrange multipliers [*Gonzalez and Woods, 1993*]:

$$J(f) = \|Q \cdot f\|^2 + \lambda_1 (\|g - H \cdot f\|^2 - \|n\|^2). \quad (5.6)$$

Differentiating (5.6) with respect to f and setting the result equal to zero yields

$$\frac{\partial J(f)}{\partial f} = 2Q^T Q \cdot f - 2\lambda_1 H^T (g - H \cdot f) = 0, \quad (5.7)$$

which leads to

$$f = (H^T H + \alpha \cdot Q^T Q)^{-1} \cdot H^T g, \quad (5.8)$$

where $\alpha \equiv 1/\lambda_1$ for simplification. This parameter must be adjusted such that the initial constraint $\|g - H \cdot f\|^2 = \|n\|^2$ is satisfied.

The choice of the linear operator Q generates different deconvolution techniques. However, in order to work on the frequency domain –as it has been demonstrated to be highly desirable– Q should be a block-circulant matrix. With this premise, two approaches have been found to provide satisfactory results: the well-known Fourier Wiener filter and the CLS filter.

The Wiener Filter establishes $Q^T Q = R_f^{-1} \cdot R_n$, where R_f and R_n are the correlation matrices of f and n , respectively. Performing the appropriate operations, it can be expressed in the frequency domain as

$$K(u, v) = \left[\frac{H^*(u, v)}{|H(u, v)|^2 + \alpha \left[\frac{S_n(u, v)}{S_f(u, v)} \right]} \right] G(u, v), \quad (5.9)$$

for $u, v = 0, 1, 2, \dots, N - 1$, where $S_n(u, v)$ and $S_f(u, v)$ are the Fourier transforms of R_n and R_f , and it is assumed that $M = N$. Note that, in the absence of noise $S_n(u, v) = 0$, the Wiener filter reduces to the simple inverse filter.

In most real applications, $S_f(u, v)$ cannot be determined, and the whole factor $\alpha \left[\frac{S_n(u, v)}{S_f(u, v)} \right]$ is reduced to an experimentally determined constant ϕ_0 ; hence, the Wiener filter of (5.9) is reduced to the least energy constraint filter [*Gonzalez and Woods, 1993*]. In the results presented in Section 5.3, the value of ϕ_0 has been selected by optimizing the product of radiometric sensitivity (ΔT) and spatial resolution (ΔS). In any real or synthetic aperture radiometers, the product $\Delta T \cdot \Delta S$ is constant. An increase in ΔT implies a decrease in ΔS and vice-versa [*Ulaby et al., 1981; Camps et al., 1998*]. Thus, when ΔS is improved, noise is indirectly added to the observations, and eventually, if this noise is too high, land moisture cannot be retrieved. In order to avoid this effect, it is usually considered that the optimum tradeoff between spatial resolution enhancement and radiometric sensitivity upholding is given by the minimum $\Delta T \cdot \Delta S$ [*Camps et al., 1998*].

The CLS filter includes a smoothing criterion function that varies with frequency and eliminates artifacts. Performing the convenient operations, the CLS filter in the frequency domain can be expressed as

$$K(u, v) = \left[\frac{H^*(u, v)}{|H(u, v)|^2 + \alpha [C(u, v)]} \right] G(u, v), \quad (5.10)$$

for $u, v = 0, 1, 2, \dots, N-1$, where $C(u, v)$ is the Fourier transform of the smoothing criterion function, and it is assumed that $M = N$. In this study, the second order Laplacian operator [Galatsanos and Katsaggelos, 1992] has been used as the smoothing criterion function.

The choice of the parameter α is a key issue. It controls the degree of smoothness of the solution and represents a tradeoff between fidelity to the signal (α small) and fidelity to the prior information about the solution (α large). When α tends to zero, the filter reduces to the simple inverse filter, and (5.5) becomes the ultrarough solution. When α tends to infinity, (5.5) becomes the ultrasmooth solution [Galatsanos and Katsaggelos, 1992]. In the results presented in Section 5.3, the value of α has been optimized using as a metric the product $\Delta T \cdot \Delta S$, as in the Wiener case.

Following the least-squares procedure, a novel basis for deriving filters has been developed with the possibility of having an extra constraint to improve its performance. As a first approach, the additional constraint is set to be $\|Tb - H \cdot f\|^2 = \|e\|^2$, where Tb is a T_B model of the image at L-band and e is a tolerance error.

Using L-band T_B and radiative transfer models, reasonably realistic T_B images can be simulated from auxiliary data. For instance, Merlin et al. [2008b] used simulated T_B images to disaggregate land moisture fields, and Camps et al. [2008] use synthetic L-band T_B images to reduce the scene-dependent bias and improve the coastline transition in the SMOS image reconstruction algorithm. In Section 5.3, Tb is set to be the T_B image that SEPS internally computes from auxiliary data and uses as the original T_B of the Earth's surface [Camps, 1996]. Hence, results show the best possible performance achievable by this novel kind of filters.

Two Lagrange multipliers λ_1 and λ_2 are used to include the two constraints so that

$$J(f) = \|Q \cdot f\|^2 + \lambda_1(\|g - H \cdot f\|^2 - \|n\|^2) + \lambda_2(\|Tb - H \cdot f\|^2 - \|e\|^2). \quad (5.11)$$

Differentiating with respect to f , setting the result to zero, and solving it for f , the following expression in the spatial domain is obtained:

$$f = (Q^T Q + \lambda_1 H^T H + \lambda_2 H^T H)^{-1} \cdot H^T (\lambda_1 \cdot g + \lambda_2 \cdot Tb). \quad (5.12)$$

At this point, the Wiener and the CLS concepts can be used to set the value of Q , therefore generating two new filters: the Wiener model filter and the CLS model filter, respectively. Making use of the diagonalization procedure, the following expression in the frequency domain can be obtained:

$$K(u, v) = \left[\frac{H^*(u, v) \cdot (G(u, v) + \rho \cdot TB)}{(1 + \rho)|H(u, v)|^2 + \alpha [L(u, v)]} \right], \quad (5.13)$$

where $L(u, v)$ represents $\left[\frac{S_n(u, v)}{S_f(u, v)} \right]$ in the Wiener-derived case and $C(u, v)$ in the CLS-derived case, $\alpha \equiv 1/\lambda_1$ and $\rho \equiv \lambda_2/\lambda_1$ for ease of notation, and TB is the Fourier transform of Tb . The parameter α controls the degree of smoothness of the solution, as in previous filters, and ρ controls the fidelity of the solution to the auxiliary information. Note that, if the second constraint is not added ($\lambda_2 = 0$) these new filters reduce to the former Wiener and CLS filters ((5.9) and (5.10)).

Apart from the least squares approach, the options of implementing on the frequency domain deconvolution algorithms that rely on statistics, such as the maximum likelihood or the maximum entropy, have also been thoroughly studied, but the results obtained for extended continuous images are considerably less satisfactory than the results obtained by the least squares technique [Demoment, 1989].

5.2.3 Wavelet-domain algorithms

The possibility of posing the problem on the wavelet domain has also been considered. The strength of the wavelet domain is that it economically represents images containing singularities and spatially localized features such as edges and ridges, in contrast to the high number of Fourier coefficients that will be needed for the same purpose. However, the wavelet transform is not well suited to represent general convolution operators and do not efficiently represent images with a high root mean square error (RMSE). The wavelet-vaguelette deconvolution technique as well as different wavelet-shrinkage-based signal's estimators [Mallat, 1998] have been applied to SEPS data, but probably because of the noisy nature of SMOS observations and of the colored noise inherent to the deconvolution process itself, they yield to unsatisfactory near-zero estimates. Note that the convolution operator is not diagonalized in the wavelet domain.

Within this frame, a combined Fourier-wavelet regularized algorithm that first performs Fourier regularized inversion and afterward applies wavelet denoising has been developed. It is inspired on the Fourier-wavelet regularized deconvolution (ForWaRD) method [Neelamani et al., 2004], and it is specifically adapted to properly work with future SMOS data. Using a metric based on the product $\Delta T \cdot \Delta S$, an optimal balance between the Fourier and the Wiener shrinkage is found, and the involved parameters are set.

The hybrid ForWaRD algorithm relies on a twofold basis. At the first stage, it exploits the well-adapted representation of the convolution operator in the Fourier domain to control noise amplification. The Wiener, CLS, Wiener model, and CLS model filters presented in Section 5.2.2 are used for this purpose, each one generating a ForWaRD-derived algorithm: Wiener-WaRD, CLS-WaRD, Wiener-WaRD model, and CLS-WaRD model, respectively.

At the second stage, the task of noise removal and signal estimation is conveniently achieved using wavelet shrinkage. The wavelet-domain signal estimation in ForWaRD remains effective since the noise corrupting the wavelet coefficients is not excessive, thanks to the previous Fourier regularization. Wavelet shrinkage is performed as follows. First, a rough estimate of the input signal is obtained by using a hard-thresholding technique. Then, this estimate is used to obtain a final refined estimate by employing Wiener estimation on each wavelet coefficient [Neelamani et al., 2004]. This wavelet processing is common to all the ForWaRD-derived algorithms implemented.

5.3 Application to SMOS simulated observations

In order to assess the performance of the deconvolution algorithms developed, a series of tests has been carried out using SEPS to evaluate, on the one hand, the spatial resolution obtained with each method and, on the other hand, the radiometric sensitivity achieved. As previously discussed, the best method is chosen as the one that provides the minimum $\Delta T \cdot \Delta S$. The simulations conducted to this end as well as the representative results are shown in this section.

A common scenario has been set in SEPS to run all simulations. It is located in the Pacific Ocean to avoid coastal effects, and the region under study comprises the upper left area of an SMOS snapshot (Fig. 5.1(b)) so that the variation of the pixels' spatial resolution, depending on their position in the FOV and their varying shapes, could be easily observed. Accordingly, SEPS has been conveniently modified to accept a synthetic image as input.

5.3.1 Spatial resolution enhancement

First, a synthetic image with point sources has been introduced in the area under study and has been processed by SEPS. The different methods have then been applied to the SEPS' output, and the spatial resolution of the results has been calculated as the diameter of the circle with the same area as the 3-dB footprint (ΔS). The top left pixel in Fig. 5.1(b) is taken as the worst case, since it is the pixel with the worst spatial resolution, the highest elongation, and the largest radiometric sensitivity among them. The bottom right pixel in Fig. 5.1(b) is taken as the best case. The results over these two extreme pixels are shown in Fig. 5.2. It can be seen that, after applying the deconvolution filters to the SEPS output, the shape of the pixels becomes rounded, and its spatial resolution is improved. Also, better spatial resolution is achieved when using the Wiener-derived filters than when using the CLS-derived ones. It is remarkable how the inclusion of the T_B model improves the spatial resolution in the worst case pixel. In the best case pixel, however, the inclusion of the model improves the spatial resolution when using Wiener-derived filters and barely worsens it when using CLS-derived ones. Regarding the wavelet processing, it has been found not to affect the spatial resolution of the result.

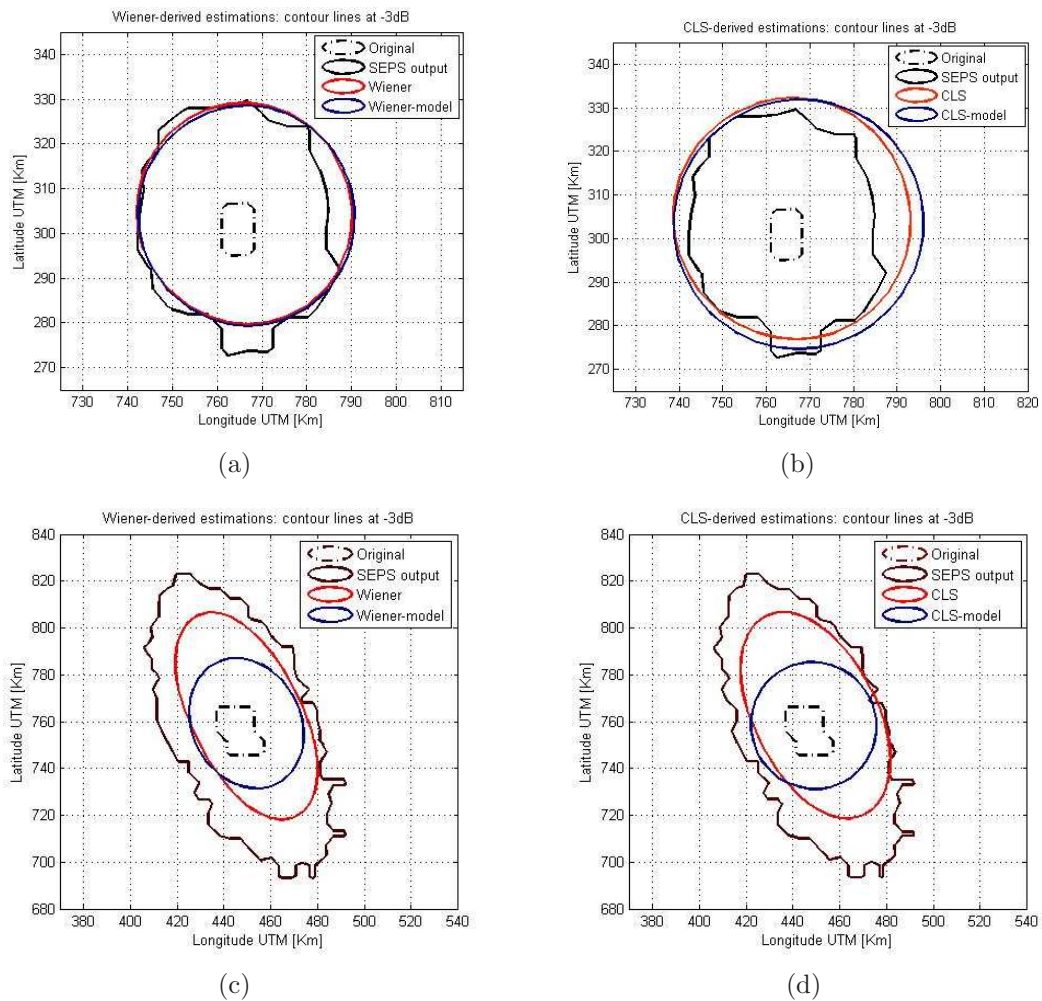


Figure 5.2 Best case pixel's contour at -3 dB after applying (a) Wiener-derived methods and (b) CLS-derived methods to Fig. 5.1(b). Worst case pixel's contour at -3 dB after applying (c) Wiener-derived methods and (d) CLS-derived methods to Fig. 5.1(b).

Discretization effects appear in the contour of the original image in Fig. 5.1(b)(c) and (d), due to the internal SEPS interpolation from the synthetic high-resolution input images used in the tests to the SMOS-like low-resolution output images, and to the resampling of SEPS low-resolution output images into a higher resolution geographic grid.

To evaluate the spatial resolution enhancement achieved with the different algorithms in an easier and more intuitive way, a set of synthetic images with vertical bars and alternative values (253 K and 120 K to represent dry land and sea, respectively) have been created with different widths. Horizontal bars have also been created so as to observe the difference between the two directions. These images have been processed by SEPS, and the different deconvolution methods have been applied over the SEPS' output. Results of these tests for representative bar widths are shown in Fig. 5.3 for Wiener-derived methods and in Fig. 5.4 for CLS-derived methods: 48 km appears to be the minimum bar width that allows one to clearly distinguish all vertical bars with all the Wiener-derived filters; when using CLS-derived filters, the minimum vertical bar width that can be distinguished is 52 km. With respect to horizontal bars, 56 km has been found to be the limiting separation between two bars in order to differentiate them with all the methods, except with Wiener-WaRD and CLS-WaRD. With these two methods, the top and top-left areas of the image are gradually blurred, following the decreasing spatial resolution pattern of SMOS observations (see Fig. 5.1), and only bars of at least 58 km width can be differentiated. Contour lines delineating the original footprint of the pixels on the upper left area of an SMOS snapshot (the area under study) have been overlaid to the images for clarity. The original spatial resolution varies from 50 km in the bottom right region to 80 km in the upper left one; after applying the deconvolution filters, the worst resolution is shown to improve from 80 to 48 km in the vertical direction and to 56 km in the horizontal direction.

It can be noticed that the filters that include the T_B model are able to discriminate the bars sharper and nicer than the other methods. In fact, follow-on experiments have shown that they could distinguish up to 40 km vertical bar widths and 44 km horizontal bar widths. Furthermore, note that better spatial resolutions are obtained with vertical bars than with horizontal bars, since in the area under study the pixels elongate having its major axis nearly in the vertical direction.

5.3.2 Radiometric sensitivity evaluation

A RMSE metric has been used to assess the radiometric sensitivity (ΔT) achieved with the different methods. It has been computed in each case with respect to the original synthetic image used as input to SEPS. To this end, a synthetic image with a step from 253 K to 120 K has been generated in the area under study and used as input to SEPS. The different methods have been applied over the SEPS output, and the corresponding ΔT values have been calculated, one for land pixels and another for sea pixels. The resulting images are shown on Fig. 5.5. The sea-land threshold is centered between 253 K and 120 K so that coastal effects are taken into account in the ΔT computation. Results will be used in Section 5.3.3 to quantify the effectiveness of the different methods.

In order to visually assess the performance of the different deconvolution schemes, the results of applying all the methods over a realistic scenario are shown in Fig. 5.6(a) for Wiener-derived filters and in Fig. 5.6(b) for CLS-derived ones. An area corresponding to Catalonia and the Balearic Islands in the northeast of Spain has been selected. It comprises a variety of land cover types, orographic features, an abrupt coastline, and the Balearic Islands, which, because of their sizes, are outstanding features upon which the spatial resolution

5.3. Application to SMOS simulated observations

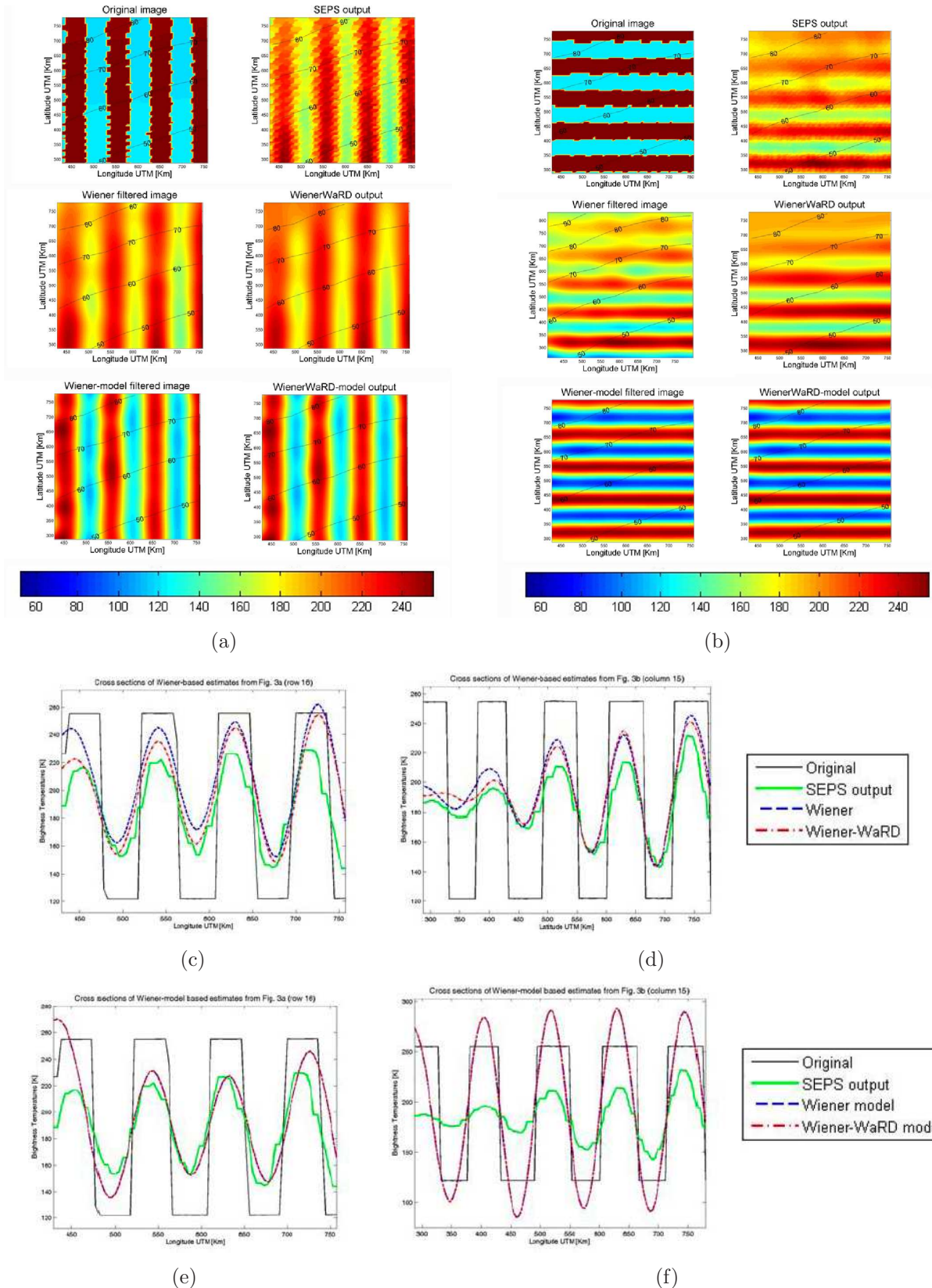


Figure 5.3 Vertical bars of 48 km width as original, SEPS output and results of applying Wiener-derived filters to SEPS output (a). Horizontal bars of 56 km width as original, SEPS output and results of applying Wiener-derived filters to SEPS output (b). Cross sections of the original image, SEPS output, Wiener and Wiener-WaRD outputs of Fig. 5.3(a) (c), and of Fig. 5.3(b) (d). Cross-sections of the original image, SEPS output, Wiener model and Wiener-WaRD model outputs of Fig. 5.3(a) (e), and of Fig. 5.3(b) (f).

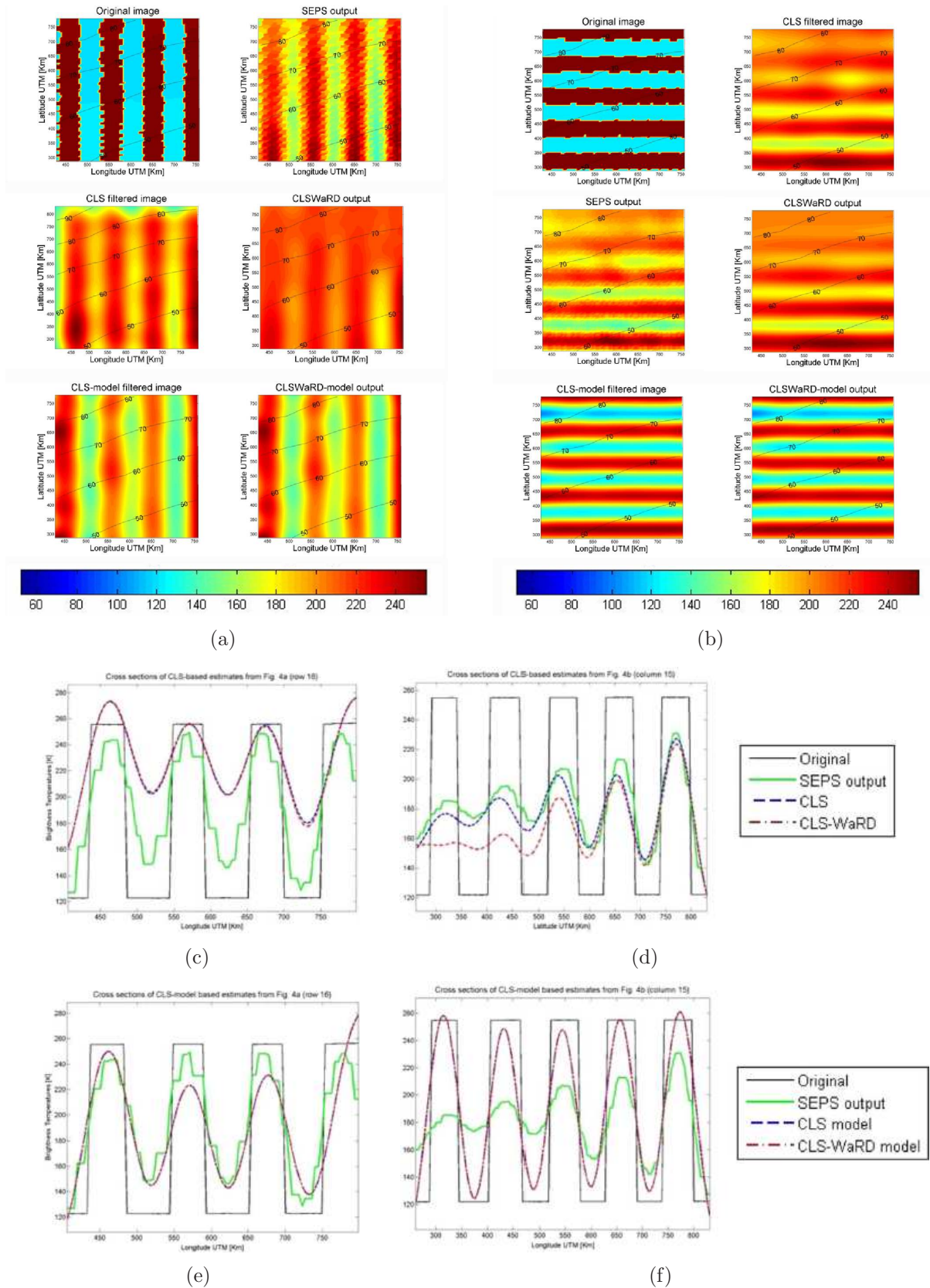


Figure 5.4 Vertical bars of 52 km width as original, SEPS output and results of applying CLS-derived filters to SEPS output (a). Horizontal bars of 56 km width as original, SEPS output and results of applying CLS-derived filters to SEPS output (b). Cross sections of the original image, SEPS output, CLS and CLS-WaRD outputs of Fig. 5.4(a) (c), and of Fig. 5.4(b) (d). Cross-sections of the original image, SEPS output, CLS model and CLS-WaRD model outputs of Fig. 5.4(a) (e), and of Fig. 5.4(b) (f).

5.3. Application to SMOS simulated observations

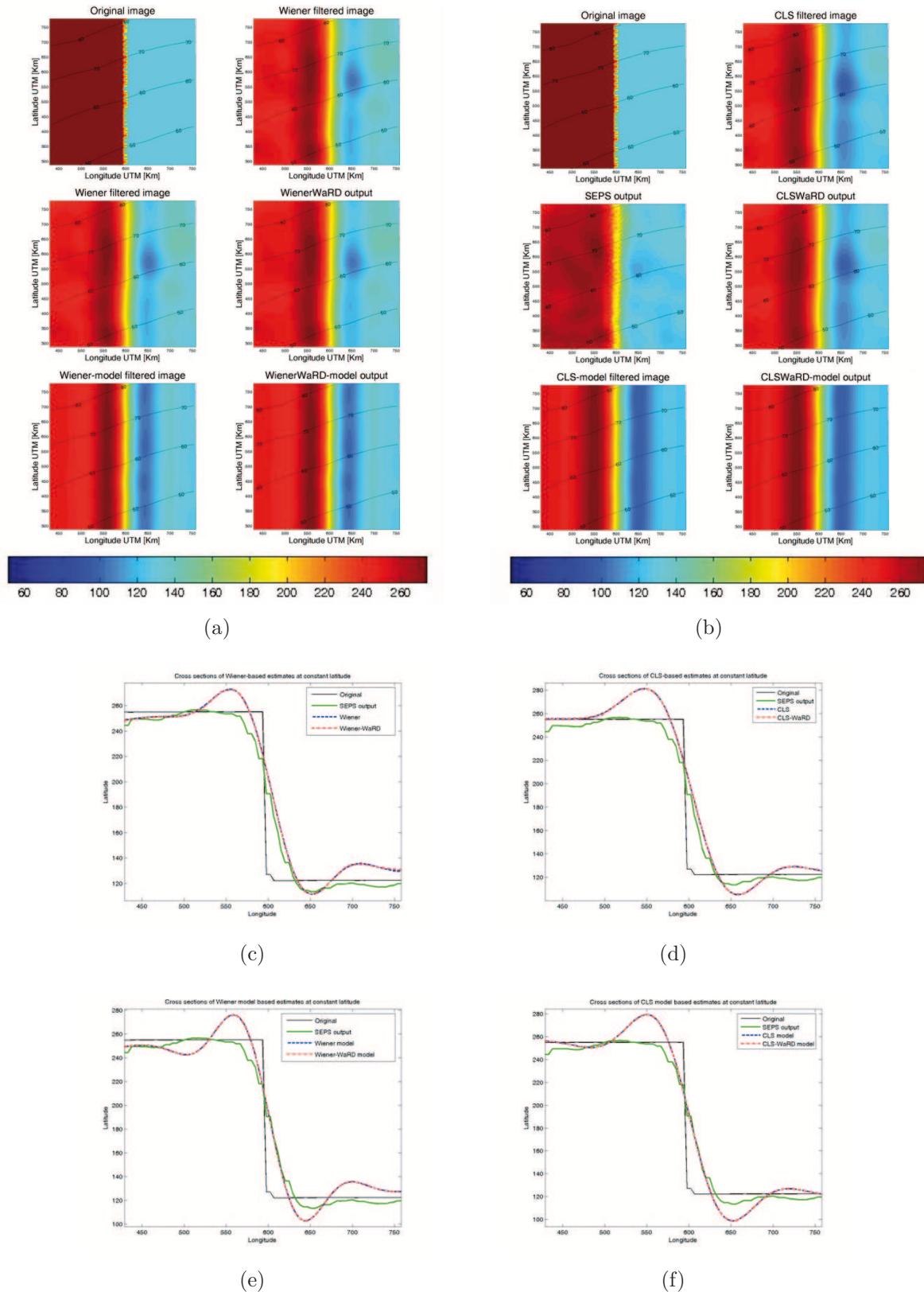


Figure 5.5 A step image as original, SEPS output and results of applying Wiener-derived filters to SEPS output (a). A step image as original, SEPS output and results of applying CLS-derived filters to SEPS output (b). Cross sections of original, SEPS output, Wiener and Wiener-WaRD outputs of Fig. 5.5(a) (c). Cross sections of original, SEPS output, CLS and CLS-WaRD outputs of Fig. 5.5(b) (d). Cross sections of original, SEPS output, Wiener model, and Wiener-WaRD model outputs of Fig. 5.5(a) (e). Cross sections of original, SEPS output, CLS model, and CLS-WaRD model of Fig. 5.5(b) (f).

improvement can be easily tested. Comparing the SEPS' output and the output of the different methods, it can be noticed that the shape and boundaries of objects are better distinguishable in the SEPS' output. However, it is not the focus of this study to improve the coastline definition or the geographic features on the image, but to improve its overall spectral information, since an improvement on the T_B image will lead to higher resolution land moisture retrievals. In Figs. 5.6(c),(d),(e), and (f), the T_B values of Figs. 5.6(a) and (b) at constant latitude are plotted so as to observe the images in higher detail. It can be noted that some ripple appears in the areas close to the land-sea transition, mainly in the seaside. As it is localized, it does not affect inland and in-sea retrievals. The effect of this phenomenon over coastal-area retrievals will be further analyzed using airborne data on Section 5.4.

5.3.3 Quantitative results

Simulation results are listed in Table 5.1, where ΔT is the RMSE between the output analyzed and the original synthetic image with a step from 253 K to 120 K that is used as input to SEPS and ΔS is the diameter of the circle with the same area as the 3-dB footprint of the worst case pixel, expressed in kilometers. The product $\Delta T \cdot \Delta S$ is the radiometer uncertainty principle [Ulaby *et al.*, 1981; Camps *et al.*, 1998], and it is taken as the criteria to evaluate the whole performance of the methods since it provides an indication of the best radiometric sensitivity and spatial resolution that can be obtained simultaneously.

Table 5.1 Results of the simulations over the area under study in terms of radiometric sensitivity (ΔT) and spatial resolution (ΔS)(worst case)

T_B image	ΔS [km]	Land Pixels		Sea Pixels	
		ΔT [K]	$\Delta T \cdot \Delta S$ [K·km]	ΔT [K]	$\Delta T \cdot \Delta S$ [K·km]
SEPS output	90.2	13.7	1240	9.86	890
Wiener	67.1	11.6	778	16.8	1131
Wiener-WaRD	67.1	11.5	775	16.8	1126
Wiener model	51.5	13.3	685	13.0	668
Wiener-WaRD model	51.5	13.3	685	13.0	668
CLS	70.5	13.8	971	15.7	1108
CLS-WaRD	70.5	13.7	969	15.7	1105
CLS model	53.6	14.5	779	14.1	758
CLS-WaRD model	53.6	14.5	779	14.1	758

In particular, it can be observed that the wavelet filtering slightly improves ΔT when applied to the Wiener and CLS filters, whereas it does not affect ΔT when the T_B model is added. Over ΔS , however, the wavelet filtering does not affect in any case.

Regarding the effect of adding the T_B model, it can be noticed that it considerably improves ΔS in all cases. Over ΔT , however, it has little or no effect. On the whole, adding the T_B model results to be of great advantage in terms of $\Delta T \cdot \Delta S$, particularly over sea pixels, since we get unacceptable high values otherwise.

It must be taken into account that the methods which include a T_B model rely on the effectiveness of the model they use and that the results obtained by these methods and

5.3. Application to SMOS simulated observations

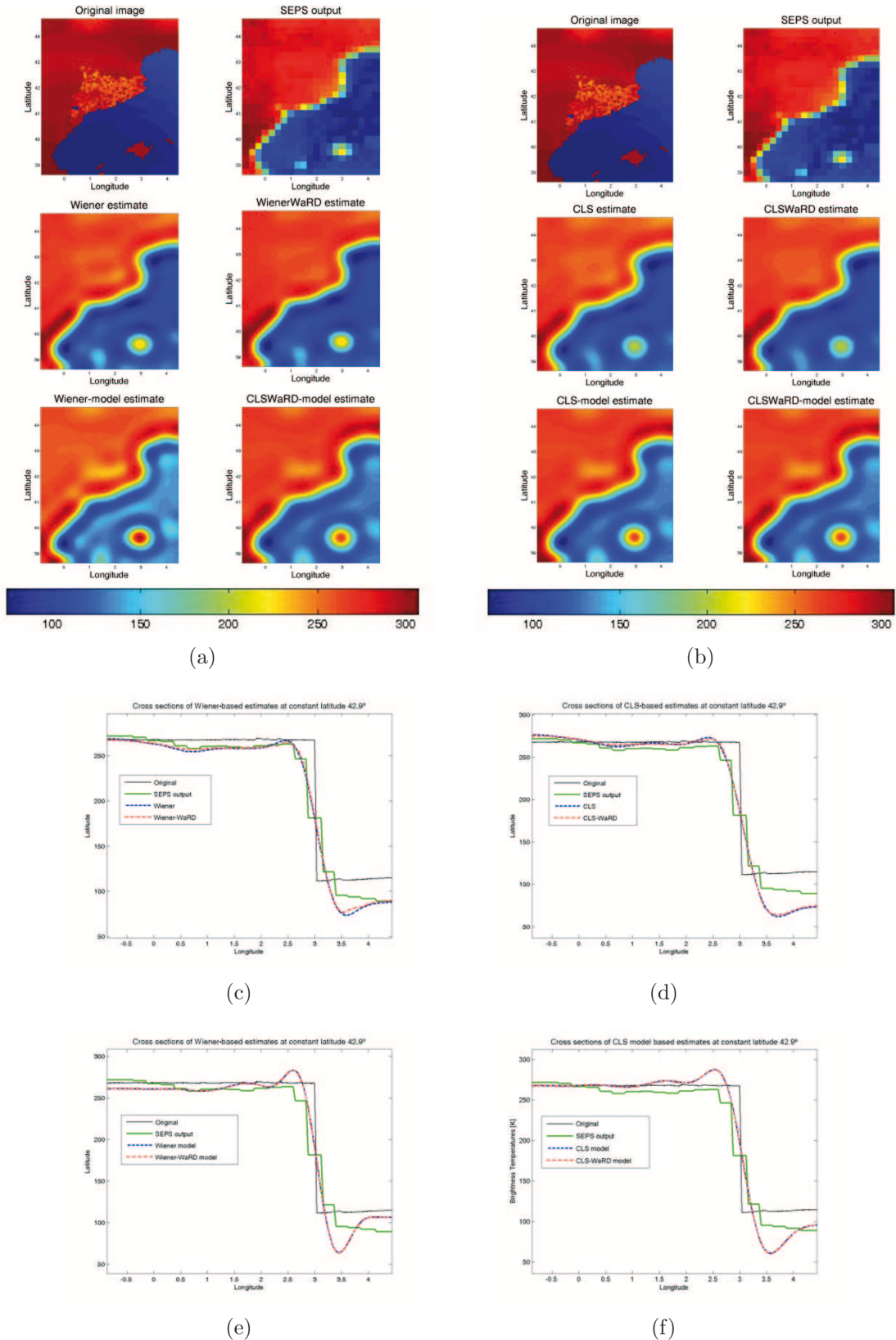


Figure 5.6 A realistic scenario as original, SEPS output and results of applying Wiener-derived filters to SEPS output (a). A realistic scenario as original, SEPS output and results of applying CLS-derived filters to SEPS output (b). Cross sections of original, SEPS output, Wiener and Wiener-WaRD outputs of Fig. 5.6(a) (c). Cross sections of original, SEPS output, CLS and CLS-WaRD outputs of Fig. 5.6(b) (d). Cross sections of original, SEPS output, Wiener model, and Wiener-WaRD model outputs of Fig. 5.6(a) (e). Cross sections of original, SEPS output, CLS model, and CLS-WaRD model of Fig. 5.6(b) (f).

shown in Table I are on a best possible basis (the T_B model used is exactly the original T_B model used in the computation of the observables). Thus, further studies with available T_B models will be needed to fully evaluate their performance.

Focusing on the overall performance of the algorithms over land pixels, it can be seen that all methods satisfactorily improve the product $\Delta T \cdot \Delta S$ obtained by SEPS' output and that best results are obtained when the Wiener model filter is used (marked in bold in Table 5.1). Focusing on the performance of the methods over sea pixels, however, the product $\Delta T \cdot \Delta S$ gets worse than SEPS' outputs when using the methods without the T_B model, which is undesirable. Again, better results over sea pixels are obtained when the Wiener model filter is used than when the CLS model filter is used.

Comparing results over sea and land pixels, it can be observed that the algorithm has a superior performance over land pixels. While ΔS remains the same for land and sea pixels, a higher noise is added to sea pixels than to land pixels in the deconvolution process. The higher value of ΔT over sea pixels is mainly due to the ripple that appears on the coastline, which is more significant on the sea side than on the land side. Note that the transition in the coast line is accounted for when calculating ΔT (see Section 5.3.2). Nonetheless, land and sea margins could be defined in non-coastal areas so that ΔT will be considerably reduced.

5.4 Application to airborne observations over the Ebro river mouth

In this Section, the deconvolution techniques are applied to airborne data acquired with the UPC Airborne RadIomEter at L-band (ARIEL) over the Ebro river mouth. The performance of the different methods will be assessed in terms of radiometric sensitivity and coast line width; the feasibility of using a land-sea mask of the observed scene as ancillary information in the deconvolution process to improve coastal retrievals from SMOS observations is analyzed.

5.4.1 Airborne system overview

In order to obtain T_B datasets within the SMOS preparatory activities, several field experimental campaigns using the UPC Airborne Radiometer at L-band (ARIEL) have been conducted [Acevo-Herrera *et al.*, 2009]. ARIEL is a light-weight nadir-looking L-band Dicke radiometer, with a radiometric sensitivity of 0.71 K for an integration time of 100 ms [Valencia *et al.*, 2008]. It is mounted on a remotely controlled aircraft or Unmanned Aerial Vehicle (UAV) of 2.5 m wingspan, 2 m long, and approximately 30 minutes of flight autonomy. A system composed by a Global Positioning System (GPS), a 3-axes inclinometer, gyros and accelerometers determine the position and the attitude of the aircraft and are used to properly geo-reference the radiometric measurements. Data is stored in onboard data-loggers for later processing. The UAV with the ARIEL radiometer can be seen in Fig. 5.7(a).

The ARIEL data processing can be divided into three main tasks: (i) radiometer's raw output voltages are converted into antenna temperatures through calibration – which is performed by measuring with the antenna pointing to an absorber (hot load) and to the sky (cold load) before and after each flight–, (ii) brightness temperatures (T_B) are obtained from antenna temperatures, taking into account the contributions of the atmosphere, and (iii) the T_B are geo-referenced and, in the case of having observations from different overpasses which are geographically coincident, they are adequately interpolated (with footprints weighted

with the antenna's radiation pattern) on a regular grid to conform an image (see Fig. 5.8). Further information on the avionics and on the ARIEL data processing can be found in [Acevo-Herrera et al. \[2009, 2010\]](#).

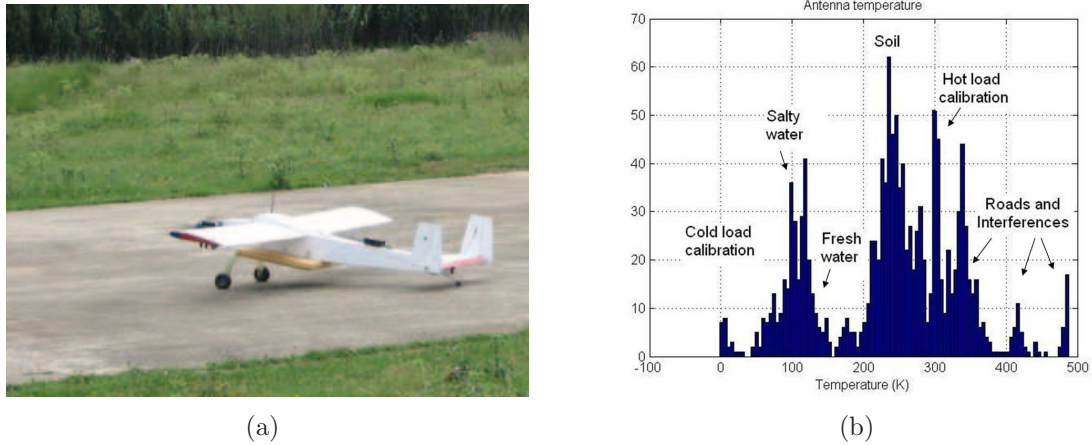


Figure 5.7 The aircraft with the ARIEL radiometer after a test flight (a). Retrieved antenna temperature histogram (b).

5.4.2 Ebro river mouth field experiment

The test site of this field experiment has been the Ebro river mouth, located 180 km South from Barcelona, because of the large variety of scenarios that can be found in a reduced area: dry land (ground), moist or flooded lands (rice fields), dry sand, fresh water (small ponds), and salty water (sea). It is one of the largest wetland areas (320 km²) in the Western Mediterranean region and is in intensive agricultural use for rice. Flights were performed over the Marquesa beach sea shore and land. The diversity of this area can be noticed on the antenna temperature histogram shown in Fig. 5.7(b). Since flights were conducted during daylight conditions, sun effects on the data have been corrected for.

5.4.3 Downscaling strategy

Flights at different heights were performed over the Ebro River Mouth with the ARIEL radiometer so that L-band observations over this area at different spatial resolutions were acquired. ARIEL T_B images obtained at heights between 40 and 170 m, and between 170 and 300 m are shown on Fig. 5.8(a) and (b), respectively. As a rule of thumb, ARIEL observations have a footprint of approximately 1/3 times the flight height. Accordingly, the observations on Fig. 5.8(a) have a pixel size between ~ 13 and 57 m, and the observations on Fig. 5.8(b) have a pixel size between ~ 57 and 100 m.

The Wiener, CLS, Wiener model, and CLS model filters have been applied to the T_B image on Fig. 5.8(b) to explore the possibility of improving its spatial resolution. The use of wavelets has not been considered in this Section, since it has been shown not to be of any advantage when applied to SMOS-like data in Section 5.3.

The effective antenna pattern function of the ARIEL radiometer has been approximated in the deconvolution filters by a 2-D Gaussian function with the observations' mean radius as half-width value. And two T_B models of the area have been used as ancillary information on two versions of the Wiener and CLS model filters: 1) a simple T_B model has been obtained



Figure 5.8 ARIEL Retrieved T_B [K] geo-referenced on Google Earth obtained at heights (a) between 40 and 170 m, and (b) between 170 and 300 m.

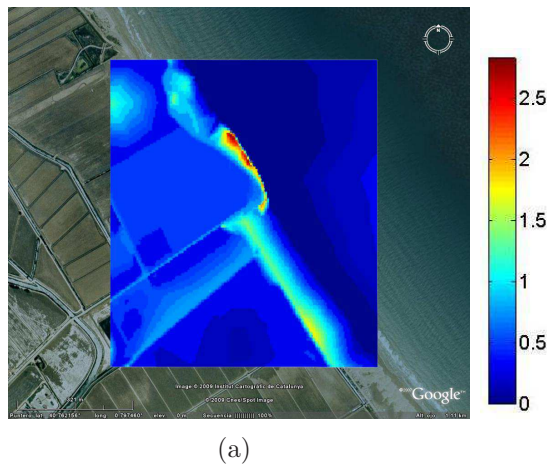


Figure 5.9 Digital Elevation Model [m] of the Marquesa beach area at 5 m spatial resolution, geo-referenced on Google Earth.

from the 5 m resolution Digital Elevation Model (DEM) shown on Fig. 5.9: a land-sea mask have been first derived from the DEM to define the model sea-land transition and constant values of 120 K and 220 K have been afterwards assigned to sea and land pixels, respectively 2) the image on figure 5.8(a) has been directly used as T_B model on a best-case version of the filters to explore their maximum capabilities. The filter's parameters have been selected in each case by optimizing the RMSE over land pixels.

5.4.4 Experimental results

To evaluate the spatial resolution achieved with the different algorithms, cross-sections at a constant latitude of the image obtained from ARIEL observations at heights 40-170 m, 170-300 m, and of the images resulting from the application of Wiener-derived and CLS-derived filters to the 170-300 m height image, are presented on Fig. 5.10. It can be observed that the coast line is sharply defined when Wiener and CLS model filters are used, which can lead to better coastal retrievals. It can also be observed that the highest definition is obtained when the 40-170 m height image is used as T_B model (best case). Therefore, it appears that the

more accurate the T_B model used on the filter, the sharper the coast-line definition of the resulting image. However, further studies will be needed to quantify the spatial resolution enhancement obtained when applying the different methods.

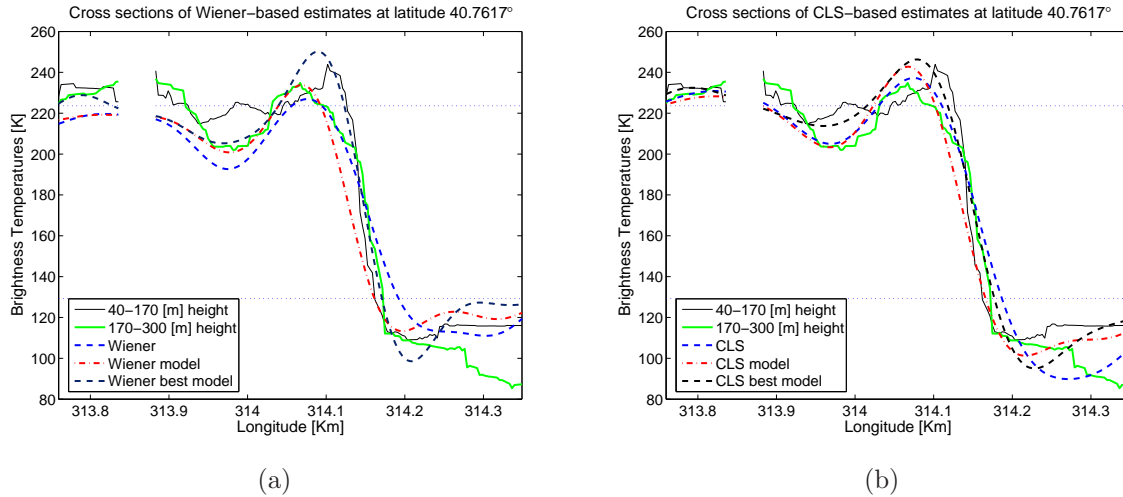


Figure 5.10 (a) Cross-sections of the image obtained from ARIEL observations at heights 40-170 m, 170-300 m, and of the images resulting from the application of Wiener-derived filters to the 170-300 m height image. (b) Cross-sections of the image obtained from ARIEL observations at heights 40-170 m, 170-300 m, and of the images resulting from the application of CLS-derived filters to the 170-300 m height image.

A RMSE metric has been used to assess the radiometric sensitivity achieved with the different methods; it is computed in each case with respect to the T_B image in Fig. 5.8(a), which is used as ground-truth data, and results are listed in Table 1. Over land pixels, it can be observed that all methods satisfactory improve the radiometric sensitivity of the observations. Over sea pixels, though, the methods practically do not achieve any improvement or even worsen the results. Note that this fact can possibly be due to the fact that the filter's parameters are set by optimizing the RMSE over land pixels and not over sea pixels. Regarding the effect of adding the T_B model, it can be noticed to considerably improve the RMSE over land pixels. This improvement is specially remarkable both over land and sea pixels when the T_B image in Fig. 5.8(a) is used as T_B model (best case). Therefore, these results indicate that the RMSE obtained with the methods which include a T_B model also relies on the effectiveness of the model they use.

Table 5.2 RMSE between the different T_B images and the highest spatial resolution T_B image at 40-170 m height, over land and sea pixels

	170-300 m height	Wiener	CLS	Wiener model/best	CLS model/best
Soil	28.5	26.6	24.8	23.4/11.4	22.5/11.7
Sea	24.5	23.4	24.0	26.8/12.4	22.1/14.6

5.5 Conclusions

An efficient deconvolution scheme has been proposed to improve the spatial resolution of future SMOS data, particularly over land, where it is more needed. Six different algorithms have been presented, which nicely explore the possibilities of working on Fourier and wavelet domains and of suitably adding an L-band T_B model of the observed scene as auxiliary information in the reconstruction process. The methods have been applied to synthetic and realistic T_B images processed by SEPS and to airborne field experimental data over the Ebro river mouth so as to visually assess and numerically quantify their performance.

Results over SMOS-like images are shown in terms of the best radiometric sensitivity (ΔT) and spatial resolution (ΔS) that can be achieved simultaneously. They confirm that the developed algorithms could significantly decrease the product $\Delta T \cdot \Delta S$ –particularly of the pixels located on the upper left area of an SMOS alias-free FOV– improving the spatial resolution from ~ 90 to ~ 50 km while keeping the radiometric sensitivity constant. The product $\Delta T \cdot \Delta S$ was decreased in a 49% over land pixels and in a 30% over sea pixels. Also, a trend to round the pixels' shape and diminish its size has been observed, with higher effects in the pixels located far from nadir. Hence, the deconvolution scheme proposed could potentially normalize the pixels shape and orientation in all the SMOS FOVs as well as improving the radiometric sensitivity and the spatial resolution of SMOS observations. Furthermore, results of its application to airborne field experimental data indicate that these methods could be adjusted in coastal areas to improve the radiometric sensitivity and the coast line definition of the observations.

*It makes all the difference whether
one sees darkness through the light
or brightness through the shadows*

David Lindsey (1876-1945)



Downscaling SMOS-derived soil moisture using higher resolution visible/infrared data

A downscaling approach to improve the spatial resolution of SMOS soil moisture estimates with the use of higher resolution visible/infrared satellite data is presented. The algorithm is based on the so-called universal triangle concept that relates visible/infrared parameters, such as Normalized Difference Vegetation Index (NDVI), and Land Surface Temperature (T_s), to soil moisture status. It combines the accuracy of SMOS observations with the high spatial resolution of visible/infrared satellite data into accurate soil moisture estimates at high spatial resolution. In preparation for the SMOS launch, the algorithm was tested using observations of the UPC Airborne RadIomEter at L-band (ARIEL) over the Soil Moisture Measurement Network of the University of Salamanca (REMEDIHUS) in Zamora (Spain), and LANDSAT imagery. Results show good agreement with ground-based soil moisture observations, and illustrate the strength of the link between visible/infrared satellite data and soil moisture status. Following the SMOS launch, a downscaling strategy for the estimation of soil moisture at high resolution from SMOS using MODIS visible/infrared data has been developed. Results of its application to the first SMOS images acquired during the commissioning phase provide a first evidence of its capabilities.

6.1 Introduction

Theoretical, ground-based, and airborne experimental studies have proven that L-band passive remote sensing is optimal for soil moisture sensing due to its all-weather capabilities and the high sensitivity of the Earth emission to soil moisture under most vegetation covers (see Section 2.2). The ESA SMOS mission, in orbit since November the 2nd 2009, uses a novel L-band passive instrument concept to provide accurate global surface soil moisture estimates (see Section 1.3.1). However, due to technological limitations, the spatial resolution of SMOS observations is limited to ~ 50 km. This resolution is adequate for many global applications, but restricts the use of the data in regional studies over land, where a resolution of 1-10 km is needed.

The possibility of using visible/infrared sensors for soil moisture sensing has been widely studied in the past, since visible/infrared sensors onboard satellites provide good spatial resolution, and controlled experiments have shown their potential to sense soil moisture

[Idso *et al.*, 1975; Price, 1977; Adegoke and Carleton, 2002; Wang *et al.*, 2007]. However, they are equally sensitive to soil types, and it is difficult to decouple the two signatures. In addition, soil moisture estimates from visible/infrared sensors usually require surface micrometeorological and atmospheric information that is not routinely available [Cracknell and Xue, 1996; Zhang and Wegehenkel, 2006]. Hence, visible/infrared sensors are commonly used to provide an indirect measurement of soil moisture, but not to retrieve it.

To achieve accuracy and high spatial resolution, it seems natural to try to combine the strength of the microwave and visible/infrared approaches for soil moisture estimation. Recently, a number of studies have documented the emergence of a triangular or trapezoidal shape when remotely sensed surface radiant temperature (T_s) over heterogeneous areas are plotted versus vegetation index (VI) measurements; an analysis of this “universal triangle” has led to different methods relating the T_s/VI space to land surface energy fluxes and surface soil moisture. A comprehensive review of these methods can be found in Carlson [2007]; Petropoulos *et al.* [2009]. Particularly, an algorithm for the operational retrieval of high-resolution surface soil moisture from future Visible Infrared Imager Radiometer Suite (VIIRS) and MIS (Microwave Imager Sounder) data, under the National Polar-Orbiting Operational Environmental Satellite System (NPOESS), is underway [Zhan *et al.*, 2002]. It has a definite theoretical basis that links soil moisture to the T_s/VI space [Carlson *et al.*, 1994], and was demonstrated using 1-km AVHRR and 25-km SSM/I in Chauhan *et al.* [2003].

This chapter presents an algorithm to synergistically combine passive L-band observations and visible/infrared satellite data into high resolution soil moisture. The algorithm involves three steps. First, a soil moisture retrieval technique is applied to the brightness temperature images to generate soil moisture maps at low resolution. In the second step, the universal triangle concept is used to link the microwave-derived soil moisture maps at low resolution to the scene visible/infrared parameters (aggregated to the microwave resolution). In the third step, the linking model is used with the visible/infrared parameters at high resolution to disaggregate microwave soil moisture into high resolution soil moisture. In Section 6.2, as part of the downscaling activities conducted at the REMEDHUS Cal/Val site, a previous study and test of the algorithm using passive L-band airborne observations and visible/infrared data from LANDSAT is presented. Following this first experiments, a downscaling strategy for improving the spatial resolution of SMOS soil moisture estimates using MODIS-derived NDVI and T_s data is introduced in Section 6.3. Results of its application to the first SMOS images acquired during the commissioning phase indicate that with this approach it is feasible to improve the spatial resolution of SMOS observations over land; the spatial variability of SMOS-derived soil moisture observations is effectively captured at the spatial resolutions of 32, 16, and 8 km. However, further studies are needed to evaluate the radiometric accuracy of the observations at the different spatial resolutions and therefore establish a downscaling limit. The use of ascending and/or descending SMOS orbits for soil moisture sensing is discussed, and soil moisture estimations are compared to *in situ* soil moisture data from the Murrumbidgee catchment, in South-eastern Australia. In Section 6.4, the main findings and contributions of this work are summarized, and the operational applicability of this downscaling technique to SMOS is discussed.

6.2 Downscaling activities at the REMEDHUS Cal/Val site

Due to the exploratory nature of the SMOS mission, calibration and validation (Cal/Val) of SMOS products is an essential activity. After SMOS commissioning phase, an intense

activity by many research groups, coordinated by ESA, will collect *in situ* data simultaneous to SMOS observations in order to improve the empirical aspects of retrieval algorithms and to validate the products generated from these observations. Also, there is a strong interest in developing and testing downscaling techniques that could enhance the spatial resolution of SMOS data (~ 50 km), since soil moisture estimates at a resolution of 1-10 km are needed for regional scale applications [Entekhabi *et al.*, 1999]. Hence, different downscaling experiments have been carried out at the REMEDHUS Cal/Val site [ISMN, 2010], within the GPS and RAdiometric Joint Observations long-term field experiment (GRAJO), to investigate the scaling nature of soil moisture and explore the possibility of improving the spatial resolution of SMOS observations over land.

Flights at different altitudes have been performed over the REMEDHUS area with the UPC Airborne RadIomEter at L-band (ARIEL), and a downscaling approach to improve the spatial resolution of ARIEL observations using higher resolution visible/infrared LANDSAT imagery is evaluated. Results from comparison with ground-truth data show that with this technique it is feasible to improve the soil moisture estimates in terms of spatial resolution (from ~ 50 m to 30 m) and accuracy (from 0.11 to 0.06 RMSE). This case study demonstrates the consistency of the visible/infrared relationship with soil moisture status, and the potential of applying this downscaling strategy to SMOS data.

6.2.1 Data description

The GRAJO long-term intensive field experiment was conducted at the REMEDHUS soil moisture network in the semi-arid area of the Duero basin, Zamora, Spain, from November 2008 to April 2010 [Monerris *et al.*, 2009]. REMEDHUS has been selected as a secondary Cal/Val site for SMOS mission, and has also been proposed as a Cal/Val site for the NASA SMAP mission. It has an area of approximately a SMOS pixel (40 x 30 km), it is homogeneous (mostly covered by crops) and counts with a complete and operational network of 23 soil moisture and temperature sensors. Its climate is continental and semiarid, with cold winters and warm summers (12°C annual mean temperature and 400 mm mean rainfall).

Airborne observations

ARIEL is a light-weight L-band Dicke radiometer, with a radiometric sensitivity of 0.71 K for an integration time of 100 ms [Valencia *et al.*, 2008]. It is mounted on an UAV of 2.5 m wingspan and 2 m long, which is able to fly at altitudes up to 400 m and has a flight autonomy of ~ 30 minutes. A system composed by a GPS and an inertial motion unit is used to geo-reference the radiometric measurements and monitor the aircraft's attitude (roll, pitch and yaw), altitude, and speed. Data is recorded into onboard data-loggers for later processing.

The ARIEL data processing mainly comprises three steps: (i) radiometer's raw output voltages are converted into antenna temperatures through calibration – which is performed by measuring with the antenna pointing to an absorber (hot load) and to the sky (cold load) before and after each flight–, (ii) brightness temperatures (T_B) are obtained from antenna temperatures, taking into account the contributions of the atmosphere, and (iii) the T_B are geo-referenced and, in the case of having observations from different overpasses which are geographically coincident, they are adequately interpolated (with footprints weighted with the antenna's radiation pattern) on a regular grid to conform an image. Detailed information on the avionics and on the ARIEL data processing can be found in Acevo-Herrera *et al.* [2009, 2010].

Figure 6.1 shows the two ARIEL T_B images that are analyzed on this study, overlapped in an aerial photography from Google Earth. They correspond to two flights undertaken the 25th of March 2009 at 9.30 am (Flight 1, image on the right), and at 4.45 pm (Flight 2, image on the left), and cover an area of $\sim 720 \times 720$ m each. These images have been obtained from ARIEL measurements acquired at heights 140 ± 30 m. As a rule of thumb, ARIEL observations have a footprint of approximately 1/3 times the flight height; accordingly, ARIEL T_B on Fig. 6.1 have a pixel size of ~ 50 m. However, since ARIEL data will be jointly used with LANDSAT data at a spatial resolution of 30 m, ARIEL observations have been conveniently re-sampled to a 60 x 60 m grid.

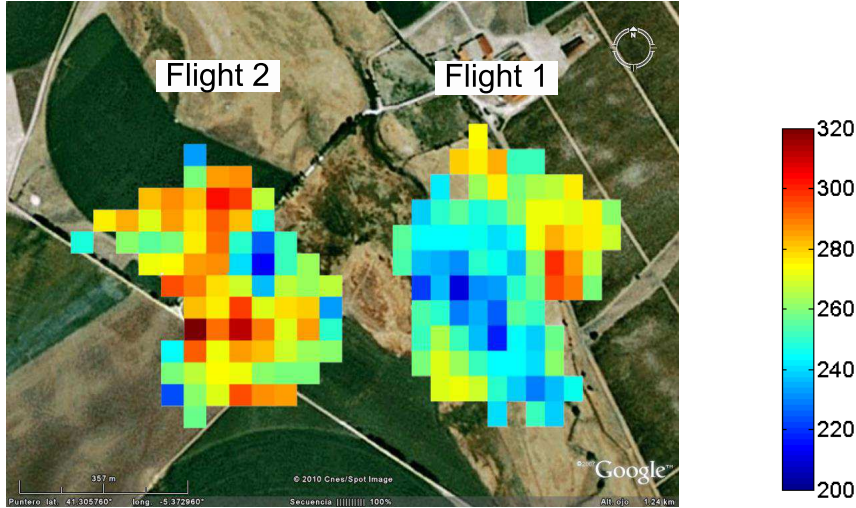


Figure 6.1 ARIEL Retrieved T_B [K] obtained at heights 140 ± 30 m (spatial resolution ~ 50 m), re-sampled to a 60 x 60 m grid and geo-referenced on Google Earth.

LANDSAT data

A LANDSAT 5 satellite image from the 23rd of March 2009, scene 201/031, has been used in the present study. The image has been geometrically corrected using orbital modeling and ten ground control points of the study area (latitude, longitude and height); the radiometric calibration has been performed according to *Chander and Markham [2003]*, and the atmospheric correction according to *Richter [1996]* and atmospheric standard values.

The Normalized Difference Vegetation Index (NDVI) of the area under study has been obtained as [*Rouse et al., 1974*]:

$$NDVI = \frac{\rho_{NIR} - \rho_R}{\rho_{NIR} + \rho_R}, \quad (6.1)$$

where ρ_{NIR} and ρ_R are the at-surface reflectance of bands 4 (Near-infrared, 0.76 - 0.90 m) and 3 (Visible, 0.63 - 0.69 m), respectively, at 30 m spatial resolution.

The surface radiant temperature (T_s) of the area under study has been obtained from band 6 (Thermal, 10.40 - 12.50 m) at 120 m spatial resolution, and has been re-sampled to 30 m.

A land cover map of the study area has been retrieved using a supervised classification by maximum likelihood algorithm, and five classes have been identified:

1. rainfed cereal.

2. irrigated cereal.
3. pasture.
4. unproductive soils comprising building areas, ploughed and tilled plots, vineyards (bare soil at the time), fallow lands and others.
5. shrublands and scattered trees.

The predominant covers are pasture (24.1%) and rainfed cereal (9.4%) for Flight 1, and bare soils (19.8%) and rainfed cereal (10.7%) for Flight 2.

Note that, since LANDSAT acquisition time is 10.40 am, data from Flight 1 (9.30 am) is expected to be more closely linked to the satellite NDVI and T_s information than data from Flight 2 (4.45 pm).

Ground-based soil moisture

Soil moisture fields over large areas are not easily described using surface observations, which difficulties the validation of remotely sensed soil moisture observations. In this study, ground measurements of 0-5 cm soil moisture at 20 sampling locations were acquired simultaneously to the airborne observations. These measurements have been interpolated to a 30 x 30 m grid using a spatial kriging interpolation technique [Burgees and Webster, 1980]. The resulting image is used in Section 6.2.4 as ground truth to calculate and compare ARIEL-derived and downscaled soil moisture errors.

6.2.2 The temperature/vegetation index space

Figure 6.2 illustrates the polygonal correlation between LANDSAT T_s and NDVI on each flight. The polygon's edges can be interpreted as the minimum/maximum reached by vegetation cover (NDVI) and soil moisture: bare soil, maximum biomass, completely dry, and fully wetted soil surface. Note that, since the vegetation temperature does not vary spatially, variations in temperature in the triangle reflect only variations in the soil surface, i.e. in the soil surface dryness. Therefore, the coldest and warmest pixels correspond to the wet and dry edges, respectively.

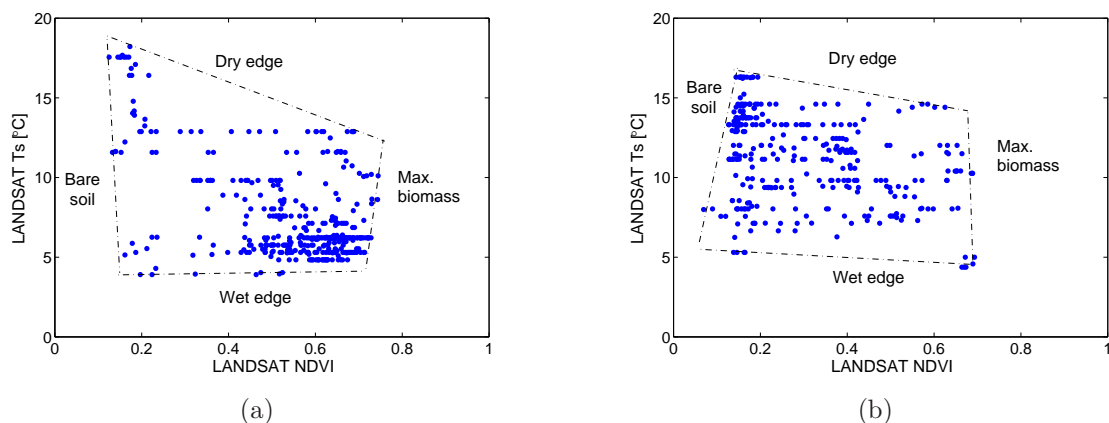


Figure 6.2 Scatter plots of LANDSAT surface radiant temperature versus LANDSAT NDVI of the areas corresponding to (a) Flight 1, and (b) Flight 2.

The predominance of rainfed cereal on Flight 1 and of bare soils on Flight 2 is clearly seen in Fig. 6.2(a) and Fig. 6.2(b), respectively. Also note that the maximum biomass edge is shorter than the bare soil edge in the two scatter plots, which evidences the low sensitivity of vegetation temperature to changes in soil moisture and the higher sensitivity of bare soil to changes in soil moisture content; the range of T_s decreases as the vegetation cover increases. Another salient aspect of the polygons is that the dry edges slope towards lower temperatures with increasing NDVI, which can be explained by the fact that sunlit vegetation is generally cooler than sunlit bare soil.

The most severe limitation of the triangle concept is that a large number of pixels reflecting a full range of soil surface wetness and fractional vegetation cover is needed to identify a “triangular” shape in the pixel distribution [Carlson, 2007]. It has to be noted that this condition prevents a full validation of the downscaling approach with the field experimental data available in the present study.

6.2.3 Downscaling approach

Theoretical and experimental studies have demonstrated that there can be a unique relationship between soil moisture (s_m), NDVI, and T_s for a given region under a wide range of climatic conditions and land surface types. This relationship can be expressed through a regression formula such as [Carlson *et al.*, 1994]:

$$s_m = \sum_{i=0}^n \sum_{j=0}^n a_{ij} \text{NDVI}^i T_s^j, \quad (6.2)$$

where n should be chosen so as to give a reasonable representation of the data.

In this study, a linking model is developed between the LANDSAT T_s /NDVI space and airborne soil moisture estimates using the following approximation of (6.2):

$$s_m = a_{00} + a_{01}T_N + a_{10}F_r + a_{11}T_NF_r + a_{02}T_N^2 + a_{20}F_r^2, \quad (6.3)$$

where T_N stands for normalized LANDSAT surface radiant temperature and F_r is the fractional vegetation cover [Gutman and Ignatov, 1998], defined as:

$$T_N = \frac{T_s - T_{min}}{T_{max} - T_{min}}, \quad (6.4)$$

$$F_r = \frac{\text{NDVI} - \text{NDVI}_{min}}{\text{NDVI}_{max} - \text{NDVI}_{min}}, \quad (6.5)$$

with T_{max} and T_{min} being the maximum and minimum T_s values for a particular scene, and, similarly, NDVI_{max} and NDVI_{min} being the maximum and minimum NDVI values for a particular scene. Normalization is preferred to reduce the dependence of T_s /NDVI on ambient conditions, and to allow further comparison of different experiments.

The downscaling approach builds on the VIIRS algorithm concept in Zhan *et al.* [2002]: it consists of aggregating high resolution visible/infrared land surface parameters to the scale of the microwave observations for the purpose of building a linking model that is afterwards applied at fine scale to disaggregate the passive soil moisture observations into high-resolution soil moisture. The algorithm involves three main steps:

1. The soil moisture at low resolution is retrieved from ARIEL observations through linear regression with the *in situ* soil moisture samples. Note that this step is used in the present study, but is not required in a possible application to SMOS data.

2. High resolution LANDSAT-derived T_N and F_r are aggregated to the scale of the airborne observations (60 m), and (6.3) is used to set up a system of linear equations for the pixels in the area under study. The system is solved to obtain the regression coefficients a_{ij} of the linking model.
3. Downscaled soil moisture at 30 m spatial resolution is obtained by applying (6.3) with the regression coefficients a_{ij} obtained in step 2, T_N , and F_r at 30 m spatial resolution.

The use of the Soil Adjusted Vegetation Index (SAVI) instead of the NDVI in (6.2) was considered as an attempt to eliminate soil-induced variations that could affect the relationship between T_s , vegetation, and soil moisture [Huete, 1988]. However, results showed no significant differences.

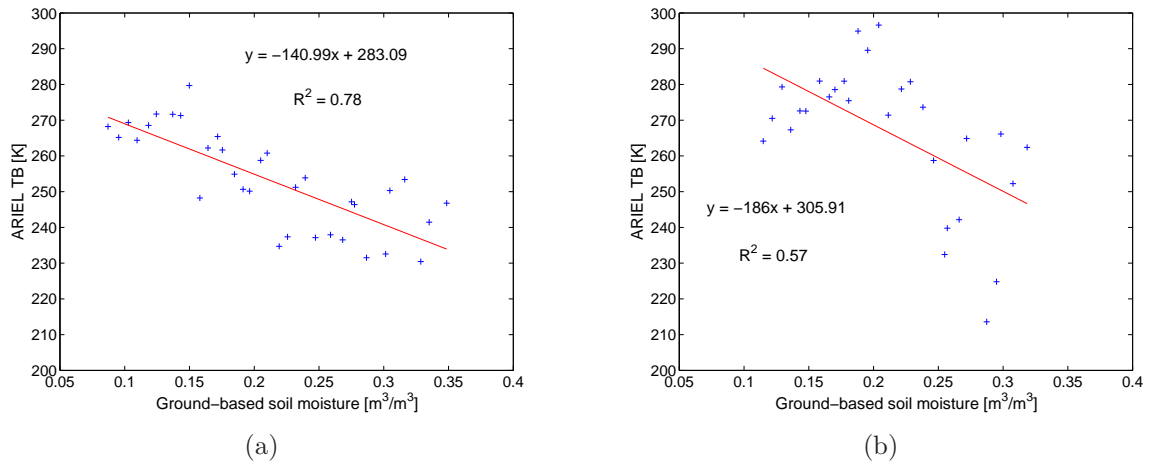


Figure 6.3 Linear regression between ARIEL T_B and coincident ground measurements of 0-5 cm soil moisture acquired during (a) Flight 1, and (b) Flight 2.

6.2.4 Results

The downscaling algorithm has been applied to Flight 1 and Flight 2 data separately. Figure 6.3 shows the correlation between ARIEL T_B and ground-based soil moisture (R^2 values of 0.78 and 0.57 are obtained for Flight 1 and Flight 2, respectively). The low correlation on Flight 1 is probably due to its acquisition time (4.45 pm), which is far from LANDSAT overpass time (10.40 am) and therefore can induce significant errors on T_s . These linear regressions are used to retrieve soil moisture maps from ARIEL observations.

Sample results of applying the downscaling technique to ARIEL-derived soil moisture are presented on Fig. 6.4. Comparing with the ground-based soil moisture, it can be seen that both the ARIEL-derived soil moisture fields and the downscaled images reproduce the spatial variations in the soil moisture measurements. The spatial distribution of the error between retrieved and downscaled soil moisture and ground-based soil moisture is further analyzed in Fig. 6.5. It shows that the RMSE between ARIEL-derived soil moisture and ground-based soil moisture is 0.11, and that it is improved in a $\sim 40\%$ when the downscaling technique is applied.

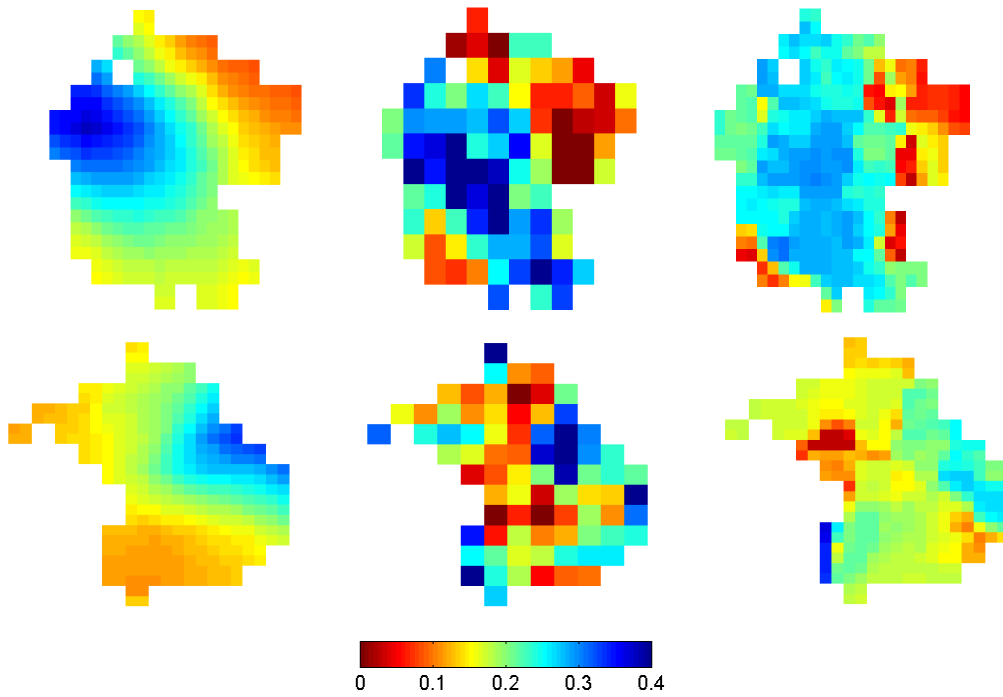


Figure 6.4 Sample results for the visual comparison of soil moisture fields [m^3/m^3]. From left to right: interpolated ground-based soil moisture, soil moisture retrieved from ARIEL T_B , and downscaled soil moisture obtained with the algorithm presented. Upper row: Flight 1; Lower row: Flight 2.

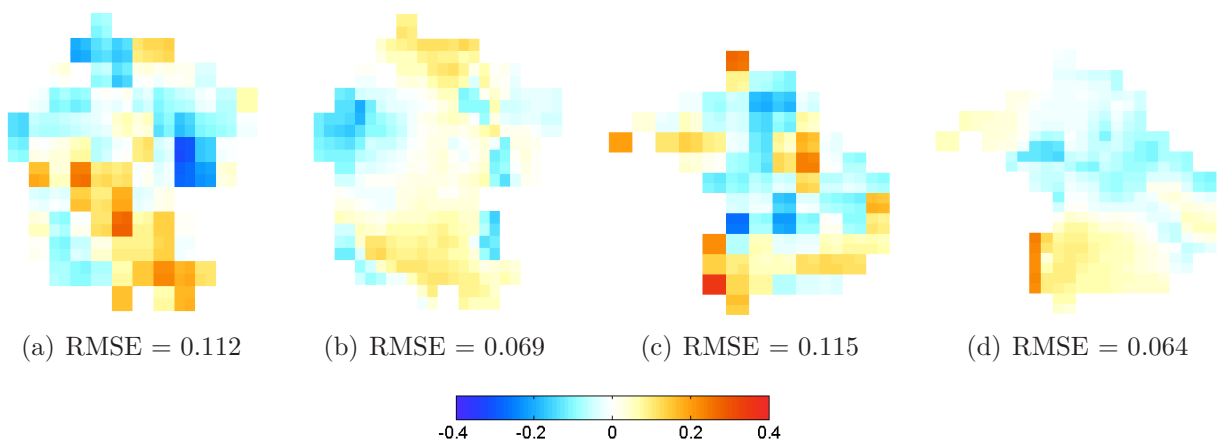


Figure 6.5 Spatial distribution of the soil moisture error [m^3/m^3] retrieved using ARIEL T_B on (a) Flight 1 and (c) Flight 2, and obtained with the downscaling algorithm on (b) Flight 1 and (d) Flight 2 observations

6.3 Downscaling approach for SMOS

Based on the experience gained from the downscaling activities presented in Section 6.2, an approach for improving the spatial resolution of SMOS soil moisture observations using MODIS-derived NDVI and T_s data has been developed. MODIS has been selected among other operational visible/infrared satellites for its suitable characteristics, mainly, its temporal resolution (1-2 days), data availability (near real time), spatial resolution (1 km), and overpass time (10.30 am for MODIS/Terra satellite). Alternatives present severe incompatibilities to be used in combination with SMOS measurements such as the 12.30 am overpass time of the AVHRR, or the 16-days repeat cycle of ASTER.

The resolution of SMOS observations varies from 30 km at nadir to 90 km at the upper borders of the FOV (see Fig. 1.6). In this work, SMOS observations are combined on a regular grid of 64 x 64 km and are downscaled to a grid of 32 x 32 km. The possibility of going into higher spatial resolutions of 16 and 8 km is also explored. However, future studies are needed to evaluate the radiometric resolution of the soil moisture estimates at the different spatial resolutions, and to establish a downscaling limit, which could be given either by the resolution of the optical sensor (which in the case of MODIS is 1 km), or by the presence of noise affecting the accuracy of the soil moisture estimates.

6.3.1 Data description

At the time of writing (20th April 2010), the SMOS commissioning phase is underway. Therefore, the SMOS Level 1c data available is limited and subject to calibration changes. Also, the SMOS Level 2 Soil Moisture Processor is not operational, so that there is no open access to SMOS-derived soil moisture data. These reasons have prevented a full validation of the downscaling approach in the present context, and further work will be needed to consolidate the algorithm once SMOS enters its operational phase. Nonetheless, this study has been oriented so as to make the most out of the data that is currently available.

SMOS data

SMOS data acquired during the commissioning phase and processed from Level 0 to Level 1c with the UPC MIRAS Testing Software (MTS) [[Corbella et al., 2008](#)] is used in the present study. For an initial validation of the algorithm, only horizontally polarized brightness temperatures are considered. Note that horizontal polarization is more sensitive to soil moisture variation than vertical polarization (see Fig. 2.7). Also, this study focuses on observations acquired at a constant incidence angle of 42.5°, which is the fixed incidence angle of SMOS Level 1c browse products [[McMullan et al., 2008](#)].

MODIS data

The MODIS instrument operates on both the Terra (10.30 am/10.30 pm) and Aqua (1.30 am/1.30 pm) spacecrafts. On this work, only MODIS/Terra products will be used, due to its closeness to SMOS overpass times (6 am/6 pm). Note that it is particularly critical for the case of T_s . Specifically, the daily MODIS/Terra T_s and the 16-day NDVI Level 3 product (datasets MOD11C1 and MOD13C1, respectively) have been employed. Both products have a spatial resolution of 0.05° (~ 5 km at the equator), and have been aggregated to 64, 32, 16 and 8 km for the present study. The NDVI composite is cloud free, whereas the T_s is not. The option of using the 8-day T_s composite was discarded, since it is not as representative

as the actual T_s and it is not cloud free in all cases. MODIS products are distributed by the U.S. Land Processes Distributed Active Archive Center (www.lpdaac.usgs.gov).

Ground-based soil moisture

Ground-based measurements of 0-5 cm volumetric soil moisture from the Australian Airborne Calibration/Validation Experiments for SMOS (AACES) are used to evaluate the algorithm performance. The AACES field experiment took place from January 18 to February 21, 2010, in the Murrumbidgee catchment (-33 to -37 S, 143 to 150 E), in South-eastern Australia, in which the permanent OzNet soil moisture monitoring network (www.oznet.unimelb.edu.au) is located. The comparison of SMOS-derived soil moisture estimates to ground-truth data will be focused on a subset of those stations, located within the Coleambally Irrigation Area, South of Yanco (referred to here as the Yanco region); it is a homogeneous and flat area of approximately 60 km by 60 km area (\sim a SMOS pixel) hosting a network of 13 soil moisture stations deployed all over the region [*Young et al., 2008*].

6.3.2 Method

The downscaling method for the estimation of soil moisture at high resolution from SMOS using MODIS-derived T_s and NDVI data consists of three main steps, which are described in the following sections.

Step 1: soil moisture at low resolution

The retrieval of soil moisture from SMOS brightness temperatures is performed by inverting a simple radiative transfer model, which is described hereafter.

Research since the mid 1970's has established and verified the physical bases for passive microwave emission of land surfaces (see Section 2.2). Hence, it is known that the emission of microwave energy is proportional to the product of the surface temperature T_s and the surface emissivity e , which is commonly referred to as the microwave brightness temperature T_B :

$$T_{Bp} = e_p \cdot T_s = 1 - \Gamma_{s,p}, \quad (6.6)$$

where the subscript p denotes either vertical (v) or horizontal (h) polarization, and $\Gamma_{s,p}$ is the reflectivity of the surface.

The emissivity depends on the dielectric constant of the medium ϵ_s ($\epsilon_s = \epsilon'_s + j\epsilon''_s$) which is, in turn, governed by the soil moisture content. Although the relationship between emissivity and T_B is linear, the relationship between emissivity and dielectric constant is nonlinear because the water content of the media has a nonlinear effect on the dielectric constant (see Section 2.2.3). The Fresnel equations (2.22) can be used to describe the relationship between reflectivity and dielectric constant in the case of a flat surface and a medium of uniform ϵ_s .

Since the contribution of the imaginary part of ϵ_s in (2.22) is relatively small, the inversion of the Fresnel equations can be simplified if only the real part of ϵ_s –effective permittivity ϵ'_s – is considered. This way, the Fresnel equations (2.22) can be inverted to estimate the

effective permittivity of the emitting layer [Jackson, 1993]:

$$\begin{aligned}\epsilon'_{s,h} &= \sin^2 \theta + \cos^2 \theta \left(\frac{\sqrt{\Gamma_{s,h}} + 1}{\sqrt{\Gamma_{s,h}} - 1} \right)^2, \\ \epsilon'_{s,v} &= a^2 + a \left(\frac{\sqrt{a^2 - 4b^2 \cos^2 \theta \sin^2 \theta}}{2b^2 \cos^2 \theta} \right),\end{aligned}\quad (6.7)$$

where $a = \sqrt{\Gamma_{s,h}} + 1$ and $b = \sqrt{\Gamma_{s,v}} - 1$, and θ is the incidence angle. Note that the use of (6.7) requires the assumption that emissivity is principally related to the real part of the complex dielectric constant; this is mostly true for the case of dry soil, but could induce significant errors in the case of wet conditions [Jackson, 1993].

The soil moisture content can therefore be determined from $\epsilon'_{s,p}$ by inverting a soil dielectric mixing model, e.g. Wang and Schmugge [1980]; Hallikainen et al. [1985]; Dobson et al. [1985]; Mironov et al. [2004].

The following additional considerations have been incorporated to this inversion procedure to consolidate the soil moisture retrieval technique:

- To account for the effects of vegetation on the observed brightness temperatures, the option of using (2.32) instead of (6.6) has been considered. In the case of using (2.32): (i) it is assumed that vegetation canopy is in thermal equilibrium with soil temperature, (ii) vegetation is assumed to be short/sparse enough so as not to contribute to a significant emission of its own ($\omega=0$), and (iii) τ is estimated using (2.31) with $\alpha=-0.05$, $\beta=-0.36$, and MODIS NDVI data [Burke et al., 2001].
- The option of correcting for the effect of surface roughness on the microwave emission from bare soil has also been included. To do so, Fresnel coefficients have been modified using (2.27), where Q_s and n have been set equal to zero, according to Wigneron et al. [2001], and h_s has been set to 0.2 (representing rather smooth surface roughness conditions).
- Three different soil dielectric mixing models will be used to retrieve soil moisture from the effective permittivity: the model in Wang and Schmugge [1980], the model in Hallikainen et al. [1985], and the model in Dobson et al. [1985].

In the present study, this retrieval approach has been applied to SMOS T_{hh} images at a constant incidence angle of 42.5° to generate soil moisture maps at 64 km. In the nominal case, the inversion procedure takes into account vegetation effects, corrects for surface roughness, and uses the soil dielectric mixing model in Hallikainen et al. [1985] with the mean Australian sand and clay fractions reported in Minasny and McBratney [2007], which are 40% and 28.6%, respectively. The effect of using other configurations (i.e. no roughness correction, no vegetation correction, or the use of other soil dielectric mixing model) is only considered when comparing with *in situ* measurements in Section 6.3.3.

Step 2: linking model

A linking model based on the triangle concept has been developed to relate SMOS-derived soil moisture to MODIS-derived NDVI and T_s (aggregated to 64 km).

As discussed in Sections 6.1 and 6.2.2, NDVI and T_s are proven indicators of the vegetative and thermal state of the land surface. Carlson et al. [1994] demonstrated that the

relationship between s_m , NDVI, and T_s for a particular region can be described using the regression formula in (6.2). In Section 6.2, the approach in (6.3) was effectively used to define the linking model between LANDSAT T_s /NDVI data and ARIEL observations. In the context of SMOS, SMOS brightness temperatures have been added to the right side of (6.2) to capture soil moisture variability and strengthen the relationship between land surface parameters and soil moisture. Thus, (6.2) is modified to:

$$s_m = \sum_{i=0}^n \sum_{j=0}^n \sum_{k=0}^n a_{ijk} \text{NDVI}^i T_s^j T_B^k. \quad (6.8)$$

Using (6.4) and (6.5), the following approximation of (6.8) has been defined as linking model between SMOS observations and MODIS-derived NDVI and T_s data:

$$s_m = a_{000} + a_{001}T_{BN} + a_{010}T_N + a_{100}F_r + a_{002}T_{BN}^2 + a_{020}T_N^2 + a_{200}F_r^2 + a_{011}T_N T_{BN} + a_{101}F_r T_{BN} + a_{110}F_r T_N, \quad (6.9)$$

where T_{BN} are the normalized SMOS brightness temperatures:

$$T_{BN} = \frac{T_B - T_{Bmin}}{T_{Bmax} - T_{Bmin}}, \quad (6.10)$$

with T_{Bmax} and T_{Bmin} being the maximum and the minimum T_B values for a particular scene.

Three main semi-empirical relationships can be found in literature to derive vegetation fraction from NDVI: [Baret et al. \[1995\]](#), [Carlson and Ripley \[1997\]](#), and [Gutman and Ignatov \[1998\]](#). No significant differences have been found on the algorithm performance when using these three alternatives, and [Gutman and Ignatov \[1998\]](#) has been adopted for simplicity.

The linking model in (6.9) is used to set up a system of linear equations for all the pixels in the image. This system is solved to obtain the regression coefficients a_{ijk} –which are specific of the scene being analyzed.

Step 3: soil moisture at high resolution

SMOS-derived soil moisture maps at 32 km are obtained by applying (6.9) with the regression coefficients a_{ijk} (from step 2), T_N and F_r aggregated to 32 km, and SMOS T_{BN} resampled to a 32 x 32 km grid. Similarly, soil moisture maps at 16 or 8 km are obtained by applying (6.9) with the regression coefficients a_{ijk} , T_N and F_r aggregated to 16 km or 8 km, and SMOS T_{BN} resampled to a 16 x 16 km or 8 x 8 km grid

6.3.3 Results

The downscaling algorithm in 6.3.2 has been applied to SMOS T_B images over different regions within Australia to evaluate the algorithm performance under different natural conditions. In this Section, sample soil moisture maps at 64 and 32 km spatial resolution, resulting from the application of the downscaling algorithm to different SMOS images are shown. Results of using (6.3) instead of (6.9) in the SMOS context (Steps 2 and 3 of the algorithm) have been included so as to compare the effect of adding or not SMOS T_B to the linking model. The use of ascending and/or descending SMOS orbits for soil moisture retrieval is discussed. Then, soil moisture estimations at 64 and 32 km are compared to

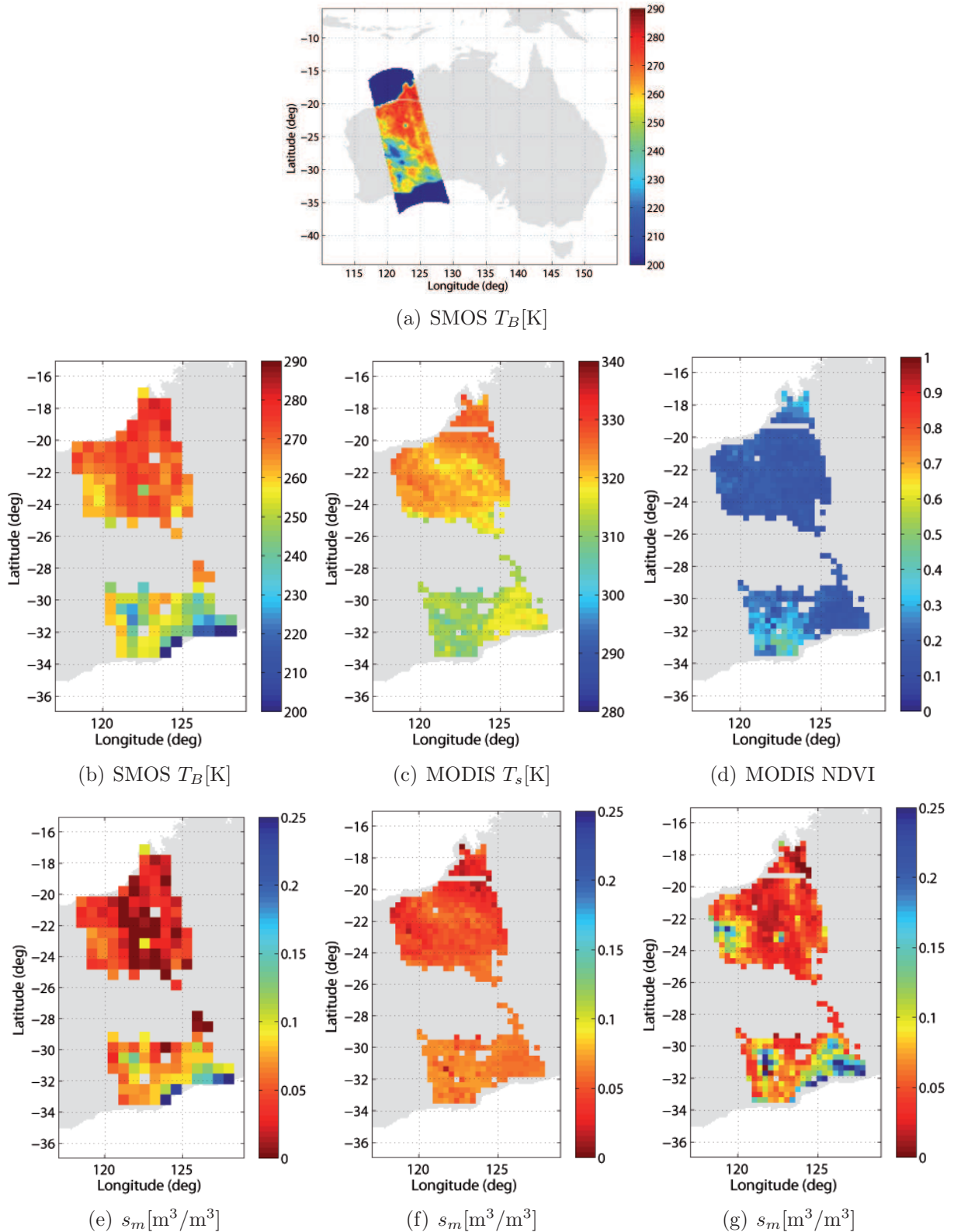


Figure 6.6 Sample results of the application of the algorithm to a SMOS image over western Australia, from December, 8, 2009 (6 am). SMOS T_B image [K] on a 16 x 16 km grid (a). SMOS T_B image [K] on a 64 x 64 km grid (b). MODIS-derived T_s [K] (c) and NDVI (d) maps aggregated to 32 km. SMOS-derived soil moisture map [m³/m³] at 64 km (e). SMOS-derived soil moisture maps [m³/m³] at 32 km using the linking model in (6.3) (f), and using the linking model in (6.9) (g). Empty areas in the images correspond to clouds masking MODIS T_s measurements.

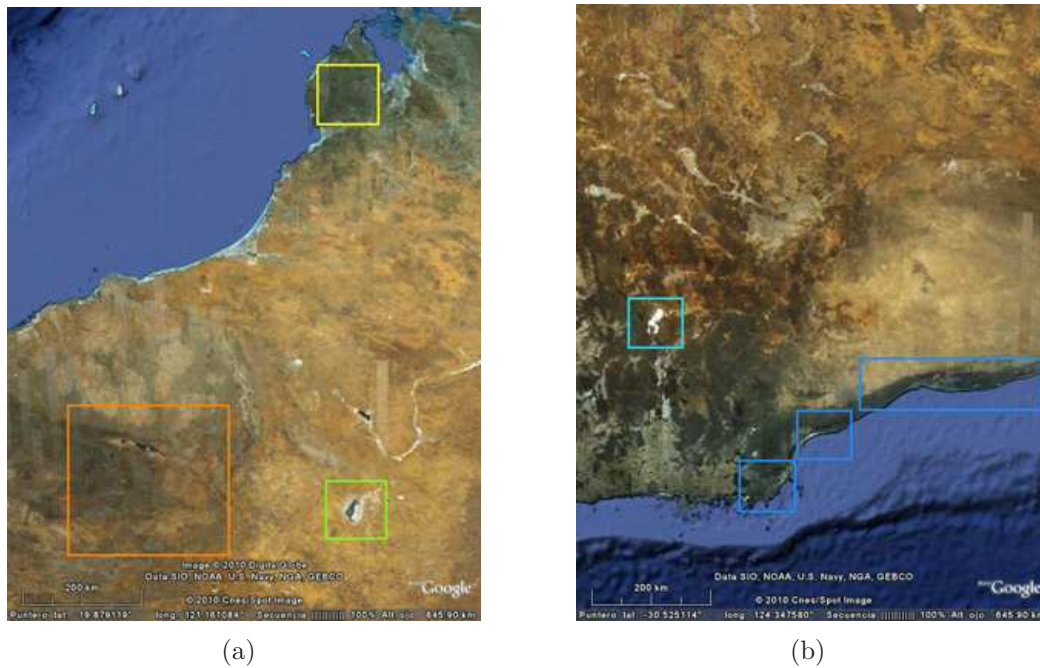


Figure 6.7 Aerial photographs covering the regions above (a) and below (b) the cloud mask in Fig. 6.6(b), from Google Earth.

in situ soil moisture data from the Murrumbidgee catchment, in South-eastern Australia. Also, the possibility of going into higher spatial resolutions of 16 and 8 km is explored.

Note that the date on the SMOS and MODIS images used in this Section are expressed in UTC, whereas the satellite overpass is expressed in local time.

Soil moisture maps

Figure 6.6 shows the results of applying the downscaling algorithm to an SMOS T_B image over western Australia, from December 8, 2009. This image could be representative of a bare soil or poorly vegetated scenario (the NDVI in Fig. 6.6(d) is less than 0.5 in all the area). It can be seen that when using the linking model in (6.3) (Fig. 6.6(f)), the downscaling method is not able to capture the soil moisture variability in Fig. 6.6(e). This is consistent with previous studies using the well-known triangle concept, which have reported the method's limitation of requiring a large number of pixels reflecting a wide range of fractional vegetation and moisture conditions [Carlson, 2007]. However, Fig. 6.6(g) shows that, when adding the SMOS T_B to the linking model, the method is capable of reproducing the variability seen in the low-resolution SMOS observations.

There are some pixels within the SMOS T_B image in Fig. 6.6 that have remarkably lower T_B (higher soil moisture content) than their surroundings. Particularly, in the region above the cloud mask in Fig. 6.6(b) there is an isolated green pixel at nearly the center of the image, an isolated yellow pixel in the top-right, and an orangish area in the left side of the image; in the region below the cloud mask, there are salient dark blue pixels near the coast line and an isolated blue pixel inland, on the left. In Fig. 6.7, these areas have been identified using coloured rectangles in two aerial photographs covering the regions above (Fig. 6.7(a)) and below (Fig. 6.7(b)) the cloud mask in Fig. 6.6(e), from Google Earth. It can be seen that the areas marked with yellow, orange and dark blue rectangles correspond to sharp changes in land cover and/or topography, that are effectively captured by SMOS.

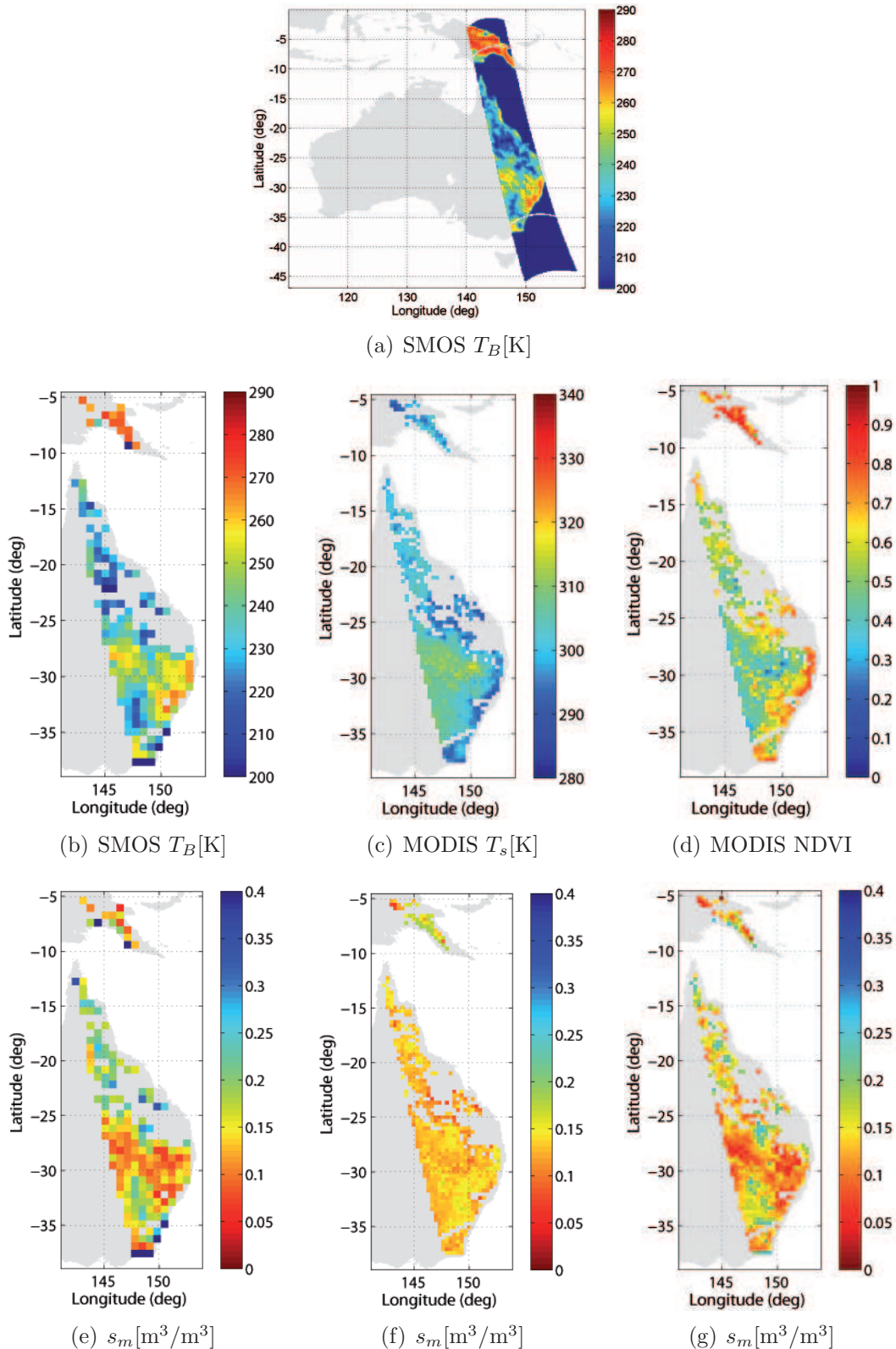


Figure 6.8 Sample results of the application of the algorithm to a SMOS image over eastern Australia, from February, 17, 2010 (6 am). SMOS T_B image [K] on a 16 x 16 km grid (a). SMOS T_B image [K] on a 64 x 64 km grid (b). MODIS-derived T_s [K] (c) and NDVI (d) maps aggregated to 32 km. SMOS-derived soil moisture map [m³/m³] at 64 km (e). SMOS-derived soil moisture maps [m³/m³] at 32 km using the linking model in (6.3) (f), and using the linking model in (6.9) (g). Empty areas in the images are due to clouds masking MODIS T_s measurements.

The areas marked with the green and blue rectangles contain the lake Disappointment and the lake Defroy, respectively, two salty lakes with dimensions of approximately 20 x 30 km. Therefore, through simple comparison to aerial photography, it can be seen that the most outstanding features of the region have been nicely detected by SMOS, and also captured at a higher spatial resolution with the downscaling algorithm using the linking model in 6.9.

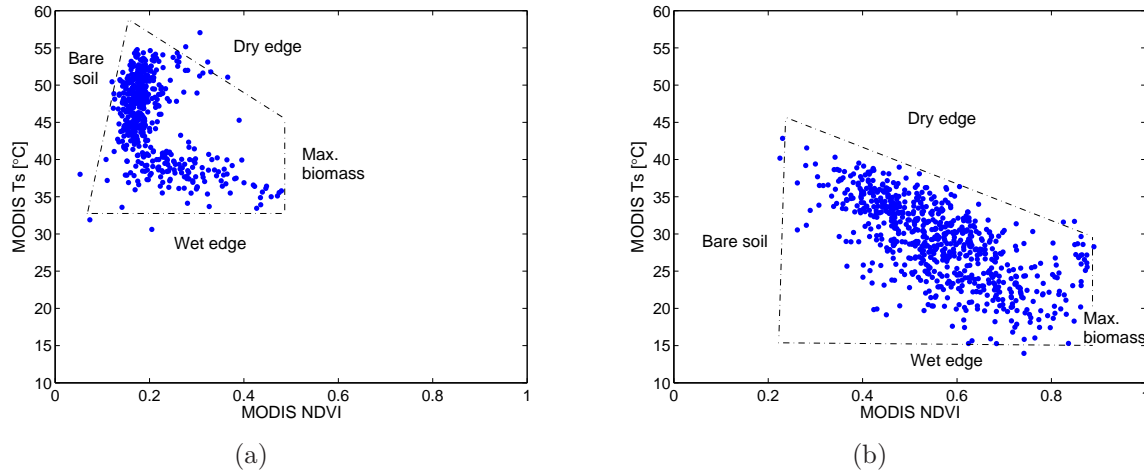


Figure 6.9 Scatter plots of MODIS surface radiant temperature versus MODIS NDVI, from Fig. 6.6 (a), and Fig. 6.8 (b).

Sample results of the application of the algorithm to an area exhibiting a full range of fractional vegetation cover is shown in Fig. 6.8. Comparing with the 64 km soil moisture map in Fig. 6.8(e), it can be observed that the method adding the SMOS T_B to the linking model (Fig. 6.8(g)) nicely captures the spatial patterns in soil moisture, and that they are only partially reproduced when using the linking model in (6.3) (Fig. 6.8(f)). Specially, note that the areas not reproduced are those exhibiting extreme low or wet moisture conditions.

Figure 6.9 illustrates the polygonal correlation between MODIS T_s and NDVI observations for the areas studied on Fig. 6.9(a), and Fig. 6.9(b). It evidences the wider range of soil surface temperature and fractional vegetation cover present in the image on Fig. 6.8, if compared to the image on Fig. 6.6. According to [Carlson \[2007\]](#), the main weakness of the triangle method is that it requires some subjectivity in identifying the dry edge (or warm edge) and the bare soil and maximum biomass extremes; identification is more easily obtained if a sufficient number of pixels with varying surface wetness and vegetation cover are present in the image. In this study, however, the edges of the polygon have been detected automatically from MODIS data, regardless of the scene. This could be certainly limiting the performance of the downscaling method when using the linking model in (6.3), but seems to be no longer a limitation when using the linking model in (6.9).

Ascending *vs.* descending orbits

SMOS is in a Sun-synchronous (polar) orbit, so that it passes over areas on the Earth's surface at the same local solar time (6 am/6 pm). The overpass time was particularly chosen so as to minimize the effect of temperature gradients within the soil and vegetation on soil moisture retrieval. Still, it is generally assumed that thermal equilibrium and near uniform conditions in the near surface soil layers and overlying vegetation are more likely to be true at 6 am than at 6 pm. Note that the presence of temperature gradients could seriously affect

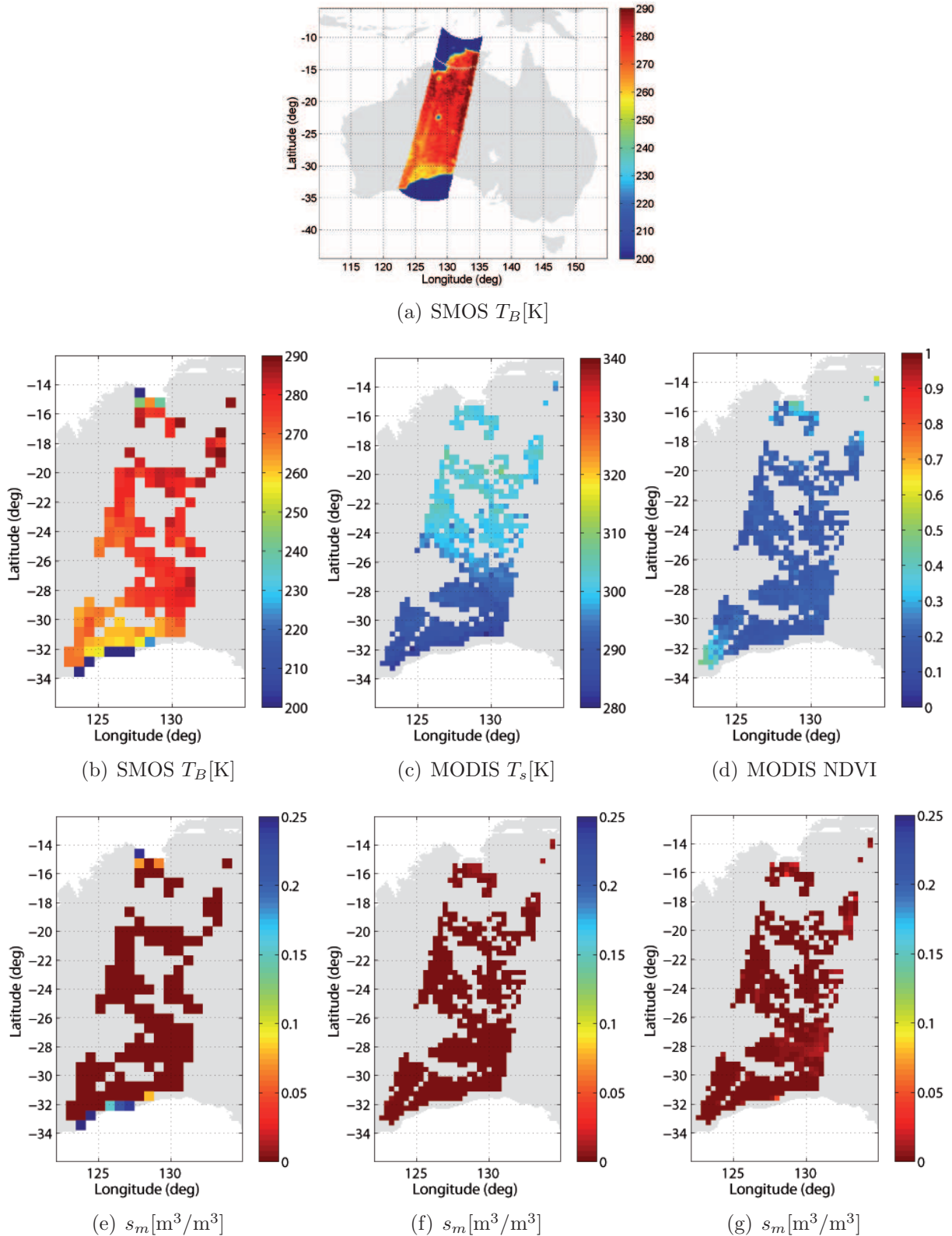


Figure 6.10 Sample results of the application of the algorithm to a SMOS image over central Australia, from December, 8, 2009 (6 pm). SMOS T_B image [K] on a 16 x 16 km grid (a). SMOS T_B image [K] on a 64 x 64 km grid (b). MODIS-derived T_s [K] (c) and NDVI (d) maps aggregated to 32 km. SMOS-derived soil moisture map [m³/m³] at 64 km (e). SMOS-derived soil moisture maps [m³/m³] at 32 km using the linking model in (6.3) (f), and using the linking model in (6.9) (g). Empty areas in the images correspond to clouds masking MODIS T_s measurements.

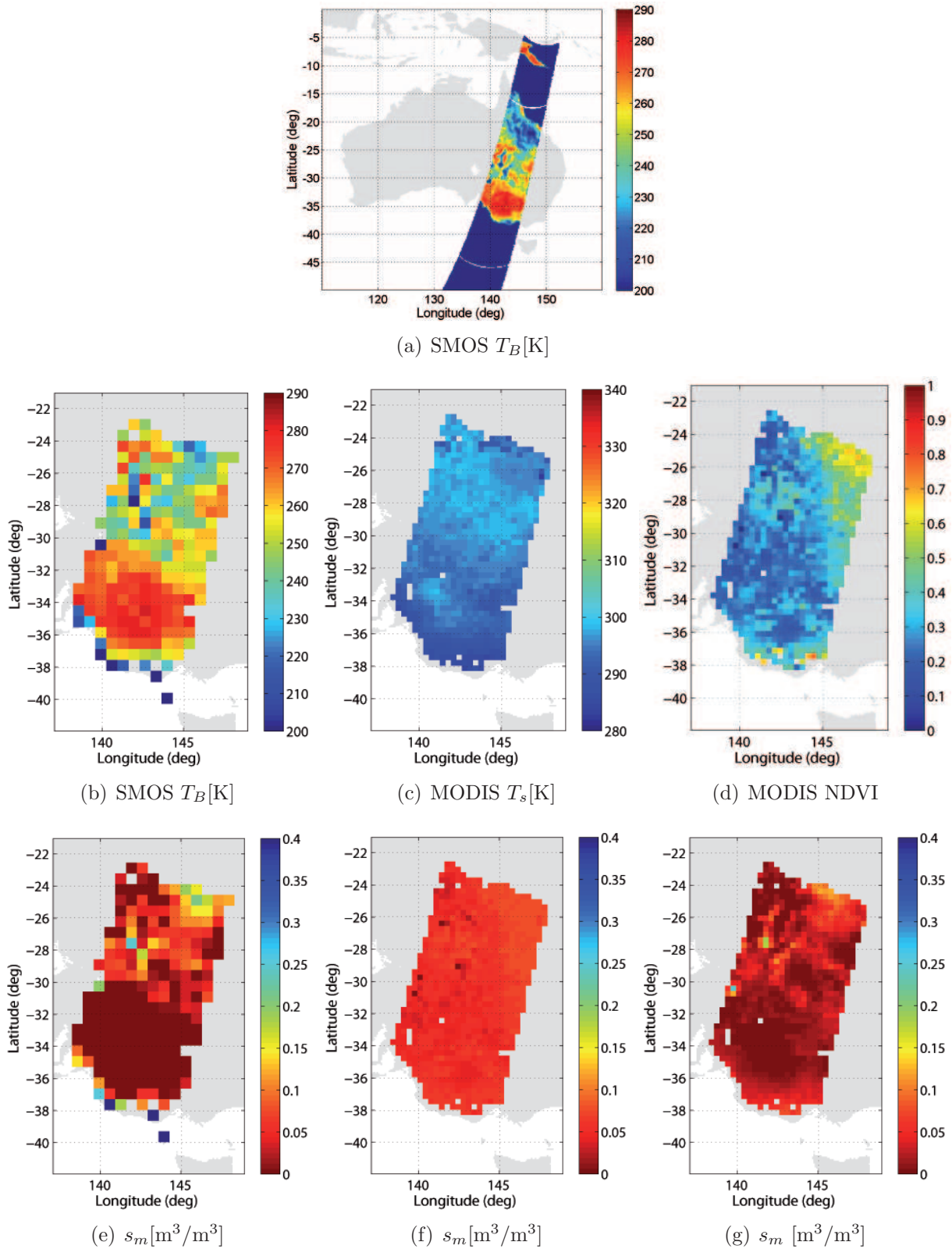


Figure 6.11 Sample results of the application of the algorithm to a SMOS image over south-eastern Australia, from February, 17, 2010 (6 pm). SMOS T_B image [K] on a 16 x 16 km grid (a). SMOS T_B image [K] on a 64 x 64 km grid (b). MODIS-derived T_s [K] (c) and NDVI (d) maps aggregated to 32 km. SMOS-derived soil moisture map [m³/m³] at 64 km (e). SMOS-derived soil moisture maps [m³/m³] at 32 km using the linking model in (6.3) (f), and using the linking model in (6.9) (g). Empty areas in the images are the result of clouds masking MODIS T_s measurements.

the performance of the soil moisture retrieval algorithms, since they are usually built upon the assumption that vegetation canopy is in equilibrium with soil temperature. Thus, in the early-stage of the SMOS mission in which we are now, it is important to confirm this general assumption, as well as to decide whether soil moisture retrievals should be performed using only ascendent orbits, using only descendent orbits, or using both of them.

Figures 6.10 and 6.11 show sample results of the application of the downscaling algorithm to SMOS images acquired on descending orbits. On these two cases, night time MODIS T_s (10.30 pm) have been used for being closer than day time MODIS T_s (10.30 am) to the SMOS overpass on descending orbits. Focusing on the Step 1 of the algorithm (Fig. 6.10(e) and Fig. 6.11(e)), it appears that the inversion technique is not able to resolve changes in soil moisture and is mostly underestimating it. Therefore, based on these analysis, SMOS images from ascending orbits seem to be far more adequate for land applications than SMOS images from descending orbits. However, this finding needs to be confirmed with the specific retrieval technique that has been developed for SMOS, which makes full use of its dual-polarization and multiangular characteristics, and include auxiliary information from global land surface parameters datasets (see Section 2.3, and Chapters 3, and 4). These images also indicate that, as expected, the performance of the downscaling algorithm is critically depending upon the soil moisture estimates obtained on Step 1; if soil moisture maps at 64 km do not effectively capture soil moisture changes, soil moisture maps at 32 km are not able to capture them either.

Comparison with *in situ* measurements

During the AACES field experiment, a significant rainfall event occurred on February 5 and 6, 2010. Two SMOS ascending T_B images – one captured before the rainfall event (January 22) and one at the end of the experiment (February 19)– over the Yanco region will be compared to *in situ* soil moisture measurements so that the algorithm performance will be assessed in extremely hot dry (January 22) and moderately dry (February 19) conditions.

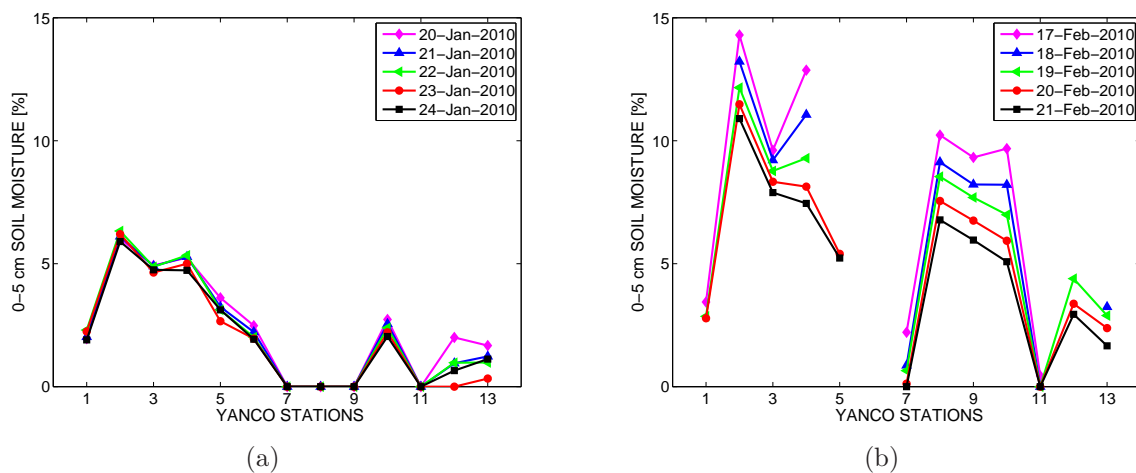


Figure 6.12 Spatial variability of 0-5 cm soil moisture measurements (6 am) of the 13 Yanco stations on days (a) January 20-24, 2010, and on (b) February 17-21, 2010.

It is important to remark that validating soil moisture estimation results is not straightforward, since there are some unresolved issues concerning the comparison of *in situ* measurements with soil moisture maps. The difficulty lies not only in the estimation process, but

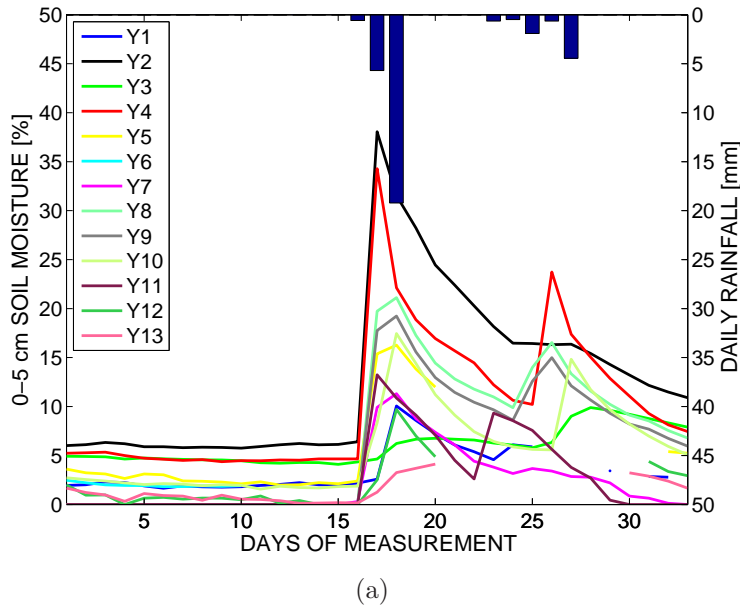


Figure 6.13 Temporal evolution of 0-5 cm continuous soil moisture measurements (6 am) and mean daily rainfall observed at 13 Yanco monitoring stations.

also in the representativeness of the *in situ* soil moisture measurements. Note that the penetration depth of the microwave signal depends on the soil moisture content itself. Therefore, the thickness of the soil layer contributing to the emitted radiation can significantly vary with moisture conditions (see Section 2.2.3 and [Monerris \[2009\]](#)). This fact could affect the representativeness of the soil moisture samples taken at a specific depth regardless surface conditions. In addition to this, the spatial distribution of soil moisture depends on soil parameters that are not distributed homogeneously in the area (e.g. soil texture, vegetation, topography, etc). And also, it should be taken into account that soil moisture could change very rapidly in the top layer. In view of these uncertainties, a study of the temporal and spatial variability of the 13 Yanco soil moisture stations the days immediately before and after the two SMOS images were acquired has been performed to analyze the consistency of the *in situ* data and, to some extent, of the validation approach.

Figure 6.12 shows the measured soil moisture variability at Yanco stations on January 20-24 (a), and on February 17-21 (b). It can be observed that there is a definite pattern in the spatial variability of soil moisture that repeats itself on all Yanco stations on the two different periods studied. This variability could be the result of changing soil properties of the area. Note that this pattern is common for the case of extremely dry and moderately dry conditions of Fig. 6.12(a), and Fig. 6.12(b), respectively, on all the stations except for 8 and 9. Still, the spatial variability appears to be consistent. The temporal variability of soil moisture measurements and the mean daily rainfall at Yanco stations from January 20 to February 21, 2010, is shown in Fig. 6.13. It can be seen how the soil moisture network nicely captures the two rainfall events occurred during these days.

Figures 6.14 and 6.15 illustrate the performance of the downscaling algorithm on two SMOS images covering the Murrumbidgee catchment, acquired on January 22 and February 19, respectively. It can be noted that the method using the linking model in (6.3) in these two scenes is better capturing the soil moisture variability of SMOS-derived soil moisture estimations at 64 km than in the previous cases on Fig. 6.6 and 6.8. This can be due to the wide range of vegetation and moisture conditions present within the area, that allows for

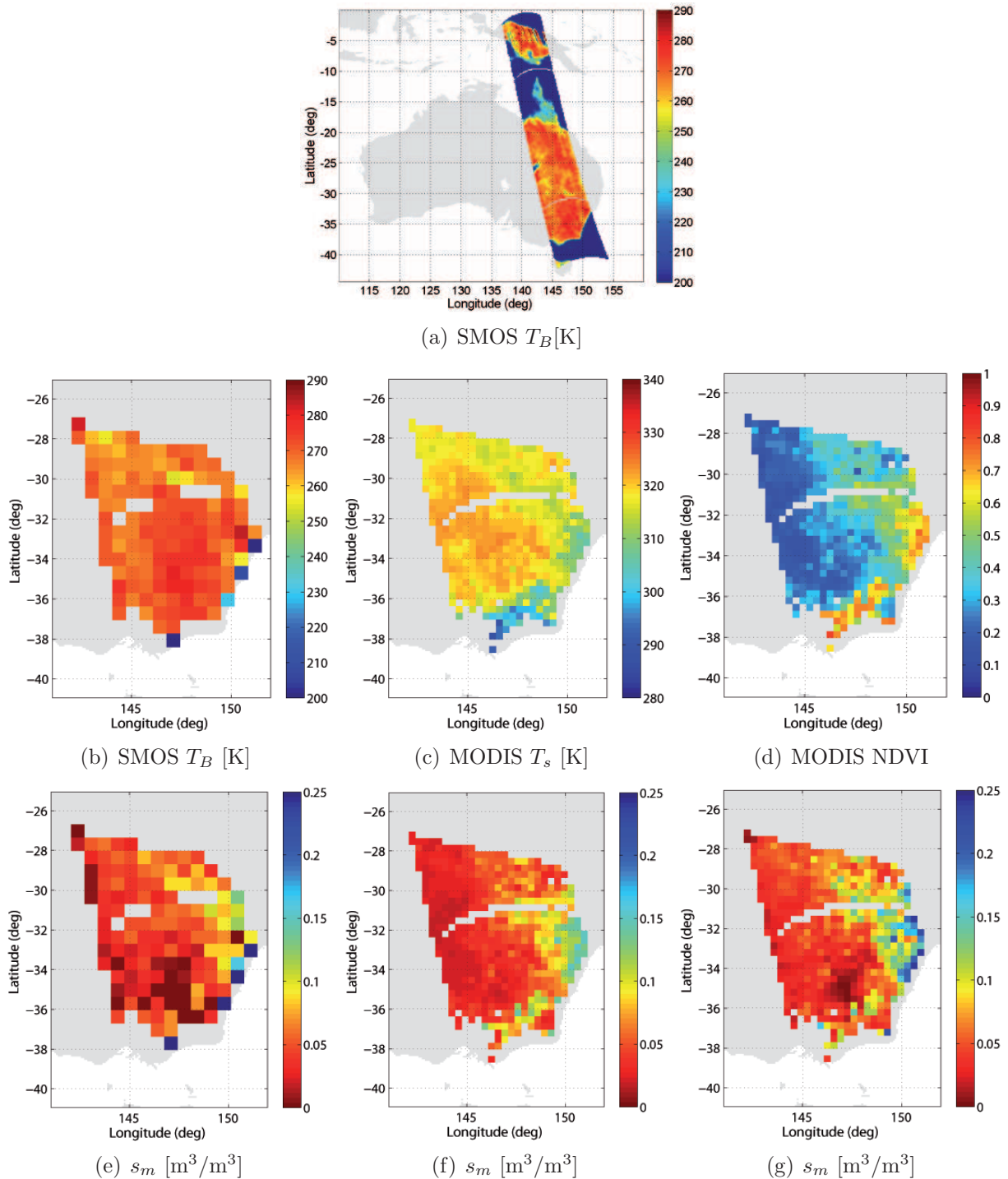


Figure 6.14 Sample results of the application of the algorithm to a SMOS image covering the Murrumbidgee catchment, from January, 22, 2010 (6 am). SMOS T_B image [K] on a 16 x 16 km grid (a). SMOS T_B image [K] on a 64 x 64 km grid (b). MODIS-derived T_s [K] (c) and NDVI (d) maps aggregated to 32 km. SMOS-derived soil moisture map [m^3/m^3] at 64 km (e). SMOS-derived soil moisture maps [m^3/m^3] at 32 km using the linking model in (6.3) (f), and using the linking model in (6.9) (g). Empty areas in the images correspond to clouds masking MODIS T_s measurements.

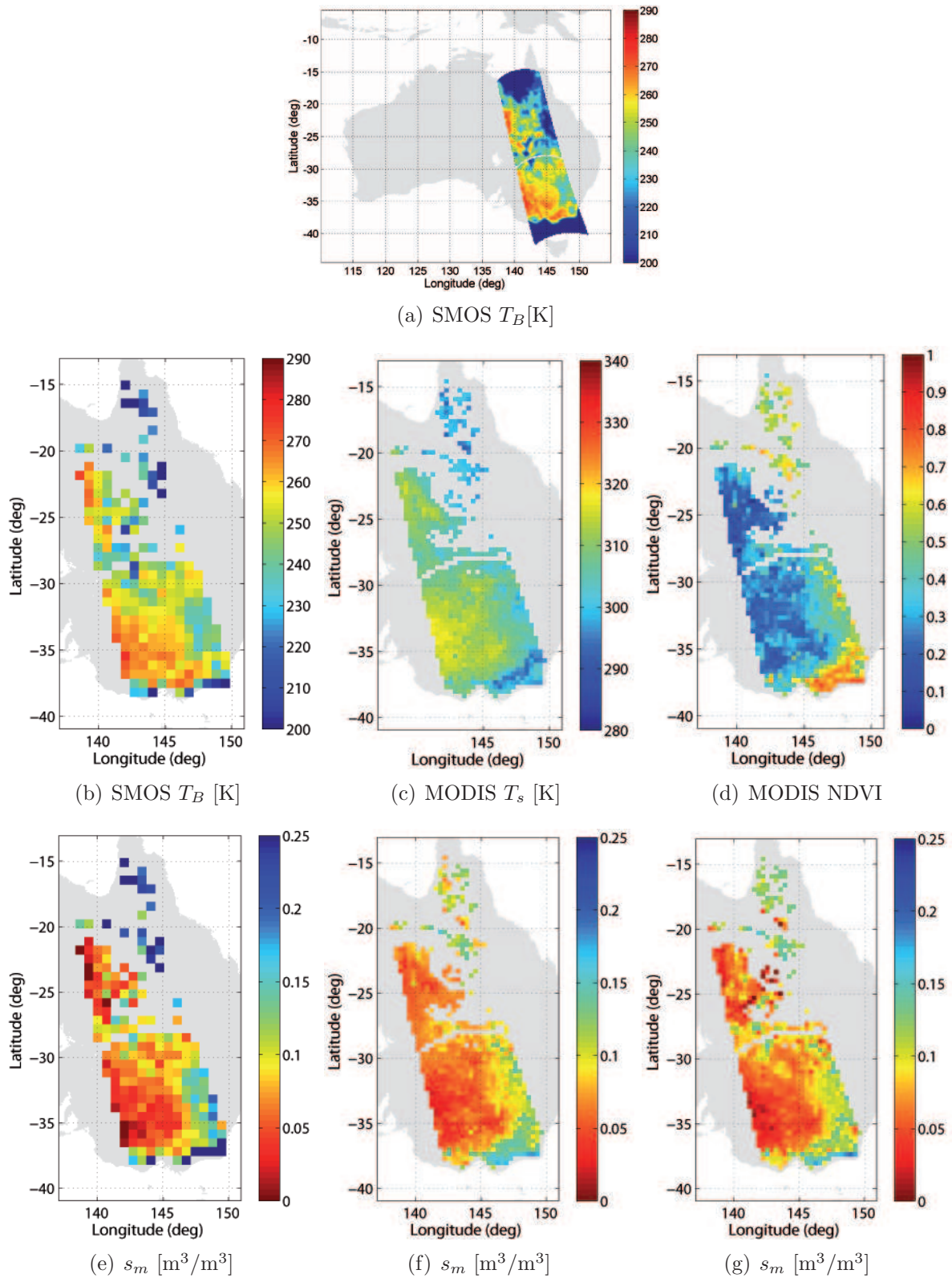


Figure 6.15 Sample results of the application of the algorithm to a SMOS image covering the Murrumbidgee catchment, from February, 19, 2010 (6 am). SMOS T_B image [K] on a 15 x 15 km grid (a). SMOS T_B image [K] on a 64 x 64 km grid (b). MODIS-derived T_s [K] (c) and NDVI (d) maps aggregated to 32 km. SMOS-derived soil moisture map [m^3/m^3] at 64 km (e). SMOS-derived soil moisture maps [m^3/m^3] at 32 km using the linking model in (6.3) (f), and using the linking model in (6.9) (g). Empty areas in the images correspond to clouds masking MODIS T_s measurements.

Table 6.1 SMOS-derived soil moisture retrievals [% vol] over the Yanco region at 64 km (\sim one pixel) and 32 km (\sim two pixels, averaged) spatial resolution, using different soil moisture retrieval configurations.

Day of measurement	s_m retrieval configuration	s_m at 64 km (Step 1)	s_m at 32 km (from (6.3))	s_m at 32 km (from (6.9))
22-Jan-2010 (averaged <i>in situ</i> $s_m = 2.18$)	Nominal	2.46	2.73	3.13
	Wang	14.05	12.48	12.37
	Dobson	1.58	1.40	1.58
	$h_s = 0$	6.29	5.78	6.29
	$\tau = 0$	0	0.97	1.47
19-Feb-2010 (averaged <i>in situ</i> $s_m = 5.84$)	Nominal	5.05	4.36	3.86
	Wang	14.48	12.83	12.05
	Dobson	2.30	2.02	1.63
	$h_s = 0$	8.25	7.16	6.54
	$\tau = 0$	2.51	1.36	1.71

a better definition of the triangle and, therefore, a better regression. Consequently, these results reinforce the scene-dependent performance of the universal triangle approach. Still, note that there are some particular features of the low resolution soil moisture image (e.g. the extremely dry areas) that are reproduced by the approach using SMOS T_B in the linking model, but are not captured by the method using the linking model in 6.3.

Zooming in, Table 6.1 focuses on the performance of the algorithm on the pixels coincident with the Yanco region (\sim one pixel of 64 x 64 km, \sim two pixels of 32 x 32 km). It shows the results of applying the nominal retrieval configuration and four variations of it in the Step 3 of the algorithm: the nominal configuration uses the dielectric mixing model in [Hallikainen et al. \[1985\]](#), $h_s = 0.2$, and τ estimated using (2.31) with $\alpha = -0.05$ $\beta = -0.36$, and MODIS NDVI data [[Burke et al., 2001](#)]; Wang configuration uses the dielectric mixing model in [Wang and Schmugge \[1980\]](#); Dobson configuration uses the dielectric mixing model in [Dobson et al. \[1985\]](#); no roughness is considered in the configuration $h_s = 0$, and no vegetation effects are corrected in the configuration $\tau = 0$.

On January 22, ground-based s_m measurements from 13 s_m stations present an average of 2.18 m³/m³, a standard deviation of 2.18 m³/m³, and minimum and maximum values of 0 and 6.33 m³/m³, respectively. On February 19, ground-based s_m measurements from 11 s_m stations report an average of 5.84 m³/m³, a standard deviation of 3.91 m³/m³, and minimum and maximum values of 0 and 12.16 m³/m³, respectively. Hence, comparing soil moisture retrievals at 64 km (in Table 6.1) with the mean of the ground-based s_m measurements, it can be seen that the nominal configuration is the one retrieving the closest s_m values, with an error of $\sim 10\%$ in the two days studied. The Wang model clearly overestimates the soil moisture, whereas the Dobson model seems to underestimate it. This is consistent with the study in [Monerris \[2009, chap. 5\]](#), where the Dobson model offered better results than the Wang model over sandy soils –note here that sandy soils are predominant within the Yanco region [[Young et al., 2008](#)]. When soil roughness is not corrected for ($h_s = 0$), the soil surface is considered to be flat (therefore having a higher reflectivity –lower emissivity– than rough terrain), and, as expected, the soil moisture is overestimated. When the attenuation by vegetation is not compensated ($\tau = 0$), results are also coherent: the soil emissivity is

assumed to be higher than it actually is, and, therefore, the soil moisture is underestimated. Regarding the accuracy of soil moisture estimations at 32 km, results from all configurations evidence that they are critically depending on the accuracy of the soil moisture estimations at 64 km. Comparing with ground-based measurements, the downscaling technique appears to overestimate soil moisture in extremely dry conditions, and to underestimate it in moderately dry conditions. However, an statistical analysis including a sufficient number of comparisons ground-truth *vs.* SMOS estimates is needed to evaluate the performance of the method in terms of radiometric resolution. Future work should definitely focus on developing an algorithm error budget.

Downscaling limit

As said, the possibility of obtaining soil moisture maps at higher spatial resolutions (up to 1 km) using the downscaling technique presented in this Chapter is subject of further research that validates the accuracy of the soil moisture retrievals at the different spatial scales. Still, the feasibility of going into higher spatial resolutions has been analyzed. To do so, sample soil moisture maps at 16 and 8 km spatial resolution have been obtained from the SMOS T_B images in Fig. 6.6(a), 6.8(a), 6.14(a), and 6.15(a), and the soil moisture error between retrievals at 32, 16 and 8 km and retrievals at 64 km has been analyzed.

Figure 6.16 illustrates the performance of the downscaling method using the linking model in (6.9) at different spatial resolutions, using the SMOS T_B image on Fig. 6.6(a). The first row shows SMOS-derived soil moisture maps at 32, 16 and 8 km spatial resolutions. It can be seen how the soil moisture variability is captured at the three different spatial scales, although the areas with high moisture conditions at 32 km (in blue) present lower moisture content at 16 and 8 km. The spatial distribution of the soil moisture error between soil moisture retrievals at 32, 16, and 8 km and soil moisture retrievals at 64 km is shown in the second row, and the histogram and statistics of the soil moisture errors is shown in the third row. Note that the soil moisture RMSE at 32 km is 0.039, and that it increases to 0.040 and 0.041 when going into 16 and 8 km, respectively. Thus, for this particular image, the increase in the soil moisture error when going into higher spatial resolutions seems to be negligible.

The standard deviation, bias, and root mean square soil moisture error between soil moisture retrievals at 32, 16, and 8 km, and soil moisture retrievals at 64 km, for the four SMOS T_B images analyzed (from December 8, 2009, and January 22, February 17 and 19, 2010), using the linking models in (6.3) and (6.9), are presented in Table 6.2. It can be observed that the soil moisture error is lower for the soil moisture map at 32 km in all the cases studied, and that it is nearly the same for the soil moisture maps at 16 and 8 km. Still, the increase in RMSE from 32 to 16 and 8 km is moderate: it is of ~ 0.01 for the images acquired on December 8, January 22, and February 19, and ~ 0.03 for the image acquired on February, 17. Also, note that results are slightly better when using the model in (6.9), than when using the model in (6.3). Thus, these results indicate that, using the downscaling technique presented on this Chapter, it is feasible to obtain soil moisture estimates from SMOS at the 1-10 km spatial resolution required for regional applications.

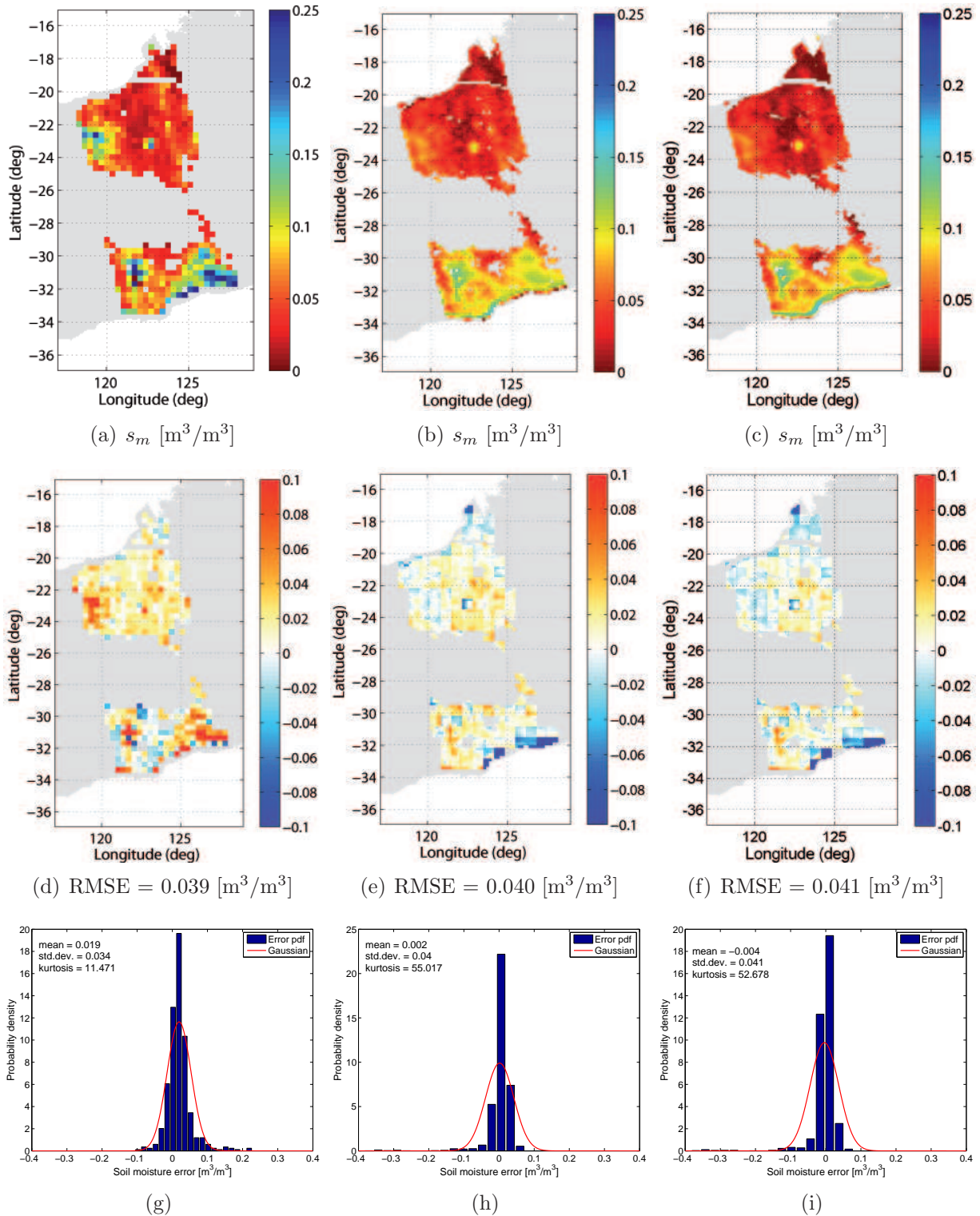


Figure 6.16 SMOS-derived soil moisture maps and error statistics at 32, 16, and 8 km spatial resolution over western Australia, from December, 8, 2009 (6 am), using the linking model in (6.9). SMOS-derived soil moisture maps [m^3/m^3] at (a) 32 km, (b) 16 km, and (c) 8 km spatial resolutions. Spatial distribution of the soil moisture error [m^3/m^3] between soil moisture retrievals at (d) 32 km, (e) 16 km, and (f) 8 km, and soil moisture retrievals at 64 km. Histogram and statistics of the difference between soil moisture retrievals at (g) 322 km, (h) 16 km, and (i) 8 km, and soil moisture retrievals at 64 km. Empty areas in the images correspond to clouds masking MODIS T_s measurements.

Table 6.2 Standard deviation, bias, and root mean square soil moisture error [m^3/m^3] between soil moisture retrievals at 32 km, 16 km, and 8 km, and soil moisture retrievals at 64 km, from the SMOS T_B images on Fig. 6.6(a), 6.8(a), 6.14(a), and 6.15(a), when using the linking model in (6.3), and when using the linking model in (6.9).

Day of measurement		$s_m(32 - 64 \text{ km})$		$s_m(16 - 64 \text{ km})$		$s_m(8 - 64 \text{ km})$	
		(6.3)	(6.9)	(6.3)	(6.9)	(6.3)	(6.9)
8-Dec-2009	mean	0.005	0.019	-0.005	0.002	-0.004	-0.004
	σ	0.039	0.034	0.050	0.040	0.052	0.041
	RMSE	0.039	0.039	0.050	0.040	0.052	0.041
22-Jan-2010	mean	0.002	0.013	-0.005	0.006	-0.015	-0.013
	σ	0.049	0.045	0.062	0.059	0.065	0.061
	RMSE	0.049	0.047	0.062	0.059	0.066	0.062
17-Feb-2010	mean	-0.023	-0.024	-0.050	-0.059	-0.041	-0.017
	σ	0.064	0.048	0.080	0.069	0.082	0.089
	RMSE	0.068	0.053	0.094	0.091	0.091	0.091
19-Feb-2010	mean	-0.013	-0.013	-0.022	0.006	-0.019	-0.016
	σ	0.054	0.051	0.061	0.058	0.063	0.060
	RMSE	0.056	0.052	0.065	0.061	0.066	0.062

6.4 Discussion and conclusions

Within the SMOS Cal/Val activities, a downscaling algorithm to improve the spatial resolution of airborne passive L-band observations using the relationship between high spatial resolution visible/infrared satellite imagery and soil moisture status was evaluated. Based on this experience, an algorithm for downscaling SMOS observations using MODIS-derived NDVI and T_s data has been developed. Results of its application to four SMOS images acquired during the commissioning phase indicate that it is feasible to improve the spatial resolution of SMOS accurate soil moisture retrievals using higher spatial resolution MODIS visible/infrared data. SMOS observations from ascending orbits seem to be more adequate for land applications than from descending ones. Results from comparison with ground-based soil moisture measurements outline that it is essential to obtain accurate soil moisture estimates from SMOS at low resolution (first step of the algorithm) to afterwards capture soil moisture variability at higher spatial resolutions (steps two and three of the algorithm). SMOS-derived soil moisture maps at 64, 32, 16 and 8 km have been obtained; the soil moisture variability is nicely captured at the different spatial scales, but further research is needed to validate the accuracy of the retrievals at every spatial resolution and establish a downscaling limit.

Following the successful launch of SMOS in orbit, and a satisfactory demonstration of its capabilities during the commissioning phase, this work could potentially contribute to enhance the spatial resolution of SMOS soil moisture estimates, which will be a new and highly relevant research development. Also, these results suggest the prospect use of a visible/infrared sensor as a secondary payload in follow-on space-borne missions dedicated to soil moisture monitoring; the visible/infrared sensor could be highly useful in both the estimation of collocated land surface temperatures to be used in the soil moisture retrievals,

and the improvement of the spatial resolution of the estimates using the universal triangle concept.

*The whole is greater
than the sum of its parts*
Max Wertheimer (1880-1943)

7

A change detection algorithm for retrieving high-resolution soil moisture from SMAP radar and radiometer observations

A downscaling algorithm to obtain global high-resolution soil moisture estimates from SMAP L-band radar and radiometer observations is presented. The approach is based on change detection and combines the relatively noisy 3 km radar backscatter cross-section and the more accurate 36 km radiometer brightness temperature into an optimal 10 km product. In preparation for the SMAP mission, an Observation System Simulation Experiment (OSSE) and field experimental campaigns using the Passive and Active L and S-band airborne sensor (PALS) have been conducted. By using the PALS airborne observations and OSSE data, the algorithm is tested and an error budget table is developed. When applied to 4-months OSSE data, the downscaling method is shown to perform better than direct inversion of the radiometer brightness temperatures alone, improving the RMSE by 2% volumetric soil moisture content. The algorithm error budget shows that the proposed algorithm meets the SMAP minimum science requirements.

7.1 Introduction

Active and Passive L-band microwave remote sensing provide a unique ability to monitor global soil moisture over land surfaces with an acceptable spatial resolution and temporal frequency [*Njoku and Entekhabi, 1996; Schmugge et al., 2002*]. Mapping radars are capable of a very high spatial resolution (~ 3 km in case of SMAP) but, since radar backscatter is highly influenced by surface roughness, vegetation canopy structure and water content, they have a low sensitivity to soil moisture under vegetated conditions. Various algorithms for soil moisture retrieval from radar backscattering have been developed, but they are only valid in low-vegetation water content conditions [*Dubois et al., 1995; Shi et al., 1997*]. In contrast, the spatial resolution of radiometers is typically low (~ 40 km), the retrieval of soil moisture from radiometers is well established, and radiometers have a high sensitivity to soil moisture under vegetated conditions [*Jackson et al., 1996*].

To overcome the individual limitations of the passive and active approaches, the NASA SMAP mission is combining the two technologies (see Section 1.3.2). This chapter describes

a downscaling algorithm for the retrieval of global high resolution soil moisture estimates from SMAP radar and radiometer data; it aims at combining the high radar resolution and the high radiometer accuracy into an optimal 10 km soil moisture product.

Change detection techniques have been demonstrated to be able to potentially monitor temporal evolution of soil moisture by taking advantage of the approximately linear dependence of radar backscatter and brightness temperature change on soil moisture change (see Section 1.4). The novel approach presented on this study is based on change detection and focuses on the idea of considering the surface soil moisture over a sample 10 km region to be composed of weighted averages of the available radar retrievals within that region and the radiometer retrieval within the radiometer footprint containing the 10 km region. The advantage of this approach is that as more radar retrievals are available within the 10 km region, more spatial structure within a radiometer footprint will become evident and, since the collection of 10 km pixels within the larger scale radiometer footprint is constrained to sum to the value indicated by the radiometer retrieval, the high resolution estimation gracefully keeps the accuracy of the radiometer retrieval.

The theoretical basis and the assumptions behind the change detection algorithm used in this study are presented in Section 7.2. In Section 7.3, field experiment data from the SMEX02 field campaign is used to validate the algorithm main assumptions. The results of applying the algorithm to a 4-months OSSE dataset are shown on Section 7.4. The performance of the method is shown in terms of comparison with synthetic ground truth soil moisture data and with the radiometer data re-sampled to 10 km. An error budget analysis of the algorithm is presented in Section 7.5 and, in the final section, the most significant results of the paper are summarized and the applicability and usefulness of the scheme to future SMAP data on an operational basis is discussed.

7.2 Change detection method

The algorithm presented in this study is based on the change detection concept. The 40 km radiometer brightness temperatures are combined with the 3 km radar backscatter observations to obtain 10 km soil moisture observations. It assumes in the first place that soil moisture and the log of radar backscatter are linearly related at a 10 km scale (Assumption I):

$$\theta(a, t) = \alpha(a) + \beta(a) \cdot \log[\sigma^0(a, t)], \quad (7.1)$$

where a represents the 10 km scale, $\sigma^0(a, t)$ is the radar backscatter aggregated to 10 km at time t and $\theta(a, t)$ is the soil moisture at 10 km at time t . The aggregation could be made in dB, but using this approach the algorithm does not converge for most pixels.

We can form time differences to remove the bias term of (7.1) and space average the result to the radiometer pixel area A of 40 km, which leads to:

$$\langle \Delta\theta(a, t) \rangle = \langle \beta(a) \cdot \Delta \log[\sigma^0(a, t)] \rangle, \quad (7.2)$$

where $\langle \cdot \rangle$ stands for the the spatial average of the a scale pixels contained into the A scale pixels.

At this point, it is assumed (Assumption II) that slope β and backscatter changes are uncorrelated. Hence, the definition of covariance $\text{Cov}\{x, y\} = \langle x \cdot y \rangle - \langle x \rangle \cdot \langle y \rangle$ can be used to write (7.2) as,

$$\langle \Delta\theta(a, t) \rangle = \langle \beta(a) \rangle \cdot \langle \Delta \log[\sigma^0(a, t)] \rangle. \quad (7.3)$$

Finally, it is assumed that variation on vegetation type occur principally at scales larger than A (Assumption III), $\beta(a) = \langle \beta(a) \rangle$, so time differences can be used to write (7.3) as:

$$\theta(a, t) = \theta(A, t - t_R) + \langle \beta(a) \rangle \cdot \Delta \log[\sigma^0(a, t)], \quad (7.4)$$

where t_R is the revisit time of the observations, three days for the SMAP case.

The radar-radiometer change-detection algorithm can be written as either the radiometer-scale soil moisture retrieval $\theta(A, t - t_R)$ updated with moisture change evident in the higher-resolution radar back-scatter change as in (7.4) or, alternatively, the 10 km soil moisture retrieval from the previous algorithm application (orbit pass) $\theta(a, t - t_R)$ can be used as the first term. However, this latter approach has the risk of accumulating errors from the relatively more noisy radar measurements.

Equation (7.4) constitutes the core of the change detection algorithm. It indicates that a soil moisture estimate at scale a and at a given time can be obtained as the previous soil moisture estimate plus a change in soil moisture, which is given by the actual radar estimates and the value of the slope $\langle \beta(a) \rangle$. From (7.3), the slope can be estimated using regression of radiometer and radar data at scale A . Better slope estimations are obtained with time, since more radar and radiometer observations are available. The first estimates are likely to be noisy due to the high uncertainty on the first calculated slopes. However, when a reasonable number of estimates (on the order of a month) are available, the uncertainty on calculating the slope becomes much lower, leading to robust soil moisture estimations (See Section 7.4).

7.3 Test of assumptions using SMEX02 data

7.3.1 SMEX02 description

Experimental data from the soil moisture experiments SMEX02 are used in this study to validate the three assumptions of the algorithm. The SMEX02 field campaign was conducted in Walnut Creek, a small watershed in Iowa, between June 25th and July 12th, 2002. The PALS sensor was mounted on an aircraft and flown over the SMEX02 region on June 25, 27, and July 1, 2, 5, 6, 7 and 8, 2002 and an extensive dataset of *in situ* measurements of volumetric soil moisture, surface and subsurface soil temperature, soil bulk density and vegetation water content was collected during all the campaign [Limaye et al., 2004]. The PALS coverage during July 1st was partial and *in situ* sampling was not done on July 2nd, so data from these two days were not used in the present study. Since the algorithm proposed in this paper is based on the change of soil moisture over time, it is not feasible to fully test it with data from aircraft-mounted instruments due to cost limitations. However, L-band PALS data and volumetric soil moisture have been properly used to validate the algorithm assumptions on Section 7.3.2. Also, SMEX02 experimental data has been used to estimate the algorithm error budget on Section 7.5.

7.3.2 Validation of the assumptions

In a previous study, it was shown that for the SMEX02 field experiment PALS L-band brightness temperatures and radar backscatter coefficients were well correlated to soil moisture [Narayan et al., 2004]. To specifically illustrate the correlation between soil moisture and radar backscatter assumed in the algorithm development (Assumption I), on Fig. 7.1,

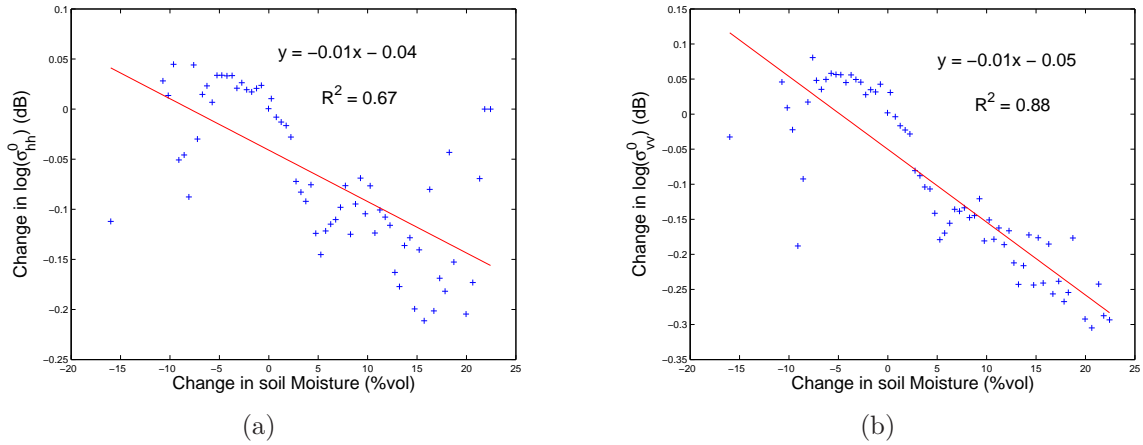


Figure 7.1 Change in log of PALS observed L-band radar backscatter at hh (a) and vv (b) polarizations plotted versus change in *in situ* volumetric soil moisture in the 0 to 6 cm soil layer for the period June 25 to June 27 and July 5 to July 7. The change in radar backscatter has been stratified by 0.05% change in volumetric soil moisture.

the change in log of radar backscatter for hh and vv polarizations is compared to the corresponding change in volumetric soil moisture at a resolution of 400-m for the time periods June 25 to June 27 and July 5 to July 7. R^2 values of 0.67 and 0.88 are obtained for hh and vv polarizations, respectively, indicating that radar sensitivity to soil moisture is significant even under the dense vegetation conditions encountered in the SMEX02 experiments with the vegetation water content of corn fields being around 4-5 kg/m² [Narayan *et al.*, 2004]. The higher correlation obtained with the radar vertical polarization is consistent with the literature on radar remote sensing of soil moisture.

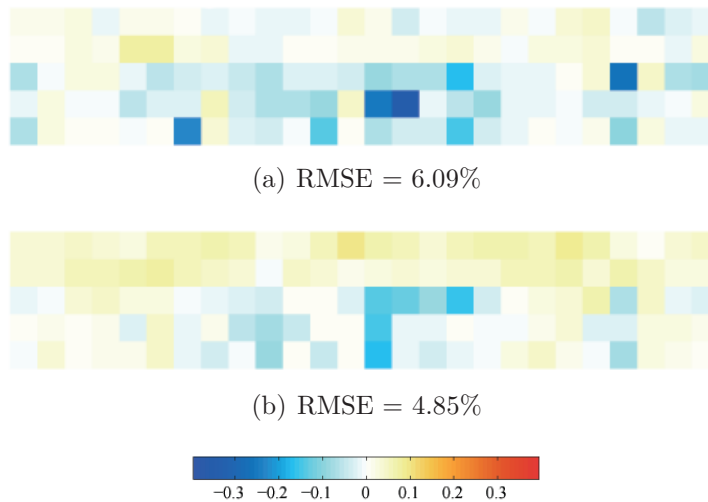


Figure 7.2 Error difference between static map of β of 400 m aggregated to 1600 m and directly computed static map of β at 400 m spatial resolution using radar hh (a) and vv (b) polarizations.

In order to demonstrate with real data that the algorithm's calculated slope and backscatter changes are uncorrelated (Assumption II), for each day of measurement the slope is calculated using linear regression from (7.3) and the change in log of radar backscatter is

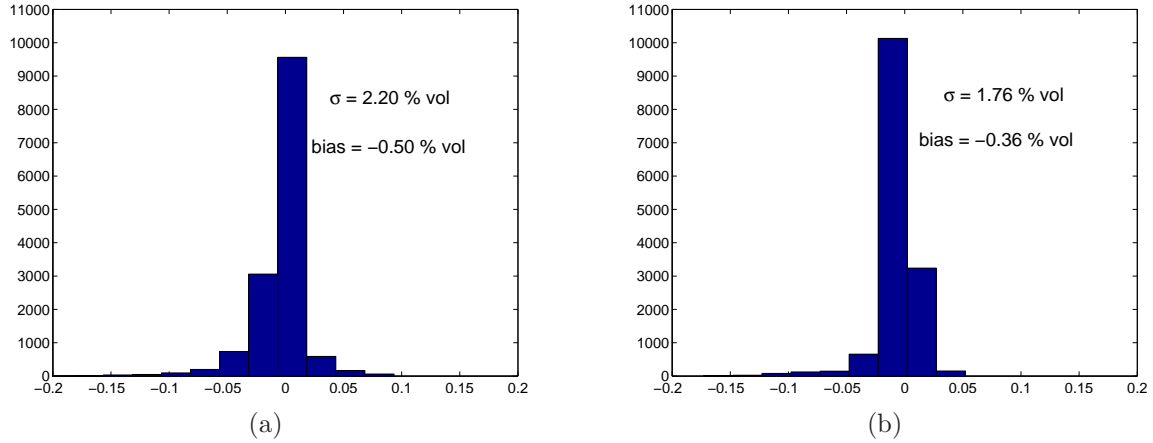


Figure 7.3 Histogram of the difference between soil moisture retrieved using static map of β of 400 m and using static map of β at 1600 m for hh (a) and vv (b) polarizations.

computed. Daily correlations between the slope and the change in radar backscatter result in values of the order of 10^{-5} , which evidences the validity of the assumption made.

Assumption III in the algorithm formulation states that the slope at 10 km resolution equals the mean of the slope over a 40 km pixel ($\beta(a) = \langle \beta(a) \rangle$). The spatial resolutions of 400 m and 1600 m will be used in this part of the study representing a and A , for compatibility with PALS data. As an initial evaluation of this point, for each pixel and for all days of measurement, static maps of β were calculated using linear regressions with brightness temperatures and radar backscatters at 400 m resolution and at 1600 m (7.3). The 400 m static map of β was then aggregated to 1600 m and compared to the maps of β using aggregated radar and radiometer measurements at 1600 m. Thus, the error difference between the two maps is essentially the error of assuming homogeneity of β . Even though the scale ratios with the PALS data are the same as SMAP radar and radiometer pixels, the absolute scales are clearly different. This mismatch may represent an under-estimation of the error due to this assumption. Nevertheless this represents a preliminary test and more detailed testing using other data sets is needed. The results of the tests on Assumption III are shown in Fig. 7.2. Results show an acceptable error, greater for horizontal than for vertical polarization. Still, for quantifying the error that this assumption is adding to the retrievals, another experiment has been conducted: from the static map of β at 400 m, the soil moisture estimates for each day are calculated, and the same procedure is followed to retrieve soil moisture estimates from the static map of β at 1600 m. Subsequently, histograms of the difference between the soil moisture retrievals acquired using $\beta(a)$ and $\langle \beta(a) \rangle$ are plotted on Fig. 7.3. With an error of $\sim 2\%$, this third assumption results to be the most critical error source for the algorithm.

The airborne campaign duration is too short and the variability in ground conditions is too limited to fully apply the change detection algorithm. Longer-duration data sets with wider range of vegetation conditions are needed. Here we augment the tests of the algorithm assumptions using airborne field experiment data with tests using synthetic observing system simulation experiments.

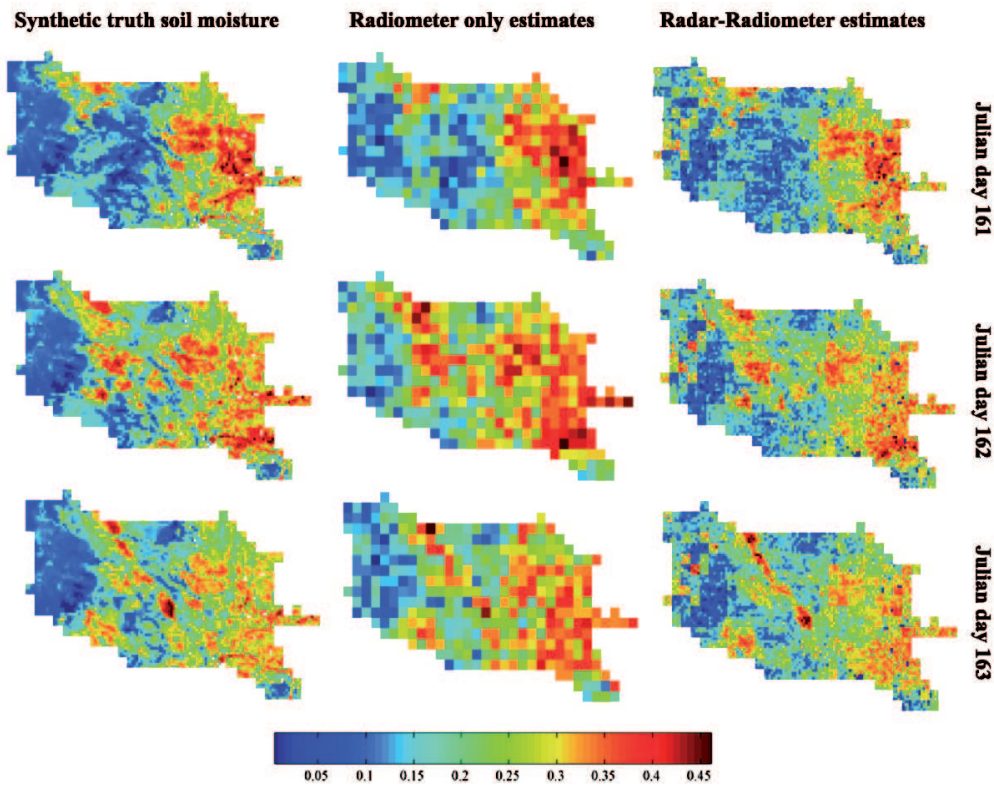


Figure 7.4 Sample results (three days) from the Observation System Simulation Experiment for the comparison of higher resolution (10 km) soil moisture estimates obtained using the active-passive method with synthetic ground truth soil moisture and with lower resolution (40 km) estimates obtained from a typical radiometer.

7.4 Application to OSSE data

7.4.1 OSSE data set

The simulated data used in this study was generated in the Hydros OSSE. The OSSE was designed to mimic as closely as possible the specific Hydros sensor and orbital characteristics and therefore is perfectly valid for SMAP purposes. The experiment was driven by high resolution land surface geophysical variables generated from a distributed land surface model within the Red-Arkansas river basin. They were used to derive a set of Hydros-like simulated brightness temperatures and radar backscatter cross-sections over the area that were then inverted back into soil moisture products using various retrieval algorithms. The OSSE adopts an easily nested fine, medium and coarse resolution grid of 3, 9, and 39 km, respectively. On this study, the OSSE resolutions of 9 km and 39 km will be used closest to SMAP 10 km and 40 km products. Complete OSSE fundamentals and details for radiometer-only soil moisture retrievals are described in [Crow *et al.*, 2005b]. Details regarding the radar and radiometer soil moisture retrievals are provided in [Zhan *et al.*, 2006].

Two sets of OSSE data are used in this study to reproduce a realistic scenario just after SMAP calibration and validation phase: one month dataset is used as background data for the algorithm, representing the data acquired during the commissioning phase; and a four months dataset is processed in near real time, simulating the first four months of data obtained in the operational phase, exactly after the commissioning phase. To meet the expected SMAP accuracies, an error of 4% (Root Mean Square Error or RMSE) is added to

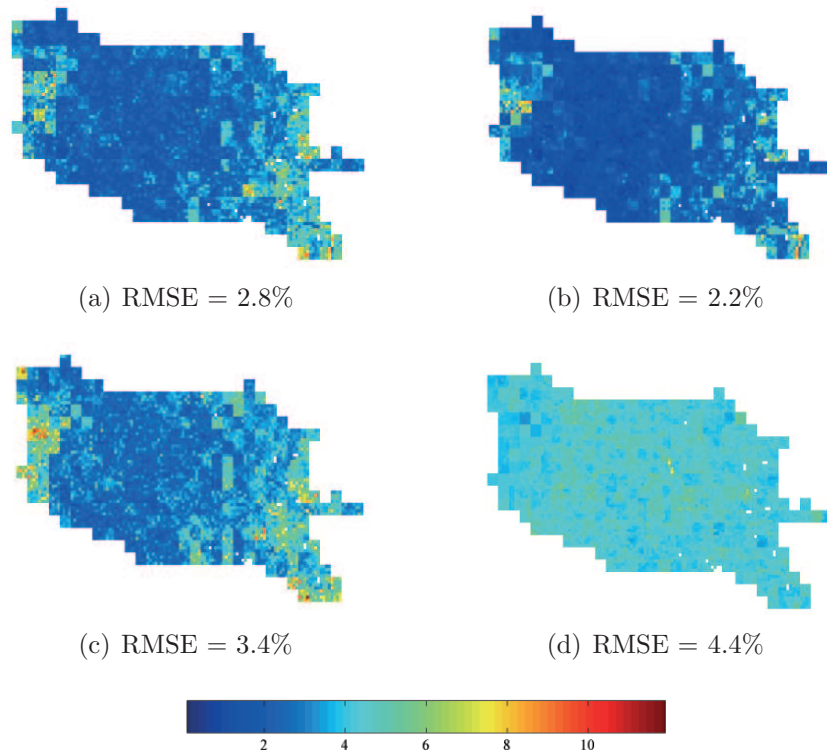


Figure 7.5 Spatial distribution of the soil moisture error retrieved using the change detection method with σ_{hh}^0 (a), σ_{vv}^0 (b), σ_{hv}^0 (c), and the radiometer only technique (d)

the radiometer retrievals and the normalized deviation K_p of radar backscatters [*Chi et al., 1986*] is set to 0.15. Independent noise is added in each measurement channel. Since the three radar polarizations (hh , vv and hv) can be used independently in the algorithm with different outcomes, the three possible solutions will be analyzed. The simulated data will be used to evaluate the algorithm performance in Section 7.4.2 and to calculate the algorithm error budget in Section 7.5.

7.4.2 Results

Sample results of applying change detection to the simulated data (with radar and radiometer noise added) are presented in Fig. 7.4 for three consecutive days. Comparing with the original soil moisture distributions and the estimates obtained from the radiometer only technique, it can be seen that the active-passive disaggregation algorithm reproduces much of the variability seen in the *in situ* soil moisture images and that these details are not captured by the radiometer only method.

Using the OSSE data sets as described previously, the performance of the change detection method is evaluated by comparing the retrieved soil moisture values of the 4-months dataset with their corresponding original data and with results from the radiometer only or minimum performance product. Minimum performance is obtained by re-sampling the 40 km radiometer data to 10 km. Fig. 7.5 shows the spatial distribution of the soil moisture RMSE after applying the change detection method and the radiometer only technique. Using the change detection algorithm on the 4-months OSSE the RMSE is reduced to 2%, with better results obtained using radar vv polarization. In addition, for a direct comparison with the minimum performance algorithm, the ratio of the change detection RMSE to the

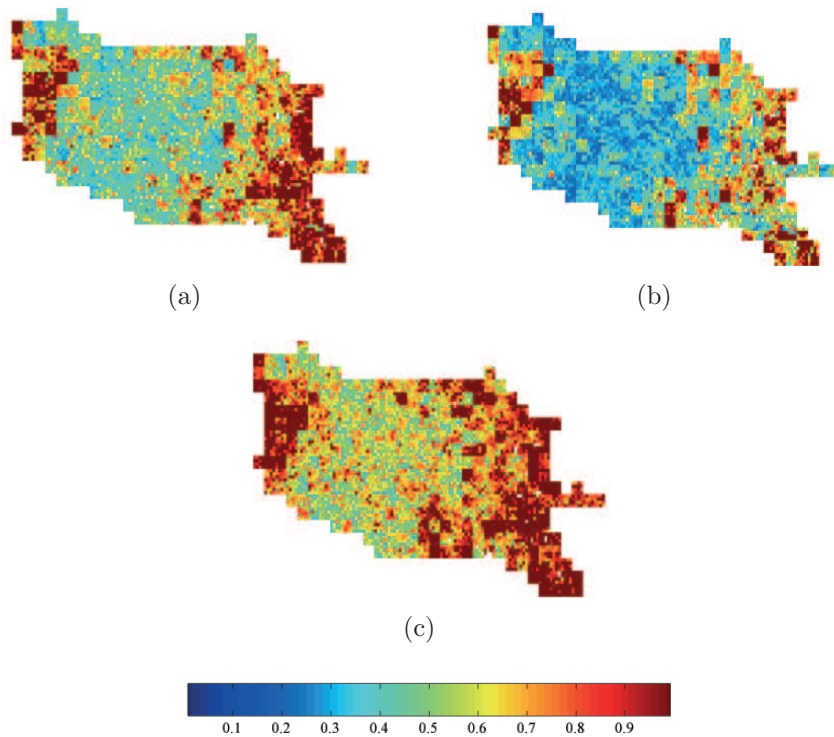


Figure 7.6 Ratio of of change detection RMSE to radiometer only RMSE using σ_{hh}^0 (a), σ_{vv}^0 (b) and σ_{hv}^0 (c).

minimum performance RMSE is shown in Fig. 7.6(a), 7.6(b) and 7.6(c) for hh , vv and hv polarizations, respectively. In all the areas of the image with a value less than unity, the active-passive approach outperforms the radiometer only technique. Notice that most estimation errors (value = 1) occur in high vegetated areas where the radar and radiometer soil moisture sensitivity is decreased. This is evidenced on Fig. 7.7, where the algorithm RMSE linear dependance with vegetation water content is shown.

A box plot of the slope for each day of the 4-month dataset is shown on Fig. 7.8. It can be observed that the uncertainty in the estimation of the slope diminishes with time and that vertical polarization leads to more robust estimates than horizontal and mixed polarizations. Hence, as an alternative to real time processing, the possibility of monthly re-processing the data was explored, resulting in marginal improvement. Further studies with real data would be needed to assess the optimal re-processing time and decide whether the re-processing is required.

7.5 Error budget

An error budget analysis has been performed in order to identify the error sources of the algorithm and fully quantify its performance. The three assumptions made in the algorithm formulation have been identified as the three algorithm error sources. The total error has then been calculated as the square root of the sum of the squares (RSS) of these three distinct errors.

To account for Assumption I errors, the algorithm-predicted soil moisture is calculated using linear regression of SMEX02 radar backscatter and soil moisture data (from (7.1)). The

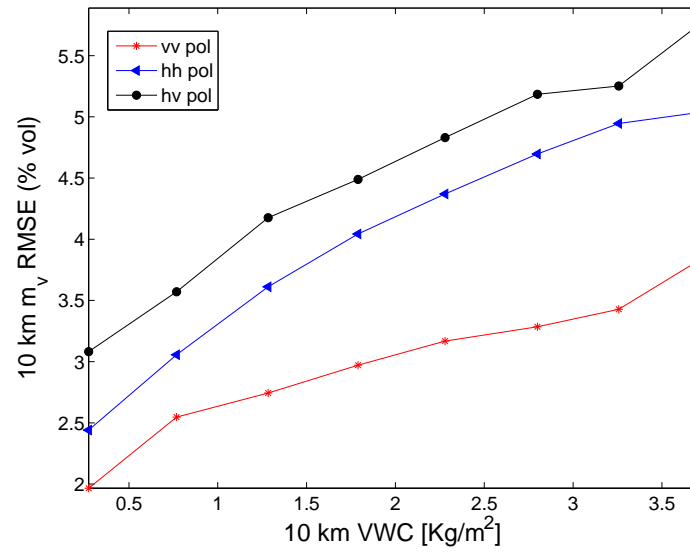


Figure 7.7 Plots of change detection RMSE at 10 km stratified by 0.5 kg/m^2 vegetation water content values

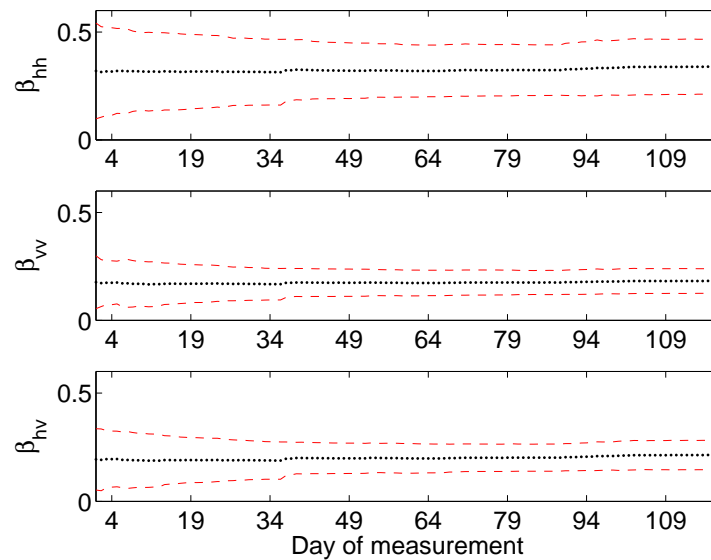


Figure 7.8 Plots of the mean slope (in black) and mean slope \pm the daily slope standard deviation (in red) for vv , hh and hv polarizations, for each day of the 4-month OSSE dataset.

Table 7.1 Results of the error budget analysis (% vol)

Errors	Horizontal polarization	Vertical polarization
Assumption #1	1.53	1.40
Assumption #2	0	0
Assumption #3	2.20	1.76
RSS	2.68	2.25

RMSE between the predicted soil moisture and the ground truth soil moisture for horizontal and vertical polarizations are presented in Table 7.1. It must be noted that field sampling errors are inevitably included in the calculations and they considerably worsen the results. Regarding the errors associated to the Assumption II, the OSSE results in Section 7.4.2 show that the covariance does not affect the retrievals and, therefore, the error contribution from this source has been set to zero. Assumption III-related errors are exactly the values of the standard deviation presented in Fig. 7.3. This figure shows the difference between the soil moisture retrieved using the slope at scale a and the soil moisture retrieved using the slope at a scale A . Note that Table 7.1 represents the algorithm assumptions error and any radiometer error has to be added to the total by RSS.

7.6 Conclusions

This chapter presents a simple and efficient technique to downscale radiometer soil moisture estimates with the use of simultaneous radar observations within a SMAP-like context. The algorithm is based on a change detection scheme that benefits from the synergy of the radar high spatial resolution and the radiometer high accuracy, leading to a balanced product with enough accuracy and spatial resolution so as to satisfy current meteorology and hydrology needs.

The algorithm has been thoroughly formulated and the assumptions made on the process have been verified using PALS data from the SMEX02 field campaign. Also, it has been successfully applied to a 4-month OSSE data producing significantly better results than radiometer only inversions, with a 2% RMSE improvement. Real time processing of the data has been shown to be feasible having a month of previous observations and, since the algorithm performance improves over time, a monthly re-processing of the data to improve the estimations' accuracy has been outlined. An error budget analysis of the algorithm estimates a total RSS of 2.68 (% vol) for horizontal polarization and 2.25 (% vol) for vertical polarization, which meet SMAP science requirements for the 10-km product. These results imply that the change detection method presented on this study is a promising approach to achieving higher resolution and more accurate soil moisture retrievals from future SMAP radar and radiometer observations.

*The important thing is not to stop
questioning*

Albert Einstein (1879-1955)

8

Conclusions and future lines

This Ph.D. Thesis has investigated the ability of measuring the Earth's surface soil moisture from space. Currently, there are two space-borne projects dedicated to soil moisture observation: the ESA SMOS mission, launched in november the 2nd 2009, and the NASA SMAP mission, with a target launch date in 2014. This work has been performed within the preparatory activities of these two missions, involving the analysis of the retrieval techniques, which have an impact on the accuracy of the estimations, and the development of downscaling algorithms to enhance the spatial resolution of the observations.

Chapter 1 describes the motivation of this work and the context in which it has been developed. The basic concepts of passive microwave remote sensing of soil moisture are presented in Chapter 2. The state-of-the-art of the soil moisture retrieval techniques and of soil moisture downscaling algorithms are given in Chapters 1 and 2, respectively. Then, the Thesis is divided into two parts: the first part is focused on studying the SMOS soil moisture inversion algorithm and devising an optimal retrieval configuration, which is crucial for the accuracy of the estimations (Chapters 3 and 4); the second part explores different approaches for the improvement of the spatial resolution of SMOS (Chapters 5 and 6) and SMAP (Chapter 7) observations. This Chapter summarizes the main conclusions of this work, remarks its original contributions, and presents suggestions for follow-on research.

8.1 Main conclusions

The SMOS mission aims at providing the first global views of the Earth's soil moisture fields with an accuracy of $0.04 \text{ m}^3/\text{m}^3$ over $50 \times 50 \text{ km}^2$ and a temporal resolution of 3 days. As a secondary objective, SMOS is expected to provide vegetation water content maps with an accuracy of $0.2 \text{ kg}/\text{m}^2$, from vegetation opacity retrievals. To make full use of SMOS multi-angular dual-polarization/full-polarimetric capabilities and achieve the required accuracy, previous studies have shown the necessity of combining SMOS brightness temperatures with auxiliary information. However, the required auxiliary data and optimal soil moisture retrieval setup need yet to be optimized.

In **Chapter 3**, the performance of different retrieval configurations has been evaluated using SMOS simulated data, considering the option of adding *a priori* information from the parameters dominating the land emission at L-band (i.e. soil moisture s_m , soil roughness h_s , soil temperature T_s , vegetation albedo ω and vegetation opacity τ) with different asso-

ciated uncertainties. Also, the impact of using vertical T_{hh} and horizontal T_{vv} brightness temperatures, or using the first Stokes parameter $T_I = T_{hh} + T_{vv}$ in the minimization process has been analyzed. Results suggest an optimal retrieval configuration for SMOS and can be summarized as follows:

- If a priori information on the land surface conditions are readily available, the use of constraints on h_s , T_s and τ with associated uncertainties $\sigma_{h_s} = 0.05$, $\sigma_{T_s} = 2$ K, and $\sigma_\tau = 0.1$ Np in the SMOS retrieval algorithm is recommended. The constraints on soil roughness and soil temperature significantly improve the accuracy of s_m retrievals over bare soils. In the presence of vegetation, results confirm that there is a remarkable decrease of the brightness temperature sensitivity to s_m ; adding information on τ (and on ω with $\sigma_\omega = 0.1$ in the case of dense vegetation) is critical to obtain accurate s_m and VWC maps.
- Soil moisture and vegetation opacity retrievals using T_I show better performance than retrievals using $T_{hh} - T_{vv}$. Also, retrievals using T_I are more robust to geometric and Faraday rotations than $T_{hh} - T_{vv}$, which can be critical from an operational point of view. Since T_I in the dual-polarization mode has a better radiometric sensitivity than in full-polarimetric mode, results also preference the use of the dual-polarization mode. Hence, although the formulation of the SMOS-derived soil moisture retrieval problem using $T_{hh} - T_{vv}$ (and therefore the use of the full-polarimetric mode) is the preferred one, these results suggest that use of the first Stokes parameter should not be discarded.

In **Chapter 4**, the SMOS soil moisture inversion algorithm has been further analyzed, both theoretically and in terms of performance with SMOS-like simulated observations. The use of adequate constraints on the cost function (from the study in Chapter 3), has been compared with the use of no constraints, and with the use of $T_{hh} - T_{vv}$, over six main surface conditions combining dry, moist and wet soils with bare and vegetation-covered soils. Simulated results are consistent with the theoretical study, and are listed below:

- The sensitivity analysis shows that the cost function sensitivity to the soil and vegetation parameters dominating the Earth's emission at L-band (s_m , h_s , T_s , ω , τ) is greatly improved with the use of adequate auxiliary information in the retrieval (from Chapter 3). Results with simulated SMOS data show that the use of these constraints significantly improves the accuracy of s_m and τ retrievals in all scenarios, and are needed to meet SMOS science requirements over land.
- The cost function formulated using T_I has a higher sensitivity to both soil and vegetation parameters. Better s_m and τ estimates are obtained if the retrieval is formulated using T_I , than if it is formulated using $T_{hh} - T_{vv}$ –considering both the case of using or not a priori information in the retrievals. Therefore, results reinforce the idea that the use of T_I should not be discarded.
- The cost function sensitivity to soil roughness is higher on wet soils than on dry soils, with or without vegetation. Results with simulated SMOS data indicate that more accurate s_m and τ estimates should be expected from wet soils than from dry soils.
- Due to SMOS geometry, better accuracies could be obtained if only the central part of the FOV is used. In this case, also the use of adequate constraints (from Chapter 3) and the formulation in terms of T_I provide the most accurate retrievals.

Following the successful deployment of SMOS in orbit, continuous efforts will be needed to consolidate an optimal soil moisture retrieval configuration. Chapters 3 and 4 of this Thesis have analyzed the soil moisture inversion algorithm, both theoretically and in terms of performance with simulated data; they have addressed key aspects for the retrieval of accurate soil moisture estimations from SMOS, and the results presented can be readily transferred to the operational Level 2 Processor to produce the much needed global maps of the Earth's surface soil moisture.

SMOS and SMAP radiometers have been designed to potentially provide accurate global views of the Earth's surface soil moisture every 3 days, but, due to technological limitations, their spatial resolution is limited to 40-50 km. Still, the retrieval of soil moisture at a higher resolution (1-10 km) from SMOS and SMAP observations is a highly relevant research area, since it could greatly extend the applicability of the data to regional scales.

A deconvolution scheme to improve the spatial resolution of SMOS radiometric observations has been presented in **Chapter 5**. Different deconvolution techniques using improved Wiener, Constrained Least Squares, and wavelet filters that may include different levels of auxiliary information in the reconstruction process have been developed. When applied to SMOS simulated observations, and using an L-band brightness temperature model of the observed scene as auxiliary information, the product spatial resolution and radiometric sensitivity of SMOS-like images was improved in a 49% over land pixels and in a 30% over sea pixels. Particularly, the spatial resolution of the pixels located on the upper left area of the FOV was improved from 90 to 50 km, while its radiometric resolution remained constant. Also, a trend to round the pixels' shape and diminish its size has been observed, with higher effects in the pixels located far from nadir. Hence, the deconvolution scheme proposed could potentially normalize the pixels shape and orientation in all the SMOS FOVs as well as improve the radiometric sensitivity and the spatial resolution of SMOS observations. Furthermore, results from its application to airborne field experimental data indicate that these methods could be applied to coastal areas to improve the radiometric sensitivity and the coast line definition of the observations.

Chapter 6 presents a downscaling strategy for the estimation of soil moisture at high resolution from SMOS using MODIS visible/infrared data. MODIS-derived T_s and NDVI at high spatial resolution are first aggregated to the SMOS scale for the purpose of building a linking model that is afterwards applied at fine scale to disaggregate the passive soil moisture observations into high-resolution soil moisture. The linking model is based on the so-called universal triangle concept that relates visible/infrared parameters to soil moisture status, and has been specially adapted for the SMOS case. Results of its application to the first SMOS images acquired during the commissioning phase indicate that it is feasible to capture soil moisture variability at a higher resolution and provide a first evidence of its capabilities. They also suggest that SMOS data from ascending orbits are more adequate for land applications than descending ones. Results from comparison with ground-based soil moisture measurements show that the retrieval of accurate soil moisture at low resolution from SMOS is critically affecting the algorithm performance. Further studies are needed to develop an algorithm error budget and establish a downscaling limit, which could be given either by the resolution of the optical sensor (which in the case of MODIS is 1 km), or by the presence of noise affecting the accuracy of the estimations.

Chapter 7 presents a simple and efficient technique to downscale radiometer soil moisture estimates with the use of simultaneous radar observations within a SMAP-like context. It is based on change detection and effectively combines the radiometer high accuracy with the radar high resolution into an optimal balanced product at 10 km. The algorithm has

been thoroughly formulated and the assumptions made on the process have been verified using airborne field experimental data. Also, it has been successfully applied to a 4-month SMAP simulated data producing significantly better results than radiometer only inversions, with a 2% RMSE improvement. Real time processing of the data has been shown to be feasible having a month of previous observations and, since the algorithm performance improves over time, a monthly re-processing of the data to improve the estimations' accuracy has been outlined. The algorithm error budget shows that the proposed algorithm meets the SMAP minimum science requirements for the 10 km product. Therefore, results imply that the change detection method presented on this study is a promising approach to achieving higher resolution and more accurate soil moisture retrievals from future SMAP radar and radiometer observations.

8.2 Original contributions

The original contributions of this Thesis are listed below:

- Proposal of an optimal retrieval configuration for SMOS, in terms of the auxiliary data that is used in the retrievals, its associated uncertainty, and the formulation using vertical and horizontal polarizations or the first Stokes parameter.
- A sensitivity analysis of the SMOS soil moisture retrieval algorithm, illustrating the influence that the geophysical variables dominating the Earth's emission at L-band have on the precision of the retrievals over six main surface conditions combining dry/moist/wet conditions with bare/vegetation-covered surfaces, for different retrieval configurations including: (i) the use of adequate constraints, (ii) the use of no constraints, (iii) the formulation in terms of vertical and horizontal polarization, and (iv) the formulation in terms of the first Stokes parameter.
- Development of a deconvolution scheme for the improvement of the spatial resolution of SMOS brightness temperatures.
- Proposal of a downscaling algorithm for SMOS using higher resolution MODIS T_s and NDVI data. Retrieval of soil moisture maps from the first SMOS observations acquired during the commissioning phase at 60 and 30 km. The possibility of downscaling to higher spatial resolutions is subject of further research that validates the accuracy of the retrievals at the different spatial scales.
- Development of a change detection algorithm that can be potentially used to combine SMAP radar and radiometer data into a 10 km soil moisture product.

8.3 Future lines

The future research lines opened by the work presented on this Thesis are:

- The application of the deconvolution algorithm to SMOS images so as to fully evaluate its possibilities in inland and coastal retrievals.

- In-depth study of the downscaling algorithm on Chapter 6 and potential improvements (e.g. more accurate soil moisture retrieval at low resolution, the use of SMOS observations at different incidence angles and two polarizations); an error budget of the algorithm should be calculated to establish a downscaling limit and evaluate the performance of the soil moisture retrievals at higher resolutions in terms of spatial resolution and radiometric accuracy.
- The prospect use of a visible/infrared sensor in follow-on space-borne missions dedicated to soil moisture monitoring. It could serve both for estimation of collocated land surface temperatures to be used in the soil moisture retrievals, and for the improvement of the spatial resolution of the estimates using the universal triangle concept.
- The possible use of the change detection algorithm on Chapter 7 in the context of the SMOS mission, using satellite infrared land surface temperatures instead of radar observations.
- Study of a potential improvement of the algorithm on Chapter 7, assuming that the radiometer brightness temperatures (instead of the radiometer-derived soil moisture) and the log of radar backscatter are linearly related at a 10 km scale.



Acronyms

AACES	Australian Airborne Calibration/Validation Experiments for SMOS
AIRSAR	AIRborne Synthetic Aperture Radar
AMSR-E	Advanced Microwave Scanning Radiometer for EOS
ARIEL	Airborne RadIomEter at L-band
ASTER	Advanced Spaceborne Thermal Emission and Reflection Radiometer
ATBD	Algorithm Theoretical Bases Document
AVHRR	Advanced Very High Resolution Radiometer
CF	Cost Function
CLS	Constrained Least Squares
DEM	Digital Elevation Model
ECMWF	European Center for Medium-range Weather Forecasts
ForWaRD	Fourier Wavelet Regularized Deconvolution
FOV	Field Of View
GPS	Global Positioning System
GRAJO	GPS and RAdiometric Joint Observations
JERS	Japanese Earth Resources Satellite
ESA	European Space Agency
ISEA	Icosahedral Snyder Equal Area
LAI	Leaf Area Index
MIRAS	Microwave Imaging Radiometer by Aperture Synthesis

Appendix A. Acronyms

MIS	Microwave Imager Sounder
MODIS	MODerate resolution Imaging Spectroradiometer
MTS	MIRAS Testing Software
NASA	National Aeronautics and Space Administration
NDVI	Normalized Difference Vegetation Index
NPOESS	National Polar-Orbiting Operational Environmental Satellite System
OSSE	Observation System Simulation Experiment
PALS	Passive and Active L- and S-band airborne sensor
PALSAR	Phased Array Type L-band Synthetic Aperture Radar
REMEDHUS	Soil Moisture Measurement Network of the University of Salamanca
RFI	Radio Frequency Interferences
RMSE	Root Mean Square Error
RSS	square Root of the Sum of the Squares
SAR	Synthetic Aperture Radar
SEPS	SMOS End-to-end Performance Simulator
SMAP	Soil Moisture Active Passive
SMOS	Soil Moisture and Ocean Salinity
SSM/I	Special Sensor Microwave/Imager
TEC	Total Electron Content
TMI	TRMM Microwave Imager
TRMM	Tropical Rainfall Measuring Mission
UAV	Unmanned Aerial Vehicle
UTC	Coordinated Universal Time
VIIRS	Visible Infrared Imager Radiometer Suite
VWC	Vegetation Water Content
WindSat	Wind Satellite

B

Symbols

Latin symbols

a	Spatial scale of 10 km
a_{ij}, a_{ijk}	Regression coefficients
A	Spatial scale of 40 km
A_r	Antenna effective area [m ²]
A_t	Total radiating area [m ²]
b	Empirical parameter used for the estimation of vegetation optical depth
$B(\theta, \phi)$	Brightness or radiance [Wsr ⁻¹ m ⁻²]
B_{av}	Average Earth's magnetic field along the propagation path [Wb/m ²]
B_{bb}	Total brightness of a blackbody [Wsr ⁻¹ m ⁻²]
$B_f(\theta, \phi)$	Spectral brightness: brightness per unit bandwidth [Wsr ⁻¹ m ⁻² Hz]
$B_i(\theta, \phi)$	Total brightness incident over an antenna [Wsr ⁻¹ m ⁻²]
B_w	Noise-equivalent bandwidth [Hz]
c	Speed of light $c = 3 \cdot 10^8$ [m/s]
C	Smoothing criterion function
C_p	Diagonal matrix containing the variances of the prior estimates of parameters p_i
C_F	Covariance matrix of the observations
d	Antenna spacing
e	Tolerance error
$e(\theta, \phi)$	Emissivity
E_h	Electric field of an electromagnetic wave at horizontal polarization
E_v	Electric field of an electromagnetic wave at vertical polarization
f	Column vector containing the unknown T_B at high resolution
f	Frequency [Hz]

Appendix B. Symbols

F	Fourier transform of f
\overline{F}^{meas}	Vector containing the SMOS measured brightness temperatures at different incidence angles
\overline{F}^{model}	Vector containing the SMOS simulated brightness temperatures at different incidence angles
t	Normalized antenna radiation pattern
$F_n(\theta, \phi)$	
F_r	Fractional vegetation cover
$F_t(\theta, \phi)$	Antenna radiation pattern
g	Column vector containing the radiometer observations
G	Fourier transform of g
h	Column vector representation of the synthetic antenna response function
h	Planck's constant $h = 6.63 \cdot 10^{-34}$ [J·s]
h_s	Effective roughness parameter
H	Matrix constructed from circular shifting of h to express the convolution operation as a product in the time domain
H	Fourier transform of h
I	First Stokes parameter
k	wavenumber [rad/m]
k_B	Boltzmann's constant $k_B = 1.38 \cdot 10^{23}$ [J/K]
K	Generic filter
K_p	Normalized deviation of radar backscatters
L_a	Atmospheric attenuation
m_g	Gravimetric soil moisture
m_v	Volumetric soil moisture
n	Column vector representing the noise added to the radiometer measurements
n	Exponential of the cosine dependence of soil emissivity with the incidence angle
N	Fourier transform of n
$NDVI_{max}$	Maximum NDVI value for a particular scene
$NDVI_{min}$	Minimum NDVI value for a particular scene
N_T	Ionospheric total electron content [electrons/m ²]
p_i	Retrieved physical parameters that may influence the modeled T_B
p_{i0}	Prior estimates of parameters p_i
P	Power collected by an antenna [W]
P_{bb}	Power collected by an antenna surrounded by a blackbody [W]
Q	Linear operator

Q	Second Stokes parameter
Q_s	Cross-polarization factor
R_f	Correlation matrix of f
R_n	Correlation matrix of n
s_m	Soil moisture
S_f	Fourier transform of R_f
S_n	Fourier transform of R_n
t	Time
t_R	Revisit time of the observations
T	Physical temperature [K]
Tb	Simulated brightness temperature image of the scene observed by the radiometer
T_{hh}	Brightness temperature at horizontal polarization, Earth reference frame [K]
T_{lc}	Left-hand circular polarized brightness temperature [K]
T_{max}	Maximum T_s value for a particular scene [K]
T_{min}	Minimum T_s value for a particular scene [K]
T_s	Soil effective temperature [K]
T_v	Vegetation effective temperature [K]
T_{vv}	Brightness temperature at vertical polarization, Earth reference frame [K]
T_{xx}	Brightness temperature at x-axis, antenna reference frame [K]
T_{xy}	Cross-polarized brightness temperature, antenna reference frame [K]
T_{yy}	Brightness temperature at y-axis, antenna reference frame [K]
T_A	Antenna temperature [K]
T_{AP}	Apparent brightness temperature [K]
T_B	Fourier transform of Tb
T_B	Brightness temperature [K]
T_{Bmax}	Maximum T_B values for a particular scene [K]
T_{Bmin}	Minimum T_B value for a particular scene [K]
T_I	First Stokes parameter in brightness temperature [K]
T_Q	Second Stokes parameter in brightness temperature [K]
T_N	Normalized soil effective temperature
T_{SC}	Downward atmospheric radiation scattered by the Earth's surface [K]
T_U	Third Stokes parameter in brightness temperature [K]
T_{UP}	Atmospheric upward radiation [K]
T_V	Fourth Stokes parameter in brightness temperature [K]
T_{45}	Brightness temperature skewed 45° with respect to normal [K]

Appendix B. Symbols

T_{-45}	Brightness temperature skewed -45° with respect to normal [K]
U	Third Stokes parameter
V	Fourth Stokes parameter
V_w	Volume of water in a soil sample [m ³]
V_T	Total volume of a soil sample [m ³]
w_d	Dry weight of a soil sample [g]
w_w	Wet weight of a soil sample [g]

Greek symbols

α	Filter parameter $\alpha \equiv 1/\lambda_1$
$\beta(a)$	Slope of the linear relationship between soil moisture and the log of radar backscatter at a scale
$\langle\beta(a)\rangle$	Spatial average of the $\beta(a)$ pixels contained into the A scale pixels
γ	Transmissivity of the vegetation layer
γ_D	Soil penetration depth [m]
$\Gamma_{o,p}$	Fresnel's soil reflectivity at p -polarisation (flat surface)
$\Gamma_{s,p}$	Soil reflectivity at p -polarization
Δf	Bandwidth [Hz]
ϵ_s	Complex dielectric constant of soils $\epsilon_s = \epsilon'_s + j\epsilon''_s$
ϵ'_s	Effective permittivity (real part of ϵ_s)
η	Directing cosine with respect to y axis $\eta = \sin\theta \sin\phi$
η_o	Electromagnetic wave impedance of the medium (120π in vacuum) [Ω]
θ	Incidence angle referred to nadir [$^\circ$]
$\theta(a, t)$	Soil moisture at a scale at time t
λ	wavelength $\lambda = c/f$ [m]
λ_1, λ_2	Lagrange multipliers
ξ	Directing cosine with respect to x axis $\xi = \sin\theta \cos\phi$
ρ	Filter parameter $\rho \equiv \lambda_2/\lambda_1$
ρ_b	Soil bulk density [g/cm ³]
ρ_{NIR}	At-surface reflectance of LANDSAT band 4 (Near-infrared, 0.76 - 0.90 m)
ρ_R	At-surface reflectance of LANDSAT band 3 (Visible, 10.40 - 12.50 m)
σ_s	Standard deviation of the surface height [m]
$\sigma_{p_{i0}}$	Uncertainty on p_{i0}
$\sigma_{p_{i0}}^2$	Variance of p_{i0}
σ_{F_n}	Radiometric accuracy for the n^{th} observation
$\sigma^0(a, t)$	Radar backscatter aggregated to a scale at time t
τ	Vegetation opacity or vegetation optical depth [Np]

ϕ	Azimuth angle referred to nadir [$^{\circ}$]
ϕ_0	Filter parameter $\phi_0 \equiv \alpha \left[\frac{S_n(u,v)}{S_f(u,v)} \right]$
φ	Faraday rotation angle [rad]
ω	Vegetation albedo
Ω	Solid angle [sr]
Ω_p	Antenna solid angle

List of Figures

1.1	Precipitation, evaporation, evapotranspiration and runoff are the processes that move water through the water cycle. Values in the diagram show the volume of water that moves along each path in a year (www.unep.org)	3
1.2	Soil moisture initialization of Numerical Weather Prediction models leading to an improved precipitation forecasts (adapted from Chen et al. [2001])	4
1.3	First uncalibrated data sent to Earth by the MIRAS instrument on ESA's SMOS satellite (from www.esa.int , 20 November 2009)	7
1.4	SMOS-MIRAS undergoing testing in the Large Space Simulator at ESA-ESTEC (a), and SMOS-MIRAS artist's view (b), from www.esa.int	8
1.5	SMOS observation geometry, from Camps et al. [2005]	8
1.6	MIRAS brightness temperature imaging process, from www.esa.int (a), and SMOS simulated field-of-view in the Earth reference frame, from Piles et al. [2009] (b)	9
1.7	SMAP measurement geometry (from smap.jpl.nasa.gov)	11
2.1	Geometry of the incident radiation from an extended source on an antenna, from Ulaby et al. [1981]	16
2.2	Comparison of Planck radiation law with its low-frequency approximation (Rayleigh-Jeans law) for $T=300$ K and $T=6000$ K.	17
2.3	Radiation incident upon an Earth-looking radiometer. Relationships between the antenna temperature T_A , apparent temperature T_{AP} , and brightness temperature T_B , from Ulaby et al. [1981]	19
2.4	Typical values of Faraday rotation angle as a function of TEC and frequency, from ITU-R P.531-6 [2001]	20
2.5	Measured dielectric constant at 1.4 GHz for five soils with different textural composition, from Hallikainen et al. [1985]	24
2.6	Measured normalized antenna temperature (emissivity) <i>vs.</i> incidence angle at 1.4 GHz for three bare soil field with different surface roughnesses, from Newton and Rouse [1980]	26
2.7	Graphical plots illustrating the brightness temperature dependence with incidence angle of (a) bare, and (b) vegetation-covered dry, moist and wet soils, from (2.32) (from Piles et al. [2010]).	28
3.1	Graphical plots of soil moisture and vegetation optical depth retrievals formulated using vertical and horizontal polarizations	36
3.2	Graphical plots of soil moisture and vegetation optical depth retrievals formulated using the first Stokes parameter	37
4.1	Contour plots of cost functions formulated using the first Stokes parameter over a bare dry soil scenario	45
4.2	Contour plots of cost functions formulated using the first Stokes parameter over a vegetation-covered dry soil scenario	46

List of Figures

4.3	Contour plots of cost functions formulated using vertical and horizontal polarizations and no constraints over bare soil scenarios	47
4.4	Contour plots of cost functions formulated using vertical and horizontal polarizations and no constraints over vegetation-covered scenarios	48
4.5	Retrieved soil moisture RMSE of simulated SMOS observations versus pixel position in the swath	52
4.6	Retrieved vegetation optical depth RMSE of simulated SMOS observations versus pixel position in the swath	53
5.1	SMOS observations with varying incidence angles, pixel spatial resolutions, and axial ratios (a). Reconstructed synthetic image with point sources over the area under study processed by SEPS (b)	58
5.2	Pixel's contours at -3dB after applying the deconvolution filters to point sources	63
5.3	Sample results of applying Wiener-derived filters to a set of synthetic images with vertical and horizontal bars	65
5.4	Sample results of applying Wiener-derived filters to a set of synthetic images with vertical and horizontal bars	66
5.5	Results of the application of Wiener-derived filters to a synthetic step image	67
5.6	Results of the application of Wiener-derived filters to an SMOS simulated image of Catalonia and the Balearic Islands, in the northeast of Spain	69
5.7	The aircraft with the ARIEL radiometer after a test flight (a). Retrieved antenna temperature histogram (b).	71
5.8	ARIEL Retrieved T_B [K] geo-referenced on Google Earth obtained at heights (a) between 40 and 170 m, and (b) between 170 and 300 m.	72
5.9	Digital Elevation Model [m] of the Marquesa beach area at 5 m spatial resolution, geo-referenced on Google Earth.	72
5.10	Cross-sections of the images obtained from ARIEL observations, and of the images resulting from the application of Wiener and CLS-derived filters to ARIEL observations	73
6.1	ARIEL Retrieved T_B [K] obtained at heights 140 ± 30 m (spatial resolution ~ 50 m), re-sampled to a 60 x 60 m grid and geo-referenced on Google Earth.	78
6.2	Scatter plots of LANDSAT surface radiant temperature versus LANDSAT NDVI of the areas corresponding to (a) Flight 1, and (b) Flight 2.	79
6.3	Linear regression between ARIEL T_B and coincident ground measurements of 0-5 cm soil moisture acquired during (a) Flight 1, and (b) Flight 2.	81
6.4	Sample results for the visual comparison of soil moisture fields [m^3/m^3]. From left to right: interpolated ground-based soil moisture, soil moisture retrieved from ARIEL T_B , and downscaled soil moisture obtained with the algorithm presented. Upper row: Flight 1; Lower row: Flight 2.	82
6.5	Spatial distribution of the soil moisture error [m^3/m^3] retrieved using ARIEL T_B on (a) Flight 1 and (c) Flight 2, and obtained with the downscaling algorithm on (b) Flight 1 and (d) Flight 2 observations	82
6.6	Sample results of the application of the algorithm to a SMOS image over western Australia, from December, 8, 2009 (6 am).	87
6.7	Aerial photographs covering the regions above (a) and below (b) the cloud mask in Fig. 6.6(b), from Google Earth.	88
6.8	Sample results of the application of the algorithm to a SMOS image over eastern Australia, from February, 17, 2010 (6 am).	89

6.9	Scatter plots of MODIS surface radiant temperature versus MODIS NDVI, from Fig. 6.6 (a), and Fig. 6.8 (b).	90
6.10	Sample results of the application of the algorithm to a SMOS image over central Australia, from December, 8, 2009 (6 pm).	91
6.11	Sample results of the application of the algorithm to a SMOS image over south-eastern Australia, from February, 17, 2010 (6 pm).	92
6.12	Spatial variability of 0-5 cm soil moisture measurements (6 am) of the 13 Yanco stations on days (a) January 20-24, 2010, and on (b) February 17-21, 2010.	93
6.13	Temporal evolution of 0-5 cm continuous soil moisture measurements (6 am) and mean daily rainfall observed at 13 Yanco monitoring stations.	94
6.14	Sample results of the application of the algorithm to a SMOS image covering the Murrumbidgee catchment, from January, 22, 2010 (6 am).	95
6.15	Sample results of the application of the algorithm to a SMOS image covering the Murrumbidgee catchment, from February, 19, 2010 (6 am).	96
6.16	SMOS-derived soil moisture maps and error statistics at 32, 16 and 8 km spatial resolution over western Australia, from December, 8, 2009 (6 am).	99
7.1	Change in log of PALS L-band radar backscatter <i>vs.</i> change in <i>in situ</i> soil moisture	106
7.2	Error difference between static map of β of 400 m aggregated to 1600 m and directly computed static map of β at 400 m spatial resolution using radar <i>hh</i> (a) and <i>vv</i> (b) polarizations.	106
7.3	Soil moisture error due to the third assumption of the algorithm	107
7.4	Sample results of applying the change detection algorithm to SMAP simulated data	108
7.5	Spatial distribution of the soil moisture error retrieved using the change detection method and the radiometer only technique	109
7.6	Ratio of change detection RMSE to radiometer only RMSE	110
7.7	Change detection RMSE <i>vs.</i> Vegetation Water Content	111
7.8	Plots of the mean slope (in black) and mean slope \pm the daily slope standard deviation (in red) for <i>vv</i> , <i>hh</i> and <i>hv</i> polarizations, for each day of the 4-month OSSE dataset.	111

List of Tables

1.1	Main scientific requirements of the SMOS mission	7
3.1	Selected values of soil moisture (s_m), soil roughness parameter (h_s), soil temperature (T_s), vegetation optical depth (τ) and vegetation albedo (ω) for the four master scenarios	34
4.1	Selected original values of soil moisture (s_m), soil roughness (h_s), soil temperature (T_s), vegetation albedo (ω) and vegetation optical depth (τ) for the six master scenarios. $\sigma_{p_i}^0$ is the nominal uncertainty of parameter p_i	43
4.2	Selected standard deviations of soil moisture (s_m), soil roughness (h_s), soil temperature (T_s), vegetation albedo (ω) and vegetation optical depth (τ) for the two selected cost function configurations CF_1 and CF_2	44
4.3	Retrieved mean, standard deviation and root mean square soil moisture error of simulated SMOS observations over the bare soil scenarios in Table 4.1, using the cost-function configurations of Table 4.2, formulated on the Earth's reference frame or using the first Stokes parameter. Soil moisture retrieval configurations with s_m RMSE ≤ 0.04 m ³ /m ³ are marked in bold.	50
4.4	Retrieved mean, standard deviation and root mean square soil moisture error of simulated SMOS observations over the vegetation-covered scenarios in Table 4.1, using the cost function configurations of Table 4.2, formulated on the Earth's reference frame or using the first Stokes parameter.	50
4.5	Retrieved mean, standard deviation and root mean square vegetation optical depth error of simulated SMOS observations over the vegetation-covered scenarios in Table 4.1, using the cost function configurations of Table 4.2, formulated on the Earth reference frame or using the first Stokes parameter.	51
5.1	Results of the simulations over the area under study in terms of radiometric sensitivity (ΔT) and spatial resolution (ΔS)(worst case)	68
5.2	RMSE between the different T_B images and the highest spatial resolution T_B image at 40-170 m height, over land and sea pixels	73
6.1	SMOS-derived soil moisture retrievals over the Yanco region.	97
6.2	Mean, standard deviation, and root mean square soil moisture error between soil moisture retrievals at 32 km, 16 km, and 8 km, and soil moisture retrievals at 64 km.	100
7.1	Results of the error budget analysis	112

References

- Acevo-Herrera, R., A. Aguasca, X. Bosch-Lluis, and A. Camps (2009), On the use of compact L-band dicke radiometer (ARIEL) and UAV for soil moisture and salinity map retrieval: 2008/2009 field experiments, in *Proc. IEEE Geoscience and Remote Sensing Symposium*. 5.4.1, 6.2.1
- Acevo-Herrera, R., A. Aguasca, X. Bosch-Lluis, A. Camps, J. Martínez-Fernández, N. Sánchez-Martín, and C. Pérez-Gutiérrez (2010), Design and First Results of an UAV-borne L-Band Radiometer for Multiple Monitoring Purposes, *Remote Sensing*, *submitted*. 5.4.1, 6.2.1
- Adegoke, J., and A. Carleton (2002), Relations between soil moisture and satellite vegetation indices in the u.s. corn belt, *American Meteorological Society*, *3*, 395–405. 1.3, 6.1
- Andrews, H., and B. Hunt (1977), *Digital Image Restoration*, Prentice-Hall. 5.2.1, 5.2.1
- Bará, J., A. Camps, F. Torres, and I. Corbella (1998), Angular resolution of two-dimensional, hexagonally sampled interferometric radiometers, *Radio Science*, *33*, 1459–1473. 5.2.1
- Baret, F., J. Clevers, and M. Stevens (1995), The robustness of canopy gap fraction estimations from red and near-infrared reflectances: a comparison of approaches, *Remote Sensing of Environment*, *54*, 141–151. 6.3.2
- Barré, H., B. Duesmann, and Y. Kerr (2008), SMOS: the mission and the system, *IEEE Transactions on Geoscience and Remote Sensing*, *46*(3), 587–593. 1.3.1, 4.4.2
- Behari, J. (2005), *Microwave Dielectric Behavior of Wet Solids*, Springer. 2.2, 2.2.3
- Brown, S., C. Ruf, and D. Lyzenga (2006), An emissivity-based wind vector retrieval algorithm for the WindSat polarimetric radiometer, *IEEE Transactions on Geoscience and Remote Sensing*, *44*, 611–621. 2.1.6
- Burgees, T., and R. Webster (1980), Optimal interpolation and isarithmic mapping of soil properties. i. the semi-variogram and punctual kriging, *Journal of Soil Science*, *31*, 315–331. 6.2.1
- Burke, E., W. Shuttleworth, and N. French (2001), Using vegetation indices for soil-moisture retrievals from passive microwave radiometry, *Hydrology and Earth System Sciences*, *5*, 671–677. 2.2.5, 6.3.2, 6.3.3
- Calvet, J., J. Noilhan, and P. Bessemoulin (1998), Retrieving the root-zone soil moisture from surface soil moisture or temperature estimates: a feasibility study based on field measurements, *Journal of Applied Meteorology*, *37*, 371–386. 1.2
- Camps, A. (1996), Application of interferometric radiometry to Earth observation, Ph.D. thesis, Universitat Politècnica de Catalunya, <http://www.tdx.cesca.es/TDX-1020104-091741/>. 5.2.2

References

- Camps, A., J. Bará, I. Corbella, and F. Torres (1997), The processing of hexagonally sampled signals with standard rectangular techniques: application to 2D large aperture synthesis interferometric radiometers, *IEEE Transactions on Geoscience and Remote Sensing*, *35*, 183–190. 1.3.1
- Camps, A., I. Corbella, J. Bará, and F. Torres (1998), Radiometric sensitivity computation in aperture synthesis interferometric radiometry, *IEEE Transactions on Geoscience and Remote Sensing*, *36*, 680–685. 5.2.2, 5.3.3
- Camps, A., I. Corbella, M. Vall-llossera, et al. (2003), The SMOS End-to-end Performance Simulator: description and scientific applications, *Proc. IEEE IGARSS*, *1*, 13–15. 1.3.1
- Camps, A., M. Vall-llossera, N. Duffo, F. Torres, and I. Corbella (2005), Performance of sea surface salinity and soil moisture retrieval algorithms with different auxiliary datasets in 2-D L-band aperture synthesis interferometric radiometers, *IEEE Transactions on Geoscience and Remote Sensing*, *43*, 1189–1200. 1.5, 2.3, 2.3, 3.1, 3.2, 4.1, 4.4.2, B
- Camps, A., M. Vall-llossera, I. Corbella, N. Duffo, and F. Torres (2008), Improved image reconstruction algorithms for aperture synthesis radiometers, *IEEE Transactions on Geoscience and Remote Sensing*, *46*, 146–158. 1.3.1, 5.2.2
- Cardot, H., P. Maisongrande, and R. Faivre (2005), Varying-time random effects models for longitudinal data: spatial disaggregation and temporal interpolation of remote sensing data, *Journal of Applied Statistics*, *30*, 1185–1999. 1.4
- Carlson, T. (2007), An overview of the “triangle method” for estimating surface evapotranspiration and soil moisture from satellite imagery, *Sensors*, *7*, 1612–1629. 1.4, 6.1, 6.2.2, 6.3.3, 6.3.3
- Carlson, T., and D. Ripley (1997), On the relation between NDVI, fractional vegetation cover, and leaf area index, *Remote Sensing of Environment*, *62*, 241–252. 6.3.2
- Carlson, T., R. Gillies, and E. Perry (1994), A method to make use of thermal infrared temperature and NDVI measurements to infer surface soil water content and fractional vegetation cover, *Remote Sensing Reviews*, *9*, 161–173. 6.1, 6.2.3, 6.3.2
- Chander, G., and B. Markham (2003), Revised Landsat-5 TM radiometric calibration procedures and postcalibration dynamic ranges, *IEEE Transactions on Geoscience and Remote Sensing*, *41*, 2674–2678. 6.2.1
- Chauhan, N., S. Miller, and P. Ardanuy (2003), Spaceborne soil moisture estimation at high resolution: a microwave-optical/IR synergistic approach, *International Journal of Remote Sensing*, *22*, 4599–4622. 1.4, 6.1
- Chen, F., T. Warner, and K. Manning (2001), Sensitivity of orographic moist convection to landscape variability: a study of the Buffalo Creek, Colorado, flash flood case of 1996, *Journal of Atmospheric Science*, *58*, 3204–3223. 1.2, B
- Chi, C., D. Long, and F. Li (1986), Radar backscatter measurement accuracies using digital doppler processors in spaceborne scatterometers, *IEEE Transactions on Geoscience and Remote Sensing*, *GE-24*, 426–438. 7.4.1

- Choudhury, B., T. Schmugge, A. Chang, and R. Newton (1979), Effect of surface roughness on the microwave emission from soils, *Journal of Geophysical Research*, *84*, 5699–5706. 2.2.4
- Chukhlantsev, A. A. (2006), *Microwave radiometry of vegetation canopies*, Springer. 2.2.3
- Corbella, I., F. Torres, N. Duffo, V. González, A. Camps, and M. Vall-llossera (2008), Fast processing tool for SMOS data, in *Proc. IEEE Geoscience and Remote Sensing Symposium*. 6.3.1
- Cracknell, A., and Y. Xue (1996), Thermal inertia determination from space - a tutorial review, *International Journal of Remote Sensing*, *17*, 431–461. 6.1
- Crow, W., E. Wood, and R. Dubayah (2000), Potential for downscaling soil moisture maps derived from spaceborne imaging radar data, *Journal of Geophysical Research*, *105*, 2203–2212. 1.4
- Crow, W., R. Bindlish, and T. Jackson (2005a), The added value of spaceborne passive microwave soil moisture retrievals for forecasting rainfall-runoff ratio partitioning, *Geophysical Research Letters*, *32*, L18,401. 1.1, 1.2
- Crow, W., et al. (2005b), An Observing System Simulation Experiment for Hydros radiometer-only soil moisture products, *IEEE Transactions on Geoscience and Remote Sensing*, *43*, 1289–1303. 7.4.1
- Davenport, I., J. Fernandez-Galvez, and R. Gurney (2005), A sensitivity analysis of soil moisture retrieval from the tau-omega microwave emission model, *IEEE Transactions on Geoscience and Remote Sensing*, *43*, 1304–1316. 3.2, 3.3, 3.4, 4.3, 4.4.2
- de Jeu, R., W. Wagner, T. Holmes, H. Dolman, N. van de Giesen, and J. Friesen (2008), Global soil moisture patterns observed by space borne microwave radiometers and scatterometers, *Surveys in Geophysics*, *29*, 399–420. 2.2.3, 4.4.2
- Delta-T Devices Ltd. (2007), Thetaprobe soil moisture sensors specifications, <http://www.delta-t.co.uk/products.html>. 3.3
- Demoment, G. (1989), Image reconstruction and restoration: Overview of common estimation structures and problems, *IEEE Transactions on Acoustic, Speech, and Signal Processing*, *27*, 2024–2036. 5.2.2
- Dobson, M., F. Ulaby, M. Hallikainen, and M. El-Rayes (1985), microwave dielectric behavior of wet soil-part ii: dielectric mixing models, *IEEE Transactions on Geoscience and Remote Sensing*, *23*, 35–46. 2.2.3, 4.1, 6.3.2, 6.3.3
- Douville, H., and F. Chauvin (2004), Relevance of soil moisture for seasonal climate predictions: a preliminary study, *Climate Dynamics*, *16*, 719–736. 1.2
- Dubois, P., J. van Zyl, and E. Engman (1995), Measuring soil moisture with imaging radars, *IEEE Transactions on Geoscience and Remote Sensing*, *33*, 915–926. 1.1, 1.3, 7.1
- England, A. (1990), Radiobrightness of diurnally heated, freezing soil, *IEEE Transactions on Geoscience and Remote Sensing*, *28*, 464–476. 2.2.3

References

- Entekhabi, D., et al. (1999), An agenda for land surface hydrology research and a call for the second international hydrological decade, *Bulletin of the American Meteorological Society*, 80, 2043–2058. 1.1, 1.2, 1.4, 5.1, 6.2
- Entekhabi, D., et al. (2004), An Earth system pathfinder for global mapping of soil moisture and land freeze/thaw: The Hydrosphere State (HYDROS) mission concept, *IEEE Transactions on Geoscience and Remote Sensing*, 42, 2659–2673. 1.3.2
- Escorihuela, M., Y. Kerr, P. de Rosnay, J. Wigneron, J. Calvet, and F. Lemaitre (2007), A simple model of the bare soil microwave emission at L-band, *IEEE Transactions on Geoscience and Remote Sensing*, 45, 1978–1987. 2.2.4
- Flores, L., D. Entekhabi, and R. Bras (2009), Assimilation of smap measurements for soil moisture-based military trafficability assessment at tactical scales, *IEEE Journal of Selected Topics in Earth Observations and Remote Sensing*, p. in press. 1.2
- Frate, F. D., P. Ferrazzoli, and G. Schiavon (2003), Retrieving soil moisture and agricultural variables by microwave radiometry using neural networks, *Remote Sensing of the Environment*, 84, 174–183. 2.3
- Gabarró, C., M. Portabella, M. Talone, and J. Font (2009), Toward an optimal SMOS ocean salinity inversion algorithm, *IEEE Transactions on Geoscience and Remote Sensing*, 6(3), 509–513. 4.3
- Galatsanos, N., and A. Katsaggelos (1992), Methods for choosing the regularization parameter and estimating the noise variance in image restoration and their relation, *IEEE Transactions on Geoscience and Remote Sensing*, 1, 322–336. 5.2.2
- Gonzalez, R., and R. Woods (1993), *Digital Image Processing*, Addison-Wesley. 5.2.1, 5.2.2, 5.2.2
- Gutman, G., and A. Ignatov (1998), The derivation of the green vegetation fraction from noaa/avhrr data for use in numerical weather prediction models, *International Journal of Remote Sensing*, 19, 1533–1543. 6.2.3, 6.3.2
- Hallikainen, M., F. Ulaby, M. Dobson, M. El-Rayes, and L. Wu (1985), Microwave dielectric behaviour of wet soil-part 1: Empirical models and experimental observations, *IEEE Transactions on Geoscience and Remote Sensing*, GE-23, 25–34. 2.2.3, 2.5, 6.3.2, 6.3.3, B
- Hansen, P. (1998), *Rank-Deficient and Discrete Ill-Posed Problems*, Philadelphia. 5.2.1
- Hornbuckle, B., and A. England (2005), Diurnal variation of vertical temperature gradients within a field of maize: implications for stellite microwave radiometry, *IEEE Geoscience and Remote Sensing Letters*, 2, 74–77. 2.2.5
- Hornbuckle, B., A. England, R. de Roo, M. Fischman, and D. Boprie (2003), Vegetation canopy anisotropy at 1.4 GHz, *IEEE Transactions on Geoscience and Remote Sensing*, 41, 2211–2222. 2.2.5
- Huete, A. (1988), A Soil-Adjusted Vegetation Index (SAVI), *Remote Sensing of Environment*, 25, 295–309. 6.2.3

- Idso, B., T. Schmugge, R. Jackson, and R. Reginto (1975), The utility of surface temperature measurements for remote sensing of soil water studies, *Journal of Geophysical Research*, *80*, 3044–3049. 1.3, 6.1
- ISMN (2010), International Soil Moisture Network, <http://www.ipf.tuwien.ac.at/insitu/>. 6.2
- ITU-R P.531-6 (2001), Ionospheric propagation data and prediction methods required for the design of satellite services and systems, *Tech. rep.*, ITU. 2.1.5, 2.4, B
- Jackson, T. (1993), Measuring surface soil moisture using passive microwave remote sensing, *Hydrological Processes*, *7*, 139–152. 6.3.2, 6.3.2
- Jackson, T., and T. Schmugge (1991), Vegetation effects on the microwave emission from soils, *Remote Sensing of the Environment*, *36*, 203–212. 1.3, 2.2.5
- Jackson, T., T. Schmugge, and J. Wang (1982), Passive microwave sensing of soil moisture under vegetation canopies, *Water Resources Research*, *18*, 1137–1142. 1.3, 2.2.5
- Jackson, T., T. Schmugge, and E. Engman (1996), Remote sensing applications to hydrology: soil moisture, *Hydrological Science Journal*, *41*, 517–530. 1.1, 7.1
- Jackson, T., D. LeVine, A. Hsu, A. Oldak, P. Starks, C. Swift, et al. (1999), Soil moisture mapping at regional scales using microwave radiometry: The Southern Great Plains hydrology experiment, *IEEE Transactions on Geoscience and Remote Sensing*, *37*, 2136–2151. 1.4, 2.2.4
- Jackson, T., A. Hsu, A. van de Griend, and J. Eagleman (2004), Skylab L-band microwave radiometer observations of soil moisture revisited, *International Journal of Remote Sensing*, *25*, 2585–2606. 1.1, 1.3
- Kerr, Y., P. Waldteufel, J. Wigneron, J. Font, and M. Berger (2001), Soil moisture retrieval from space: The soil moisture and ocean salinity (SMOS) mission, *IEEE Transactions on Geoscience and Remote Sensing*, *39*, 1729–1735. 1.1, 1.3.1, 1.3.1
- Kim, G., and A. Barros (2002), Downscaling of remotely sensed soil moisture with a modified fractal interpolation method using contraction mapping and ancillary data, *Remote Sensing of the Environment*, *83*, 400–413. 1.4
- Kirdiashev, K., A. Chukhantsev, and A. Shutko (1979), Microwave radiation of the Earth's surface in presence of vegetation cover, *Radio Engineering Electronics Physics*, *24*, 256–264. 2.2.5, 2.2.5
- Krajewski, W., et al. (2006), A remote sensing observatory for hydrologic sciences: A genesis for scaling to continental hydrology, *Journal of Water Resources Research*, *42*. 1.1
- Kurum, M., R. Lang, P. O'Neill, A. Joseph, T. Jackson, and M. Cosh (2009), L-band radar estimation of forest attenuation for active/passive soil moisture inversion, *IEEE Transactions on Geoscience and Remote Sensing*, *47*, 3036–3040. 2.3
- LeVine, D. M., and S. Abraham (2002), The effect of the ionosphere on remote sensing of the sea surface salinity from space: absorption and emission at L-band, *IEEE Transactions on Geoscience and Remote Sensing*, *40*, 771–782. 2.1.5

References

- Limaye, A., W. Crosson, C. Laymon, and E.G.Njoku (2004), Land cover-based optimal deconvolution of PALS L-band microwave brightness temperatures, *Remote Sensing of the Environment*, *92*, 497–506. 7.3.1
- Mallat, S. (1998), *A Wavelet Tour of Signal Processing*, Elsevier. 5.2.3
- Marquardt, D. (1963), An algorithm for least-squares estimation of nonlinear parameters, *Journal of the Society for Industrial and Applied Mathematics*, *11*, 431–441. 2.3
- Martín-Neira, M., S. Ribó, and A. J. Martín-Polegre (2002), Polarimetric mode of MIRAS, *IEEE Transactions on Geoscience and Remote Sensing*, *40*, 1755–1768. 1.3.1, 2.1.6
- Martínez-Vázquez, A., A. Camps, J. M. López-Sánchez, M. Vall-llossera, and A. Monerris (2009), Numerical simulation of the full-polarimetric emissivity of vines and comparison with experimental data, *Remote Sensing*, *1*, 300–317. 2.2.5
- Masson, V., J. Champeaux, F. Chauvin, and C. Meriguet (2003), A global database of land surface parameters at 1-km resolution in meteorological and climate models, *Journal of Climate*, *16*, 1261–1282. 3.2, 4.2
- McMullan, K., M. Brown, M. Martín-Neira, W. Rits, J. Martí, and J. Lemanczyk (2008), SMOS: The payload, *IEEE Transactions on Geoscience and Remote Sensing*, *46*, 594–605. 1.3.1, 6.3.1
- Meesters, A., R. de Jeu, and M. Owe (2005), Analytical derivation of the vegetation optical depth from the microwave polarization difference index, *IEEE Geoscience and Remote Sensing Letters*, *2*, 121–123. 2.2.5, 2.3, 3.4
- Merlin, O., A. Chehbouni, Y. Kerr, E. Njoku, and D. Entekhabi (2005), A combined modeling and multipectral/multiresolution remote sensing approach for disaggregation of surface soil moisture: application to SMOS configuration, *IEEE Transactions on Geoscience and Remote Sensing*, *46*, 2036–2050. 1.4
- Merlin, O., J. Walker, A. Chehbouni, and Y. Kerr (2008a), Towards deterministic down-scaling of SMOS soil moisture using MODIS derived soil evaporative efficiency, *Remote Sensing of the Environment*, *112*, 3935–3946. 1.4
- Merlin, O., A. Chehbouni, J. Walker, R. Panciera, and Y. Kerr (2008b), A simple method to disaggregate passive microwave-based soil moisture, *IEEE Transactions on Geoscience and Remote Sensing*, *46*, 786–796. 1.4, 5.2.2
- Minasny, B., and A. McBratney (2007), Estimating the water retention shape parameter from sand and clay content, *Soil Science Society of America Journal*, *71*, 1105–1110. 6.3.2
- Mironov, V., M. Dobson, V. Kaupp, V. Komarov, and V. Kleshchenko (2004), Generalized refractive mixing dielectric model for moist soils, *IEEE Transactions on Geoscience and Remote Sensing*, *42*, 773–785. 2.2.3, 6.3.2
- Mission Objectives and Scientific Requirements of the SMOS mission (2003), MRD, version 5, *Tech. rep.*, European Space Agency, <http://www.cesbio.ups-tlse.fr/>. 1.1, 1.3.1, 3.1, 4.1
- Mo, T., B. Choudhury, T. Schmugge, and T. Jackson (1982), A model for microwave emission from vegetation-covered fields, *Journal of Hydrology*, *184*, 101–129. 2.2.5, 3.1

- Monerris, A. (2009), Experimental estimation of soil emissivity and its application to soil moisture retrieval in the SMOS mission, Ph.D. thesis, Universitat Politècnica de Catalunya, <http://www.tesisenxarxa.net/TDX-1228109-101841/>. 1.3.1, 1.4, 4.2, 6.3.3, 6.3.3
- Monerris, A., et al. (2009), The GPS and radiometric joint observations experiment at the REMEDHUS site (Zamara-Salamanca region, Spain), in *Proc. IEEE Geoscience and Remote Sensing Symposium*. 6.2.1
- Narayan, U., V. Lakshmi, and E. Njoku (2004), Retrieval of soil moisture from passive and active L/S band sensor (PALS) observations during the Soil Moisture Experiment in 2002 (SMEX02), *Remote Sensing of the Environment*, 92, 483–496. 1.4, 7.3.2
- Narayan, U., V. Lakshmi, and T. Jackson (2006), High resolution estimation of soil moisture using L-band radiometer and radar observations made during the SMEX02 experiments, *IEEE Transactions on Geoscience and Remote Sensing*, 44, 1545–1554. 1.4
- National Research Council (2007), Earth science and applications from space: national imperatives for the next decade and beyond, *Tech. rep.*, Space Studies Board, National Academies Press, (Available at <http://www.nap.edu>). 1.1, 1.3.2
- Neelamani, R., H. Choi, and R. Baraniuk (2004), ForWaRD: Fourier-Wavelet Regularized Deconvolution for Ill-Conditioned Systems, *IEEE Transactions on Signal Processing*, 52, 418–433. 5.2.3
- Newton, R., and J. Rouse (1980), Microwave radiometer measurements of soil moisture content, *IEEE Transactions on Antennas and Propagation*, 28, 680–686. 2.2.4, 2.6, B
- Njoku, E., and D. Entekhabi (1996), Passive microwave remote sensing of soil moisture, *Journal of Hydrology*, 184, 101–129. 1.1, 1.3, 7.1
- Njoku, E., W. Wilson, S. Yueh, S. Dinardo, F. Li, T. Jackson, V. Lakshmi, and J. Bolten (2002), Observations of soil moisture using a passive and active low-frequency microwave airborne sensor during SGP99, *IEEE Transactions on Geoscience and Remote Sensing*, 40, 2659–2673. 1.1, 1.3, 1.4
- Owe, M., R. de Jeu, and J. Walker (2001), A methodology for surface soil moisture and vegetation optical depth retrieval using the microwave polarization difference index, *IEEE Transactions on Geoscience and Remote Sensing*, 39, 1643–1654. 2.2.5
- Panciera, R., J. Walker, J. Kalma, E. Kim, K. Saleh, and J. Wigneron (2009), Evaluation of the SMOS L-MEB passive microwave soil moisture retrieval algorithm, *Remote Sensing of the Environment*, 113, 435–444. 2.2.4
- Pardé, M., J. Wigneron, P. Waldteufel, Y. Kerr, A. Chanzy, S. Sobjaerg, and N. Skou (2004), N-parameter retrievals from L-band microwave observations acquired over a variety of crop fields, *IEEE Transactions on Geoscience and Remote Sensing*, 42, 1168–1178. 2.3, 3.1, 3.2, 3.3, 3.4, 4.1, 4.2, 4.3, 4.4.2
- Peake, W. (1959), Interaction of electromagnetic waves with some natural surfaces, *IEEE Transactions on Antennas and Propagation*, 7, 324–329. 2.2.4

References

- Pellarin, T., J. Wigneron, J. Calvet, and P. Waldteufel (2003), Global soil moisture retrieval on a synthetic L-band brightness temperature data set, *Journal of Geophysical Research*, *108*, 4364. 3.1, 3.2, 4.1
- Pellenq, J., Y. Kerr, and G. Boulet (2003), Scaling and assimilation of SMOS data for hydrology, *Proc. IEEE Geoscience and Remote Sensing Symposium*, *5*, 3064–3066. 1.4
- Petropoulos, G., T. Carlson, M. Wooster, and S. Islam (2009), A review of Ts/VI remote sensing based methods for the retrieval of land surface energy fluxes and soil surface moisture, *Progress in Physical Geography*, *33*, 224–250. 6.1
- Piles, M., A. Camps, M. Vall-llossera, and M. Talone (2009), Spatial-resolution enhancement of SMOS data: a deconvolution-based approach, *IEEE Transactions on Geoscience and Remote Sensing*, *47*(7), 2182–2192. 1.6, B
- Piles, M., M. Vall-llossera, A. Camps, M. Talone, and A. Monerris (2010), Analysis of a least-squares soil moisture retrieval algorithm from L-band passive observations, *Remote Sensing*, *2*, 352–374. 2.7, B
- Portabella, M., and A. Stoffelen (2004), A probabilistic approach for SeaWinds data assimilation, *Quarterly Journal of the Royal Meteorological Society*, *130*, 127–152. 4.3
- Price, J. (1977), Thermal inertia mapping: a new view of the Earth, *Journal of Geophysical Research*, *82*, 2582–2590. 1.3, 6.1
- Randa, J., et al. (2008), Recommended terminology for microwave radiometry, *Tech. rep.*, National Institution of Standards and Technology, <http://www.grss-ieee.org/education/standard-terminology/>. 2.1.5, 2.1.6, 2.1.6
- Richter, R. (1996), A spatially adaptive fast atmospheric correction algorithm, *International Journal of Remote Sensing*, *17*, 1201–1214. 6.2.1
- Rouse, J., R. Hass, J. Shell, D. Deering, and J. Harlan (1974), Monitoring the vernal advancement of retrogradation of natural vegetation. final report., *Tech. rep.*, NASA/GSFC, Type III. 6.2.1
- Sabia, R., A. Camps, M. Talone, M. Vall-llossera, and J. Font (2010), Determination of sea surface salinity error budget in the soil moisture and ocean salinity mission, *IEEE Transactions on Geoscience and Remote Sensing*, *48*, 1684–1693. 1.3.1
- Sahr, K., D. White, and A. Kimerling (2003), Geodesic Discrete Global Grid Systems, *Cartography and Geographic Information Science*, *30*, 121–134. 1.3.1
- Saleh, K., et al. (2009), Soil moisture retrievals at L-band using a two-step inversion approach (COSMOS/NAFE'05 Experiment), *Remote Sensing of the Environment*, *113*, 1304–1312. 1.4, 2.2.4, 2.3, 3.2, 4.2
- Schmugge, T., P. O'Neill, and J. Wang (1986), Passive microwave soil moisture research, *IEEE Transactions on Geoscience and Remote Sensing*, *24*, 12–22. 1.1, 1.3, 2.2
- Schmugge, T., W. Kustas, J. Ritchie, T. Jackson, and A. Rango (2002), Remote sensing in hydrology, *Advances in Water Resources*, *25*, 1367–1385. 7.1

- Schneeberger, K., M. Schwank, C. Stamm, P. de Rosnay, C. Mätzler, and H. Flüßler (2004), Topsoil structure influencing soil water retrieval by microwave radiometry, *Vadose Zone Journal*, *3*, 1169–1179. 2.2.4
- SEPS Architectural Detailed Design Document (2006), ADDED V5.0, *Tech. rep.*, European Space Agency, <http://cassiopea.estec.esa.int/SEPS/Documents/>. 1.3.1, 4.4.1
- Shaman, J., and J. Day (2005), Achieving operational hydrologic monitoring of mosquito-borne disease, *Emerging Infectious Diseases*, *11*, 1343–1350. 1.2
- Shi, J., J. Wang, A. Hsu, P. O'Neill, and E. T. Engman (1997), Estimation of bare surface soil moisture and surface roughness parameter using L-band SAR image data, *IEEE Transactions on Geoscience and Remote Sensing*, *35*, 1254–1266. 1.1, 1.3, 7.1
- Shutko, A., and E. M. Reutov (1982), Mixture formulae applied in estimation of dielectric and radiative characteristics of soils and grounds at microwave frequencies, *IEEE Transactions on Geoscience and Remote Sensing*, *GE-20*, 29–32. 1.1
- SMOS Algorithm Theoretical Bases Document (2007), ATBD, Issue 3.a, *Tech. rep.*, European Space Agency, <http://www.cesbio.ups-tlse.fr/>. 2.3, 3.2, 4.2, 4.3, 4.4.1, 4.5
- Talone, M., A. Camps, B. Moure, R. Sabia, M. Vall-llossera, J. Gourrion, C. Gabarró, and J. Font (2009), Simulated SMOS Levels 2 and 3 products: the effect of introducing ARGO data in the processing chain and its impact on the error induced by the vicinity of the coast, *IEEE Transactions on Geoscience and Remote Sensing*, *47*, 3041–3050. 1.3.1
- Tsegaye, T. D., W. Crosson, C. Laymon, M. Schamschula, and A. Johnson (2003), *Scaling Methods in Soil Physics*, chap. Application of a neural network-based spatial disaggregation scheme for addressing scaling of soil moisture, pp. 261–277, CRC Press. 1.4
- Ulaby, F., and A. Wilson (1985), Microwave attenuation properties of vegetation canopies, *IEEE Transactions on Geoscience and Remote Sensing*, *GE-23*, 746–753. 2.2.5, 3.1
- Ulaby, F., R. Moore, and A. Fung (1981), *Microwave remote sensing active and passive, Vol. 1 and 2*, Artech House. 1.1, 2.1, 2.3, 2.2.3, 4.3, 5.2.2, 5.3.3, B
- Valencia, E., et al. (2008), Initial results of an airborne light-weight L-band radiometer, in *Proc. IEEE Geoscience and Remote Sensing Symposium*. 5.4.1, 6.2.1
- van de Griend, A., and J. Wigneron (2004), The b-factor as a function of frequency and canopy type at H-polarization, *IEEE Transactions on Geoscience and Remote Sensing*, *42*, 786–794. 2.2.5, 3.1, 3.3, 4.1, 4.4.2
- Wagner, W., G. Blsch, P. Pampaloni, J. Calvet, B. Bizarri, J. Wigneron, and Y. Kerr (2007), Operational readiness of microwave remote sensing of soil moisture for hydrologic applications, *Nordic Hydrology*, *38*, 1–20. 1.1
- Waldteufel, P., and G. Caudal (2002), About off-axis radiometric polarimetric measurements, *IEEE Transactions on Geoscience and Remote Sensing*, *40*, 1435–1439. 3.2
- Waldteufel, P., J. Boutin, and Y. Kerr (2003), Selecting an optimal configuration for the soil moisture and ocean salinity mission, *Radio Science*, *38*, 8051. 1.3.1

References

- Walker, J., and P. Houser (2004), Requirements of a global near-surface soil moisture satellite mission: accuracy, repeat time, and spatial resolution, *Advances in Water Resources*, *27*, 785–801. 1.2
- Wan, Z. (2008), New refinements and validation of the MODIS land-surface temperature/emissivity products, *Remote Sensing of the Environment*, *112*, 59–74. 3.3
- Wang, J. (1983), Passive microwave sensing of soil moisture content: the effects of soil bulk density and surface roughness, *Remote Sensing of the Environment*, *13*, 329–344. 2.2.4
- Wang, J., and B. Choudhury (1981), Remote sensing of soil moisture content over bare field at 1.4 GHz frequency, *Journal of Geophysical Research*, *86*, 5277–5282. 1.3, 2.2.4
- Wang, J., and T. Schmugge (1980), An empirical model for the complex dielectric permittivity of soils as a function of water content, *IEEE Transactions on Geoscience and Remote Sensing*, *GRS-18*, 288–295. 2.2.3, 3.2, 4.1, 4.2, 6.3.2, 6.3.3
- Wang, X., H. Xie, H. Guan, and X. Zhou (2007), Different responses of MODIS-derived NDVI to root-zone soil moisture in semi-arid and humid regions, *Journal of Hydrology and Earth System Sciences*, *340*, 12–14. 1.3, 6.1
- Wigneron, J., A. Chanzy, J. Calvet, and N. Bruguier (1995), A simple algorithm to retrieve soil moisture and vegetation biomass using passive microwave measurements over crop fields, *Remote Sensing of the Environment*, *51*, 331–341. 2.2.5, 2.2.5, 3.1
- Wigneron, J., P. Waldteufel, A. Chanzy, J. Calvet, and Y. Kerr (2000), Two-dimensional microwave interferometer retrieval capabilities over land surfaces (SMOS-mission), *Remote Sensing of the Environment*, *73*, 270–282. 3.4
- Wigneron, J., L. Laguerre, and Y. Kerr (2001), A simple parameterization of the L-band microwave emission from rough agricultural soils, *IEEE Transactions on Geoscience and Remote Sensing*, *39*, 1696–1707. 2.2.4, 3.2, 4.2, 6.3.2
- Wigneron, J., J. Calvet, T. Pellarin, A. V. der Griend, M. Berger, and P. Ferrazzoli (2003), Retrieving near-surface soil moisture from microwave radiometric observations: current status and future plans, *Remote Sensing of the Environment*, *85*, 489–506. 2.3
- Wigneron, J., Y. Kerr, P. Waldteufel, et al. (2007), L-band Microwave Emission of the Biosphere (L-MEB) model: description and calibration against experimental data sets over crop fields, *Remote Sensing of the Environment*, *107*, 639–655. 2.3
- Young, R., J. Walker, N. Yeoh, A. Smith, K. Ellett, O. Merlin, and A. Western (2008), Soil moisture and meteorological observations from the Murrumbidgee catchment, *Tech. rep.*, Department of Civil and Environmental Engineering, University of Melbourne. 6.3.1, 6.3.3
- Yueh, S. (2000), Estimates of Faraday rotation with passive microwave polarimetry for microwave remote sensing of Earth surfaces, *IEEE Transactions on Geoscience and Remote Sensing*, *38*, 2434–2438. 2.1.5
- Yueh, S., W. Wilson, F. Li, S. Nghiem, and W. Ricketts (1995), Polarimetric measurements of sea surface brightness temperatures using an aircraft K-band radiometer, *IEEE Transactions on Geoscience and Remote Sensing*, *33*, 86–92. 2.1.6

- Zhan, X., S. Miller, N. Chauhan, L. Di, and P. Ardanuy (2002), Soil moisture visible/infrared radiometer suite algorithm theoretical basis document, *Tech. rep.*, Raytheon systems company. 6.1, 6.2.3
- Zhan, X., P. Houser, J. Walker, and W. Crow (2006), A method for retrieving high-resolution surface soil moisture from Hydros L-band radiometer and radar observations, *IEEE Transactions on Geoscience and Remote Sensing*, *44*, 1534–1544. 1.4, 7.4.1
- Zhang, Y., and M. Wegehenkel (2006), Integration of MODIS data into a simple model for the spatial distributed simulation of soil water content and evapotranspiration, *Remote Sensing of the Environment*, *104*, 393–408. 6.1
- Zundo, M., H. Barré, and A. Hahne (2005), SMOS product definition baseline SO-TN-ESA-GS-1250, *Tech. rep.*, ESA/ESTEC. 1.3.1

List of publications

Journal papers

1. **M. Piles**, A. Camps, M. Vall-llossera, A. Monerris, M. Talone, and J.M. Sabater, Performance of Soil Moisture Retrieval Algorithms using Multiangular L-band Brightness Temperatures, *Water Resources Research*, in press, 2010.
2. **M. Piles**, A. Camps, M. Vall-llossera, M. Talone and A. Monerris, Analysis of a Least-Squares Soil Moisture Retrieval Algorithm from L-band Passive Observations, *Remote Sensing*, vol. 2, pp. 352-374, January 2010.
3. **M. Piles**, D. Entekhabi and A. Camps, A Change Detection Algorithm for Retrieving High-Resolution Soil Moisture from SMAP Radar and Radiometer Observations, *IEEE Transactions on Geoscience and Remote Sensing*, vol. 47, pp. 4125-4131, December 2009.
4. **M. Piles**, A. Camps, M. Vall-llossera, M. Talone, Spatial Resolution Enhancement of SMOS Data: a Deconvolution-based Approach, *IEEE Transactions on Geoscience and Remote Sensing*, vol. 47, pp 2182-2192, July 2009.
5. A. Monerris, P. Benedicto, M. Vall-llossera, A. Camps, E. Santanach, **M. Piles**, R. Prehn, Assessment of the Topography Impact on Microwave Radiometry at L-band, *Journal of Geophysical Research*, vol. 113, December 2008.
6. M. Talone, A. Camps, A. Monerris, M. Vall-llossera, P. Ferrazzoli and **M. Piles**, Surface Topography and Mixed-Pixel Effects on the Simulated L-Band Brightness Temperatures, *IEEE Transactions on Geoscience and Remote Sensing*, vol. 45, pp. 1996-2003, July 2007.

Conference papers

1. **M. Piles**, A. Camps, M. Vall-llossera, N. Sánchez, J. Martínez-Fernández, A. Monerris, G. Baroncini-Turricchia, C. Pérez-Gutiérrez, A. Aguasca, R. Acevo, and X. Bosch-Lluís, Soil Moisture Downscaling Activities at the REMEDHUS Cal/Val site and its Application to SMOS, *Proc. 11th Specialist Meeting on Microwave Radiometry and Remote Sensing Applications*, Washington DC, US, March 2010.
2. A. Monerris, C. Pérez-Gutiérrez, J. 'Alvarez-Mozos, M. Vall-llossera, E. Valencia, J. Martínez-Fernández, G. Baroncini-Turricchia, N. Rodríguez- Álvarez, **M. Piles**, N. Sánchez, and A. Camps, Preparatory Activities at the REMEDHUS SMOS Cal/Val Site: Characterization of Bare Soils and Effect of Surface Roughness, *Proc. 11th Specialist Meeting on Microwave Radiometry and Remote Sensing Applications*, Washington DC, US, March 2010.

3. **M. Piles**, D. Entekhabi, and A. Camps, A Change Detection Algorithm for Retrieving High Resolution Soil Moisture from SMAP Radar and Radiometer Observations: Flood Applications, *Proc. 11th Plinius Conference on Mediterranean Storms*, Barcelona, Spain, September 2009.
4. C. Pérez-Gutiérrez, N. Sánchez-Martín, J. Martínez-Fernández, G. Baroncini-Turricchia, J. Álvarez-Mozos, M. Vall-llossera, A. Aguasca, A. Camps, A. Monerris, N. Rodríguez-Álvarez, **M. Piles**, R. Acevo, Determinación de parámetros de rugosidad y vegetación in situ para la estimación de la humedad del suelo: El experimento GRAJO(GPS and Radiometric Joint Observations), *Congreso de la Asociación Española de Teledetección*, Calatayud, Spain, September 2009.
5. A. Monerris, N. Rodríguez, A. Camps, M. Vall-llossera, **M. Piles**, J. Martínez-Fernández, N. Sánchez-Martín, C. Pérez-Gutiérrez, G. Baroncini-Turricchia, R. Acevo, A. Aguasca, The GPS and Radiometric Joint Observations Experiment at the REMED-HUS site (Zamora-Salamanca Region, Spain), *Proc. IEEE Geoscience and Remote Sensing Symposium*, Cape Town, South Africa, July 2009.
6. **M. Piles**, D. Entekhabi, A. Camps, A Change Detection Algorithm for Retrieving High-Resolution Surface Soil Moisture from SMAP L-band Radar and Radiometer Observations, *Proc. IEEE Geoscience and Remote Sensing Symposium*, Cape Town, South Africa, July 2009.
7. E. Valencia, J. F. Marchán-Hernández, A. Camps, N. Rodríguez-Álvarez, J. M. Tarongí, **M. Piles**, I. Ramos-Perez, X. Bosch-Lluis, M. Vall-Llossera, P. Ferré, Experimental Relationship between the Sea Brightness Temperature Changes and the GNSS-R Delay-Doppler Maps: Preliminary Results of the ALBATROSS Field Experiments, *Proc. IEEE Geoscience and Remote Sensing Symposium*, Cape Town, South Africa, July 2009.
8. M. Talone, A. Camps, J. F. Marchan-Hernandez, J. M. Tarongí, **M. Piles**, X. Bosch-Lluis, I. Ramos-Perez, E. Valencia, N. Rodriguez-Alvarez, M. Vall-Llossera, P. Ferré, Preliminary Results of the Advanced LBand Transmission and Reflection Observation of the Sea Surface (ALBATROSS) Campaign: Preparing the SMOS Calibration and Validation Activities, *Proc. IEEE Geoscience and Remote Sensing Symposium*, Cape Town, South Africa, July 2009.
9. **M. Piles**, A. Camps, M. Vall.llossera and M. Talone, Spatial Resolution Enhancement of SMOS data: a Combined Fourier Wavelet Approach, *Proc. IEEE Geoscience and Remote Sensing Symposium*, Boston, USA, July 2008.
10. A. Camps, M. Vall.llossera, **M. Piles**, F. Torres, I. Corbella and N. Duffo, Improving the Spatial Resolution of Synthetic Aperture Radiometer Imagery using Auxiliary Information: Application to the SMOS Mission, *Proc. IEEE Geoscience and Remote Sensing Symposium*, Boston, USA, July 2008.
11. A. Monerris, M. Vall-llossera, A. Camps, and **M. Piles**, Rock Fraction Effects on the Surface Soil Moisture Estimates from L-Band Radiometric Measurements, *Proc. IEEE Geoscience and Remote Sensing Symposium*, Boston, USA, July 2008.

12. J.F. Marchán-Hernández, M. Vall-llossera, A. Camps, N. Rodríguez-Álvarez, I. Ramos-Pérez, E. Valencia, X. Bosch-Lluis, M. Talone, J. M. Tarongí and **M. Piles**, Ground-based GNSS-R Measurements with the PAU Instrument and their Application to the Sea Surface Salinity Retrieval: First Results, *Proc. IEEE Geoscience and Remote Sensing Symposium*, Boston, USA, July 2008.
13. A. Monerris, M. Vall-llossera, A. Camps and **M. Piles**, Radiometric Observations of Vines from the Green Period to the Withering, *Proc. 10th Specialist Meeting on Microwave Radiometry and Remote Sensing Applications*, Firenze, Italia, March 2008.
14. A. Monerris, P. Benedicto, M. Vall-llossera, A. Camps, **M. Piles**, E. Santanach and R. Prehn, Topography Effects on the L-band Emissivity of Soils: TuRTLE 2006 Field Experiment, *Proc. IEEE Geoscience and Remote Sensing Symposium*, Barcelona, July 2007.
15. **M. Piles**, A. Camps, M. Vall-llossera, A. Monerris, M. Talone and J.L. Álvarez-Pérez, Deconvolution Algorithms in Image Reconstruction for Aperture Synthesis Radiometers, *Proc. IEEE Geoscience and Remote Sensing Symposium*, Barcelona, July 2007.
16. M. Talone, A. Camps, A. Monerris, M. Vall-llossera, P. Ferrazzoli and **M. Piles**, Surface Topography and Mixed Pixel Effects on the Simulated L-band Brightness Temperatures, *Proc. 9th Specialist Meeting on Microwave Radiometry and Remote Sensing Applications*, San Juan, Puerto Rico, March 2006.
17. Monerris, E. Santanach, M. Vall-llossera, A. Camps, M. Cardona, **M. Piles** and C. Cantero, Roughness Effects on the L-band Emission of Bare Soils: The T-REX Field Experiments, *Proc. IEEE Geoscience and Remote Sensing Symposium*, Denver, Colorado, August 2006.
18. Monerris, M. Vall-llossera, A. Camps, R. Sabia, A. Martínez-Vázquez, I. Ledesma and **M. Piles**, Field Experiments to Improve the Soil Emission Models at L-band: Contribution of the UPC to the ESA SMOS Mission, *Proc. Recent Advances in Quantitative Remote Sensing*, Valencia, Spain, September 2006.

Workshops

1. **M. Piles**, A. Camps, M. Vall-llossera, N. Sánchez-Martín, A. Monerris, J. Martínez-Fernández, A. Aguasca, R. Acevo, C. Pérez-Gutiérrez and G. Baroncini, Downscaling of SMOS-derived Soil Moisture during SMOS Calibration/Validation Phase at the REMEDHUS site, *European Space Agency Living Planet Symposium*, Bergen, Norway, July 2010.
2. **M. Piles**, A. Camps, M. Vall-llossera, R. Acevo, A. Aguasca, and X. Bosch-Lluis, An evaluation of soil moisture downscaling techniques using L-band airborne observations, *3rd International workshop on Marine Technology*, Barcelona, Spain, November 2009.
3. A. Monerris, N. Rodríguez-Álvarez, **M. Piles**, M. Vall-llossera, and A. Camps, Microwave radiometry and GNSS reflectometry over land, *Earth Observation and Water Cycle Workshop*, ESA/ESRIN, Frascati, Italy, November 2009.

References

4. **M. Piles**, A. Camps, A. Monerris, M. Vall.llosera, J. Martínez-Fernández, N. Sánchez-Martín, C. Pérez- Gutiérrez and G. Baroncini, Calibration and Validation of SMOS-derived soil moisture data in the central part of the Duero basin: experimental activities, *International Workshop on Microwave Remote Sensing for Land Hydrology Research and Applications*, Oxnard, California, USA, October 2008.
5. A. Monerris, N. Rodríguez-Álvarez, A. Camps, M. Vall-llossera and **M. Piles**, Overview of UPC Field Experiments over Land Surfaces, *International Workshop on Microwave Remote Sensing for Land Hydrology Research and Applications*, Oxnard, California, USA, October 2008.